NASA Contractor Report 4199

An Analysis for High Speed Propeller-Nacelle Aerodynamic Performance Prediction

Volume I—Theory and Application

T. Alan Egolf, Olof L. Anderson,
David E. Edwards, and Anton J. Landgrebe
United Technologies Research Center
East Hartford, Connecticut

Prepared for
Lewis Research Center
under Contracts NAS3-20961,
NAS3-22142, and NAS3-22257

National Aeronautics
and Space Administration

Scientific and Technical
Information Division

1988

FOREWORD

The original development of the analysis presented herein was sponsored by the NASA Lewis Research Center under contract number NAS3-20961. Additional program development and application was funded under contract numbers NAS3-22142 and NAS3-22257. The NASA Project Manager for the first two contracts was Mr. Lawrence J. Bober while Mr. Chris Hughes was the manager for the last contract. Their assistance in providing the input data and test results for the test cases, implementing the computer analysis on the NASA Lewis Research Center's computer system, and extensively applying the analysis at NASA to further exercise the code is gratefully acknowledged.

Principal UTRC participants in the original contract activity were Mr. T. Alan Egolf, Dr. Olof L. Anderson, Mr. David E. Edwards and Mr. Anton J. Landgrebe. Mr. Egolf was the principal investigator with primary responsibility for the propeller portion of the analysis and was the principal preparer of the final report. Dr. Anderson was a co-investigator with primary responsibility for the nacelle portion of the analysis which is based on his earlier developed diffuser code. Mr. Edwards provided valuable technical support to the nacelle activity. Mr. Landgrebe (Manager, Aeromechanics Research) was the UTRC Project Manager and formulator of the earlier blade/wake technology upon which the propeller portion of the analysis is based.

The authors wish to extend their appreciation to Mr. Richard Ladden and other personnel of the Hamilton Standard Division of the United Technologies Corporation who provided technical assistance based upon their own developmental experience with Prop-Fan analyses, and developed the isolated airfoil data package incorporated in the computer analysis. Also, acknowledgement is given to Dr. James E. Carter, of UTRC, for his application of an alternate nacelle analysis to the test case reported herein.

This report is divided into the following two volumes: Volume I, Theory and Application, and Volume II, User's Manual.

SUMMARY

A computer program, the Propeller/Nacelle Aerodynamic Performance Prediction Analysis (PANPER), was developed for the prediction and analysis of the performance and airflow of propeller-nacelle configurations operating over a forward speed range inclusive of high speed flight typical of recent prop-fan designs. A propeller lifting line, wake program was combined with a compressible, viscous center body interaction program, originally developed for diffusers, to compute the propeller-nacelle flow field, blade loading distribution, propeller performance, and the nacelle forebody pressure and viscous drag distributions. The computer analysis is applicable to single and coaxial counter-rotating propellers. The blade geometries can include spanwise variations in sweep, droop, taper, thickness, and airfoil section type. In the coaxial mode of operation the analysis can treat both equal and unequal blade number and rotational speeds on the propeller disks. The nacelle portion of the analysis can treat both free air and tunnel wall configurations including wall bleed.

The analysis was applied to many different sets of flight conditions using selected aerodynamic modeling options. The influence of different propeller-nacelle-tunnel wall configurations was studied. Comparisons with available test data for both single and coaxial propeller configurations are presented along with a discussion of the results.

TABLE OF CONTENTS

TABLE OF CONTENTS (Cont'd)

TABLE OF CONTENTS (Cont'd)

INTRODUCTION

Brief History of the Problem

The recognition by NASA and Hamilton Standard in 1974 of the potential for improved fuel efficiency of a high speed propeller relative to the conventional gas-turbine engine, for aircraft which cruise at high subsonic speeds, has established a renewed interest in this propulsion concept. This interest has resulted in a major participation in the technical evaluation of this concept by the Hamilton Standard Division (HSD) of the United Technologies Corporation (reference 1). A photograph of a conceptual model of the high speed propeller (Prop-Fan) is presented in Figure 1. In initial model tests conducted in a wind tunnel at the United Technologies Research Center (UTRC), under a NASA contract to Hamilton Standard, sufficiently high values of propeller efficiency were measured to encourage further interest in the concept (reference 2). The requirement for a computer analysis to assist in the design of the high speed propeller and the spinner-nacelle was recognized, and the task for the development of such an analysis was awarded to UTRC. Since these initial model tests, several different model designs have now been successfully tested by Hamilton Standard at UTRC and at NASA Lewis Research Center. The models tested have varied from blades of basically straight design to blade designs with severe blade sweep. Thus the requirement that the analysis be able to handle a high range of blade geometry designs is well established.

Due to the aerodynamic complexity associated with the high speed propeller, previously existing analyses had clearly identifiable limitations. Development of a propeller-nacelle system for operation at high subsonic or transonic speeds resulted in several problems due to the transonic flow regime and the contemplated propeller design. Of particular concern were the problems associated with calculating the correct local inflow conditions at the high speed propeller blades due to the interference effect of the nacelle and the strong compressibility effects on the airfoil characteristics and induced inflow calculations. The severe blade geometry designs also have a significant impact on the induced velocity calculations for the propeller (reference 3). Figure 2 illustrates the large variation of blade geometry in a fixed coordinate system with changes in blade pitch angle which must be handled correctly. It is recognized that the high speed operating conditions and geometric configurations of the Prop-Fan compromise many of the assumptions associated with the methodology used for conventional low speed propeller designs. Analyses based on higher level modeling assumptions (full potential, Euler, and Navier-Stokes) are desirable and have been developed to some degree. However, these analyses are computationally expensive to run. As a result, the propeller analysis to be described was developed to model the propeller

induced flow field using a computationally efficient lifting-line theory with ad-hoc aerodynamic modeling features to approximate the influence of the transonic operating conditions and three-dimensionality of the Prop-Fan design.

In addition to the difficult propeller aerodynamic problem, the propeller-nacelle flow field is expected to be influenced by viscous effects. Since friction losses due to the nacelle boundary layer will be considerably higher at transonic speeds than at subsonic speeds, a reliable propeller-nacelle flow field prediction method should have the ability to account for viscous phenomena.

A procedure, which includes viscous effects, has been developed at UTRC for predicting circumferentially averaged flow in compressor stages (references 4 and 5). The procedure solves a set of viscous flow equations in the flow region of interest and thereby simultaneously accounts for blade effects and endwall effects. (In a propeller-nacelle field, the nacelle is analogous to the compressor endwall.)

For application to the high speed propeller problem, the above analysis for the blade-nacelle interaction was expanded to include blade and wake induced aerodynamic effects through the coupling with a lifting line propeller model and an appropriate propeller wake model. This analysis was also modified to treat the propeller nacelle problem under free flight conditions or wind tunnel conditions including wall bleed by using appropriate boundary conditions.

The United Technologies Research Center, along with the Hamilton Standard and Sikorsky Aircraft Divisions of UTC, has been actively engaged in the development and evaluation of computer analyses for predicting the induced effects of propellers and single and dual counter-rotating helicopter rotors. In particular, a propeller performance analysis was developed at Hamilton Standard based on an earlier UTRC analysis, which has recently been adapted to high speed propellers. With this background, existing computer methods for lifting line and wake modeling techniques were combined into a new propeller analysis to handle the special requirements of the high speed propeller, and the propeller analysis was combined with the blade-nacelle analysis to provide a self-consistent propeller-nacelle performance prediction analysis.

Technical Background

The usual method of approaching the propeller design problem is based upon lifting line-vortex theory or momentum theory approaches to determine the blade loading distribution (references 6 through 19), described briefly in the following section. Although these approaches, as commonly used, can be applied successfully for certain flow situations, they do suffer two serious drawbacks. First, either these approaches do not account for the interaction between the nacelle and propeller flow field at all, or they account for the interaction via empirical correction factors. Secondly, usual propeller analyses ignore cascade effects along the inner portion of the propeller disk which may be important for propellers having a large number of blades. Considering the interaction problem first, it should be noted that the blade nacelle interaction flow represents a highly complex nonlinear process in which the nacelle and blades mutually interact to a significant extent. Both the physical contour of the nacelle and the viscous boundary layer developing on the nacelle surface can affect the propeller-nacelle performance. For example, the nacelle shape and viscous effects can modify the propeller wake development thereby modifying the induced velocity at the propeller flow. In addition, the nacelle can modify the pressure distribution and the resulting velocities through the propeller blade row, particularly in the inner region of the blade disk thereby again affecting propeller loading and performance.

Similarly the flow about the nacelle is affected by the presence of the propeller blades. The nacelle drag (viscous drag due to the nacelle boundary layer and drag due to the pressure field) is expected to be influenced by the presence of the blades. Although the propeller-nacelle interaction problem has not been addressed in detail, in propeller calculations to date, similar interactions have been addressed in compressor design analyses. In particular, a computer program developed at UTRC (the UTRC ADD code), which calculates the circumferentially averaged flow through a compressor stage and which includes the effects of endwalls, has been used successfully for the compressor through flow problem (references 4 and 5). The code solves the entire flow field at once and does not require an iteration between the viscous wall flow and the nominally inviscid flow in the center of the stage. This same procedure also takes into account the cascade effects which occur in a compressor stage and which as previously mentioned, are expected to occur in the inner portion of a propeller disk. Therefore, based upon previous experience with this compressor stage code, the propeller-nacelle interaction problem was considered to be a reasonable application for this code.

Propeller Analysis

The field of low speed propeller and rotor aerodynamics is abound with literature describing the need for and use of variable inflow performance analyses and the use of vortex wake models (e.g., references 5 through 33). UTRC has recognized this requirement and has helped develop these analyses to a high level of sophistication. Today most all rotor and propeller manufacturers use some type of a variable inflow model based on wake modeling for accurate performance predictions.

Goldstein (reference 6), Theodorsen (reference 7), and other early investigators realized the need for accurate descriptions of the propeller inflow distributions for performance predictions based on consideration of the propeller wake. Early lifting line performance analyses (references 6 through 8) used helical, uncontracted Goldstein type wake models (classical undistorted wake models) to obtain variable inflow distributions for performance predictions. These analyses gave better predictions than simple momentum and blade element analyses, but for many applications they still left a large gap between the analytical and actual test results. Distorted wake geometries which more accurately represent the actual physical wake geometry were required.

For static thrust conditions, investigators attempted to compute wake distortions numerically using free wake interaction analyses where the wake was free to move under its own induced influence (references 14 and 15). These analyses, although more accurate than undistorted wake analyses, are too time consuming in terms of computer costs to be used in standard design procedures. Therefore, several investigators studied the results of these calculations and flow visualization studies (references 21 through 27) in an attempt to develop accurate empirical wake description formulae. In particular, pioneering efforts by Gray (reference 25), Landgrebe (reference 26), and Ladden (reference 17) experimentally defined the wake geometry characteristics of hovering rotors and statically thrusting propellers. Their results were generalized to give simple analytical expressions for the distorted wake geometries based on the operating conditions and rotor parameters. The generalized wake equations of Landgrebe and Ladden have now been used for several years by both the helicopter and propeller manufacturers in lifting line performance analyses for static thrust conditions with some modifications for each application. A sample of the distorted wake and classical wake geometries is represented in figure 3.

At low or moderate propeller forward flight speeds, the need for induced inflow distributions and vortex wake modeling is also of importance. At these flight speeds a much larger portion of the propeller wake transport velocity comprises the forward flight speed. Because of this, axial wake distortions do not play as important a role in the wake geometry's influence on the inflow

distribution at the propeller blades as in the static thrust case. However, propeller self-induced radial contraction effects on the wake geometry are still of importance for accurate descriptions of the inflow distributions. Although normally neglected in previous operational propeller analyses for moderate speed flight, it is recognized that the nacelle does displace the propeller wake and alter the flowfield at the propeller disk. However, this effect is stronger in the region of the blade root and not near the blade tip where it would be most influential on the blade loading.

At high speeds, accurate performance calculations also require the prediction of detailed inflow distributions which are dependent on vortex wake modeling. The propeller self-induced wake distortions of lower flight speeds are small at high flight speeds and the wake transport velocity is dominated by the propeller forward flight speed. At these speeds other factors may affect the wake geometry more than the induced effects of the wake on itself. Such influences as the effects of nacelle body blockage (or accelerations) can distort the wake geometry, particularly near the inboard regions of the propeller blades. Also, the effect of compressibility can alter the wake's influence at the propeller disk. The influence of the propeller wake and the resulting inflow distribution at the propeller blades is thus important for accurate performance predictions.

Nacelle Analysis

In previous compressor analyses for the circumferential average flow, two broad assumptions are generally made. The first assumption, or quasi-steady assumption, states that the flow is steady (constant in time) when examined in a coordinate system rotating with the angular velocity of the propeller. Thus, at each radial position, temporal and circumferential averages of the flow are the same. This assumption is equally applicable to a compressor or propeller for axial freestream flow. The second assumption states that the flow is primarily inviscid and implies viscous forces are small compared to blade induced forces on the airflow. This assumption is also generally applicable to either the compressor or propeller problem (except in the immediate vicinity of the compressor endwall or propeller nacelle). Based on these assumptions, the circumferential averaged equations of motion may be derived. In the past, two methods have been developed to solve these equations: the matrix through flow analysis (references 34 and 35), and the streamline curvature method (references 36 and 37). Both procedures solve for a "core" flow, which is inviscid, and account for the presence of blade forces by arbitrarily specifying work and loss distributions at the blade trailing edge. Once the core flow is calculated the annulus wall boundary layer (nacelle boundary layer) may be calculated from the known pressure distribution. If the growth of the annulus boundary layer significantly affects the pressure distribution, a solution of the strong interaction problem exists and requires an iteration between two flow fields: the core flow, and the boundary layer flow.

Recently, this strong-interaction problem was solved at UTRC in a more direct manner without iteration between flow fields (references 37 and 38). This viscous method, which forms the basis for the UTRC ADD code, can be described in the following manner. First an orthogonal coordinate system is constructed from a plane potential flow solution such that the stream function forms the coordinate normal to the wall and the velocity potential forms the coordinate tangent to the wall. The equations of motion may be greatly simplified by assuming that the velocity normal to the potential flow streamlines is small compared to the streamwise velocity. Such an assumption is quite reasonable as the potential flow streamlines are expected to be a good approximation to the actual streamlines. This procedure reduces the governing viscous flow equations to a parabolic system of partial differential equations which can be solved by a forward marching numerical integration procedure. Furthermore, it can be shown that the resulting solution has the same order of accuracy for viscous flows as the streamline curvature method has for inviscid flows. Thus the viscous-flow strong interaction with the wall (nacelle) boundary layer is solved without the need for iterations between different flow fields; i.e., the inviscid core flow away from the nacelle and the nacelle boundary layer flow.

Combined Analysis

The approach taken to create the combined propeller-nacelle analysis was to use a modified version of the original UTRC ADD code which includes the required refinements necessary for the nacelle-propeller problem. The calculation of the blade forces was handled by creating as a portion of the combined analysis an expanded propeller lifting line solution procedure based on existing UTC propeller and helicopter performance analyses. This combined analysis consists of two portions (propeller and nacelle) which compute the combined propeller-nacelle performance by interfacing the required transfer of internal data (flow field properties, wake geometry displacements, and blade forces) which will influence the respective solution procedures from the two different portions of the analysis. This procedure allows the combined analysis to have the ability to also calculate isolated propeller or isolated nacelle performance for comparisons with the combined propeller-nacelle configuration performance predictions. A simplified diagram of the program task structure of the combined analysis is presented in figure 3. The details of the technical approach of each portion of the analysis and the coupling procedure of the combined analysis are presented in the following sections.

TECHNICAL APPROACH - PROPELLER

Overview

In the following sections, a method of analysis for the predictions of the integrated and local spanwise blade air loading for the high speed propeller is presented. The analysis presented for the high speed propeller portion of the combined propeller-nacelle code is a logical extension of the development of the Prescribed Wake Method of Landgrebe (reference 26) for hovering rotors which was modified and applied to statically thrusting propellers by Landgrebe and then Ladden (reference 17). Although this analysis is directed towards the high speed propeller flight regime, no restrictions have been made in the assumptions which would limit it to only high speed flight. Briefly the Prescribed Wake method is derived utilizing lifting line theory, and incorporates a wake model consisting of a finite number of trailing vortex filaments. The trajectories and positioning of these filaments must be prescribed. Figure 4 is an illustration of two types of prescribed wake models used for hovering rotors (similar representations are used for propellers). Once the position of the wake is fixed, a matrix solution is solved utilizing the Kutta-Joukowski and Biot-Savart relations, and the airfoil lift properties. This solution yields the blade circulation distribution and the corresponding induced velocities. The blade element velocity diagram is then constructed, and with the use of two-dimensional airfoil data corrected for three-dimensional tip effects, the airloading distribution (lift and drag) is obtained. The total thrust and power are then established through spanwise integration.

The use of the propeller analysis in conjunction with the nacelle code is handled in a coupled manner, whereby the nacelle's influence on the propeller is incorporated through modifications to the noninduced inflow at the propeller disk and to the wake model. The theory of the analysis as outlined in the following sections does not make direct reference to the nacelle's influence on the velocites. It is thus understood that the noninduced velocity terms include the nacelle's influence in the following propeller related sections.

Coordinate Systems

Within the lifting line propeller analysis there are three coordinate systems used. Two of these coordinate systems are fixed to the same origin. These are a cartesian and a cylindrical coordinate system whose origin is defined by the intersection of the propeller's axis of rotation and the blade pitch axis of rotation (which are always assumed to intersect). The axial coordinate directions for both of these coordinate systems are identical and coincident with the axis of rotation of the propeller, positive in the direction of flight. The blade pitch axis of rotation is coincident with the x axis in the cartesian coordinate system. The relationships between the x, y plane and the r, ϕ plane are the conventional relationships for right handed coordinate systems. Figure 5 illustrates these two coordinate systems. The cartesian coordinate system is used to define the input blade geometry, while the cylindrical coordinate system is used for computations involving the wake and blade geometry because of the symmetry of the problem in this coordinate system.

The third coordinate system is called the blade element coordinate system. The local origins for this system are defined by a reference line running along the blade in the spanwise direction. Generally the quarter chord line, which is not necessarily straight, is used for the reference line. This is a locally orthogonal coordinate system whose unit directions are defined in the local spanwise, chordwise and normalwise directions. The local spanwise direction is defined as positive in the direction from the root to the tip along the local tangent to the blade reference line noted above. The local chordwise direction is defined to be perpendicular to the local spanwise direction and in the plane of the zero angle of attack of the local airfoil section, positive in the direction of the trailing edge to the leading edge. The local positive normalwise direction is defined as the direction of the local vector cross product of the spanwise to the chordwise direction vectors.

Figure 6 is an illustration of this coordinate system. The blade element coordinate system is the computational coordinate system used in the lifting line analysis solution. The reasons for using this coordinate system will be explained in the following sections. The transformation relationships for the various quantities used in the analysis between the various coordinate systems are shown in Appendix A.

Propeller Lifting Line Theory

The concept of a prescribed wake lifting line theory applied to propellers consists essentially of assuming that the blade of each propeller can be represented by a segmented bound vortex lifting line located along the propeller blade quarter chord line with a spanwise varying concentrated circulation strength which at each segment is proportional to the local blade lift (Kutta-Joukowski Law). The wake is assumed to be modeled by a system of discrete trailing vortices whose circulation strength is a function of radial variations in the blade loading (lift) distribution. A finite length wake is used which is of sufficient length to approximately model an infinite length wake. Figure 7 is an illustration of this modeling procedure. There are N segments modeling the blade which can be arbitrary in length. The circulation strength of the bound vortex over each segment is assumed to be constant, and the values of the strength are determined by the aerodynamics of the problem which are discussed in the next section. Because the flow field sensed by the single propeller under steady axial flight conditions is time independent, there is no azimuthal variation in blade loading for the single propeller configuration. The wake shed by the blade can be modeled by a series of trailing segmented vortex filaments shed from the junction points of the blade bound vortex segments whose circulation strength is constant over the complete length of the filament and equal to the difference in the circulation strengths of the adjacent bound vortex segments. Figure 7 also illustrates this feature. The trailing filament segmentation is defined by a specified azimuthal step size ($\Delta\psi$), each segment modeled by a straight line vortex segment. The location of the trailing wake segment end points are prescribed by using various types of wake models.

The influence of the bound and trailing vortex elements at any field point is computed by using the Biot-Savart Law for finite length, straight line segments of constant strength (reference 8) as shown in Appendix B. In this analysis the calculation is done in the cylindrical coordinate system and then transformed to the blade element coordinate system. The induced velocity vector, $\bar{v}_{TR}$, at a local blade element in the local blade element coordinate system due to any trailing segment can be written as

$$\bar{v}_{TR} = v_{TR_s}\ \bar{i}_s + v_{TR_c}\ \bar{i}_c + v_{TR_n}\ \bar{i}_n \qquad (1)$$

where the subscripts s, c and n denote the spanwise, chordwise and normalwise directions respectively. Any one of these induced velocity components can be expressed as the sum of the products of the trailing segment circulation strength and the appropriate component of the geometric influence coefficient computed from the Biot-Savart Law as noted in Appendix B. For example the normalwise induced velocity from the lth segment of the kth filament of the mth blade is

$$v_{TR_n} = \Gamma_{TR}(k,m)GC_{TR_n}(\ell,k,m) \tag{2}$$

Because the trailing filament circulation for a single propeller configuration is the same for all blades at a fixed radial position and constant along the trailing filament, the induced velocity component at a field point can be expressed as a summation over all of the blades and filament segments of the kth filament.

$$v_{TR_n} = \Gamma_{TR}(k) \cdot \sum_m \sum_\ell GC_{TR_n}(k,\ell,m) \tag{3}$$

Letting

$$GC^*_{TR_n}(k) = \sum_m \sum_\ell GC_{TR_n}(k,\ell,m) \tag{4}$$

the normalwise induced velocity component at a blade element point due to the kth filament of all blades then can be written as

$$v_{TR_n} = \Gamma_{TR}(k)GC^*_{TR_n}(k) \tag{5}$$

For the discrete modeling process, the trailing circulation is the difference between adjacent bound circulations. Making this substitution in the above equation, summing the influence for all filaments and regrouping the influence coefficients for like bound circulations into new influence coefficients yields the total normalwise induced velocity component for the complete trailing wake geometry at a blade element point in terms of the bound circulation from N segments and the respective wake influence coefficients

$$v_{TR_n} = \sum_{i=1}^{N} \Gamma(i)\tilde{GC}_{TR_n}(i) \tag{6}$$

Computing the bound vortex influences at a blade element point from all of the blades yields a similar expression for the normalwise induced velocity component in terms of the bound influence coefficients, GC_{B_n} and bound circulations.

$$v_{B_n} = \sum_{i=1}^{N} \Gamma(i)GC_{B_n}(i) \tag{7}$$

Combining the above two relationships to define the total induced velocity component at a blade element point yields for the normalwise component.

$$v_n = v_{B_n} + v_{TR_n} = \sum_{i=1}^{N} \Gamma(i) GC_n(i) \qquad (8)$$

Similar expressions exist for the chordwise and spanwise components of induced velocity. Of course, if the blade element point is near a filament segment (bound or trailing wake) the influence for the particular segment must be handled correctly due to the strong singularity. Generally a core radius is assigned to the segment and if the blade element point is within that radius the influence is neglected or modified in a prescribed manner as described in a later section (Vortex Core Modeling).

Thus, for a prescribed wake geometry and lifting line geometry, the induced influence can be defined in terms of the unknown bound circulation distribution. Blade element theory is then used to define the relationships necessary to solve for the bound circulation.

Blade Element Aerodynamics

The modeling of the propeller blade by the lifting line approach defines the inflow and the effective angle of attack at each blade segment in the aerodynamic model. Tabulated airfoil data is used to relate the effective angle of attack at each blade segment to the local lift and drag characteristics. Also, the use of tabulated airfoil data, acquired from two-dimensional airfoil tests, inherently accounts for the chordwise vorticity distribution (related to chordwise pressure distribution) and the Kutta condition. This permits the blade segments to be represented by bound vortex segments which have a circulation strength representative of the integrated chordwise vorticity distribution. For a lifting line model, the unknown quantity is then the spanwise bound circulation distribution which is related to the lift distribution through the Kutta-Joukowski relationship as will be described.

In figure 8 the relationships between the relative velocity vectors and the geometric quantities in the local blade element coordinate system are illustrated. It is assumed that the propeller is operating in steady axial flight. This blade element coordinate system is the computational coordinate system and the solution for the blade forces is done in this coordinate system. One reason to use this coordinate system is that the angle of attack is small and the chordwise velocity is the dominant velocity term in this coordinate system. This makes the solution numerically easier to obtain in the blade element coordinate system. Another reason to use this coordinate system is that the resolution of the blade geometry quantities and velocities into this coordinate system implicity handles the concept of yaw or skewed flow aerodynamics. The concept of skewed flow aerodynamics (in the two-dimensional sense) basically states that the pressure force on an airfoil section is independent of the spanwise flow velocity component, and thus a function of only the velocity components in the plane normal to the local chordwise direction (reference for local blade element coordinate system). In the relationships to follow, the aerodynamic quantities used are assumed to be those which correspond to the local blade element coordinate system. Each blade element section is treated as a two-dimensional section with the influence of the other sections transmitted through the induced flowfield.

Linear Aerodynamics

The aerodynamic relationships for the blade forces include nonlinear behavior with certain quantities. The nonlinear solution is obtained by using the linearized solution with the appropriate nonlinear iteration techniques as will be described in the next section.

In the blade element coordinate system the local velocity vector diagrams appear similar to the equivalent velocity vector diagrams of a statically thrusting propeller. In this coordinate system the solution on the blades is independent of time. For this reason, the linearization procedure and

solution techniques are best performed in the local blade element coordinate system. The linearizations follow directly from those presented in reference 17 for the statically thrusting propeller.

Consider a local blade element section, at station i, of chord length c_i and thickness t_i, whose zero angle of attack line is at an angle θ_{Bi} with the local noninduced velocity vector in the plane defined by the normalwise and chordwise unit normals. The local lift force, per unit span, L_i, can be related to the circulation strength of the bound vortex, Γ_i at the quarter chordline by the Kutta-Joukowski relationship:

$$L_i = \rho V_i \Gamma_i \tag{9}$$

where V_i is the magnitude of the total velocity vector normal to the blade element section (including induced terms).

This relationship can be rewritten in terms of the local section lift coefficient C_{ℓ_i}, as:

$$\Gamma_i = \frac{1}{2} c_i V_i C_{\ell_i} \tag{10}$$

Assuming operation below stall, and linearizing the local section lift coefficient as the combination of linear section lift curve slope a_i, and effective section angle of attack α_i, the relationship for the circulation becomes:

$$\Gamma_i = \frac{1}{2} a_i c_i V_i \alpha_i \tag{11}$$

This lift curve slope, obtained from tabulated airfoil data, is of course a function of the airfoil type and Mach number for the local section. It is noted that the linear lift curve slope assumption and other linearizations introduced below are removed by the nonlinear techniques to be described in the next section.

The magnitude of the local velocity vector* in the normalwise chordwise plane is just,

---

* In this section and the following section, upper case V's with subscripts denoting component direction always denote noninduced velocity, while lower case v's with subscripts denoting component direction always denote induced velocity. V_i is the magnitude of the total velocity (noninduced and induced).

$$V_i = \left[(V_{c_i} + v_{c_i})^2 + (V_{n_i} + v_{n_i})^2 \right]^{1/2} \tag{12}$$

Assuming that in the blade element plane the induced and normal velocities are small compared with the chordwise noninduced velocity yields the following approximation for the section circulation.

$$\Gamma_i = \frac{1}{2} c_i a_i V_{c_i} \alpha_i \tag{13}$$

From figure 7 it can be seen that the blade element section angle of attack is just:

$$\alpha_i = \tan^{-1}\left(\frac{V_{n_i} + v_{n_i}}{V_{c_i} + v_{c_i}} \right) \tag{14}$$

If the chordwise induced velocity is neglected, the section angle of attack is assumed to be small, and the normal velocity is also small with respect to the chordwise value, the blade circulation is further approximated as

$$\Gamma_i = \frac{1}{2} c_i a_i V_{c_i} \left(\theta_{B_i} + \frac{v_{n_i}}{V_{c_i}} \right) \tag{15}$$

where

$$\theta_{B_i} = \frac{V_{n_i}}{V_{c_i}} \tag{16}$$

The normalwise induced velocity, v_{n_i} is a function of the combined wake geometry from all blades and the blade circulations, where the normalwise geometric influence coefficients are computed using the Biot-Savart Law (see section entitled: Lifting Line Theory). Then from equation (8), the blade circulation of section i can be written as:

$$\Gamma_i = \frac{1}{2} a_i c_i \left(V_{c_i} \theta_{B_i} + \sum_{j=1}^{N} GC_{n_j} \Gamma_j \right) \tag{17}$$

This relationship is valid under the above assumptions for each blade element section, thus a system of simultaneous linear equations in terms of the unknown blade circulations for each section can be written as a matrix equation in the form:

$$[M] \cdot \{\Gamma\} = \{C\} \tag{18}$$

and the solution for the circulations can be obtained directly using standard solution techniques, either iterative or direct techniques. Because the number of unknowns is relatively small, the analysis uses a Gauss-Jordan reduction technique.

Once the blade circulations are known, the section angle of attack is known. Using this angle of attack, the actual sectional lift and drag coefficients are obtained from tabulated airfoil data (C_ℓ and C_d) for each section. The components for forces in the blade element coordinate system are then computed from this information. Transformation of these forces to the cylindrical coordinate system and with the appropriate integrations in the axial and rotational directions results in the thrust and torque respectively for the propeller blades. The thrust and power coefficients are computed as

$$C_T = \frac{T}{\rho n^2 D^4} \tag{19}$$

$$C_P = \frac{P}{\rho n^3 D^5} \tag{20}$$

Nonlinear Aerodynamics

The assumptions used to obtain a linear solution for the blade aerodynamics can be invalid for several reasons; the linearization of the airfoil data may be inappropriate for high Mach number or stalled conditions, the small angle assumptions may not be appropriate, and neglecting the induced velocities to determine certain quantities may introduce further error. The cumulative effect of all of the assumptions may introduce significant differences in the solution for certain conditions. To remove all of the assumptions used in the linearized aerodynamic model, a technique based upon the linearized aerodynamic solution is used. This nonlinear solution technique is identical to that presented in reference 17. For this iterative technique, the nonlinear aerodynamic relationships are expressed in terms of both the linearized relationships and the difference between the linear and nonlinear terms, where the difference is obtained from a previous solution iteration level. The formulation follows.

The assumption that the local section lift coefficient is linearized is removed by rewriting the section lift coefficient as a linear portion and a correction to the linear portion:

$$C_{\ell_i}^{\nu} = a_i \alpha_i^{\nu} + C_{\alpha_i}^{\nu-1} \tag{21}$$

where

$$C_{\alpha_i}^{\nu-1} = C_{\ell_i}^{\nu-1} - a_i \alpha_i^{\nu-1} \tag{22}$$

The superscripts denote iteration level. Here, the local lift coefficient is obtained from the tabulated airfoil data as a function of the blade element section airfoil type, local section blade element Mach number computed including induced velocities, and the nonlinear angle of attack. The assumption that the total velocity can be approximated by the chordwise value is removed by expressing the total velocity as

$$V_i^{\nu} = V_{c_i}^{\nu} + C_{v_i}^{\nu-1} \tag{23}$$

where

$$C_{v_i}^{\nu-1} = \left[(V_{n_i} + v_{n_i}^{\nu-1})^2 + (V_{c_i} + v_{c_i}^{\nu-1})^2\right]^{1/2} - V_{c_i} \tag{24}$$

represents the correction term to the original linear assumption.

The small angle assumption is removed by computing the section angle of attack as

$$\alpha_i^{\nu} = \theta_{B_i} + \phi_i^{\nu} + C_{\phi_i}^{\nu-1} \tag{25}$$

where

$$\phi_i^{\nu} = \frac{v_{n_i}^{\nu}}{V_{c_i}} \tag{26}$$

and

$$C_{\phi}^{\nu-1} = \tan^{-1}\left(\frac{V_{n_i} + v_{n_i}^{\nu-1}}{V_{c_i} + v_{c_i}^{\nu-1}}\right) - \theta_{B_i} - \phi_i^{\nu-1} \tag{27}$$

is the nonlinear correction term. Combining the relationships in the original equation for the blade section circulation and expressing the induced velocity in terms of the geometric influence coefficients yields:

$$\Gamma_i^{\nu} = \frac{1}{2} c_i a_i \left(V_{c_i} \theta_{B_i} + \sum_{j=1}^{N} GC_{n_j} \Gamma_j^{\nu} + C_{F_i}^{\nu-1}\right) \tag{28}$$

where

$$C_{F_i}^{\nu-1} = C_{v_i}^{\nu-1}\left(\frac{C_{\alpha_i}^{\nu-1}}{a_i} + \theta_{B_i} + \frac{v_{n_i}^{\nu-1}}{V_{c_i}} + C_{\phi_i}^{\nu-1}\right) + V_{c_i}\left(\frac{C_{\alpha_i}^{\nu-1}}{a_i} + C_{\phi_i}^{\nu-1}\right) \tag{29}$$

is the combined nonlinear correction term.

If the combined nonlinear correction term, C_{F_i}, is set to zero, the linearized equation for the blade circulation results. If the above equation is rewritten in matrix form in terms of the unknown blade circulations, a system of simultaneous linear equations results where the correction term is lagged in iteration level.

$$\left|M\right| \left\{\Gamma^{\nu}\right\} = \left\{C + C_F^{\nu-1}\right\} \tag{30}$$

This system of equations can be solved by direct or indirect methods for each iteration level where the previous solution is used to obtain the latest nonlinear correction terms for each iteration. The initial correction terms are obtained from the initital linearized solution. In the current analysis the Gauss-Jordan reduction technique is used to obtain the solution at each iteration level.

The resulting local blade forces in the chordwise and normalwise directions are obtained in the same manner as is done for the linearized solution, and the resultant integrated forces are obtained.

Skewed Flow Drag Model

As noted in an earlier section (Blade Element Aerodynamics), the calculation of the blade forces in the blade element coordinate system removes the necessity of considering skewed flow in an explicit manner in the aerodynamic relationships for the pressure lift and pressure drag forces. However, the drag coefficient data available for airfoils generally does not distinguish between the pressure drag and friction drag components. Since the friction drag should be dependent on the total velocity, a skewed flow drag model is formulated below using the tabulated drag coefficient data. This model attempts to include the additional component of skin friction drag neglected by the blade element aerodynamic model described in the previous section.

Figure 9 is a vector diagram of the drag force and components of the drag force at a local blade element station for a condition with a velocity component in the spanwise direction. From this diagram it can be seen that the total drag force, D (per unit area), has been broken into two portions, a pressure drag force, D_{pr}, and a skin friction drag force, D_{fr}. The pressure drag acts only in the direction of the flow in the plane defined by the chordwise and normalwise directions, while the friction drag is assumed to act in the direction of the total velocity. The conventional method of neglecting the spanwise velocity component, and computing the drag force, with the

pressure and friction forces combined in the drag coefficient (C_d), yield the following expression for the components of drag per unit area in the blade element coordinate system.*

$$D_s = 0 \tag{31}$$

$$D_c = \frac{1}{2} \rho \, C_d \, V_c \, (V_c^2 + V_n^2)^{1/2} \tag{32a}$$

$$D_n = \frac{1}{2} \rho \, C_d \, V_n (V_c^2 + V_n^2)^{1/2} \tag{33a}$$

Separating the drag coefficient into pressure and friction portions and expanding yields

$$D_c = \frac{1}{2} \rho V_c \left[C_{d_{pr}} (V_c^2 + V_n^2)^{1/2} + C_{d_{fr}} (V_c^2 + V_n^2)^{1/2} \right] \tag{32b}$$

$$D_n = \frac{1}{2} \rho V_n \left[C_{d_{pr}} (V_c^2 + V_n^2)^{1/2} + C_{d_{fr}} (V_c^2 + V_n^2)^{1/2} \right] \tag{33b}$$

for the conventional formulation.

If the friction drag and pressure drag components are known separately it can be seen from the diagram in figure 9 that the components of the drag force should be

$$D_s = \frac{1}{2} \rho V_s \, C_{d_{fr}} (V_c^2 + V_s^2 + V_n^2)^{1/2} \tag{34}$$

$$D_c = \frac{1}{2} \rho V_c \left[C_{d_{pr}} (V_c^2 + V_n^2)^{1/2} + C_{d_{fr}} (V_c^2 + V_s^2 + V_n^2)^{1/2} \right] \tag{35}$$

$$D_n = \frac{1}{2} \rho V_n \left[C_{d_{pr}} (V_c^2 + V_n^2)^{1/2} + C_{d_{fr}} (V_c^2 + V_s^2 + V_n^2)^{1/2} \right] \tag{36}$$

---

* In this section, V_c, V_n and V_s denote velocity components which include noninduced and induced velocities.

From these relationships it can be seen that for large spanwise velocities, the drag force components can be significantly different as compared with the conventional formulation. The above formulation has been incorporated into the analysis as an optional feature by assuming that the skin friction drag coefficient is approximately represented by the drag coefficient of the section at zero angle of attack, C_{d_o}, and thus the pressure drag coefficient is just the difference between the total drag coefficient and C_{d_o}.

$$C_{d_{pr}} = C_d - C_{d_o} \tag{37}$$

Tip Relief Models

The high speed propeller tip experiences high subsonic and transonic flow conditions at normal design operating conditions. These flow conditions, coupled with the high degree of three-dimensionality of the problem and the use of two-dimensional airfoil characteristics, make the application of the lifting line model inappropriate without some type of tip relief scaling procedures applied to the airfoil characteristics in the tip region. Two such models have been incorporated into the propeller analysis. The first is a model based on unswept fixed wing theory. The second is a model based on conical flow theory applied to swept wings.

Evvard Tip Relief Model

For flow conditions where the tip Mach number is greater than one and the forward speed Mach number less than one, it is necessary to correct the pressure forces in the propeller tip Mach cone region. Figure 10 illustrates the region on the blade under consideration. In reference 41, charts for a scaling factor which is a function of the ratio of blade chord to blade radius, radial location on the blade, and tip Mach number are presented which can be used to correct the spanwise variation of lift and drag due to lift. These charts where derived from the results for fixed wings presented by Evvard in reference 42. In the current analysis this scaling factor is included as an option to the aerodynamic model. It should be noted that this model was developed from fixed wing results for application to conventional propeller blades without sweep, thus the application to swept blades is questionable.

The application of the scaling function to the lift and drag due to lift is done by determining the spanwise location where the tip Mach cone intersects the blade at a specified fraction of the chord from the leading edge

(generally the trailing edge is used). All blade stations from this location to the blade tip are modified by the appropriate scaling value if the local free stream Mach number is greater than or equal to one. These scaling values are tabulated and are an integral part of the analysis. Both the spatial location used to define the point for the definition of the tip Mach cone location and the fraction of the chord for the intersection location can be varied in the analysis. An analytical description for the tip relief scaling values is also available in the analysis and it gives slightly different values than the original tables.

Conical Flow Theory Tip Relief Model

Generally, high speed propeller designs require significant blade sweep, therefore the application of the tip relief model based on Evvard's model may not be appropriate for these applications. Conical flow theory for thin swept wings with sweep can be used to provide a tip relief model for application to the swept propeller blade. The model as developed for application to swept propeller blades in based on a tapered, swept, fixed wing configuration which assumes that the wing leading edge is linear and subsonic and that the wing trailing edge is linear and supersonic for a constant supersonic freestream Mach number distribution. Furthermore, the span of the wing is assumed to be of sufficient length to avoid overlap of the tip Mach cones on the wing surface and the wing tip is squared off. These assumptions result in the existence of two regions on the surface of the wing for which a scaling function based on the ratio of the three-dimensional section lift to the two-dimensional section lift can be obtained. The regions on the surface of the wing are depicted in figure 11 which also defines the wing planform shape and the coordinate system used in the formulation. On the surface of the wing in region I along any section chordline of length c, the chordwise pressure distribution based on conical flow theory (reference 43) for a subsonic leading edge in the above configuration can be integrated along the chordline to obtain the appropriate section lift in the region,

$$C_{L_I} = \frac{4m\alpha}{\beta E'(k)} \frac{1}{c} \int_{x_{LE}}^{x_2} \frac{x}{(x^2 - x_{LE}^2)^{1/2}} \, dx = \frac{4m\alpha}{\beta E'(k)} \frac{1}{c} \left(x_2^2 - x_{LE}^2\right)^{1/2} \qquad (38)$$

where $\beta = (M^2-1)^{1/2}$, $m = \beta \cot \Lambda_{LE}$, $k = (1-m^2)^{1/2}$

and $E'(k)$ is the complete Elliptic Integral of the second kind of modulus k.

On the surface of the wing in region II the chordwise integration of the pressure distribution, approximately a constant deficit along the chordline from the value at the edge of this region, is performed to obtain the appropriate section lift in the region.

$$C_{L_{II}} = \frac{4m\alpha}{\beta E'(k)} \frac{1}{c} \int_{x_2}^{x_{TE}} \left[\frac{x_2}{(x_2^2 - x^2)^{1/2}} - \frac{1}{\sqrt{2(1+m)(1-y/s)}} \right] dx$$

$$= \frac{4m\alpha}{\beta E'(k)} \frac{(x_{TE} - x_2)}{c} \left[\frac{x_2}{(x_2^2 - x_{TE}^2)^{1/2}} - \frac{1}{\sqrt{2(1+m)(1-y/s)}} \right] \tag{39}$$

These two section lifts are combined to obtain the total section lift. The two-dimensional section lift for the same freestream Mach number is known.

$$C_{L_{2D}} = \frac{4\alpha}{\beta} \tag{40}$$

The scaling function is then just the ratio of the three-dimensional to the two-dimensional section lift.

$$f = \frac{m}{E'(k)} \frac{1}{c} \left\{ (x_2^2 - x_{LE}^2)^{1/2} + (x_{TE} - x_2) \left[\frac{x_2}{(x_2^2 - x_{TE}^2)^{1/2}} - \frac{1}{\sqrt{2(1+m)(1-y/s)}} \right] \right\} \tag{41}$$

This scaling function can then be applied to the supersonic region of the propeller tip by assuming that the length of this region is equivalent to the semi-span of a supersonic wing with a freestream Mach number equal to the propeller tip Mach number. This scaling function is included as an option in the analysis. Since the model as derived is based on a constant Mach number and the propeller blade senses a radially varying distribution, an approximation for this effect can be incorporated by scaling the relationship of equation (40) by the ratio defined below based on Prandtl-Glauert compressible scaling rule.

$$f_M = \frac{\sqrt{M_T^2 - 1}}{\sqrt{M(y)^2 - 1}} \tag{42}$$

This feature is also included in the analysis as an option available to the user.

Airfoil Data

The use of tabulated two-dimensional airfoil data in the lifting line analysis allows for the real effects of compressibility and airfoil type to be modeled. The two-dimensional effects for transonic flow operation are thus implicity incorporated in the analysis through the use of transonic airfoil data. This, of course, means that to obtain reasonable results within the limitations of the assumptions of the analysis, the airfoil data must be as accurate as possible. The current analysis has available two different sets of isolated airfoil data for the NACA 16 series airfoil. This type of airfoil is currently used for high speed propeller designs. The details of these isolated airfoil data sets as used in the analysis are explained in the following sections.

For the inboard regions of the high speed propeller designs, the use of cascade data is more realistic than the use of isolated data. Because the inboard sections are generally thicker airfoil types, the NACA 65 series airfoil data for cascades has been included in the analysis. Again, two sets of data are available. This data is also explained in more detail in a following section.

Hamilton Standard NACA Series 16 Airfoil Data (Manoni)

Lift, drag and pitching moment data were obtained for a Series of NACA 16-series airfoils having a thickness ratio range from 0.02 to 0.10 and a design lift coefficient from 0 to 0.6 over a Mach number range of 0.4 to 1.25 and an angle of attack range of $-4°$ to $+8°$. This data was obtained in the UTRC main wind tunnel for the Hamilton Standard Division (HSD) of United Technologies Corporation as reported in reference 46. It is generally called the "Manoni" airfoil data after the author of this reference. A generalization of lift and drag coefficients for the NACA Series 16 airfoil family spanning a complete Mach number range, based on the data of the reference supplemented by other existing data, was made by HSD personnel for application in propeller performance analyses. The transonic similarity parameter approach was used because it enables one to generalize data for a limited number of sections. Then, the generalization can be used to define aerodynamic characteristics for a large number of airfoil sections over a complete Mach number range. In the transonic similarity form, the aerodynamic equations of motion are treated as in dimensional analyses to obtain parameters controlling the forces acting on a family of airfoils. This results in a group of equations of which the following are of primary interest:

$$\tilde{C}_{L_\alpha} = C_{L_\alpha}(t/c)^{1/3} = f_1(\zeta, h/t) \tag{43}$$

$$\tilde{C}_{D_p} = C_{D_p}(t/c)^{-5/3} = f_2(\zeta, h/t) \tag{44}$$

$$\tilde{C}_{DC_L^2} = C_{DC_L^2}(t/c)^{-1/3} = f_3(\zeta, h/t) \tag{45}$$

$$\zeta = (M^2-1)(t/c)^{-2/3} \tag{46}$$

The above symbols are defined in the List of Symbols.

In order to make the generalization applicable to higher thickness ratios, additional adjustments had to be included. This resulting generalization spans the following ranges:

Mach Number	0.3 to 1.25
Angle of Attack	-4° to +8°
Thickness Ratio	0.02 to 0.40
Design Lift Coefficient	0 to 0.7

and has been implemented into this propeller-nacelle performance analysis.

Published NACA Series 16 Airfoil Data (NACA)

In reference 47 two-dimensional airfoil data for NACA Series 16 airfoil sections are presented. The data was developed from a compilation of all the data available up to the early 1950's and the effort was somewhat handicapped by the lack of data throughout the transonic Mach number region. The data cover a range of thickness ratios of 4 to 21 percent and design lift coefficient of 0 to 0.7. The lift data are presented in the form of curves of lift coefficient, C_L, as a function of freestream Mach number and airfoil design lift coefficient. Data from the reference was partially computerized by HSD personnel spanning the following ranges:

Mach Number	0.3 to 1.15
Angle of Attack	-6° to +12°
Thickness Ratio	0.03 to 0.09
Design Lift Coefficient	0 to 0.2

The data was extrapolated to obtain 0.03 thickness ratio. The thickness ratio and design lift coefficient ranges can be extended from the data provided in the reference. This data is generally labeled the "NACA" airfoil data.

Cascade Airfoil Data (NASA SP-36)

Since the inboard sections of a high speed propeller design can approach gap to chord ratios which represent cascade airfoil conditions, a set of cascade airfoil data correlations has been incorporated in the analysis for typical high speed propeller design requirements. The cascade correlation is based on the NACA 65 series A = 1 meanline. This cascade correlation is valid

for gap to chord ratios greater than 0.8 for a Mach number range up to 1.0. The correlation is valid for ±10.0 degrees in angle of attack and the thickness to chord ratio available up to 0.1, with a numerical design lift coefficient range of -3.75 to 3.75 (camber angles of ±90 degrees). The description of the theory used to relate the cascade correlation parameters to isolated airfoil parameters so that it can be used in the lifting line solution follows.

Theory - Cascade Correlation

The theory used for the cascade correlations used in this subroutine is given in NASA SP-36 (reference 40). It is based on the observation that the exit flow angle from a blade is close to the metal angle, or trailing edge angle, α_2^* (see figure 12). Thus, only the deviation angle δ_o is correlated with cascade parameters. This basic correlation has the form

$$\alpha_2 = \alpha_s - \frac{\phi_c}{2} + \delta_o \tag{47}$$

where the deviation angle δ_o has the form

$$\delta_o = K_{\delta_s} \cdot K_{\delta_t} \cdot \delta_{oo} + M_\sigma \phi_c / \sigma^b \tag{48}$$

The parameters appearing in the above equation were obtained by curve fitting to the charts in reference 40.

The minimum loss incidence angle i_{mo} has the form

$$i_{m_o} = K_{i_t} \cdot K_{\delta_s} \cdot i_{oo} + n\phi_c \tag{49}$$

where again the parameters were obtained by curve fitting the charts in reference 40.

The minimum loss is based on the correlation of reference 40,

$$z_{Bm} = 2\sigma\, \Phi(D) \cos^2 \alpha_1 / \cos^3 \alpha_2 \tag{50}$$

where $\Phi(D)$, a correlation parameter, is obtained by curve fitting and the diffusion parameter D is given by

$$D = 1 - \frac{\cos\alpha_1}{\cos\alpha_2} + \frac{1}{2}\frac{\cos\alpha_1}{\sigma}\left[\tan\alpha_1 - \tan\alpha_2\right] \tag{51}$$

Equations (47) through (51) are the basic relations used in reference 40.

These relations have been modified and expanded as follows. The first is a back pressure correction given by

$$\alpha_{2c} = \tan^{-1}\left[\frac{\tan\alpha_2}{(\rho U_z)_2/(\rho U_z)_1}\right] \tag{52}$$

The second is a calculation of loss at any incidence angle given by

$$z_B = z_{Bm}\left[1 + \left(\frac{i - i_{mo}}{\Delta i}\right)^A\right] \tag{53}$$

where i is the incidence angle for twice the loss which is determined by curve fitting. These empirical relations yield predictions in good agreement with Pratt and Whitney Aircraft cascade predictions.

Theory - C_L, C_D Correlations

The C_L, C_D data correlations are based on thin airfoil theory and the data given in reference 48 and in particular the series 6 airfoils which were developed for low drag at the design lift coefficient C_{l_d}. The theoretical lift curve slope is given by

$$C_{L\alpha_0} = 2\pi \tag{54}$$

Since the data shows that the actual lift curve slope is less, the theoretical lift curve slope is modified by an empirical factor

$$C_{L\alpha_0} = 2\pi(1-\epsilon) \tag{55}$$

Thus, for thin airfoils, the lift is given by

$$C_L = C_{L_o} + C_{L_{\alpha_o}} \alpha \tag{56}$$

as shown in figure 13.

For thin airfoils C_{L_o} is primarily a function of camber angle ϕ_c. It can be shown that the design lift coefficient is related to the equivalent circular arc camber by the relation

$$C_{\ell_d} = \phi_c (1 - 0.05\phi_c^2) \tag{57}$$

Thus, C_{L_o} is determined empirically by the ratio of design lift coefficients,

$$C_{L_o} = C_{L_{oe}} \frac{C_{\ell_d}}{C_{\ell_{de}}} \tag{58}$$

and C_{L_o} is determined from data for a reference airfoil. At large angles of attack, the C_L departs from the linear relation. Hence, experimental data was fitted to an equation of the form

$$C_L = C_{L_o} + C_{L_{\alpha_o}} \alpha + A(\alpha - \alpha_o)^n \tag{59}$$

If $C_{L_{max}}$, α_{max} are given,

$$n = \left(1 - \frac{C_{L_{max}}}{C_{L_{\alpha_o}} \alpha_{max}}\right)^{-1} \tag{60}$$

$$A = -\frac{C_{L_{\alpha_o}}}{n \alpha_{max}^{n-1}} \tag{61}$$

Finally, for Mach numbers less than the critical Mach number M_{cr}, the Prandtl Glauert rule is used.

$$C_L = \frac{C_{L_I}}{\sqrt{1 - M^2}} \qquad M < M_{cr} \tag{62}$$

The drag coefficient in the drag bucket is fitted to an equation of the form

$$C_D = C_{D_{BO}} \left[1 + \Delta C_{D_{BO}} \left(\frac{\alpha - \alpha_{min}}{\Delta \alpha_1} \right)^{n C_{D_{BO}}} \right] \tag{63}$$

and outside the drag bucket to an equation of the form

$$C_D = C_{D_O} \left[1 + \Delta C_{D_O} \left(\frac{\alpha - \alpha_{2O}}{\Delta \alpha_2} \right)^{n C_{D_O}} \right] \tag{64}$$

where the respective quantities are shown in figure 13.

The conversion of lift and drag coefficients (C_L, C_D) to an exit angle (α_2) and loss coefficient (Z_B) is based on the resolution of the forces whose directions are shown in figure 12. The axial and tangential forces T_Z and T_ϕ, for a two-dimensional cascade using compressor terminology and the definition of C_L, C_D are given by

$$T_z = N_B \frac{1}{2} \rho_1 U_e^2 c \left(C_L \sin \alpha_e - C_D \cos \alpha_e \right) \tag{65}$$

$$T_z = N_B g \left[(P_2 - P_1) + \frac{(\rho U_z)_2 + (\rho U_z)_1}{2} (U_{z_2} - U_{z_1}) \right] \tag{66}$$

$$T_\phi = N_B \frac{1}{2} \rho_1 U_e^2 c \left[C_L \cos \alpha_e + C_D \sin \alpha_e \right] \tag{67}$$

$$T_\phi = N_B g \frac{(\rho U_z)_2 + (\rho U_z)_1}{2} (U_{\phi_2} - U_{\phi_1}) \tag{68}$$

where the effects of skewed flow are reflected in C_L and C_D predictions based on the local blade element coordinate system. Dividing these equations through by $(1/2\ \rho U_e^2)\ N_B c$ we have the force coefficients,

$$C_z = C_L \sin \alpha_e - C_D \cos \alpha_e \tag{69}$$

$$C_z = \frac{1}{\sigma \left(\frac{1}{2} \rho_1 U_e^2 \right)} \left[(P_2 - P_1) + \frac{(\rho U_z)_2 + (\rho U_z)_1}{2} (U_{z_2} - U_{z_1}) \right] \tag{70}$$

$$C_\phi = C_L \cos\alpha_e - C_D \sin\alpha_e \tag{71}$$

$$C_\phi = \frac{1}{\sigma\left(\frac{1}{2}\rho_1 U_e^2\right)} \cdot \frac{(\rho U_z)_2 + (\rho U_z)_1}{2} \left(U_{\phi_1} - U_{\phi_2}\right) \tag{72}$$

Rewriting equations (69) and (72) in terms of cascade parameters we have

$$C_z = \frac{1}{\sigma}\left(\frac{U_1}{U_e}\right)^2 \left\{\left(\frac{P_2}{P_1} - 1\right)\frac{2}{\gamma M_1^2} + \cos^2\alpha_1 \left[1 + \frac{(\rho U_z)_2}{(\rho U_z)_1}\right]\left[\frac{U_{z_2}}{U_{z_1}} - 1\right]\right\} \tag{73}$$

$$C_\phi = \frac{1}{\sigma}\left(\frac{U_1}{U_e}\right)\cos^2\alpha_1 \left[1 + \frac{(\rho U_z)_2}{(\rho U_z)_1}\right]\left[\tan\alpha_1 - \frac{U_{z_2}}{U_{z_1}}\tan\alpha_2\right] \tag{74}$$

where

$$\left(\frac{U_e}{U_1}\right)^2 = \left(\frac{U_{z_2} - w_z}{U_1}\right)^2 + \left(\frac{U_{\phi_2} - w_\phi}{U_1}\right)^2 = \left(\cos\alpha_1 - \frac{w_z}{U_1}\right)^2 + \left(\sin\alpha_1 - \frac{w_\phi}{U_1}\right) \tag{75}$$

The static pressure ratio across the blade row is given by.

$$\left(\frac{P_2}{P_1}\right) = \frac{P_{02}}{P_{01}}\,\frac{P_2}{P_{02}}\,\frac{P_{01}}{P_1} = \frac{P_{02}}{P_{01}}\left(\frac{1 + (\gamma - 1/2)\,M_1^2}{1 + (\gamma - 1/2)\,M_2^2}\right)^{\gamma/\gamma-1} \tag{76}$$

$$\frac{P_{02}}{P_{01}} = 1 - z_B \frac{\gamma M_1^2/2}{(1 + (\gamma - 1/2)\,M_1^2)^{\gamma/\gamma-1}} \tag{77}$$

and M_2 is given

$$M_2 = \left(\frac{C_m}{1 - (\gamma - 1/2)\,C_m^2}\right)^{1/2} \tag{78}$$

where

$$C_m = \left(\frac{M_1}{(1+(\gamma-1/2)M_1^2)^{1/2}}\right) \cdot \frac{U_{z_2}}{U_{z_1}} \frac{\cos\alpha_1}{\cos\alpha_2} \tag{79}$$

The axial and tangential momentum induced velocity can be related to the thrust and torque.

$$w_z = T_z / \left\{ N_B g \left[(\rho U_z)_2 + (\rho U_z)_1 \right] \right\} \tag{80}$$

$$w_\phi = T_\phi / \left\{ N_B g \left[(\rho U_z)_2 + (\rho U_z)_1 \right] \right\} \tag{81}$$

hence

$$\frac{w_z}{U_1} = \sigma \left(\frac{U_e}{U_1}\right)^2 C_z / \left\{ 2\cos\alpha_1 \left[\frac{(\rho U_z)_2}{(\rho U_z)_1} + 1 \right] \right\} \tag{82}$$

$$\frac{w_\phi}{U_1} = \sigma \left(\frac{U_e}{U_1}\right)^2 C_\phi / \left\{ 2\cos\alpha_1 \left[\frac{(\rho U_z)_2}{(\rho U_z)_1} + 1 \right] \right\} \tag{83}$$

For many blades the momentum or gap average induced velocities approach the local induced velocity. Finally, we note that the resultant angle of attack can be approximated as

$$\alpha_i = \alpha_1 - \tan^{-1}\left(\frac{\sin\alpha_1 - w_z/U_1}{\cos\alpha_1 - w_\phi/U_1}\right) \tag{84}$$

which can be used to obtain the effective C_L and C_D from the cascade correlations.

Solution Algorithm

For the cascade correlation the exit air angle α_2 and loss coefficient Z_B are known. The lift and drag coefficients and induced velocities can be determined directly as follows. The total pressure ratio P_{o2}/P_{o1} is given by

equation (77) and the downstream Mach number M_2 by equation 78. Then the compressor force coefficients when corrected to account for the absence of the induced velocity,

$$F_z = \left(\frac{U_e}{U_1}\right)^2 C_z$$
$$F_\phi = \left(\frac{U_e}{U_1}\right)^2 C_\phi \tag{85}$$

are determined by equations (73) and (74). Then the induced velocities are determined by equations (82) and (83). The resultant velocity is determined by equation (75) and the induced angle by equation (84). Then the resultant angle is given by

$$\alpha_e = \alpha_1 - \alpha_i \tag{86}$$

and equations (69) and (71) solved simultaneously for C_L and C_D with C_Z, C_ϕ, and α_e known.

NASA 65A = 1 Series Airfoils

The NASA equivalent circular arc camber angle for the A = 1 meanline is arbitrarily defined so as to produce good data correlations. The leading edge and trailing edge metal angles are defined relative to chord angle α_s by

$$\alpha_1^* = \tan^{-1}\left(\frac{dy}{dx}\right)_{x=0.005} = \tan^{-1}(0.4212\, C_{\ell_d}) \tag{87}$$

$$\alpha_2^* = \tan^{-1}\left(\frac{dy}{dx}\right)_{x=0.95} = \tan^{-1}(-0.2343\, C_{\ell_d}) \tag{88}$$

and the camber angle by

$$\phi_c = 4\tan^{-1}(0.1103\, C_{\ell_d}) \tag{89}$$

Hence, we have

$$\alpha_1^* = \alpha_s + \tan^{-1}(0.4212\, C_{\ell_d}) \qquad (90)$$

$$\alpha_2^* = \alpha_s + \tan^{-1}(-0.2343\, C_{\ell_d})$$

with α_1^* and α_2^* given, equation (90) may be solved for α_s and C_{l_d}. Thus the camber is given by equation (89).

Cascade Airfoil Data (Mellor)

An alternate source of cascade data is provided in the analysis based on the theoretical and empirical correlations of Mellor (references 49 to 51) and the data of reference 52. This cascade correlation is for the NACA 65 series airfoil sections and also includes several other airfoil types. In the current analysis the module which contains the correlations has been programmed to provide only the 65 series correlation, but this can be easily modified at some future date. The correlations as developed by Mellor are for incompressible flow, and as such should be used with the recognition of that limitation in the application to the high speed propeller. The correlations in the analysis are functions of camber, gap-to-chord ratio, thickness ratio, blade stagger angle, Reynolds number, and angle of attack.

Cascade Correction for Isolated Airfoil Data (Flat Plate Theory)

Included in the analysis is an analytic cascade correction which may be applied to isolated airfoil data for which actual cascade data does not exist. The correction procedure as used in the analysis comes from reference 44 and is based on analytical results presented in reference 45 for two dimensional flat plate airfoils and can be used for cambered airfoils if the local geometric blade angle Θ, and the angle of attack, α are measured to the zero lift direction.

This correction consists of modification of the isolated airfoil angle of zero lift due to the influence of camber by a difference $\Delta\alpha_o$, and thus modifies the angle of attack for the table lookup of the lift coefficient. The resulting lift coefficient is then scaled by the cascade correction factor K, which is a function of the local gap to chord ratio, g/c and local geometric blade angle Θ.

$$C_\ell = K C_\ell(\alpha - \Delta\alpha_0) \tag{91}$$

The values of K used in the analysis are presented in figure 14. Because of the approximate nature of this model, it is preferable to use actual cascade data if possible.

Cascade Correction for Isolated Airfoil Data (Mellor)

As a consequence of providing a cascade correlation using the correlation of Mellor (reference 49), the same correlation can be used to provide a cascade correction for isolated airfoils. The correction is an optional feature in the analysis which can be used in place of the correction based on flat plate theory. The correction is obtained by calculating the ratio of section lift coefficients of the NACA 65 series at the desired gap-to-chord ratio versus an infinite gap-to-chord ratio for the isolated airfoil operating conditions. This ratio is then used to scale the isolated airfoil section lift coefficient obtained from the appropriate data base of isolated airfoil characteristics at the operating conditions.

Cascade and Isolated Airfoil Data Interpolation

An interpolation procedure is available in the analysis to provide airfoil characteristics along the blade in the transition region for which cascade data does not exist and isolated airfoil data does not rigorously apply. The interpolation procedure in this region is based on the gap-to-chord ratio (τ). The airfoil characteristics are obtained by scaling the isolated airfoil characteristics for the particular blade element section by the use of an interpolation function.

$$\begin{aligned} C_\ell &= C_{\ell_{ISO}} f_\ell(\tau) \\ C_d &= C_{d_{ISO}} f_d(\tau) \end{aligned} \tag{92}$$

This function is based on the concept that the airfoil characteristics in the transition region must approach the isolated airfoil characteristics from the cascade values in a continuous and asymptotic manner. A function which has this behavior is

$$f(\tau) = \frac{a + \tau^n}{1 + \tau^n} \tag{93}$$

where the exponent (n) on the gap-to-chord ratio is defined by the user. The value of the exponent controls the rate at which the function asymptotically approaches unity for large gap-to-chord ratios. Larger values of the exponent increase the rate. The value of the parameter (a) is determined in the analysis by the ratio of the cascade to isolated airfoil characteristics (R_c), where the cascade data is obtained from the existing correlations for a gap-to-chord ratio at the boundary of the correlation data (σ_B).

$$a = R_c + \sigma_B^n (R_c - 1) \tag{94}$$

This modeling option can be used in place of the cascade correction for isolated airfoils described in the previous sections.

Wake Modeling

The use of a lifting line model in this analysis requires that the wake geometry be prescribed for computational purposes. As noted earlier the wake is represented by a system of trailing vortex filaments. Within this analysis it is possible to prescribe internally several different wake geometries or input the wake geometry from an external source. The reasons for this versatility are twofold. First, at the conventional operating conditions for the high speed propeller, the true shape of the wake is not known, thus the need for the ability to include a versatile range of wake geometries. It is however clear that the wake shape at these speeds is not significantly distorted. Secondly, at low speed or static flight conditions the wake shape is highly distorted as shown in reference 26, thus the need for wake models which can vary significantly in shape is well documented. The use of the appropriate selection of the wake geometry model for the flight condition under investigation is important for accurate propeller induced velocity predictions. Preferred wake models for the various flight speed regimes will be indicated. However, the final selection of wake model should be based on the results of a wake sensitivity study which remains to be conducted in future applications of the analysis. The wake models which can be used in the analysis are described in the following sections.

Classical Wake Model

Early lifting line models, for either static or forward flight conditions, generally used what is called a classical wake model. This model consists of defining the axial wake transport velocity as the addition of the forward speed and the momentum induced velocity for the thrust and flight condition being investigated.

$$V_t = V_0 + v_{i_{mom}} \tag{95}$$

No radial wake contraction is used. The resulting wake shape is an uncontracted helix for which the pitch rate depends on the flight condition and thrust level. Figure 15 illustrates the model. This model can be used in the analysis for any flight condition. Although it is known that for static thrust conditions this type of wake model will give incorrect answers, it is in the analysis because the self-induced distortions of the propeller wake decrease with forward speed. The classical wake or the classical wake as modified by superposition of the nacelle influence (to be discussed) can be used for the high speed propeller application.

Modified Classical Wake Model

Variations of the classical wake model can be used in the analysis if desired to approximately account for both the nacelle influence and/or the

self-induced wake distortion. One model allows for a radially varying axial wake transport velocity which replaces the uniform value used in the classical wake model.

$$V_t = f_v(x) \cdot V_0 + v_{i_{mom}} \tag{96}$$

where the function $f_v(x)$ represents a spanwise velocity scaling distribution which varies radially along the blade. As in the classical wake model there is no radial wake contraction. The function $f_v(x)$ is normally obtained from knowledge of the nacelle influence at the blades. If desired, it can also account for the difference between the propeller self-induced velocity spanwise distribution and the momentum values. Figure 16 illustrates this wake model. The use of this model is assumed to be more representative of the wake of the high speed propeller nacelle configurations than that generated by a classical wake model. However, alternate procedures will be described.

Generalized Wake Model

For static thrust conditions, wake distortions are significant in terms of propeller performance predictions. Because of this fact, a wake model which has been shown to accurately model the statically thrusting propeller or hovering helicopter rotor wakes (reference 17 and reference 27) can be used in the analysis. This wake model is known as the generalized wake model. It is based on empirical results, and has radially varying axial wake transport velocities and radial contraction of the wake. Figure 16 illustrates the general character of this wake model for a statically thrusting propeller (see also figure 4). The wake geometry varies in both the axial and radial directions and is highly dependent on wake age, ψ_w. The wake age of a point in the wake, ψ_w, is the azimuth interval of blade rotation between the current blade azimuth and the azimuth at the time the wake point was emitted from the blade. A detailed explanation of the wake model is available in reference 17 or reference 26. The equations for the tip vortex coordinates normalized by the blade radius are noted below:

$$z_{TIP} = \begin{cases} K_1 \psi_w & ; 0 \le \psi_w \le \dfrac{2\pi}{N_B} \\ K_1 \dfrac{2\pi}{N_B} + K_2 \left(\psi_w - \dfrac{2\pi}{N_B}\right) & ; \psi_w > \dfrac{2\pi}{N_B} \end{cases} \tag{97}$$

$$r_{TIP} = A + (1-A)e^{-\lambda \psi_w} \tag{98}$$

in terms of the generalized wake parameters.

The cross sections of the vortex sheet from each blade are essentially lines rather than discrete points, as is the case for the tip vortex cross sections. The vortex sheet cross sections are assumed to be linear, the axial position of a vortex sheet at a given azimuth can be defined by two points. For simplicity, the two points are the imaginary extensions of the cross section to r = 0 at one end and to r = 1.0 at the other end, as shown in figure 17. These two points establish the intercept at the axis of rotation and the slope of the vortex sheet. It was assumed that the radial position of such intercepts (e.g., point A of figure 17) is linearly proportional to the radial coordinate of the intersection of the vortex sheet with the vortex sheet boundary (point B). With the exception of the immediate vicinity of the blade ($\psi_w < 2\pi/b$), the vortex sheet boundary was assumed to be equivalent to the boundary formed by the locus centers of the tip vortex cross sections (equivalently, tip vortex streamline). For ψ_w less than the blade spacing, $2\pi/b$, the boundary was faired from the point of maximum circulation on the blade (point $\bar{D}$ of figure 17) to the tip vortex boundary. The constant of proportionality was assumed to be the ratio of the radial position of the origination of the filament streamline at the blade (point C) to the radial position of the vortex sheet boundary at the blade (point D). The equations for the vortex sheet coordinates normalized by the blade radius are noted below:

$$z_{r=1} \begin{cases} K_{1r=1}\psi_w \; ; 0 \le \psi_w \le \frac{2\pi}{N_B} \\ K_{1r=1}\frac{2\pi}{N_B} + K_{2r=1}\left(\psi_w - \frac{2\pi}{N_B}\right) ; \psi_w > \frac{2\pi}{N_B} \end{cases} \tag{99}$$

$$z_{r=0} \begin{cases} 0 & ; 0 \le \psi_w \le \frac{\pi}{2} \\ K_{2r=0}\left(\psi_w - \frac{\pi}{2}\right) & , \psi_w > \frac{\pi}{2} \end{cases} \tag{100}$$

$$r_A = \frac{r_C}{r_D} r_B \tag{101}$$

The generalized wake coefficients ($A, \lambda, K_1, K_2, K_{1r=1}, K_{2r=1}, K_{2r=0}$) which define the wake shape must be determined in advance and input to the analysis. The values can be determined from experiment or from reference 17 for static propellers or reference 26 for hovering rotors.

Because the wake geometry must change smoothly from the highly distorted shape under static thrust conditions to a basically undistorted shape at high forward speeds with a nacelle, the generalized wake geometry noted above has the radially varying velocity distribution (neglecting the momentum induced velocity) superimposed on it to account for the flight speed and the influence of the nacelle. Thus if the wake shape can be determined for low forward speeds from some source of information, it is expected that this model will be useful in modeling that flight regime's wake characteristics with the appropriate input wake coefficients.

Nacelle Influences on the Wake Geometry

The presence of the propeller nacelle can alter the local flow at the propeller blades and wake, particularly near the nacelle walls. The wake model described in the Modified Classical Wake section is based on the assumption that the nacelle does not influence the radial location of the wake geometry and that the axial transport velocity is constant for all axial locations. In reality this is not the case. In the analysis, it is possible to apply a second approximate wake perturbation model which is a function of the influence of the nacelle over the complete region exterior to the nacelle boundary. This allows the wake to accelerate and decelerate, expand or contract to follow the flow around the nacelle. This model is based on the superposition of the nacelle's influence (e.g., as determined from the nacelle streamline solution) on one of the previously described wake models as used to represent the isolated propeller wake. That is, once a wake model is selected for an isolated propeller, the wake can be corrected for the presence of the nacelle. The equations for the nacelle influence are presented in a later section (Nacelle Wake Corrections). Figure 18 illustrates this concept. It is recognized that this model, based on the principle of superposition is only an approximation to the actual wake. However, it is believed to be the most accurate method available, short of prescribing empirical values from measured data, which does not require calculating the complete coupled propeller-nacelle wake interaction problem numerically.

Wake Input Models

Since it may be necessary to prescribe wake geometries which are not compatible with any of the currently available wake models, the analysis will accept wake geometry input compatible with the cylindrical coordinate system mentioned in an earlier section. Thus, if it is determined that low or high speed flight conditions require currently unknown wake geometries for the propeller-nacelle configurations under consideration, the analysis will be able to accept these geometries.

Wake Rollup Modeling

The representation of the wake of a propeller blade as noted earlier consists of modeling the shed sheet of vorticity with discrete vortex filaments. The actual wake, however, is known to roll up into a tip vortex and inboard sheet. The tip vortex has, in general, a strength equal to the maximum circulation strength on the blade, as shown in figure 19. The occurrence of a rolled up root vortex has not been clearly demonstrated for hovering rotors or statically thrusting propellers, where wake distortions are most important. The modeling of this phenomena, if it exists at all, is generally not considered. For conditions where wake distortions are important, it is generally the distortion of the tip vortex which dominates the flow field characteristics. In the analysis, it is possible to prescribe the wake rollup for either the inboard or tip region if so desired. The age of the wake rollup and the concentration of circulation strength are determined from input quantities. Generally the tip vortex rollup is modeled to occur within 10 to 15 degrees behind the blade. The use of inboard wake rollup is not justified from a physical point of view as noted above; however, for conditions where a significant length of wake is required (static thrust) it is possible to reduce the computation time in the analysis by specifying inboard rollup to occur in the far field wake without sacrificing computational accuracy.

Vortex Core Modeling

If in the course of the use of this analysis, the prescribed wake model is such that a vortex filament segment is positioned close to a field point (blade segment center) where the induced velocity is being calculated, the predictions using the Biot-Savart Law for the magnitude of the induced velocity may exceed those which actually occur in real life for a discrete line vortex such as the tip vortex or where the vortex sheet is modeled by discrete vortex filaments. To resolve this problem, the analysis includes a vortex core model which is normally used. This model assumes that the variation of the velocity magnitude in the core is constant with variation in the direction normal to the filament segment and equal to the velocity at a specified core radius. Figure 20 illustrates this model for a finite length vortex segment. Although it is known that the velocity in the core of a discrete vortex decays from the peak value at the core radius approximately linearly to zero at the center, this simple model is felt to be as valid as any other, on the basis that if a close passage does occur, the modeling of the blade and wake by discrete vortex filaments is in itself inappropriate.

Compressibility Considerations for Induced Velocity

When the performance of two-dimensional airfoils is found from the airfoil data, the effects of compressibility are included, as the data is tabulated as a function of Mach number. To use the airfoil data for the case where the propeller is operating at high forward Mach numbers, compressibility effects on the induced velocity must also be determined.

The conditions for which the effects of compressibility on the induced velocity need to be considered are outlined in reference 41. In summary, if the local section Mach number (total of the rotational and forward Mach numbers) at the blade exceeds the local speed of sound, it is necessary to consider the effects of compressibility on the induced velocity. The procedure to incorporate the effects of compressibility is also outlined in the above reference for vortex models. To compute the effect, it is necessary to consider the finite speed of the pressure disturbances in comparison with the speed of the blade section being analyzed. This leads to the rule of forbidden signals when some of the sections are operating at section Mach numbers above one. Thus the effects of the line vortex shed from a section operating at a section Mach number above one are considered only at points in the region of its aft Mach cone, where the apex of the Mach cone is attached to the section from which the line vortex is shed on the propeller blade. Figure 21 (from reference 41) is a pictorial representation of this concept and illustrates the blade and Mach cone which defines the limits of the possible induced influence of the trailing line vortex. For the case of a high speed propeller operating with blade section Mach numbers greater than one but forward Mach numbers less than one, the initial portion of the trailing line vortices shed from these blade sections will have no influence at the propeller blades. However, after some finite period of time the influence of a portion of the line vortex will reach the propeller disk. Figure 22 (also from reference 41) illustrates this concept, where the position of the blade and the Mach cone boundary are plotted for different rotational positions of the blade (time). It is shown in this figure that for a forward Mach number less than one, the induced influence of a portion of the line vortex does eventually reach the blade after some finite time (between time C and D in figure 22).

To calculate the induced inflow velocity of a propeller operating at a tip Mach number exceeding one and a forward Mach number less than one, it is necessary to evaluate the effects of the trailing vortices that lie in the zone of influence only. Thus, unlike the incompressible flow case where effects of the vortices are considered from the propeller plane to infinity instantaneously, it becomes necessary to discriminate against the effects of the vortices outside the zone of influence or the Mach cone as shown in figure 21. Thus the portion of the trailing vortex filaments which has no influence on a blade segment at a particular time should not be considered when the

calculation of the geometric influence coefficients using the Biot-Savart Law is made as noted in the section entitled: Lifting Line Theory. This approach has been included in the analysis. The concept of the induced influence of a trailing line vortex limited by compressibility considerations can also be applied to the bound vortex segments representing the blade. The validity of applying this concept to the bound vortex influence has not been established; however, it is available in the analysis if so desired.

As noted above, the concept of wake compressibility as outlined in reference 41 assumes infinite propagation of the induced field of the trailing line vortices shed from blade sections operating at section Mach numbers less than unity and finite propagation (speed of sound) of the induced influence when the sections are operating at section Mach numbers greater than unity. A second feature, which is not normally used, is provided in the analysis for exploring the influence of finite rather than infinite propagation speed for blade sections with a section Mach number less than one. That is, a provision is included which assumes that the influences of all bound and/or trailing wake elements propagate at the speed of sound.

Coaxial Theory - Equal Blade Number and Rotational Speeds

For the coaxial, counter-rotating propeller analysis, the assumption of an axisymmetric steady state flow problem with respect to the blade coordinate system must be removed. In the blade coordinate system, the circulation solution becomes periodic with half blade spacing for equal blade number and rotational speeds. This feature is demonstrated in figure 23 where it can be seen that the geometry of the problem is periodic with half blade spacing. The half blade spacing is the azimuthal interval of blade rotation between the two propellers required for the relative geometry to repeat itself. The use of lifting line theory is still valid within the constraints of the other assumptions noted in earlier sections. In this analysis the only major conceptual difference between the single and coaxial solutions at the blade rows is the above noted periodicity. The coaxial analysis assumes quasi-steady aerodynamics. Thus the relationships used to determine the unknown blade circulations only need to be modified to include the solution periodicity. The details of such a deviation are straightforward and only the resulting relationships are represented herein.

Coordinate Systems

Within the coaxial lifting line analysis, definitions of the coordinate systems are identical with those in the single propeller analysis. The cartesian and cylindrical coordinate systems are referenced with respect to each blade row, with the definitions of positive quantities consistent with the respective direction of rotation of each blade row. In the analysis there is no distinction between which blade row is rotating in which direction, only that they are counter-rotating; this is because the problem is symmetric in nature. The definitions of velocities computed at a blade row are consistent with that blade row's coordinate system. Figure 24 illustrates the above noted coordinate systems. For calculation purposes, the analysis requires that the hubs of the two propellers be separated by a finite axial displacement. Propeller one (in terms of input ordering) is assumed to lie in front of propeller two, and a positive hub displacement positions propeller two behind propeller one (figure 24). The blade element coordinate system for each blade row is consistent with the respective cartesian and cylindrical coordinate systems.

Lifting Line Theory

As noted earlier, the addition of a counter-rotating propeller requires the inclusion of geometric periodicity and hence circulation periodicity in the relationships used to compute the solution. For the calculation of the induced velocity at a field point using lifting line theory, the relationships

derived earlier must be expanded to include the periodic nature of the circulation solution of each blade row and the wake influence. The resulting relationship for a component of induced velocity, in this case the normalwise component, at an arbitrary field point is:

$$v_n = \sum_{p=1}^{2} \sum_{i=1}^{N} \sum_{j=1}^{L} \Gamma_{ijp} \, GC_{n\,ijp} \tag{102}$$

where it is assumed that there are identical number of blade stations (N) at each blade row and that there are L propeller positions between half blade spacings for a given blade azimuth step size. The term, propeller position, means the discrete azimuthal location of the propeller within a specified rotational interval, defined by a finite azimuthal step size. In this case, the interval is the half blade spacing, and the discrete azimuthal locations are defined by the azimuthal wake segmentation interval.

Blade Element Aerodynamics

The effect of including a second propeller blade row on the aerodynamic relationships is to expand the number of unknown bound circulation strengths, and hence the size of the matrix of equations which must be solved using either the linear or nonlinear solution. The relationship for the unknown circulation at station i for propeller position j of propeller p for the nonlinear solution becomes:

$$\Gamma_{ijp} = \frac{1}{2} a_i c_i \left[V_{C_i} \theta_{B_i} + \sum_{p=1}^{2} \sum_{i=1}^{N} \sum_{j=1}^{L} GC_{n\,ijp} \, \Gamma_{ijp}^{\nu} + C_{F\,ijp}^{\nu-1} \right] \tag{103}$$

where the correction term $C_{Fijp}^{\nu-1}$ has the appropriate modifications for the coaxial propeller condition. Dropping the superscripts and the correction term yields the linear solution. From this relationship for the unknown bound circulation at each station on each propeller blade for each propeller position a matrix of NxLx2 simultaneous equations can be written, and the same solution methods can be applied as for the single propeller condition.

The resulting blade forces can be computed and integrated for each propeller at each propeller position. The resulting values can be averaged over the propeller positions to obtain the steady thrust and torque. For the nacelle code these steady forces are the values used for the coaxial case since the nacelle analysis assumes steady flow conditions.

Other Considerations for Coaxial Propellers

The use of the different wake models and airfoil data for the coaxial propeller configuration is the same for the single propeller configuration. There is only one restriction in the analysis which limits the use of these portions of the analysis to single propeller configurations. That restriction is the application of the rule of forbidden signals to the bound vortex which is noted in the section entitled: Compressibility Considerations on the Induced Velocity Calculation. The analysis will not allow the application of this modeling feature to the coaxial configuration. The reason is that the formulation for this model as applied to the bound vortex has not been developed for the coaxial configuration because this model is in itself questionable.

Because the wake of the leading propeller can pass close to the lifting line representation for the blades on the following propeller, care should be taken to inspect the resultant blade loadings to look for large gradients in loading due to close blade-vortex interactions. The validity of the solutions where these close passages occur is questionable. The use of different core radii for the wake vortex systems can influence the answers when these close passages occur, and so careful selection of the appropriate values should be made for the coaxial configuration.

Coaxial Theory - Unequal Blade Number and Rotational Speeds

For the coaxial configuration, the introduction of unequal number of blades and unequal rotation speeds on the propeller disks creates an additional complexity in the analysis. The concept of periodicity of the propeller blade/wake geometry and periodicity of the circulation solution still exists, but the definition of azimuthal interval must be replaced with a time interval as the quantity which defines this periodicity. This is due to the fact that the propeller blades do not necessarily rotate at the same speed. In general, it can be shown that the time interval for which the propeller blade and wake geometry are periodic is,

$$t = \frac{2\pi}{b(\Omega_1+\Omega_2)} \tag{104}$$

where b is the maximum of the number of blades on each of the propeller disks. This relationship reduces to the conventional one for coaxial propellers with equal number of blades and rotational speeds on each disk; the periodic azimuthal interval is one half of the blade azimuth interval.

The relationships for the formulation of the numerical solution procedure are no different than those for the conventional coaxial configurations. However, the implementation of the formulation in the computer code must be made in terms of time intervals instead of azimuth intervals. For unequal rotational speeds on the propellers, this results in different azimuth intervals used to define the propeller positions and wake geometries.

The analysis includes this feature to treat the unequal number of blades and rotational speeds with certain limitations. These limitations are related to computer program storage requirements and are not conceptual in nature. Large variations between the number of blades on each propeller disk, or large variations in rotational speeds, result in periodic time intervals which require a large number of unknowns in the solution formulation. This increase in the number of unknowns increases the physical storage needed in the program and the computational time required to obtain the solution. The current analysis is limited to combinations of blade number and rotational speed which result in periodic time intervals with corresponding azimuthal intervals on the respective propeller disks of no less than five (5.0) degrees. This limitation can be relaxed by re-dimensioning the computer code if deemed necessary at some future time. The analysis controls the selection of the actual time increments used in the definition of the wake geometries based on

the periodic time interval relationship defined above. The analysis attempts to find a time increment which is at least one third of the periodic time interval for the particular selection of blade numbers and rotational speeds and which does not result in an azimuthal interval for either propeller less than the current limit of five degrees. The user can also limit the time interval to result in an azimuthal interval on either propeller which is not greater than a specified value.

The analysis has been coded in such a manner that the unequal blade number and rotational speed feature does not result in a significant computer overhead penalty when applied to the more conventional or coaxial operating configurations.

TECHNICAL APPROACH - NACELLE

Overview

A large and important class of problems is represented by viscous turbulent flows over axisymmetric nacelles with the following properties: 1) moderate to high Reynolds numbers, 2) strong inviscid-viscous interactions, 3) large regions of inviscid flows, and 4) significant "elliptic" effects due to streamline curvature and streamline divergence. Accurate and reliable calculation of such flows is of immediate and practical interest in the prediction of flows over a nacelle for either external or internal flow.

This section consists of several parts. First, a procedure is presented for constructing an orthogonal coordinate system from the planar potential flow solution using the stream function as a normal coordinate and the velocity potential as the streamwise coordinate. Since the potential flow streamlines approximate the viscous flow streamlines, the thin channel approximation, references 4 and 5, may be applied to the Navier-Stokes equations written in this potential flow coordinate system to reduce them to a set of parabolic equations which can be solved by forward marching numerical methods. Second, a method using conformal mapping based on the Schwartz-Christoffel transformation is presented for obtaining the plane potential flow solution for the flow over an axisymmetric nacelle. This procedure has the important property that the inverse solution is obtained directly through the transformation so that equipotential lines and streamlines can be used to construct the coordinates. Third, a solution algorithm based on the two point box scheme is presented for solving the viscous flow equations. It should be noted here that the term, duct, is used even when considering the external flow problem of the propeller-nacelle geometry. For these external flow problems, the outer wall of the duct becomes the outer limit for the computational region with the appropriate modifications to the boundary conditions, and the inner wall becomes the nacelle profile. And finally, because of the particular requirements of the nacelle application, streamline curvature corrections to the thin channel approximation are necessary (reference 53) and are included in the analysis.

Streamline Coordinates

The equations of motion are solved in a streamline orthogonal coordinate system (n, s, ϕ). This coordinate system is generated by first solving for the plane potential flow (independent of ϕ) through a duct with the same cross-section that the annular duct makes with the meridonal plane. The normal coordinate n is the stream function and the streamwise coordinate s is the velocity potential. Rotation about the axis of symmetry produces an axisymmetric orthogonal coordinate system uniquely suited to solve the problem.

The (n, s) coordinates are related to the physical coordinates (r, z) through Laplaces' equation.

$$\frac{\partial^2 n}{\partial r^2} + \frac{\partial^2 n}{\partial z^2} = 0 \tag{105}$$

$$\frac{\partial^2 s}{\partial r^2} + \frac{\partial^2 s}{\partial z^2} = 0 \tag{106}$$

The metric scale coefficients are the same in both directions and are equal to the inverse of the magnitude of the potential flow velocity, V.

$$v^2 = \left(\frac{\partial n}{\partial r}\right)^2 + \left(\frac{\partial n}{\partial z}\right)^2 = \left(\frac{\partial s}{\partial r}\right)^2 + \left(\frac{\partial s}{\partial z}\right)^2 \tag{107}$$

Lengths along the streamlines and potential lines are given by

$$dx = ds/V \tag{108}$$

$$dy = dn/V \tag{109}$$

and curvature of streamlines and potential lines are given by

$$\frac{1}{R_s} = \frac{\partial V}{\partial n} \tag{110}$$

$$\frac{1}{R_n} = \frac{\partial V}{\partial s} \tag{111}$$

In this coordinate system (n, s) are independent variables and (r, z) dependent variables. While one could solve this problem numerically, an alternate, more efficient procedure is available. Solution of the inverse problem (r(n,s), z(n,s)) can be obtained by conformal mapping using the Schwartz-Christoffel transformation (reference 54). If a curved wall duct is approximately represented by straight line segments in the W plane to form a many sided polygon, the Schwartz-Christoffel transformation may be used to transform the interior of this polygon into the upper half of the ζ plane (figure 24). Then a point source at the origin of the ζ plane transforms into the potential flow through the duct in the W plane. The only approximation used in this approach involves the segmentation of the geometry, which would occur in any finite difference solutions of equations (105) and (106).

The complex potential for a source at the origin of the ζ plane is given by

$$F = \ln\zeta = s + in \tag{112}$$

where

$$-\infty < s < \infty \tag{113}$$

$$0 < n < \pi \tag{114}$$

In the W plane, using the Schwartz-Christoffel transformation, we have

$$\frac{dW}{d\zeta} = \frac{1}{\zeta} \prod_{I=1}^{N} (\zeta - b_I)^{-a_I/\pi} \tag{115}$$

where b_I is the location of the Ith pole in the ζ plane corresponding to the Ith corner of the polygon in the W plane. In equation (115), the a_I's are known, but the b_I's must be chosen to fit the duct. If the b_I's are known, equation (112) and equation (115) may be combined to obtain

$$\frac{dW}{dF} = \frac{d(z+ir)}{d(s+in)} = \frac{dw}{d\zeta} \Big/ \frac{dF}{d\zeta} \tag{116}$$

Integration of equation (116) with n constant, produces a streamline, and integration of equation (116) with s constant, produces a potential line. The metric scale coefficient is equal to the inverse of the magnitude of the potential flow velocity and is given by

$$v = \left\| \frac{dF}{dW} \right\| = \frac{dF}{dW} \cdot \frac{\overline{dF}}{dW} \tag{117}$$

The unknown b_I's are determined iteratively by comparing the calculated length along each wall with the actual length. In the ζ plane, the inner wall cooresponds to $n = 0$ and the outer wall to $n = \pi$ as shown in figure 25. However, since the poles also lie on the ζ axis, the numerical integration of the wall contour using equation (116) is obtained by setting $n = \varepsilon$ and $\pi = \varepsilon$. Hence for b_I assumed, the calculated length along each wall for the νth iteration and Ith pole is

$$L_I^{\nu} = L(s_I^{\nu}) = \int_{s_0}^{s_I} \left\| \frac{dW}{dF} \right\| ds = \int_{s_0}^{s_I} \frac{ds}{v^{\nu}} \tag{118}$$

The actual length along the wall to the Ith pole is known and given by

$$L_I = L(z(s_I)) = \int_0^{z_I} \left\| \frac{dW}{dz} \right\| dz \tag{119}$$

and the error in calculating the location of the Ith pole is

$$e_I = \left| L_I - L_I^{\nu} \right| \tag{120}$$

Therefore, to minimize the error by Newton's method, we have from equation (118) and equation (119) the recursion formula

$$S_I^{\nu+1} = S_I^{\nu} + V_I^{\nu}(L_I - L_I^{\nu}) \tag{121}$$

where $S_I^{\nu+1}$ is the location of the pole in the ζ plane in terms of (n, s) coordinates. The value of $b_I^{\nu+1}$ is obtained from equation (112),

$$b_I^{\nu+1} = \exp(s_I^{\nu+1})\cos(n) \tag{122}$$

where n = 0 for the inner wall and n = π for the outer wall. If initial values for b_I are assumed, equation (118) may be integrated along each wall to obtain L_I^{b} and V_I^{ν}. Then, equations (121) and (122) are used to obtain the next guess. This procedure is repeated until $e_I \leq e_o$.

Equations of Motion

The equations of motion may be written in the streamline coordinate system (n, s, ϕ) with the corresponding metric scale coefficients (1/V, 1/V, r). Assuming that the plane potential flow streamlines approximate the real flow streamlines, the thin channel approximation (reference 55) may be made by taking

$$U_n/U_s = O(\epsilon) \tag{123}$$

and dropping terms of $O(\epsilon^2)$. The resulting equations of motion are given by

$$\frac{\partial \psi}{\partial n} = \frac{g\rho U_s}{V} \tag{124}$$

$$\frac{V}{g}\frac{\partial \psi}{\partial n}\frac{\partial U_s}{\partial s} - \frac{V}{g}\frac{\partial \psi}{\partial s}\frac{\partial U_s}{\partial n} - \frac{\rho U_\phi^2}{r}\frac{\partial r}{\partial s} + \frac{\partial P}{\partial S} = \frac{V}{g}\frac{\partial}{\partial n}\left(\frac{g\tau_{ns}}{V}\right) - \left(\frac{\tau_{ns}}{V}\right)\frac{\partial V}{\partial n} + \frac{F_s}{V} \tag{125}$$

$$\frac{\rho U_s^2}{V}\frac{\partial V}{\partial n} - \frac{\rho U_\phi^2}{r}\frac{\partial r}{\partial n} + \frac{\partial P}{\partial n} = 0 \tag{126}$$

$$\frac{V}{g}\frac{\partial \psi}{\partial n}\frac{\partial U_\phi}{\partial s} - \frac{V}{g}\frac{\partial \psi}{\partial s}\frac{\partial U_s}{\partial n} + \frac{\rho U_s U_\phi}{r}\frac{\partial r}{\partial s} =$$

$$\frac{V}{g}\frac{\partial}{\partial n}\left(\frac{g\tau_{n\phi}}{V}\right) - \frac{\tau_{n\phi}}{r}\frac{\partial r}{\partial n} + \frac{f_\phi}{V} \tag{127}$$

$$T\frac{V}{g}\frac{\partial \psi}{\partial n}\frac{\partial I}{\partial s} - T\frac{V}{g}\frac{\partial \psi}{\partial s}\frac{\partial I}{\partial n} = \frac{V}{g}\frac{\partial}{\partial n}\left(\frac{gq_n}{V}\right) + \frac{\tau_{ns}^2 + \tau_{n\phi}^2}{V\mu_T} + \frac{I_B}{V} \tag{128}$$

$$\mu_T \frac{\partial}{\partial n}(VU_s) = \tau_{ns} \tag{129}$$

$$\mu_T r V \frac{\partial}{\partial n}\left(\frac{U_\phi}{r}\right) = \tau_{n\phi} \tag{130}$$

$$C_p \frac{\mu_T}{Pr}\left(V\frac{\partial T}{\partial n}\right) = q_n \tag{131}$$

$$P = \rho RT \tag{132}$$

$$I - I_r = C_p \ln(T/T_r) - R\ln(P/P_r) \tag{133}$$

where the stream function ψ has been defined to satisfy the continuity equation and the normal velocity U_n is given by

$$\frac{\partial \psi}{\partial s} = - \frac{\mathcal{R} \rho U_n}{V} \tag{134}$$

Equations (124) through (133) form a set of eight first order partial differential equations and two algebraic equations which may be used to solve for ten unknowns. The boundary conditions for this problem are given by

$$\left.\begin{aligned} U_s(0,s) &= 0 \\ U_\phi(0,s) &= 0 \\ q_n(0,s) &= 0 \\ \psi(0,s) &= 0 \end{aligned}\right\} \tag{135}$$

for the inner wall and

$$\left.\begin{aligned} U_s(\pi,s) &= 0 \text{ (Internal flow)} \\ &= U_\infty \text{ (External flow)} \\ U_\phi(\pi,s) &= 0 \\ q_n(\pi,s) &= 0 \\ \psi(\pi,s) &= \psi(\pi) \end{aligned}\right\} \tag{136}$$

for the outer wall.

The remaining unknown is the viscosity. For laminar flow, Sutherlands law is used to obtain the molecular viscosity $\mu(T)$. For turbulent flow empirical relations are used to obtain the effective turbulent viscosity μ_T.

Turbulence Model

The turbulence model used for these calculations is an equilibrium turbulence model in which the turbulent stress is proportional to the local rate of strain of the mean flow based on simple mixing length concepts. Two turbulent regimes are used according to the observed characteristics of turbulence described in reference 56. In regions far removed from the wall (freestream), the turbulence is assumed "wake like" with an eddy viscosity which is a function of s only. In regions near the wall, the turbulence is strongly affected by the wall, and a wall turbulence model is used.

In the freestream two scale factors are required to describe turbulence; a length scale and a velocity scale. The length scale, according to mixing length theory, is proportional to the largest turbulent eddy size. This length scale is taken to be the duct height. The velocity scale is a measure of the kinetic energy of the turbulence and according to mixing length theory, reference 57, is proportional to a velocity difference. For duct flows with arbitrary velocity distributions, this velocity difference is taken to be the difference between the maximum and mean velocity. Hence the freestream turbulent viscosity is given by

$$\mu_T = \chi \frac{\rho_\infty U_\infty}{2} \int_0^h \left(1 - \frac{U}{U_\infty}\right) dy \tag{137}$$

where P_∞ and U_∞ are the maximum values at a given s. Since the mean velocity $\bar{U}$ is defined by

$$\bar{U}h = \int_0^h U dy \tag{138}$$

equation (137) reduces to a wake mixing length model given by:

$$\mu_T = \chi \frac{\rho_\infty h}{2} (U_\infty - \bar{U}) \tag{139}$$

where χ is an empirical constant determined by experiment.

Near the wall, the turbulence model derived by Van Driest (reference 58) is used.

$$\frac{\mu_T}{\mu_w} = 1 + \kappa^2 Y^{+2}\left[1-\exp(-Y^+/A^+)\right]^2 \frac{dU^+}{dY^+} \qquad (140)$$

where U^+ and Y^+ are defined by

$$U^+ = U/\sqrt{\tau_w/\rho_w} \qquad (141)$$

$$Y^+ = \rho_w Y \sqrt{\tau_w/\rho}\,/\,\mu_w \qquad (142)$$

Two empirical constants are used κ and A^+ which are taken to be 0.40 and 26.0, respectively.

The empirical constant χ remains to be determined. It is noted that two boundary layers exist in the duct. Hence for uniform freestream flow, equation (137) reduces to

$$\mu_T = \chi \rho_\infty U_\infty \delta^* \qquad (143)$$

where δ^* is the boundary layer displacement thickness. The value for χ has been obtained by Clauser (reference 59) and is taken to be 0.016.

Initial Conditions

The initial conditions for this problem require specification of all dependent variables ψ, U_s, U_ϕ, P, ρ, T, I, τ_{ns}, $\tau_{n\phi}$, q_n as a function of n. In the freestream, it is assumed that τ_{ns}, $\tau_{n\phi}$, and q_n, flow swirl angle are zero. Then the remaining variables are uniquely defined by $P_o(n)$, $\beta(n)$, $T_o(n)$, $\psi(\pi)$ using the isentropic flow relations and equations (124) and (126) to insure that the continuity equation and radial momentum equation are satisfied.

In the nacelle boundary layer, $\tau_{ns}(n)$, $\tau_{n\phi}(n)$, $q_n(n)$ must be specified in such a manner as to be consistent with the turbulence model. This is accomplished by using Coles' law (reference 60) for the mean velocity profile assuming colateral flow (β = constant). Thus we have

$$U^* = U_c^* + 2\Pi_c \sin^2\left(\frac{\pi}{2}\,\frac{y}{\delta}\right) \tag{144}$$

with Coles' shape parameter Π_c given by

$$\Pi_c = \kappa\,\frac{\delta^* U_\infty}{\delta\, U^*} - 1 \tag{145}$$

The function $U_c^+(y^+)$ is the contribution from the law of the wall. This is obtained by integrating

$$\frac{\mu_T\, dU^*}{\mu_w\, dY^*} = 1 \tag{146}$$

using equation (140) for the turbulent viscosity μ_T. The friction velocity U^* is obtained from Coles' friction law

$$\frac{U_\infty}{U^*} = \frac{1}{\kappa}\left\{\ln\left(\frac{\delta U_\infty}{\nu}\right) + 2.2 + 2\left(\kappa\,\frac{\delta^* U_\infty}{\delta U^*} - 1\right)\right\} \tag{147}$$

If the displacement thickness δ^* and shape factor H_{12} are input parameters describing the boundary layer we have

$$\frac{\delta}{\delta^*} = \frac{H_{12}+1}{H_{12}-1} \tag{148}$$

and Coles' law (equation (147)) can be evaluated for U^*.

The temperature distribution is obtained from the velocity distribution using the relation

$$\frac{T}{T_\infty} = 1 + P_r^{1/3} \frac{\gamma-1}{\gamma} M_\infty^2 \left[1-\left(\frac{U}{U_\infty}\right)^2\right] \tag{149}$$

With the mean boundary layer profiles calculated, τ_{ns}, $\tau_{n\phi}$ and q_n are obtained using the relations for turbulent viscosity μ_T and stress (equations (129) to (131) and (140)).

Inviscid Flow Calculation

The solution for the inviscid flow around the nacelle is used to calculate the propeller wake corrections due to the influence of the nacelle on the propeller wake and is also used to calculate the influence of the nacelle on the flow at the lifting line.

For inviscid flows with no work or heat addition, the total temperature T_o, total pressure P_o, and angular momentum (rU_ϕ) are conserved streamlines. These quantities, however, may vary from streamline to streamline. Therefore along a streamline the isentropic flow relations may be used. Furthermore, since the coordinate n is the stream function for the potential flow around the nacelle, the curve $n(r,z) = n_o$ approximates the inviscid flow streamlines. Hence P_o, T_o, and (rU_ϕ) are functions of n only. Thus the following equations can be used to calculate the solution for the inviscid flow.

$$\frac{T_o(n)}{T(n,s)} = 1 + \frac{\gamma-1}{2} M^2 \tag{150}$$

$$\frac{P_o(n)}{P(n,s)} = \left(1 + \frac{\gamma-1}{2} M^2\right)^{\frac{\gamma}{\gamma-1}} \tag{151}$$

$$rU_\phi = r_1 U_{\phi_1}(n) \tag{152}$$

In addition the inviscid flow must satisfy the continuity equation, equation (124), and the normal momentum equation, equation (126).

$$\frac{d\psi}{dn} = \frac{\rho U_s}{V} \tag{153}$$

$$\frac{dP}{dn} = \frac{\rho U_s}{V}\frac{\partial V}{\partial n} + \rho\frac{U\phi^2}{r}\frac{\partial r}{\partial n} \tag{154}$$

which may be expressed as

$$\frac{\partial\psi}{\partial n} = \sqrt{\frac{\gamma}{RT_o}}\, P\left\{\frac{2}{\gamma-1}\left(\frac{P_o}{P}\right)^{\frac{\gamma-1}{\gamma}}\left[\left(\frac{P_o}{P}\right)^{\frac{\gamma-1}{\gamma}}-1\right]\right\} \tag{155}$$

$$\frac{\partial P}{\partial n} = \frac{2\gamma}{\gamma-1}\left[-\frac{\cos^2\alpha}{V}\frac{\partial V}{\partial n}+\frac{\sin^2\alpha}{r}\frac{\partial r}{\partial n}\right]P\left\{\left(\frac{P_o}{P}\right)^{\frac{\gamma-1}{\gamma}}-1\right\} \tag{156}$$

The solution of equations (153) through (156) produces the inviscid compressible flow field. This solution is obtained by the following transformation of variables.

Let

$$\chi = \left(\frac{P_o}{P}\right)^{\frac{\gamma-1}{\gamma}} \tag{157}$$

and

$$a = 2\left[-\frac{1}{V}\cos^2\alpha\frac{\partial V}{\partial n}+\frac{1}{r}\sin^2\alpha\frac{\partial r}{\partial n}\right] \tag{158}$$

Equation (109) becomes

$$\frac{dX}{dn} + \left\{a + \frac{\gamma-1}{\gamma}\frac{d}{dn}\left[\ell n(P_o)\right]\right\} X = a \tag{159}$$

which is an ordinary first order linear equation.

The solution is given by

$$\phi(n) = \exp\left[\int_0^n a\,dy + \frac{\gamma-1}{\gamma}\,\ell n\left(\frac{P_o}{P_{oH}}\right)\right] \tag{160}$$

$$\Phi(n) = \int_0^n a\phi(y)dy \tag{161}$$

$$X = \left(X_H + \Phi(n)\right)/\phi(n) \tag{162}$$

The boundary conditions for the solution of the problem are:

$$\left.\begin{aligned}\psi(0) &= 0\\ P(1) &= P_\infty\end{aligned}\right\} \tag{163}$$

For the case of the nacelle in a wind tunnel, the boundary conditions are:

$$\left.\begin{aligned}\psi(0) &= 0\\ \psi(n) &= \psi_n\end{aligned}\right\} \tag{164}$$

since mass flow is conserved in the tunnel.

Perforated Wall Bleed Model

For some tunnels, the use of a zero normal flow boundary condition is inappropriate when the tunnel is run using bleed. This type of operation can be modeled as described below.

If one treats a single hole in a perforated wall as an orifice, then the mass flow can be derived in terms of the plenum stagnation conditions and the local static pressure inside the tunnel, Holman (reference 61). Then an expression for the mass flow added to the tunnel flow is given by

$$(\rho U_n)_w = C \frac{A_h}{A_s} \frac{\gamma P_T}{\sqrt{\gamma R T_T}} \left(\frac{P_T}{P}\right)^{-\frac{1+\gamma}{2}} \left\{\frac{2}{\gamma-1}\left[\left(\frac{P_T}{P}\right)^{\frac{\gamma-1}{\gamma}} - 1\right]\right\}^{1/2} \tag{165}$$

where P_T and T_T are the plenum conditions, P is the local tunnel static pressure, A_h/A_s is the ratio of the hole area to surface area, and C the effective discharge coefficient which is a property of the perforated wall. If the tunnel static pressure is greater than the plenum total pressure, the mass flow bleed is out of the tunnel. Under these conditions, P_T and T_T are taken from the wind tunnel conditions, and P is the plenum pressure which is assumed known.

The mass flow bleed is related to the stream function by

$$-\frac{\partial \psi}{\partial s} = \frac{G}{V} \frac{(\rho U_n)_w}{\rho_r U_r} \tag{166}$$

Equations (165) and (166) provide the boundary conditions for a perforated wall relating two dependent variables ψ and P in terms of the characteristics of the perforated wall and the plenum conditions.

Since perforated walls have very high rates of bleed which suck off or blow off the boundary layer, the boundary conditions were taken to be

$$\psi_{KL}^{J+1} = \psi_{KL}^{J} - \frac{G}{V} \frac{(\rho U_n)_w}{\rho_r U_r} \Delta s \tag{167}$$

$$\tau_{ns_{KL}} = 0 \tag{168}$$

$$\tau_{n\phi_{KL}} = 0 \tag{169}$$

Nacelle Wake Corrections

The presence of the nacelle can significantly alter the velocity distribution at the propeller blade. The flow, and hence the streamline, can accelerate or decelerate to follow the shape of the nacelle. Thus if a wake model is known for an isolated propeller, then the isolated wake should be corrected for the presence of the nacelle by addition of the nacelle's influence on the streamline due to its presence in the flow (figure 18).

The nacelle wake corrections are determined by comparing the calculated streamlines for the flow over the nacelle to the classical wake streamlines. Since the vorticity shed from the lifting line is convected by the streamlines, the location of a vortex element is given by

$$z = z_0 + U_\infty t \tag{170}$$

$$r = r_0 \tag{171}$$

$$\psi_w = \psi_0 + \Omega t \tag{172}$$

for the classical wake where U_∞ is the freestream velocity and Ω the propeller rotational speed. The location of the vortex filament in the flow field about the nacelle is given by:

$$z = z_0 + \int_0^t U_z \, dt \tag{173}$$

$$r = r_0 + \int_0^t U_r \, dt \tag{174}$$

$$\psi_w = \psi_0 + \int_0^t \frac{U_\phi}{r} \, dt \tag{175}$$

The wake corrections (displacement from classical wake) for each streamline passing through the lifting line at the point r_o is given by

$$\Delta z(r_o,t) = \int_o^t (U_z - U_\infty)\, dt \tag{176}$$

$$\Delta r(r_o,t) = \int_o^t U_r\, dt \tag{177}$$

$$\Delta \psi(r_o,t) = \int_o^t \left(\frac{U_\phi}{r} - \Omega\right) dt \tag{178}$$

Since the lifting line theory uses ψ_w as in independent variable referenced to the blade at t = o (ψ_o = o).

$$\psi_w = \int_o^t \Omega\, dt \tag{179}$$

where the dimensional time is

$$dt = \frac{ds}{VU_s} \tag{180}$$

and V is the metric scale coefficient.

Blade Force

The action of the propeller blades on the circumferential average flow is treated by using body forces (force/volume) in the streamwise and tangential momentum equations, equations (125) and (127) and by using a dissipation function in the energy equation, equation (128). A rigorous derivation of these terms is given in reference 5.

The forces produced by the propeller are calculated using lifting line theory as derived in the propeller portion of the report. These forces (force/span) act on the lifting line and are resolved in the axial, tangential, and radial direction so that thrust and torque (power) can be calculated. Resolution of these forces in the (n, s, ϕ) directions is given by

$$f_s = f_z \cos\theta + f_r \sin\theta \tag{181}$$

$$f_n = f_z \sin\theta - f_r \cos\theta \tag{182}$$

$$f_\phi = -f_p \tag{183}$$

where θ is the angle that the coordinate streamline makes with the z axis (figure 25) and where it is noted that (f_s, f_n, f_ϕ) are forces applied by the propeller to the flow field and (f_r, f_z, f_p) are the forces applied to the propeller by the flow. An assumption that the dissipation of energy is small compared to the work done is made, and thus ϕ_B, the rate of dissipation of energy of the blade boundary layer is neglected. Furthermore, it is assumed that the normal force is small.

The body forces (force/volume F_s, F_ϕ) are calculated from the lifting line forces (f_s, f_ϕ) by assuming uniform distribution over the blade chord passing through the lifting line and projected onto the (r,z) plane. Thus

$$F_s = V\frac{\partial f}{\partial s} = \frac{f_s}{c\cos\alpha} \tag{184}$$

$$F_\phi = V\frac{\partial f}{\partial s} = \frac{f_\phi}{c\cos\alpha} \tag{185}$$

where α is the angle between the chord line and z direction.

Nacelle Drag

The nacelle drag is composed of two parts; pressure drag and friction drag. The pressure drag is the resultant force in the axial direction produced by the static pressure acting on the body surface area. This force D_{pr} is given by

$$D_{pr} = \int_A \vec{P} \cdot d\vec{A}_z \tag{186}$$

where $\vec{P}$ is the static pressure acting normal to the body surface and $d\vec{A}_z$ is the differential area in the axial direction. For axisymmetric bodies, as shown in figure 27, equation (186) becomes,

$$D_{pr}(x) = \pi r_1^2 P_1 + \int_{x_1}^{x} P \sin\theta \, 2\pi r \, dx - \pi r^2 P_B \tag{187}$$

The first term is the contribution due to the pressure acting on the area within the centerbody. The second term is the contribution of the static pressure acting on the nacelle surface and the last term is the contribution of the base pressure acting on the nacelle afterbody. Analytical treatment of the separated flow on nacelle afterbody is not sufficiently developed to predict the base pressure drag. Therefore it is assumed that the base pressure P_B equals the local static pressure P.

Following the usual convention, the drag coefficient is defined using the maximum projected area in the axial direction.

$$C_{D_{pr}} = \frac{D_{pr}}{\frac{1}{2}\rho U_\infty^2 (2\pi r_{max}^2)} \tag{188}$$

The nacelle friction drag is produced by the nacelle boundary layer. This is determined by integrating the axial component of wall stress acting on the wetted area on the nacelle as shown in figure 27.

$$D_{fr}(x) = \int_{x_1}^{x} \tau_{ns} \cos\theta \, 2\pi r dx \tag{189}$$

The friction drag coefficient is then given by

$$C_{D_{fr}} = \frac{D_{fr}}{\frac{1}{2} \rho U_\infty^2 (2\pi r_{max}^2)} \tag{190}$$

where the projected area rather than wetted area is used to keep it consistent with the definition of pressue drag coefficient.

Numerical Solution

With the relationship between μ_T and the mean flow specified, equations (124) through (133) can be solved by an implicit forward marching numerical integration scheme. These equations are first linearized by expanding all dependent variables in a Taylor series expansion in the marching direction (s), and terms of 0 (Δs^2) are dropped. Finite difference equations are then obtained using the two point centered difference scheme of Keller (references 62 and 63). The resulting matrix equations are (10 x 10) block tridiagonal and are solved by block factorization using the method of Varah (reference 64).

This numerical solution is second order accurate in the n direction, first order in the s direction, and linearly stable. The Δs step size is limited not by linear stability conditions, but by the required accuracy in the Taylor series expansion in s.

Streamline Curvature Analysis

The derivation of governing code equations which are solved in the ADD code is given by Anderson (reference 4). This derivation consists of constructing an orthogonal coordinate system from the potential flow solution and parabolizing the Navier Stokes equations by assuming that the velocity component normal to the inviscid flow streamline (streamwise coordinate) is small compared to the streamwise component of velocity. As shown in reference 4, one important effect of this assumption is to replace the actual viscous flow streamline curvature with the approximate potential flow streamline curvature. Furthermore, it is noted that the potential flow streamline curvature was calculated from two dimensional incompressible potential flow obtained by conformal mapping. These approximations are valid for a large variety of flows (reference 65). However, when the streamline curvature departs significantly from that of the incompressible plane potential flow, then these approximations lead to errors in the prediction of the flow field (reference 53). In addition to a viscous flow analysis, an approximate inviscid flow analysis was derived which was based on this streamline curvature approximation. This inviscid flow analyses is capable of treating axisymmetric compressible swirling flow with variations in total pressure and total temperature from streamline to streamline (i.e., rotational flow). Both the viscous and inviscid analysis are dependent on this streamline curvature approximation and show significant errors under the same circumstances. The purpose of this section is to derive streamline curvature corrections to reduce the error in calculating the solution of both the viscous and inviscid flow equations.

Basic Equations

The basic parabolized Navier Stokes equations used by the ADD code (reference 4) and including all convection terms are given below. These relationships neglect the body forces for the development of the curvature corrections and are presented in a normalized form.

Continuity Equation

$$\frac{\partial}{\partial n}\left(\frac{GPU_n}{V}\right) + \frac{\partial}{\partial s}\left(\frac{GPU_s}{V}\right) = 0 \tag{191}$$

$$\frac{GPU_s}{V} = \frac{\partial \psi}{\partial n} \tag{192}$$

$$\frac{GPU_n}{V} = -\frac{\partial \psi}{\partial s} \tag{193}$$

S Momentum Equation

$$\frac{GPU_s}{V}\frac{\partial U_s}{\partial s} + \frac{GPU_n}{V}\frac{\partial U_s}{\partial n} - \frac{GPU\phi^2}{VR}\frac{\partial R}{\partial s} + \frac{1}{\gamma M_r^2}\frac{G}{V}\frac{\partial \Pi}{\partial s} = V\frac{\partial}{\partial n}\left(\frac{G\Sigma_{ns}}{V^2}\right) \tag{194}$$

ϕ Momentum Equation

$$\frac{GPU_s}{V}\frac{\partial U_\phi}{\partial s}+\frac{GPU_n}{V}\frac{\partial U_\phi}{\partial n}+\frac{GPU_sU_\phi}{VR}\frac{\partial R}{\partial s}+\left\{\frac{GPU_nU_\phi}{VR}\frac{\partial R}{\partial n}\right\}=\frac{1}{R}\frac{\partial}{\partial n}\left(\frac{GR\Sigma_{n\phi}}{V}\right) \quad (195)$$

n Momentum Equation

$$\left\{\frac{GPU_s}{V}\frac{\partial U_n}{\partial s}+\frac{GPU_n}{V}\frac{\partial U_n}{\partial n}-\frac{GPU_nU_s}{V^2}\frac{\partial V}{\partial s}\right\}+\frac{GPU_s^2}{V^2}\frac{\partial V}{\partial n}-\frac{GPU_\phi^2}{VR}\frac{\partial R}{\partial n}+\frac{1}{\gamma M_r^2}\frac{G}{V}\frac{\partial \Pi}{\partial n}=0 \quad (196)$$

Energy Equation

$$\frac{GPU_s}{V}\Theta\frac{\partial I}{\partial s}+\frac{GPU_n}{V}\Theta\frac{\partial I}{\partial n}=-\frac{\gamma}{\gamma-1}\frac{\partial}{\partial n}\left(\frac{GQ}{V}\right)+\gamma M_r^2(\Sigma_{ns}E_{ns}+\Sigma_{n\phi}E_{n\phi}) \quad (197)$$

Stress/Heat Flux

$$\Sigma_{ns}=\left(\frac{\mu_E}{\mu_r}\right)\frac{1}{Re_r}\left\{V\frac{\partial U_s}{\partial n}+U_s\frac{\partial V}{\partial n}\right\}=\left(\frac{\mu_E}{\mu_r}\right)\frac{E_{ns}}{Re_r} \quad (198)$$

$$\Sigma_{\phi n}=\left(\frac{\mu_E}{\mu_r}\right)\frac{1}{Re_r}\left\{V\frac{\partial U_\phi}{\partial n}-\frac{U_\phi}{R}\frac{\partial R}{\partial n}\right\}=\left(\frac{\mu_E}{\mu_r}\right)\frac{E_{n\phi}}{Re_r} \quad (199)$$

$$Q=\frac{1}{Re_rP_{r_T}}\left(\frac{\mu_E}{\mu_r}\right)V\frac{\partial\Theta}{\partial n} \quad (200)$$

Thermodynamic Relations

$$\Pi=P\Theta \quad (201)$$

$$I=\frac{\gamma}{\gamma-1}\ln\Theta-\ln\Pi \quad (202)$$

$$\frac{\Theta_T}{\Theta}=1+\frac{\gamma-1}{2}M^2 \quad (203)$$

$$\frac{\Pi_T}{\Pi}=\left[1+\frac{\gamma-1}{2}M^2\right]^{\frac{\gamma}{\gamma-1}} \quad (204)$$

$$I=\frac{\gamma}{\gamma-1}\ln\Theta_T-\ln\Pi_T \quad (205)$$

$$M^2=M_r^2\frac{U^2}{\Theta}=M_r^2\frac{U_s^2+U_n^2+U_\phi^2}{\Theta} \quad (206)$$

Curvature

$$K_n = \frac{1}{R_n} = -\frac{\partial V}{\partial s} \tag{207}$$

$$K_s = \frac{1}{R_s} = -\frac{\partial V}{\partial n} \tag{208}$$

$$K_\phi = \frac{1}{R} \tag{209}$$

Velocity Components

$$U_n = U \sin\theta \tag{210}$$

$$U_s = (U \cos\theta)\cos\alpha \tag{211}$$

$$U_\phi = (U \cos\theta)\sin\alpha \tag{212}$$

Vorticity

$$\omega_n = \frac{V}{R}\frac{\partial}{\partial s}(RU_\phi) \tag{213}$$

$$\omega_s = -\frac{V}{R}\frac{\partial}{\partial n}(RU_\phi) \tag{214}$$

$$\omega_\phi = V^2\left\{\frac{\partial}{\partial n}\left(\frac{U_s}{V}\right) - \frac{\partial}{\partial s}\left(\frac{U_n}{V}\right)\right\} \tag{215}$$

The terms in the brackets in equations (195) and (196), the tangential and normal momentum equations, are dropped in the ADD code equations but are retained for the purpose of deriving streamline curvature corrections. The curvatures are given by equations (207) through (209). K_n is the curvature of the coordinate potential line; K_s is the curvature of the coordinate streamline; and K_ϕ is the curvature of the swirl flow.

The velocity components are given by equations (210) through (212). It is noted that the angles are defined relative to the (n, s, ϕ) ADD code coordinates. With no swirl, $U_\phi = 0$ and θ is the angle between the velocity vector and the streamwise coordinate S.

The vorticity components are given by equations (213) through (215). If there exists variations in total pressure and total temperature from streamline to streamline, then by Crocco's theorem (reference 66), these vorticity components are not zero.

The ADD code equations used in reference 4 are given by equation (192) and equations (194) through (202) with the terms in brackets in equations (195) and (196) dropped. These equations are based on the assumption that the actual streamlines lie close to the assumed streamlines which in this case are the coordinate streamlines obtained by a conformal mapping solution of the two dimensional incompressible potential flow equations. Under these conditions U_n is small compared to U_s and the terms in the brackets in equations (195) and (196) may be dropped. These equations are parabolic differential equations (see reference 4) and can be solved by forward marching numerical integration.

If the terms in the brackets of the normal momentum equation, equation (196), are retained, then the set of equations is elliptic. This can easily be demonstrated by substituting the equations for the stream function, equations (192) and (193) into equation (196). The resulting equation will have a $\partial^2\psi/\partial S^2$ term which will make the equations elliptic. If, however, the terms in the bracket are treated as known, the equations remain parabolic.

Streamline Curvature Correction

When the terms in the brackets of equation (196) are neglected, the actual streamline curvature is taken to be the streamline curvature K_s of the coordinates. Three sources of error are then introduced. First, the effects of axisymmetric flow on curvature are neglected and replaced by two dimensional effects. For many gas turbine ducts the ratio of inside radius to outside radius approaches one and this effect is small. However, for the high speed propeller this effect is significant. Second, the effects of compressibility are neglected. Again, however, in curved ducts as choked flow is approached, the effects of compressibility on streamline curvature may be significant. Third, viscous effects are neglected. These viscous effects are principally due to displacement of the streamline produced by the growth of the boundary layer. Near separation, the boundary layer grows very rapidly and significant changes in streamline curvature may occur.

The normal momentum equation, equation (196) can be written in the following convenient form;

$$-\left(\frac{K_s+\Delta K_s}{V}\right) PU_s^2 - \frac{PU\phi^2}{R}\frac{\partial R}{\partial n} + \frac{1}{\gamma M_r^2}\frac{\partial \Pi}{\partial n} = 0 \qquad (216)$$

where

$$\Delta K_s = -V\left\{\frac{1}{U_s}\frac{\partial U_n}{\partial s} + \frac{U_n}{U_s^2}\frac{\partial U_n}{\partial n} - \frac{U_n}{U_s}\frac{1}{V}\frac{\partial V}{\partial s}\right\} \qquad (217)$$

The term ΔK_s is the curvature of the actual streamline relative to the coordinates. It can be seen in equation (216) that the form of the ADD code normal momentum equation is preserved. Furthermore, it should be noted that if ΔK_s is known a-priori, the ADD code equations remain parabolic.

The set of equations, equation (192) and equations (194) through (202) with equation (216) replacing equation (196) and with ΔK_s included can be solved as an elliptic set of equations using a multi pass method by lagging ΔK_s. This procedure, however, may incur severe stability problems. An alternate procedure, adopted here, is to neglect viscous effects but include axisymmetric and compressibility effects by calculating the streamline curvature of compressible axisymmetric potential flow and using it in place of $(K_s + \Delta K_s)$ in equation (216). Since this streamline curvature is known a-priori, the set of equations remains parabolic and can be solved in a single pass.

Compressible Potential Flow

If there are no gradients in total temperature and total pressure and no swirl, then by Crocco's theorem the flow is irrotational and the vorticity components, equations (213) through (215), vanish everywhere in the flow field. Under these conditions equations (192), (193) and (215) may be combined to yield a single equation for the stream function,

$$\frac{\omega\phi}{V^2} = \frac{\partial}{\partial n}\left(\frac{1}{PG}\frac{\partial \Psi}{\partial n}\right) + \frac{\partial}{\partial s}\left(\frac{1}{PG}\frac{\partial \Psi}{\partial s}\right) = 0 \qquad (218)$$

where the density ρ is given by

$$P = P_{T\infty}\left[1 + \frac{\gamma-1}{2} M_r^2 \frac{U_s^2 + U_n^2}{\Theta_{T\infty}}\right]^{-\frac{1}{\gamma-1}} \tag{219}$$

U_s and U_n are obtained from the stream function using equations (192) and (193). For incompressible flow $\rho = \rho_\infty$ is constant. Equations (218) and (219) replace the two momentum equations, equations (194) and (196). Equation (218) is an elliptic equation and requires that ψ be prescribed on the boundary.

$$\psi(0,s) = 0 \tag{220}$$

$$\psi(1,s) = \psi_\infty \tag{221}$$

$$\psi(\eta,0) = U_{so}\int_0 \left(\frac{GP}{V} \Big/ \frac{d\eta}{dn}\right)_{s=0} d\eta \tag{222}$$

$$\psi(\eta,s_L) = U_{so}\int_0^{\eta} \left(\frac{GP}{V} \Big/ \frac{d\eta}{dn}\right)_{s=s_L} d\eta \tag{223}$$

Equations (222) and (223) and all following equations contain a coordinate stretching function for the normal coordinate which is given by

$$\eta = \tanh(Bn)/\tanh(B) \tag{224}$$

where B is an arbitrary parameter.

Equations (218) and (219) can be solved iteratively. If $\rho(n,s)$ is assumed known, then equation (218) can be solved by line relaxation. If we choose the line of unknowns to be along the normal coordinate (S = constant) and J is an index for the streamline and K is an index for the normal line, then the finite difference equation for equation (218) is given by

$$\frac{F_K^J}{\Delta\eta^2}\left(\tilde{\Psi}_{K+1}^J - 2\tilde{\Psi}_K^J + \tilde{\Psi}_{K-1}^J\right)\left(\frac{d\eta}{dn}\right)^2 - \frac{(F_K^J)^2}{(2\Delta\eta)^2}\left(1/F_{K+1}^J - 1/F_{K-1}^J\right)\left(\tilde{\Psi}_{K+1}^J - \tilde{\Psi}_{K-1}^J\right)\left(\frac{d\eta}{dn}\right)^2 \tag{225}$$

$$+ \frac{F_K^J}{(2\Delta s)^2} + \frac{F_K^J}{2\Delta\eta}\left(\tilde{\Psi}_{K+1}^J - \tilde{\Psi}_{K-1}^J\right)\frac{d^2\eta}{dn^2} + \frac{F_K^J}{\Delta s^2}\left(\Psi_K^{J+1} - 2\tilde{\Psi}_K^J + \Psi_K^{J-1}\right)$$

$$- \frac{F_K^J}{(2\Delta s)^2}\left(1/F_K^{J+1} - 1/F_K^{J-1}\right)\left(\Psi_K^{J+1} - \Psi_K^{J-1}\right) = 0$$

where

$$F_K^J = 1/(PG)_K^J \tag{226}$$

Treating $\tilde{\psi}_K^J$ as the unknown and collecting coefficients we have

$$A_K = \left[\frac{F_K^J}{(\Delta\eta)^2} + \frac{F_K^J}{(2\Delta\eta)^2}\left(1/F_{K+1}^J - 1/F_{K-1}^J\right)\right]\left(\frac{d\eta}{dn}\right)^2 - \frac{F_K^J}{2\Delta\eta}\frac{d^2\eta}{dn^2} \tag{227}$$

$$B_K = 2F_K^J\left[\frac{1}{(\Delta\eta)^2}\left(\frac{d\eta}{dn}\right)^2 + \frac{1}{(\Delta s)^2}\right] \tag{228}$$

$$C_K = \left[\frac{F_K^J}{(\Delta\eta)^2} - \frac{(F_K^J)^2}{(2\Delta\eta)^2}\left(1/F_{K+1}^J - 1/F_{K-1}^J\right)\right]\left(\frac{d\eta}{dn}\right)^2 + \frac{F_K^J}{2\Delta\eta}\frac{d^2\eta}{dn^2} \tag{229}$$

$$D_K = \frac{-F_K^J}{(\Delta s)^2}\left(\Psi_K^{J+1} - \Psi_F^{J-1}\right) + \frac{(F_K^J)^2}{(2\Delta s)^2}\left(1/F_K^{J+1} - 1/F_K^{J-1}\right)\left(\Psi_K^{J+1} - \Psi_K^{J-1}\right) \tag{230}$$

and equation (225) reduces to

$$A_K\tilde{\Psi}_{K-1}^J + B_K\tilde{\Psi}_K^J + C_K\tilde{\Psi}_{K+1}^J = D_K \tag{231}$$

with the boundary conditions

$$\left.\begin{aligned}\tilde{\Psi}_1^J &= 0\\ \tilde{\Psi}_{KL}^J &= \Psi(1)\end{aligned}\right\} \tag{232}$$

The matrix equation (231) is tridiagonal and can be solved by Gaussian elimination using the following algorithm.

$$\left.\begin{aligned} E_1 &= 0 \\ F_1 &= 0 \end{aligned}\right\} \tag{233}$$

$$\left.\begin{aligned} E_K &= -C_K/(B_K + A_K E_{K-1}) \\ F_K &= (D_K - A_K F_{K-1})/(B_K + A_K E_{K-1}) \end{aligned}\right\} \quad K = 2, KL \tag{234}$$

$$\left.\begin{aligned} \tilde{\Psi}^J_{KL} &= \Psi(1) \\ \tilde{\Psi}^J_K &= E_K \tilde{\Psi}^J_{K+1} + F_K \end{aligned}\right\} \quad K = KL-1, 1 \tag{235}$$

Then the new guess for $(\psi^J_K)^{\nu+1}$ is given by

$$(\Psi^J_K)^{\nu+1} = (\Psi^J_K)^{\nu} + \Omega\left[\tilde{\Psi}^J_K - (\Psi^J_K)^{\nu}\right] \tag{236}$$

where Ω is a relaxation parameter ($0 < \Omega < 2$). When an iterative guess for the whole field is known $\psi(n,x)$, a new iterative guess for the density is obtained from equations (192), (193) and (219). This iteration procedure is repeated until

$$\left.\begin{aligned} \left|\Psi^{\nu+1} - \Psi^{\nu}\right| &< \epsilon_\Psi \\ \left|P^{\nu+1} - P^{\nu}\right| &< \epsilon_P \end{aligned}\right\} \tag{237}$$

Flow Angle and Curvature

Once the solution for ψ is obtained from equation (218), the flow angle is determined from equations (210) and (211).

$$\cos^2\theta = 1 - \frac{U_n^2}{U_s^2 + U_n^2} \tag{238}$$

The normal pressure gradient is determined by differentiating equation (204) where Π_T is constant for the flow field. Then

$$\frac{\partial \Pi}{\partial n} = -\gamma M_r^2 P \frac{\partial}{\partial n}\left(\frac{U^2}{2}\right) \tag{239}$$

Equating equation (239) to equation (216) where $U_\phi = 0$, results in

$$K_c = -\frac{V}{\cos^2\theta U_s^2}\frac{\partial}{\partial n}\left(\frac{U^2}{2}\right) \tag{240}$$

where K_c is the streamline curvature for axisymmetric compressible flow which is to be used in equation (216) in place of $(K_s + \Delta K_s)$.

Approximate Inviscid Analysis

The ADD code contains an approximate inviscid flow analysis which is used to obtain blade forces using blade element strip theory (see references 5 and 65). This inviscid flow theory is derived using the same streamline curvature approximation that is used in the viscous flow analysis. Since gas turbine flows are swirling compressible flows with variations of total temperature and total pressure from streamline to streamline, they are rotational flows. The approximate inviscid analysis in the ADD code was developed to treat these flow fields. The purpose of this section is to derive the streamline curvature corrections for this analysis. Later it shall be shown that if exact streamline curvatures are used in the analysis, the analysis is also exact.

For inviscid flow, Q_n, E_{ns}, $E_{n\phi}$ are zero. Then equations (195) and (197) with the use of equations (192) and (193) reduce to

$$\frac{\partial \Psi}{\partial n}\frac{\partial I}{\partial s} - \frac{\partial \Psi}{\partial s}\frac{\partial I}{\partial n} = 0 \tag{241}$$

$$\frac{\partial \Psi}{\partial n}\frac{\partial}{\partial s}(RU_\phi) - \frac{\partial \Psi}{\partial s}\frac{\partial}{\partial n}(RU_\phi) = 0 \tag{242}$$

The form of the solution to equations (241) and (242) can be written as

$$I = I(\Psi) \tag{243}$$

$$RU_\phi = f(\Psi) \tag{244}$$

Then using equation (205),

$$\Pi_T = \Pi_T(\Psi) \tag{245}$$

$$\Theta_T = \Theta_T(\Psi) \tag{246}$$

Equations (243) through (246) demonstrate the well known theorem that in inviscid flow, I, (RU_ϕ), Π_T, Θ_T are constant along streamlines but may vary from streamline to streamline. The normal momentum equation (equation (196)) is written in the following form

$$\frac{\partial \Pi}{\partial n} = \gamma M_r^2 \cos^2\theta \left[\frac{K_s + \Delta K_s}{V} \cos^2\alpha + \frac{1}{R}\frac{\partial R}{\partial n} \sin^2\alpha\right] PU^2 \tag{247}$$

The approximate inviscid solution assumes that the potential flow streamline used to construct the coordinates approximates the actual streamline. Hence

$$\left.\begin{aligned} \Psi &= n \\ \theta &= 0 \\ \Delta K_s &= 0 \end{aligned}\right\} \tag{248}$$

and the equations listed above are easily integrated according to the current method. Clearly, if the flow angle Θ and the curvature K_c from equation (240) replacing $(K_s + \Delta K_s)$ can be specified then a more accurate solution for the inviscid flow can be obtained.

COUPLING PROCEDURE

Assumptions Affecting the Coupling

As noted in the Introduction, the coupling of the two separate procedures for the nacelle and propeller portions of the analysis requires the transfer of pertinent data affecting the respective solution procedures of the analysis. The ability to use this solution technique to obtain the combined propeller-nacelle performance prediction is based upon the following major assumptions related to the coupling process which are noted below.

As was noted in the technical approach for the propeller solution procedure, the flow field is steady with respect to the propeller blades; however, this is not true when the point of reference is the nacelle wall boundary. Because the nacelle analysis does assume time-averaged properties, an assumption concerning the propeller's influence must be made in order to use the nacelle analysis and to avoid the necessity to calculate the local time varying induced flow field about the nacelle due to the rotating propeller and wake. The assumption is made that the inclusion of the effects of the propeller on the nacelle and surrounding flow field can be handled in a time-averaged manner by including only the addition of the local blade forces at the blade row locations and that this model will adequately approximate on a time-averaged basis the effects of the combined blade and trailing wake system in the flow, to predict the flow field about the combined propeller-nacelle configuration.

To calculate the forces on the propeller blades it is necessary to assume that the nacelle flow field solution is representative of the actual flow field. Since this is a basic assumption of the nacelle portion of the combined analysis, no further explanations are necessary concerning the nacelle portion of the analysis in terms of the coupling procedure. The assumptions concerning the influence of the nacelle on the wake geometry were described in the section entitled: Nacelle Influence on the Wake Geometry, and are not repeated here.

Description of the Combined Analysis Solution Procedure

To obtain the combined propeller-nacelle performance solution, the interfacing of the propeller and nacelle solution procedures requires the transfer of data between the two portions of the analysis. In the combined analysis, the propeller portion requires that the local inflow conditions (velocity, density and speed of sound) at the blade row(s) be specified and that the wake geometry be corrected for the presence of the nacelle, if so desired. The nacelle portion requires that the lifting line geometry and local blade forces (radial, tangential, axial) per unit length be specified for the propeller blade row(s). Figure 28 is a simplified flow diagram of the combined solution procedure with the required transfer of data noted, as developed for this application. The major tasks performed in the analysis associated with the pertinent features of the combined analysis are also shown in this flow diagram.

The structure of the solution procedure is shown in the diagram. Within the analysis there are two ways in which the combined analysis can be used. First, the program can be run with only the inviscid flow field calculated to define the inflow and wake perturbations for the propeller portion of the analysis to obtain the combined propeller and nacelle performance; however, the blade forces are not included in the inviscid nacelle solution. This may be desirable for cost considerations if it is shown that the viscous solution does not significantly change the propeller performance predictions as compared with the inviscid propeller performance predictions, and, if the inclusion of the blade force's influence on the nacelle performance is not desired. Second, if the viscous solution is desired, the analysis can also be made to cycle through the viscous portion a selected number of times. This mode will include the blade force's influence on the nacelle performance. The selection of the number of cycles required to obtain compatible solutions must be determined from the user's experience. Based on the experience gained in the development of the computer analysis, it is believed that generally only one cycle will be required. However, this assumption remains to be proven in actual practice. It should also be noted that for the viscous solution's influence at the blade, it is not currently possible to separate, from the viscous velocity field solution, the portion of the inflow due to the addition of the blade forces. To resolve this problem, the calculation of the flow field due to the nacelle at the blade row is performed at the blade leading edge in the viscous solution procedure. This approach removes the blade force's influence on the flow field at the propeller because of the parabolic nature of the problem. That is, the inclusion of the blade forces, distributed over the blade surface, is not felt at the leading edge of the propeller blades, only downstream of this location.

INITIAL APPLICATION OF THE ANALYSIS

The initial application of the analysis was performed under Contract NAS3-20961 and was limited to a single propeller-nacelle configuration and test condition. The results obtained from this application indicated that the inflow velocities due to the nacelle body were incorrectly predicted at the blade row. This finding was verified by the use of an alternate nacelle analysis to predict the velocity profile at the blade row location. In addition to this problem, the use of the computer program requires the selection of various propeller aerodynamic modeling features which can significantly affect the performance predictions. As a result, Contract NAS3-22142 was established to refine and modify the analysis to remove known problems and to expand the scope of the application of the analysis to include different propeller nacelle configurations, test conditions, and modeling features. Following this effort additional applications of the analysis have been made under Contract NAS3-22257 to configurations and operating conditions for which test data is available for comparison.

In general, the results of the initial application of the analysis will not be reported herein because of the limited nature of that study. It is sufficient to note that this single application led to the more expanded application and refinement effort for the contracts noted above. The results of this expanded application are reported below. This study includes a comprehensive investigation of the effects of the propeller aerodynamic modeling features, the sensitivity of results to the airfoil characteristics defined for the same airfoil section from different sources, the application of the analysis to different operating conditions, and the application of the analysis to different propeller-nacelle configurations which include single and coaxial geometries.

NACELLE FLOW FIELD PREDICTIONS

The combined analysis requires that both the flow field around the nacelle body and the blade loading solution be predicted with reasonable accuracy. Both solutions are predicted based on the super-position of the individual solutions in a cyclic manner. The refinements to the original axisymmetric duct flow field solver (ADD Code, references 4 and 5) to treat axisymmetric nacelle configurations with or without wind tunnel wall influence (including tunnel wall bleed) have resulted in an analysis (PANPER) capable of treating a wide range of high speed propeller configurations when combined with the propeller blade loading analysis. The verification of the ability of the analysis to predict the flow field perturbations around the nacelle for these high speed conditions was performed by comparing predictions for an isolated nacelle at Mach Numbers of .2, .7, and .8 with the predictions obtained using an established transonic, inviscid flow field solver for axisymmetric bodies (RAXBOD, references 67 and 68). The results of this comparison are presented for the .8 Mach Number condition. The results at .2 and .7 Mach number will not be presented, but are similar in the degree of correlation.

In figure 29, the predicted nacelle wall pressure distributions for the SR-3 Nacelle design at .8 Mach Number are shown for both the PANPER and the RAXBOD codes. An example of this propeller blade planform is shown in figure 30 for illustration purposes. Superimposed on figure 29 is the corresponding nacelle profile and the approximate location of the blade lifting line. The prediction for the pressure distribution using the PANPER analysis differs from the RAXBOD prediction near the nose of the nacelle. This is due to the use of an optional smoothing process in the PANPER analysis applied to the nacelle profile coordinates resulting in slightly different local profile coordinates. Further downstream, past the blade row in the region of the high curvature of the nacelle profile, the predicted solutions also exhibit some differences. The RAXBOD analysis predicts a lower pressure distribution corresponding to a region of transonic flow. The PANPER analysis, which is not a transonic flow analysis, clearly does not predict the same pressure distribution. It should be noted that the PANPER analysis yielded nearly identical results for both the inviscid and viscous pressure distributions for the other lower Mach number conditions. These comparisons indicate that the general character and level of the nacelle wall pressure distributions are reasonably predicted, although regions of supersonic flow are not correctly modeled. However, this discrepancy is probably not significant for propeller performance predictions in the region of the blade lifting line location as will be shown in the next section.

During the course of this investigation test measurement data for the flow field upstream of a non-lifting propeller, obtained in the NASA Lewis Research Center test facilities, was made available to UTRC and has been presented in reference 69. The results of applying the nacelle code to these test results are included herein as an additional example of the code's predictive capability. This study also illustrates the need to include the effect of blade thickness in the nacelle flow field solution procedure when using the analysis to predict the flow field upstream of the blade row. The condition investigated was at .8 Mach Number for the non-lifting SR-3 propeller/nacelle configuration. The flow measurements were obtained using laser velocimetry techniques at an axial position .09 propeller radii upstream of the propeller blade row. Three different nacelle flow field solutions were obtained to demonstrate the effect of different streamline curvature models and the presence of the blades in the solution procedure. The results in figure 31 present the measured and predicted Mach Number distributions along the blade lifting line location for this condition. The results of the different streamline curvature models, without blade thickness, illustrate the improvement in the predictive capability of the nacelle code when the two-dimensional streamline curvature model of the original analysis was modified to an axisymmetric streamline curvature model for propeller application. The inclusion of the blade thickness in the axisymmetric streamline curvature model further improves the flow field predictions near the high solidity region of the propeller blades where the presence of the blade should be most strongly felt. The discrepancy in the overall level of the flow field (Mach Number) away from the nacelle wall may indicate that the actual condition tested is not a true 0.8 Mach number condition. If the analysis were run to match the implied freestream Mach Number of the test results, the correlation would be excellent over most of the range of radial positions measured. Near the nacelle wall, the results would differ slightly. This difference could be due to either the numerical model or a slight difference in the location of the measured data compared with the position used in the analysis. Another possible reason for the difference is that the SR-3 propeller is never truly non-lifting in a local sense. The blade's integrated lift may be zero, but the local blade loading can be non-zero. Thus, there could be the effect of a local lift induced flow field in the test results. The analysis was run without the blade forces, and thus there are no lift induced velocities included in the predictions.

The use of the nacelle induced flow field at the propeller blade as predicted by the nacelle portion of the PANPER analysis requires that the locations along the blade at which the velocity components are calculated be specified. Traditional Prandtl lifting line theory under uniform freestream conditions requires that the angle of attack at the wing quarter-chordline be defined using the freestream velocity and the induced velocity. The propeller lifting line solution is an extension of this concept to the propeller environment which includes the rotational and nacelle induced velocity fields. Near the nacelle, the nacelle induced flow field varies in the radial and axial directions (axisymmetric assumption). Thus, the nacelle induced flow field used in the propeller portion of the analysis is affected by the selection of the location (blade quarter-chordline, leading edge, etc.) at which this information is calculated. The selection of these locations has not yet been clearly defined. In figure 32, the axial component of the nacelle flow field, as predicted using the nacelle portion of the PANPER analysis, is presented along the blade leading edge and the blade quarter-chordline with and without the inclusion of the blade thickness in the streamline curvature model. The results indicate that the axial velocity is relatively insensitive to the selection of the prediction location for the solution obtained neglecting the blade thickness influence in the streamline curvature model. However, when the blade thickness is included in the solution procedure, the axial velocity component shows a strong sensitivity to the selection of the prediction location. It should be noted that the radial velocity component does not exhibit this strong sensitivity as shown in figure 33.

The sensitivity of the axial velocity to the selected prediction location introduces an additional uncertainty in the use of the analysis. Since the propeller portion of the analysis already recognizes the high solidity regions of the blade near the hub walls through the use of the cascade characteristics, the use of the blade thickness influence in the prediction of the nacelle induced flow field solution is actually "double accounting" for the blade thickness. Thus, for propeller performance predictions, the most appropriate way of using the analysis may be to either; include the blade thickness in the nacelle induced flow field solution without using cascade characteristics in the lifting-line propeller solution, or conversely, use the cascade characteristics in the propeller solution without the blade thickness influence in the nacelle flow field solution. However, for the first method the selection of the prediction location (leading edge, quarter chordline, trailing edge) for the nacelle induced velocities as used in the propeller analysis has not been adequately investigated. As a result, the analysis is generally run for propeller performance predictions using the second method of neglecting the blade thickness influence in the nacelle induced flow field. For nacelle induced flow field predictions away from the propeller disk, the nacelle analysis should be run including the effects of blade thickness as was done for the results presented in figure 31. This is necessary because the lifting-line models do not account for thickness in the propeller induced field.

SINGLE PROPELLER PERFORMANCE PREDICTIONS

Aerodynamic Modeling Features

The development of the propeller portion of this analysis is based on the application of methodologies which have been extended to the limits of their operational applicability to attempt to provide a useful, numerically efficient performance analysis. To provide this type of analysis tool using the incompressible lifting line model required the inclusion of many different aerodynamic modeling features. These features attempt to include in a rational manner the effects of compressibility on the propeller tip loading, the effects of compressibility on the propeller wake induced velocity field, the influence of the nacelle flow field, the effects of the high solidity inboard blade sections using cascade data or corrections to isolated airfoil data for the cascade influence, the effects of highly swept blades, and the selection of different sources of isolated airfoil and cascade characteristics. This large number of modeling features has resulted in an even larger number of combinations of these features which can be used when predicting the propeller performance. In addition, these features do not address the question concerning the inclusion of the blade thickness influence in the nacelle flow field solution procedure noted earlier. Obviously many combinations are unrealistic, however there are still a large number of realistic combinations which can be used. This investigation has attempted to define a reasonable combination of these features by applying the analysis to different propeller-nacelle configurations and operating conditions to study the results, examine the sensitivities to modeling options and compare the predictions with test data where available. These comparisons are presented to provide some useful insight into the best selection of these modeling features.

Through out this report the terms net and apparent efficiency are used. For clarity they are defined herein. The net efficiency (η) is that measured in the tunnel by the force balance for the total system installation. In a simplistic sense this is the total of the propeller forces and nacelle body forces. The apparent efficiency (η_A) is the component due only to the propeller forces generated in the presence of the nacelle. Since the effect of the actual body is to reduce the efficiency, the apparent efficiency is usually higher than the net by some small correction ($\Delta\eta$).

$$\eta_A = \eta + \Delta\eta \tag{249}$$

The analysis can only predict the apparent efficiency since the nacelle body force predictions are valid only up to the termination of the body model or the separation point. Since separation usually occurs for the afterbodies used for these studies, the model was truncated reasonably far downstream from the blade row, but did not have closure on the geometry. Estimates for the back pressure can be made, but they are not of sufficient accuracy for this study. For comparisons without test results, the apparent efficiencies are used. In this report, the choice of the use of apparent or net efficiencies for comparison with test data was based on the effort required to adjust either the data or the predictions. Where the amount of test data was small compared to the number or prediction cases run, the data was correct to apparent efficiency. For the cases where the amount of data was larger, the predicted efficiencies were corrected to net values. These corrections were supplied by NASA.

The results presented herein start with the application of the analysis to selected propeller and nacelle configurations to compare the different aerodynamic modeling features. The influence of the nacelle on the solution is neglected for these preliminary applications. The intention is to define and illustrate the sensitivity of the propeller performance predictions to the modeling features. The analysis is then applied to conditions for which test data are available. For this application the effects of the different modeling features are again studied with the number of features limited in scope based on the first series of applications. However, because test data are available, the nacelle influence is included for this study. And finally, the analysis is applied to configurations in selected wind tunnel facilities to identify any potential problems in the use of the different facilities with the model scaling selected.

Single Propeller-Nacelle Configurations

Fundamentally the single propeller-nacelle configurations studied represent variations in blade design and nacelle shape. The variation in blade design include blade sweep, taper, twist, solidity, and thickness changes for the different blade geometries. The nacelle geometries studied were either the area ruled or conical shaped profiles. These nacelle profiles are shown in figure 34. The propeller geometries were the NASA designated SR-2, SR-1, SR-1M, and SR-3 designs; representing respectively, straight to moderately swept blades (0, 30, and 45 degrees). The difference between the SR-1 and the SR-1M designs is the blade tip twist and section camber. The airfoil sections were the NACA Series 16, transitioning to series 65 near the blade root. The blade design characteristics for each propeller configuration are presented in graphical form in figures 35 to 37. The plan forms were shown earlier in figure 30 for these designs.

Single Propeller-Nacelle Operating Conditions

The range of operating conditions studied was based on the range of early unpublished test data provided by NASA. The range in free-stream Mach number was from 0.6 to 0.8. For the initial studies, which investigated sensitivities to the modeling options, the variations in rpm at a fixed power loading (constant power) provided advance ratio variations in the range of 2.6 to 3.2. For the performance map predictions shown later, the advance ratio variations were in the range of 2.5 to 4.5 with blade angle variations in the range of 58 to 63 degrees depending on the propeller configurations and free-stream Mach number conditions (0.6 and 0.8). The range in power coefficients studied has from near windmilling conditions to as high as 3.0 depending on the combination of conditions. The design condition, when referenced herein, corresponds to an advance ratio fo 3.07 with a power coefficient of 1.69.

To help in determining when operating conditions represent supersonic tip speeds, the following relationship can be used to find the advance ratio which corresponds to a tip Mach number of 1.0.

$$M_{Tip} = M_{\infty} \left[1 + \left(\frac{\pi}{J} \right)^{1/2} \right]^{-1/2} \tag{250}$$

For the 0.6 free-stream Mach number condition there was no advance ratio condition studied which had supersonic tips. At the 0.7 Mach number condition, supersonic tip conditions existed for advance ratios less than 3.079. However, at the design point advance ratio (3.07) for this Mach number, the fraction of blade radius which experiences supersonic flow is very small (0.003R). For the 0.8 Mach number condition all advance ratio conditions less than 4.189 had supersonic tip Mach numbers. At the design point the outer 25 percent of the blade is operating in supersonic flow.

Effect Of Compressible Tip Loss Models

The analysis currently has four compressible flow tip loss models available along with the non-tip loss model. These models were described in an earlier technical section, but for convenience they will be briefly described here. The first model is the Evvard model (tabulated solutions) which is based on fixed wing, rectangular tipped geometries applied to the non-rectangular geometries of the high speed propeller designs. The second model is an exact analytical integration of the relations used in conical flow

theory for the rectangular wing tip. In theory this model is identical to the Evvard model which is available in tabular form, however there are small differences in practice. The third model is based on conical flow theory for swept wings assumed to be operating at a free-stream Mach number equal to the propeller tip Mach number. The fourth model is a variation of this model where the tip loss correction is further scaled using the ratio of the Prandtl Glauert compressibility corrections based on the propeller's local section and tip. Only the tabulated Evvard and the swept conical flow models were studied in depth and Mach numbers compared with the non-tip loss model results. The analysis was applied using the SR-1, SR-2, and SR-3 propellers with the area ruled spinner and nacelle geometry at; (1) the design advance ratio for a variation in free-stream Mach number at the design power coefficient, (2) the design advance ratio with a variation in the design power coefficient for a fixed Mach number, and (3) the design power coefficient for a variation of the advance ratio at a fixed Mach number. For some of the conditions investigated using the swept conical flow tip loss models, solutions were not obtained because the combination of blade geometry and operating condition violated assumptions used in the model. For this study, the analysis was applied using the cascade data correlations from reference 40 and the cascade correction based on flat plate theory was applied to the isolated airfoil data of Manoni over the blade transition region. The compressible wake model was used for all of the above cases. In addition, the influence of the nacelle was neglected for this study and thus the predicted results should not be considered indicative of the actual propeller performance capabilities. The results are presented separately in figures 38 to 40 for each propeller configuration. In these figures, the propeller efficiency is plotted on a greatly expanded scale as a function of the free-stream Mach number to illustrate the differences in the predictions using the various tip loss models.

The results of the application of the analysis to the unswept propeller blade design (SR-2) are presented in figure 38. At the 0.7 Mach number (tip Mach number 1.005), all tip loss models appear to function in the analysis, but the results are identical. This is because the supersonic region is too small (0.3 percent of radian) relative to the size of the lifting line segments along the blade and does not activate any of the models. The swept conical flow tip loss models are not used at the 0.8 Mach number for this propeller geometry because the assumptions used to develop the model are violated; the trailing edge of the blade must be supersonic. The effect of the Evvard tip loss model for all of the conditions at this Mach number is to reduce the propeller efficiency for a specified power level. When the analysis was run at a specified blade pitch the same effect was noted, although these results are not presented.

For the SR-1 propeller, a 30 degree swept blade design, the results of the application of the different tip loss models are shown in figure 39. Again, the lower Mach number condition (0.7) does not activate any of the models and the swept conical flow tip loss models can not be applied for this design at the 0.8 Mach number conditions. The Evvard model again results in the reduced efficiency compared with the non-tip loss model.

For the SR-3 propeller, a 45 degree swept blade design, the results of the application of the different tip loss models are presented in figure 40. At the 0.7 Mach number the swept conical flow models are again not applicable because the supersonic trailing edge requirement of the model is not met. At this Mach number the difference between the non-tip loss and the Evvard tip loss model results are small. The results for the application at 0.8 Mach number vary depending on the loading condition and advance ratio. The reduced loading condition (Cp=1.5) at the 3.07 advance ratio exhibits no significant difference between the swept conical flow tip loss models and the non-tip loss model while the use of the Evvard model results in a reduced efficiency prediction. At the design loading condition (Cp=1.7) for this advance ratio the swept conical flow tip loss models do result in a difference in the predicted efficiency at the 0.8 Mach number. The conical flow model, with the variable Mach number distribution scaling, results in relatively little effect on the performance. For the lower advance ratio case at this Mach number the use of the conical flow models results in reduced efficiency, and both models yield about the same level of reduction. For all cases at this Mach number the Evvard model results in reduced efficiencies.

As a result of this study the decision was made to only use the Evvard tip loss model in the applications to follow. This decision was made because the conical flow model is sensitive to propeller trailing edge geometry and Mach number as evidenced in the above results. This makes it unacceptable for general application. This selection of the Evvard model is not meant to imply that it is better than the swept conical flow tip loss models, but that as implemented, the conical flow tip loss model is not reliable as an investigative tool for all of the geometries studied in this investigation.

Effect of Cascade Models

The modeling of the propeller blade lift and drag characteristics is a critical aspect of the propeller portion of the analysis. The performance predictions can be no better than the lift and drag characteristic data used in the analysis. Within the analysis the inboard blade regions (NACA series 65 airfoil sections) operate at large chord-to-gap ratios for the high speed propeller designs under investigation by NASA. Isolated airfoil characteristics do not represent these cascade type blade sections. Two different

sources of cascade data have been provided in the analysis to model these blade section lift and drag characteristics. Both models are correlations, the first based on the NASA method of reference 40, the second on the method by Mellor (references 49 to 51). In addition the analysis has corrections which can be applied to isolated airfoil data based on either flat plate cascades or the Mellor correlation.

To study the influence of the cascade data on the performance predictions, the analysis was applied to the SR-1 propeller geometry using both of the cascade correlation models at the 0.8 Mach number condition for a variation in the advance ratio with a fixed blade pitch angle (60.2 deg.). For both cascade correlations used in the inboard regions, the flat plate cascade correction was used to correct the isolated airfoil characteristics along the blade transition region to attempt to model the airfoil characteristics in this region. In addition, a case was run with the isolated airfoil characteristics in this region corrected based on the Mellor correlation. (The inboard and transition regions are shown in figures 35 through 37.) This case used the Mellor correlation model, resulting in three different cascade characteristic models for comparative purposes. The variation in rpm represents the range of advance ratio from near 3.0 to windmill at a fixed Mach number. Again, no nacelle influence was included for this study. The predicted propeller efficiency, power coefficient, and thrust coefficient are presented respectively in figures 41 to 43 for these conditions. The plot of efficiency versus propeller rpm (figure 41) indicates a maximum difference between the predictions for the three cascade models of about 2.5 points in efficiency except at the lowest rpm studied. At this windmill condition the difference in the predicted efficiencies is quite significant because the propeller is essentially developing zero power as shown in figure 42. The outboard regions of the blades are so lightly loaded in relation to the inboard regions that differences in the inboard cascade data result in very significant differences in efficiency. For the more highly loaded conditions near the design advance ratio the outboard sections carry most of the airloading and thus the differences in the cascade data on the inboard regions do not have as significant of an effect. At these higher rpm conditions (lower advance ratio) the results obtained using the different cascade models do not show a consistent behavior in terms of the differences in predicted efficiencies for the variation in rpm; except that the efficiencies obtained using the NASA correlation model are always the highest or equal to the others. Over this rpm region the average variation in predicted efficiency is just under 1.0 point. The predicted power coefficients using these different models are shown in figure 42 to illustrate the windmill effect as the propeller rpm is reduced. The variation of the power coefficient with propeller rpm is more consistent than the efficiency was. For completeness, figure 43 shows the variation of the thrust coefficient with rpm for these different cascade models. Note that at the windmill condition the propeller is creating a drag force.

Effect Of Transition Region Interpolation Model

The transition region on the propeller blade represents the change from the NASA 65 Series airfoil sections on the inboard region of the blades to the NASA 16 Series airfoil sections on the outboard region. The analysis can currently model the airfoil characteristics in this transition region by two methods. The first method assumes that the airfoil characteristics in the transition region can be modeled by using the isolated NASA 16 Series airfoil characteristics scaled by an analytic function based on either flat plate cascade theory or the Mellor correlation to incorporate the cascade influence as a function of the local gap-to-chord ratio. Thus with this model the cascade influence diminishes concurrently with the transition to the outboard section characteristics. However, this model ignores the fact that the airfoil section in this region is neither a 16 or 65 NACA series, thus any cascade correction to the isolated 6 series data is not a true representation. The second method attempts to rectify this deficiency. It is based on an interpolation function which uses the inboard cascade data and the outboard isolated airfoil data as end point conditions to provide a functional relationship between spanwise location (gap-to-chord ratio) and section airfoil characteristics. In the analysis the behavior of the interpolation function can be varied via input of the exponent on the gap-to-chord ratio as noted in an earlier section of this report. The sensitivity of the propeller performance predictions to the modeling of the transition region characteristics is also shown in figures 41 to 43. In figure 41 from the previous section, the predicted propeller efficiency is presented as a function of advance ratio for the SR-1 propeller design using different cascade correlations along with a variation in the transition region model. The variation in the transition region model is shown between the flat plate and Mellor model correction to the isolated airfoil characteristics using the Mellor cascade correlation for the inboard cascade data. The two different correction models result in relatively small differences in the predicted efficiencies, except at the windmill condition. Near the design advance ratio the difference is about two points in efficiency. Figure 44 shows the effect of applying the interpolation function to the SR-1, SR-2, and SR-3 propeller designs at design point. For this study, two different exponent values were used for both the NASA and Mellor cascade correlations. For comparative purposes, the flat plate cascade correction to the isolated airfoil characteristics was also included. As was the case for the previous studies, the nacelle influence was neglected. Comparing the results obtained using the various transition region models holding all other variables fixed indicates that the differences between the models are small, a maximum of about 2 points in efficiency. Further comparison of only the interpolation model results for the two different exponents in the same manner shows an even smaller difference on the predicted efficiencies. The effect of replacing the cascade correction to isolated airfoil data with the interpolation function in the transition region

varies for the different propeller designs. The effect on the SR-1 is negligible, the efficiency is increased for the SR-2 using the interpolation model, and the efficiency is reduced or does not change for the SR-3 when the interpolation model is used. To demonstrate the sensitivity of the interpolation function model to the exponent used in the model the exponent was varied from 1.0 to 2.0. This variation resulted in an inconsistent behavior with increasing exponent for the different propeller designs as shown in figure 44. Generally, it appears that the use of the interpolation model in place of the correction model will increase the predicted efficiencies a small amount.

Effect of Viscous Nacelle Induced Inflow

An initial application of the analysis was performed using the SR-3 propeller/nacelle configuration to provide a performance map of propeller efficiency versus propeller rotational speed for selected blade angles at a 0.8 Mach number condition. The predictions were obtained using both the inviscid and viscous nacelle induced influence in the solution procedure for three different blade angles at the 8440 rpm condition. The differences between the results obtained using the inviscid or viscous nacelle induced inflow are so small for the conditions studied that they are not worth presenting. As a result, the need to include the viscous nacelle induced inflow solution in the prediction of high speed propeller designs such as the SR-3 at design flight conditions does not appear to be warranted and in general it is not used in the studies to follow.

Effect of Centrifugal Blade Twist

After these SR-3 cases had been run, the SR-3 propeller design was found to have a measurable steady-state torsional deflection due to centrifugal effects. The measured deflections were for the 8440 rpm condition and are presented in figure 45 in the form of a comparison between the aerodynamic blade angle distribution with and without the centrifugal effect. As a result of this finding, the cases were rerun with the measured torsional deflections included in the analysis. In addition, the other rpm conditions were run including the measured torsional deflections scaled by the square of the ratio of the actual rpm to the reference 8440 rpm. The results of this application are presented in figure 46. At the time of the performance of this activity, most of the effort had been directed towards the SR-3 configuration, but not all combinations of modeling features had been studied. And as a result, the combination of modeling features used to obtain the results presented in figure 46 are not necessarily the most appropriate. The actual combination used for this study was the AIR24 (NACA data) without cascade data and a tip loss model, with the compressible wake model. From the results presented in

figure 46 it is evident that the effect of including torsional deflections due to dynamic or aerodynamic effects can significantly alter the performance predictions. The inclusion of the measured torsional deflections of over one degree in the working sections of the blade for the SR-3 propeller resulted in an increase in the predicted efficiencies of 2.5 to 3.0 points. For all studies presented hereafter, this torsional deflection is included for the SR-3 configuration. For the other configurations the effect is not known, but it is assumed to be small due to the severe swept angles.

Comparison With Data

In the previous sections the results of applying the analysis with different aerodynamic modeling features was presented. From these studies a selected combination of modeling features were chosen for further investigation and comparison with test data. The unpublished test data was provided by NASA Lewis Research Center and was obtained in the NASA Lewis Research Center's test facilities. Initially the analysis was run including the nacelle's induced influence from both the inviscid and viscous solutions in the propeller performance portion of the analysis. These early cases were run on the NASA Lewis Research Center's Univac computer system.

As noted earlier, the results from these cases supported two major conclusions concerning the use of the analysis made during the early application and code development work. First, the use of either the inviscid or viscous flow solution resulted in essentially identical propeller performance solutions for the high speed conditions investigated. This result is not surprising in view of the assumption made in the nacelle flow field solution; that the flow field away from the body surface can be characterized by the inviscid compressible flow solution. Since a very large fraction of the propeller blade is operating in this region, the small differences in the local flow field near the nacelle surface due to viscous effects have very little effect in the propeller performance solution. Second, the need to cycle between the nacelle and propeller solution portions of the analysis is unnecessary for the high speed conditions studied. Again, this result is not surprising since the effect of the propeller for the conditions being studied is to induce an incremental increase in the flow around the nacelle body (on a momentum basis) of less than four percent relative to the freestream velocity. It should be noted that this method of using the PANPER analysis may not be applicable to low speed conditions, and flight conditions where the local flow is nearly choked or nearly sonic since the inclusion of the blade forces in the nacelle solution may be important.

Based upon the results of these cases the analysis was rerun at UTRC using the nacelle induced inflow as prescribed input to the propeller portion of the analysis. In this manner the effects of the different aerodynamic modeling features were studied without the computational expense of running the nacelle portion of the analysis. Thus a large matrix of results was obtained for the different modeling features, flight conditions, and propeller types for comparison with test data. The propeller configurations studied were those noted earlier along with a variation in the spinner shape, conic verses area ruled. The flight conditions studied consisted of three Mach number variations at a fixed advance ratio and power coefficient level and three advance ratio variations at a fixed Mach number and power level. A variation in the source of the isolated airfoil data was made, the Manoni (AIR23) and the NACA data (AIR24). And finally eight different combinations of aerodynamic modeling features were included in this study. The effect of using cascade data (NASA data with flat plate corrections in the transition region) versus isolated data alone was investigated. The use of the compressible wake model (Mach cone region of influence model) was compared with the conventional incompressible wake model. And the effect of the tip loss model (Evvard) was studied. In total this comparison with test results included 384 separate cases to establish the sensitivity of the performance predictions to selected modeling features. The results of this comparison are presented in the following sections and are also provided in Tables I, II, and III.

Variation with Mach Number

The effect of varying flight speed (Mach number) at a fixed advance ratio and fixed power coefficient on propeller efficiency are presented in figures 47 to 53 for the different isolated airfoil data sources, modeling features, and propeller types. These results are also presented in tabular form in Table I. For all of these conditions studied the area ruled spinner geometries were used to calculate the nacelle influence. The three propeller geometries used were the SR-1M, SR-2, and the SR-3 designs. Thus the results presented in these figures also represent the effect of different blade sweep along with twist, camber, and chord distribution variations. Figure 47 presents the unpublished NASA test results for the three different propeller/nacelle configurations studied. These test results indicate that the swept blade designs (SR-1M and SR-3) are more efficient than the unswept design (SR-2). However, the moderately swept design (SR-1M) is more efficient at the lower Mach number conditions than the highly swept design (SR-3). As the Mach number increases, the highly swept design's performance increases until it becomes the most efficient design at the highest Mach number studied.

C-2

One of the effects of increasing the Mach number is to increase the size of the supersonic region on the propeller blades. To determine the sensitivity of the performance predictions to the aerodynamic modeling features used to model the compressible flow effects, several of these features were varied in this study. The compressible wake model incorporated in the analysis to account for compressibility effects on the wake induced flow field is studied along with the tip loss models in this comparison. The effect of different sources of airfoil data (some airfoil) is also studied in conjunction with the influence of cascade data. The comparisons of the different prediction models with the test results are presented below proceeding from the unswept to the highly swept design.

SR-2 Propeller Design

In figure 48, the effect of the tip loss and compressible wake model are shown without the use of the cascade data on the unswept SR-2 propeller for both sets of isolated airfoil data. The most obvious difference is that the use of the NACA airfoil data (AIR24) for the 16 series airfoil characteristics consistently results in a higher predicted efficiency. At the higher Mach number (0.8) where the effect of the compressible wake and tip loss models are significant, the effect of the use of tip loss model is seen to reduce the propeller efficiency. The effect of the use of the compressible wake model is to increase the propeller efficiency. In figure 49 the same results are presented using the cascade data. The effects of the different aerodynamic modeling features are identical to those in figure 48. However, the effect of the different airfoil data sources on the efficiency is relatively small and does not show a consistent trend with Mach number. This implies that the major differences in the airfoil data sources are at the higher chord-to-gap ratios, thickness ratios, and or the lower Mach numbers associated with the inboard sections of the blades of the SR-2 propeller. A careful comparison of the results in figures 48 and 49 obtained for the use of the cascade data versus not using the data shows that the cases using the NACA airfoil data (AIR24) is most affected by the use of the cascade data. The use of the Manoni Airfoil data (AIR23) is only slightly affected by replacing the inboard airfoil data with the cascade data. From the results presented in both figures for the SR-2 design, it is apparent that the best overall prediction of the character of the test results with Mach number are generally obtained in the cases which use the compressible wake model. The efficiency predictions, based on the compressible wake model, with or without tip loss, are within 2 percent of the test data.

SR-1M Propeller Design

The same format is used for presentation of the comparisons of predicted results with data for the moderately swept propeller design (SR-1M) as was used for the unswept design. The comparisons are presented in figures 50 and

51 for the non-cascade and cascade data cases respectively. The results are essentially identical to the SR-2 results with the following exceptions. The use of the different isolated airfoil data set results in a larger difference in predicted efficiency. The AIR24 data again yields the higher efficiencies for the non-cascade data cases (figure 50). For the cases which included the cascade data (figure 51), sensitivity to airfoil data is again reduced. Generally, similar results are achieved with the various modeling options at the 0.6 and 0.7 Mach numbers. Significant differences are evident at the 0.8 Mach number.

SR-3 Propeller Design

Similar results are presented in figures 52 and 53 for the highly swept SR-3 blade design. Comparing predicted versus test values of propeller efficiency for the non-cascade data cases in figure 52 shows that the same behavior with airfoil data source as was noted in the other propeller designs has occurred. The difference in efficiencies between the predicted values is even greater than for the SR-1M cases. However, the difference in the predicted results using the different airfoil data sources for the cascade data cases is again small. Inclusion of the compressible wake model again increases the efficiency predictions and the inclusion of the tip loss model reduces the predicted efficiencies for both the cascade and non-cascade results. For this propeller configuration the character of the measured test results is well predicted using most of the models investigated. However, the simultaneous use of both the compressible wake and the tip loss models with AIR24 airfoil data results in a large exaggeration of the predicted loss of efficiency with increasing Mach number compared with the behavior exhibited in the test results for this SR-3 propeller design. The compressible wake model without tip loss results in good correlation for the SR-3 propeller.

Variation With Advance Ratio

The effect of varying the propeller advance ratio for a fixed power output at a fixed Mach number of 0.8 on the measured efficiency is shown in figures 54 to 60 for three propeller/nacelle configurations. For this study the area ruled spinners were used for the three different propeller designs; the SR-1M, SR-2, and SR-3. The power output level studied corresponded to the design value at the 3.07 advance ratio condition. As illustrated by the test results presented in figure 54, the effect of increasing the advance ratio at a fixed power level is to reduce the propeller efficiency. For the fixed free-stream Mach number, increasing the advance ratio corresponds to decreasing the propeller rotational speed, and when done at a fixed power level the increase in advance ratio also corresponds to an increase in the propeller blade pitch angle. This increase in blade angle reduces the lift-to-drag ratio that the blade sections operate at and the result is reduced propeller efficiency. At this Mach number (0.8), the effect of increasing blade sweep is to increase the efficiency. This behavior is consistent over the range of advance ratio studied, but at the higher advance ratios the difference between the highly swept (SR-3) and the moderately swept (SR-1M) designs vanishes because the SR-3 results exhibit a larger negative gradient with advance ratio. The prediction capability of the analysis is demonstrated in figures 55 to 60 for this study, where the predicted propeller efficiencies are compared with the measured results using the same format as was used in the previous sections. The predicted efficiencies for this study are also presented in tabular form in Table II.

SR-2 Propeller Design

In figure 55 the results of applying the analysis to the unswept propeller design are presented for the cases run without cascade data. The effect of the use of the different isolated airfoil data sets is seen to be similar to the behavior noted in the studies performed for the variation with Mach number. That is, the use of the AIR24 data results in consistently higher predicted efficiencies over the advance ratio range investigated. Again, the inclusion of the compressible wake model results in higher efficiencies and the inclusion of the tip loss model results in lower efficiencies. In figure 56, the same comparisons are presented including the use of the cascade data. Use of the cascade data again reduces the differences in the predicted efficiencies between results for the two isolated airfoil data sets to relatively small values. In general, all of the results from the prediction models studied follow the trends of the test results, but the overall levels are not always well predicted. The general character of the test results seems to be well predicted in most cases. The best correlation with test results is obtained with the compressible wake model. The predictions using the combination of the compressible wake and tip loss models

with or without cascade data show an unrealistically strong sensitivity to the compressibility effects associated with increasing tip Mach number (lowering advance ratio) compared with the behavior of the test results.

SR-1M Propeller Design

In figures 57 and 58, the results of applying the modeling features and airfoil characteristics to the moderately swept blade design (SR-1M) are presented with and without the use of cascade data respectively. The predicted results exhibit essentially the same characteristics for the different modeling features as exhibited by the unswept propeller results described above. The general character of the test results is reproduced using the prediction analysis with all of the different models, however, the gradient of the curves with advance ratio is usually larger than the test results indicate. Generally better correlation was again obtained with the compressible wake model.

SR-3 Propeller Design

Application of the same set of modeling features to the highly swept SR-3 propeller design is presented in figures 59 and 60. Again, the overall behavior of the predicted results with the different modeling features is consistent with the results from the other propeller designs. The most obvious difference between these predicted results and the results obtained for the SR-2 and SR-1M propellers is the larger negative gradients with advance ratio. The increased gradient is consistent with the test results which exhibit the same behavior (figure 54), but the predicted slopes are significantly greater than the test results indicate. This behavior is exhibited for all of the combinations of the modeling features.

Variation With Blade Twist and Spinner Shape

The effect of spinner design and blade twist on the measured propeller efficiency as measured is presented in figure 61. The results presented in this figure are for a propeller blade twist variation (SR-1M versus SR-1) using the conic spinner geometry, and a spinner design variation (conic versus area ruled) for the SR-1M propeller. The configurations studied were run at a fixed Mach number (0.8) and a fixed power output level equal to the design power as was the case for the previous study. From the test results (figure 61) it can be seen that the effect of decreasing the blade twist (SR-1M in place of the SR-1) along with increasing the blade camber on the tip region of the propeller blade is to improve the efficiency over most of the advance ratio range investigated. The effect of using the area ruled spinner in place of the conical geometry also results in an increase in the measured propeller

efficiency over the complete advance ratio range. The results of the application of the various modeling features of the analysis are shown in figures 57, 58, and 62 to 65 in the same format as was used for the previous investigation. The tabulation of the predicted efficiencies is provided in Table III.

SR-1M Propeller With Area Ruled Spinner

The results for this propeller design have been presented in the previous study (figures 57 and 58).

SR-1M Propeller With Conic Spinner

The results of the use of the analysis to predict the performance of the SR-1M propeller with the conic spinner for the different modeling feature is presented in figures 62 and 63. In figure 62 the efficiencies using the different modeling features are presented without using the cascade data, while in figure 63 the results for the same combination of modeling features are presented with the cascade data. Comparing the results presented in figures 62 and 63 with those presented in figures 57 and 58, it is noted that the increase in efficiency of the area ruled spinner over the conic spinner, indicated by the test data, is not predicted by the PANPER analysis. Relative to all preceding theory-test comparisons, the conic spinner predictions exhibit the poorest correlation with test data.

SR-1 Propeller With Conic Spinner

Results are shown in figures 64 and 65 for the SR-1 propeller design and the conic spinner. With this configuration there is an improved prediction of the gradient of efficiency with advance ratio. Comparing the results presented in figures 64 and 65 with those presented in figures 62 and 63, it is noted that increased efficiency with increased blade twist (SR-1M vs. SR-1) is predicted. This is the general trend of the test data (figure 61), although the magnitude of the difference is overpredicted, especially at the lower advance ratio where the measured efficiencies merge.

Correlation of Efficiency at Prescribed Power Levels

The preceding comparisons of predicted propeller efficiency with test data at prescribed power coefficients or power loadings, presented in figures 48 through 65, indicate that the predictions are sensitive to the choice of aerodynamic modeling features and airfoil data. The test data trends of decreasing efficiency with increasing free-stream Mach number and increasing advance ratio are generally predicted by most of the modeling options. The general influence of twist is overpredicted, and the predicted influence of

sweep and nacelle design (conic vs. area ruled) is not generally consistent with test. Sensitivity to airfoil data selection is apparent without the use of cascade data, but the differences with airfoil data are small when cascade data is used. Overall, it is difficult to select a "best" modeling option because there is not one that demonstrates consistent correlation throughout. The use of the compressible wake option generally results in improved correlation. The results of the use of tip loss are inconsistent between propeller designs. The modeling option combination of compressible wake with no tip loss was selected as the primary modeling option for the forthcoming performance map predictions. With the notable exception of the SR-1M, conic nacelle predictions, the predicted apparent efficiencies with this modeling option are generally within approximately ± 2 percent of the test data when an average of the AIR23 - AIR24 predictions is used. Considering the limitations of lifting line theory, as applied to the severe propfan design features and operating conditions, the sensitivity to the airfoil data and modeling options, and the accuracy of the test data, the degree of correlation is not unreasonable.

Performance Map Prediction and Comparison with Test Data

A final comparison with data is presented in this section for the single propeller mode of operation. In this section predicted performance maps are compared with measured performance maps for the SR-1M, SR-2, and SR-3 propeller configurations at the 0.6 and 0.8 Mach number conditions of the previous sections. The unpublished test data was supplied by NASA Lewis in graphical form for the three configurations at these Mach numbers. The maps are plots of propeller efficiency (net) and power coefficient as functions of advance ratio for several fixed blade angles. For this study, the analysis was run for three different comparisons using different combinations of aerodynamic modeling features and several blade angles to illustrate the range of correlation that can be obtained. For modeling option 1, the aerodynamic modeling features used consisted of the AIR24 data without cascade data, no compressible wake, and no tip loss models. Modeling option 1 was applied to the SR-2 and the SR-1M configurations. For modeling option 2 the compressible wake was used without the tip loss model, and the AIR24 data was used in conjunction with the cascade data and transition region interpolation feature. For modeling options 1 and 2, the PANPER analysis was run at measured blade angles. To illustrate the trending capabilities of the analysis, modeling option 3 was applied using the same combination of modeling features as modeling option 2, but the blade angles were adjusted by a constant value so that the measured and predicted power coefficients matched at one Cp, J point for each Mach number condition for each configuration. The point chosen was generally near the design point condition. Modeling options 2 and 3 were applied to all three propeller configuations. Both the test and predicted

results are presented in figures 66 to 71 for the SR-2, SR-1M, SR-3 respectively. The predicted results are also provided in Tables IV to VI for the same configurations respectively. These results are described for each configuration in the following sections.

SR-2 Results

The performance predictions for the unswept SR-2 propeller, using the three modeling options, are presented in figures 66 and 67. At the 0.6 Mach number (figure 66a), the predicted efficiencies for modeling option 1 are higher than the test values and the peaks occur at greater advance ratio for each blade angle studied. The predicted power coefficients are also higher than the test values for the same blade angle. The difference in power coefficient is consistent with the fact that the analysis has been unable to correlate with measured efficiency and power at the measured blade angle, while efficiency correlations have been much better when trimmed in blade angle to match Cp. The comparison obtained with modeling option 2 for this Mach number (figure 66b) is very similar. Peak efficiencies are not well predicted in either amplitude or advance ratio, while the power coefficient levels are too high. However, if the blade angle is adjusted to match advance ratio and power level for one point on the test data (modeling option 3), the results are greatly improved (figure 66c). Peak efficiencies are better predicted in both absolute value and in terms of the advance ratio (at which they occur) as compared with the other modeling options. At the 0.8 Mach number (figure 67a), the predicted efficiencies for modeling option 1 were closer to the test values than the 0.6 Mach number results, but the peak values were still predicted to occur at greater advance ratio than the test results indicate. For modeling option 2 (figure 67b), the comparison is slightly degraded. The results obtained using modeling option 3 (figure 67c) are improved in terms of the predicted power coefficient behavior as a function of blade angle and advance ratio. But, the predicted propeller efficiencies are now higher than the test results and the predictions obtained using modeling option 1.

SR-1M Results

The performance predictions for the SR-1M propeller, using the three modeling options, are presented in figures 68 and 69. For the 0.6 Mach number condition (figure 68a), the degree of correlation is similar to the SR-2 correlation using modeling option 1. No significant improvements were obtained at this Mach number for modeling option 2 (figure 68b). When modeling option 3 was used, the correlation (figure 68c) was again improved, efficiencies and power levels were better predicted. For the 0.8 Mach number comparison with modeling option 1 (figure 69a), the SR-1M predicted results were higher than the test results for both the efficiency and power

coefficient comparisons. The peak efficiencies were also predicted to occur at higher advance ratio than the test results. Again, no significant improvements were noted when modeling option 2 (figure 69b) was used. The comparison based on modeling option 3 (figure 69c) indicated some improvement in power coefficient correlation, but little improvement in predicted efficiency.

SR-3 Results

The performance predictions for the SR-3 propeller are presented in figures 70 and 71. At the 0.6 Mach number condition (figure 70a), the correlation using modeling option 2, for both the efficiency and power coefficient, is very good relative to the other configurations. The results obtained for modeling option 3 are slightly different than for the other options because the trim point is slightly different (figure 70b). At the 0.8 Mach number condition (figure 71a), both the power coefficient and the efficiency are over-predicted for modeling option 2, although the peak efficiency predictions do not occur at higher advance ratio as was the case for the other two configurations. The correlations obtained for modeling option 3 (figure 71b) for this Mach number are not as good as those for the 0.6 Mach number condition. Overall the SR-3 correlation is the best of the three configurations studied.

Performance Map Discussion

These performance map comparisons illustrate that the analysis can be tuned to provide useful trending results if a reference point is known in advance (modeling option 3). The correlations for the SR-2 and SR-1M could be improved by selecting different sets of aerodynamic modeling options which are best suited for their particular geometries and adjusting the blade angle to match power coefficient at one point. However, without this type of information in advance, the predictions are sensitive to the selection of modeling options and the results can vary significantly.

WIND TUNNEL APPLICATION

A major task supported by the contract activity was to apply the analysis to several wind tunnels and propeller/nacelle configurations to study the effect of the tunnel-propeller/nacelle geometry on the predicted performance of the propeller. The tunnels selected for the study were the U.S. Tullahoma tunnel and the French Modane tunnel. Details concerning these tunnel facilities can be found in references 70 and 71 for the Tullahoma and Modane tunnels respectively. The key geometry feature used in the modeling of the tunnel with an axisymmetric code is the wall diameter. The tunnel wall diameter for the Tullahoma tunnel is 5.6 meters (18.054 ft) and the Modane tunnel diameter is 8.0 meters (26 ft). Several SR-3 propeller/nacelle configurations were studied with propeller diameters of 3.08, 2.76 and 2.29 meters (11, 9, and 7.465 ft) and nacelle diameters of 1.27, 1.04, and 0.85 meters respectively (4.122, 3.373, and 2.754 ft). The resulting propeller to nacelle diameter ratios are essentially constant so that the geometric variations studied represent the effect of propeller to tunnel wall diameter ratios. The operating conditions studied consisted of variations in Mach number and power coefficient. Since the Tullahoma tunnel can be operated with tunnel wall bleed, most of the conditions were run for this tunnel with the wall bleed model. Because the actual bleed rate is unknown, selected values were used in the predictions to study the influence on the propeller performance. The cases studied are summarized in Table VII, which includes the predicted propeller efficiencies. The application of the analysis to these conditions was made during a period of the contract activity when the most appropriate combination of modeling features was felt to be the AIR24 isolated airfoil data used without any cascade data, with the compressible wake model, and without the tip loss model.

Effect of Tunnel/Propeller Geometry

The matrix of conditions and configurations studied (Table VII) is not complete in terms of all of the possible variations that could be studied. However, there is sufficient information to identify predicted trends due to the effect of the nacelle to tunnel diameter ratio on the performance of the propeller. In figure 72 the effect of this geometric ratio is illustrated, where the apparent efficiency is plotted against the ratio of propeller to tunnel diameter for the 0.8 Mach number conditions. In addition, the nacelle to tunnel wall diameter ratio is presented on the plot. When the ratio is zero, the condition corresponds to free air (no tunnel) and when the ratio is equal to unity, the propeller would completely fill the tunnel. The results presented in this figure are for the non-bleed configurations at the various power coefficients levels studied. Within the limitations in terms of the range of the data, the effect of increasing the propeller diameter relative to

the tunnel diameter is shown to be relatively insensitive up to about the ratio of about 0.3 depending on the loading condition. Beyond this region the effect of increasing the ratio is to reduce the predicted efficiencies. A case was run for a value of this ratio of 0.61 and the nacelle portion of the code failed to run completely through the solution procedure. The failure was identified as being caused by the predicted choking of the flow in the sense that a mass flow balance could not be maintained through the tunnel with this particular nacelle diameter size. This numerically predicted result indicated that the use of this configuration would be inappropriate to consider for testing in the actual tunnel at the 0.8 Mach number. The effect of power loading in relation to the nacelle to tunnel diameter ratio variation is also shown in this figure. The predicted behavior of the propeller efficiency with decreasing power loading is shown to increase regardless of the nacelle to tunnel ratio. This result is consistent with the results demonstrated in figure 71 at the corresponding advance ratio (2.9). There is an indication that the effect of the nacelle to tunnel ratio is greater for the higher loading conditions, although the data is too limited to make a strong statement. The influence of tunnel size on the predicted propeller performance is shown in figure 73 for a fixed propeller/nacelle geometry, power coefficient, and propeller tip speed as a function of Mach number, again for the non-bleed conditions. The efficiency is seen to increase with increasing Mach number and increase with increasing tunnel diameter. The free air result shown is slightly lower in efficiency than the largest tunnel result, but the difference may be attributed to the exactness of the modeling of the free air condition with the analysis or to the fact that the bleed model as incorporated in the analysis should include an iteration between the calculation of the local bleed rate and the local pressure field solution.

Effect of Wall Bleed

The analysis currently includes the treatment of wall bleed in the viscous nacelle flow solution portion of the computer program. For this study, the bleed rate is defined as the total mass loss or gained in the tunnel (positive bleed or negative bleed, respectively) through the tunnel wall divided by the initial mass flow. Since the bleed model is only applied over the region of the tunnel wall modeled in the viscous flow solution procedure, this definition for the bleed rate is non-standard. This region starts from the axial location on the tunnel wall which corresponds to the start of the nacelle and extends to the end of the computational region. Thus a large fraction of the complete tunnel wall is neglected. The analysis was run using various bleed rate values by prescribing the plenum stagnation pressure and temperature and the hole size and discharge coefficient. The actual bleed rate varies along the wall surface and is a function of the solution, thus it is not possible to define the bleed rate a priori. The bleed rate is calculated once the inviscid solution is known to define the value for use in

the viscous solution. Thus the values used for this study are not necessarily realistic values that would be used in an actual test. The intention of this study is to show the sensitivity and capability of the analysis. The results presented in Table VII demonstrate the effect of the use of the wall bleed model on the predicted propeller efficiencies for a fixed propeller/nacelle and tunnel wall configuration. The variation in bleed rate was from -2.0 to 5.0 percent. The variation in the predicted efficiencies with bleed rate is seen to increase with the inclusion of either positive or negative bleed, with the exception of one condition which had a larger tunnel to nacelle diameter ratio. The results are plotted in figure 74 for the 0.8 Mach number with the nacelle tunnel diameter ratio of 0.499. An interesting result shown in this figure is that the small (essentially zero) bleed rate conditions result in an increase in the predicted efficiency as compared with the no bleed model values shown on this figure (solid wall). It may be that the use of the wall bleed model with such low rates, either positive or negative, allows the solution to be locally unconstrained compared with the conventional zero normal flow tunnel wall boundary conditions. In fact, for the lower negative bleed rates nearly zero (-0.1 percent net loss) the local bleed is positive (mass gained) for some distance along the wall upstream of the propeller blade row. Thus the perforated tunnel wall acts like a partial free air boundary for low bleed rates. This result is not really surprising in view of the fact that one of the functions of the perforated tunnel wall is to alleviate the tunnel wall influence on the tunnel flow. The free air results for two of the loading conditions are also shown on this figure. These results illustrate that the use of the bleed model in the analysis does tend to result in predicted propeller efficiencies nearly equal to the free air results.

In general, the use of the feature to model the influence of tunnel walls, with or without wall bleed, shows definable trends with the parameters of interest. This feature could be used to study the potential influence of particular model to tunnel size configurations to determine the merits of the selected configurations and the interference effects. With this capability it is possible to numerically define the relative differences between different tunnel facilities for comparing the test results obtained in the different tunnels using the same models.

COAXIAL PROPELLER PERFORMANCE PREDICTIONS

The analysis is capable of treating counter-rotating propeller/nacelle configurations. In order to demonstrate this capability and to provide a preliminary assessment of the predictive accuracy of the analysis in this mode of operation, the analysis was applied to three propeller/nacelle configurations. The flight speeds consisted of three moderate to high Mach number conditions (0.6, 0.7, and 0.8) for two of the propeller/nacelle geometries and one low Mach number condition (0.04) for the remaining propeller/nacelle geometry. The conditions and geometries studied are defined in the following sections.

Counter-Rotation Application - Low Speed

The analysis was applied to the propeller/nacelle geometry described in reference 72 for three combinations of blade angle. For each blade angle setting, the propeller advance ratio was varied to provide a performance map of efficiencies and power coefficients. Initially, the AIR23 airfoil data base was used because of the limits on the range of design lift coefficient in the AIR24 airfoil data base. The propeller design lift coefficients varied from 0.1 to 0.3 while the AIR24 data was limited from 0.0 to 0.2. The predicted performance results of this application are presented in Table VIII for each condition. The performance predictions were obtained using the combination of modeling features deemed best for the single propeller application. No tip loss or compressible wake models were used, and because the propeller design was a 3x2 (three blades per blade row) the use of cascade data was clearly unnecessary. The nacelle and tunnel wall influence was calculated from a single propeller/nacelle case at the lowest Mach number for which the nacelle portion of the analysis would run (0.2). The resulting nacelle induced influence was used as input to the propeller portion of the analysis for all of the conditions which were run. The predictions are compared in figures 75 to 77 with the measured results obtained from figure 8 and figure 12 of the above reference.

In figure 75, figure 8 of reference 72, a comparison of the predicted and measured power coefficients versus advance ratio are presented for three blade angles (55, 60, and 65 degrees). Included on the predicted curves are the predicted efficiencies at the discrete advance ratio points for which the analysis was run. The power coefficients tend to be over-predicted at the lower advance ratios and under-predicted at the higher advance ratios when compared with the measured values. The predicted efficiencies tend to be lower than the measured values. Figure 76 presents a comparison of the propeller thrust coefficient as a function of advance ratio for the three blade angles. The correlation between predicted and measured thrust results

is better than the power coefficient results, although the difference between measured and predicted values increases with increasing blade angle and the peak values are progressively under-predicted with increasinf blade angle. Thus in general, the differences between the measured and predicted results tend to become larger with increasing blade angle. These differences could be attributable to two problems. First, the propeller blades were made of wood and thus the blade angles and twist distributions used in the test are of questionable accuracy. This problem was noted in the reference (pages 7 and 9). The question of retwisting the blades due to centrifugal and aerodynamic loading of the thin wood blades may also be important. The comparisons exhibit the trend of increasing difference as the blade angle and propeller rpm increase (increased blade airloading) which is symptomatic of the blade twisting with increased loading. As shown in an earlier section of this report, the effect of centrifugal loading on the blade twist is important and the sensitivity of the performance predictions to blade angle is quite strong. Second, the airfoil data base may not adequately represent the actual airfoil characteristics. For the higher power coefficients the range in angle of attack of the airfoil data tables was exceeded introducing an artificial stall like behavior into the solution as noted in Table VIII. This probably explains why the peak thrust coefficients are under-predicted.

In figure 77, a comparison of the section blade thrust distributions are shown at two blade angles (55 and 65 degrees). The overall trending is well predicted. The largest differences occur outboard on the propeller for the 55 degree blade angle and inboard for the 65 degree blade angle. Again, this may be due to twisting of the blade with aerodynamic load increasing as the blade angle is increased.

To further illustrate the sensivity of the solution process to small variations in blade twist and airfoil section properties associated with testing uncertainies, the analysis was rerun using the AIR24 data base. With this data base, if the section design lift coefficient range (0.0 to 0.2) was exceeded, the lift and drag coefficient values at the bounds (0.0 or 0.2) were used. One blade angle (60.0 degrees) was studied using only the change in airfoil data base and these results are also included in figures 75 and 76. The predicted efficiency was increased significantly with a slight drop in predicted power coefficient in the range of advance ratio for which the range in angle of attack in the airfoil tables was not exceeded. The results of increasing the blade angle by one-half degree using the AIR24 airfoil data base are also included in figures 75 and 76. These results show the need to have very accurate blade angle measurements for the test conditions; and by inference, an accurate measure of the twist distribution.

Counter-Rotation Application - Moderate to High Speeds

The analysis was applied to two propeller/nacelle configurations consisting of different spinner designs, A and B, described in reference 73 and shown graphically in figure 78. For the A spinner, two blade angles (60.0 and 65.0 degrees) were run for three Mach number variations (0.6, 0.7, and 0.8). For each of these conditions an advance ratio variation was made to provide performance maps of predicted efficiencies and power coefficients. For the B spinner only one Mach number-blade angle condition (0.7,65.0 deg.) was investigated. The predicted performance results for these conditions are presented in Table IX. The aerodynamic modeling options used for this study were the compressible wake model with the tip loss model. The influence of the nacelle and tunnel wall was included in the propeller portion of the analysis in the same manner as noted above, by applying the nacelle portion of the analysis once to each Mach number condition. The spinner designs resulted in inflow profiles which were essentially uniform for spinner A, while the spinner B inflow profiles exhibited deceleration and acceleration of the flow at the roots of the front and rear propeller blades respectively. This comparison is shown in figure 79. Again, the AIR23 airfoil tables were used because the blade design lift coefficients were off the tabulated range in the data base. The performance predictions are compared in figures 80 to 83 with the measured test results obtained from figures 8d, 8e, 8g, 9b, 10b, 14d, 14e, 14g, 15b, and 16b of the reference noted above.

The test results were obtained with different front and rear blade angles. The values noted above are the front propeller values. Two different cases are presented; one with a differential blade angle between the front and rear blade angles which varied with pitch setting and which corresponded to equal power loading on both propellers (assummed optimum) near the advance ratio corresponding to peak efficiency, and one with a fixed value of 0.8 degrees. The details of the values used and the propeller designs are available in reference 73. The optimum differential blade angles were blade angle dependent. For the 60.0 degree blade angle condition (front) the value was 2.0 degrees, and for the 65.0 degree blade angle condition the value was approximately 2.5 degrees.

In figure 80, the effect of Mach number and blade angle is illustrated for the optimum differential blade angle. For this comparison four blades were used on each propeller. The predicted power and thrust levels are greater than the measured values for all blade angles and Mach numbers investigated. The efficiencies are under-predicted at low advance ratio and over-predicted at higher advance ratio for all of the conditions studied. Increasing Mach number is seen to decrease the predicted efficiency which is consistent with the trending of the measured results. A comparison of the variation in the power loading between front and rear propellers for these

conditions is shown in figure 81. Although the level is over-predicted, the trends are well predicted for the 0.6 and 0.7 Mach number conditions. At the 0.8 Mach number the trending is not predicted as well, in so much as the advance ratio corresponding to equal power loading is not predicted correctly.

The results shown in figure 82 illustrate the effect of the spinner design on the propeller performance for three bladed propellers operating with a differential blade angle of 0.8 degrees at the 0.7 Mach number. The spinner induced inflows, as predicted by the analysis, were shown in figure 79 to be significantly different. Both the measured and predicted results show slightly higher performance for Spinner A, which had essentially no effect on the flow field. However, the difference in predicted efficiency for the two spinners is very small. Overall, the predicted thrust and power levels for both spinner designs were greater than those measured. It should be noted that for these three bladed propeller configurations the range in angle of attack on the airfoil data base was exceeded for most conditions. The corresponding variation of power loading between front and rear propellers for this study is shown in figure 83. Again, the levels are over-predicted but the trends are well predicted.

The results of this coaxial propeller comparison, based on test data from reference 73, show generally adequate correlation in terms of predicted versus measured trends, but the over all performance (power and thrust) is over-predicted. This discrepancy has not been adequately resolved. Some of the differences could be due to airfoil characteristics not being modeled correctly with the existing data base, and differences in the measured blade angles and blade twist could account for some of the differences. The fact that the trends are well predicted for the lower Mach numbers studied indicates some problems with either the airfoil data base or that the selection of aerodynamic modeling features used in this study are inappropriate. As was the case for the low speed study, some conditions resulted in stalled airfoil sections as noted in Table IX. As shown in the previous low speed study, the use of different airfoil data helped the correlation. The use of the AIR24 data was not investigated for this moderate speed study because the range in design lift coefficient for this airfoil data base (0.0 to 0.2) was so far removed from that associated with the test geometry range (0.1 to 0.5) that it would be a meaningless study.

CONCLUDING REMARKS AND RECOMMENDATIONS

The Propeller/Nacelle Aerodynamic Performance Prediction Analysis (PANPER) was developed to provide an efficient propeller performance and propeller/nacelle airflow prediction code. This was performed by combining two existing methods to treat the influence of the individual components (propeller and nacelle) on each other by super-imposing their respective influences in the individual solution processes where appropriate within the constraints of the analyses. The propeller portion of the analysis predicts the propeller performance and the nacelle portion of the analysis predicts the steady axisymmetric airflow. Since the propeller analysis uses inviscid, incompressible, lifting-line theory with some ad-hoc features to approximate many of the compressible and three-dimensional aspects of the flow problem, there are many modeling features which can be used to tune the predictions. As a result, a large number of cases have been run to study the sensitivity of the predictions to flight conditions and combinations of these modeling features. These cases do not represent all possible combinations of these features, but they do serve to demonstrate the sensitivities of the predictions to the assumptions. The nacelle analysis was originally developed and successfully validated for compressible, viscous, internal flow problems. The modification of the original analysis to treat external flows was a significant extension of the methodology. The comparisons shown between the predicted and measured results represent an attempt to test the assumption of steady axisymmetric flow for the prediction of a time averaged unsteady flow and to ascertain the success of the method to this application.

The use of the PANPER analysis for the prediction of the aerodynamic performance of high speed propellers (Propfans) has been demonstrated. The analysis was applied to a large variety of operating conditions applicable to the high speed propeller designs. The propeller operating conditions studied included windmilling to high speed conditions with supersonic tip speeds. The designs used for the studies included both single and coaxial configurations. The analysis was applied to configurations including wind tunnel wall geometry with and without wall bleed effects. Comparisons with data were made wherever possible to illustrate the degree of correlation possible which can be obtained using this analysis and to define the limitations of the use of the analysis. Based on these studies the following conclusions have been made.

Nacelle Flow Induced Velocities

1. The use of the analysis for propeller performance predictions requires that the nacelle induced flow field be accurately predicted. The limited comparisons with data indicate that the nacelle portion of the analysis does a reasonable job of predicting the velocity field upstream of the non-lifting blades. Since the general shape of the predicted inflow profile

is very similar to the measured profile, the differences between the test results and the predictions would appear to be due to inaccuracies in the assumed freestream conditions. It should be noted that inaccuracies in the assumed freestream velocity will strongly affect the correlations made at fixed blade angle.

2. Inflow predictions at the blade row from the nacelle analysis have exhibited strong sensitivity to blade thickness modeling and the chordwise location at which the prediction is made (leading to trailing edge). This can have a significant effect on the effective section pitch distribution, and therefore the predicted performance. The inclusion of blade thickness effects in the predicted velocity profiles was shown to be necessary for good correlation with measured values upstream of the blade rows. However, the inclusion of blade thickness effects in the analysis to predict the nacelle induced velocity at the blade row introduces the question of the use of cascade airfoil data in the propeller analysis portion, since this data also contains the effect of blade thickness.

Single Propeller Performance

1. Based on the single propeller designs studied, the analysis is generally capable of predicting the high speed propeller performance to within two efficiency points about the design conditions when trimmed in blade angle to the measured power. However, the selection of aerodynamic modeling features and the accuracy of measured airfoil characteristics and actual blade pitch distributions strongly affect the correlation results as demonstrated; this correlation was obtained knowing the test results beforehand. This sensitivity is due in part to the transonic nature of the problem and also the low aspect ratios and swept geometries of the propeller blades for which the lifting-line concept is not rigorously applicable (although desirable from a computational efficiency viewpoint).

2. Comparisons of predicted and measured results at fixed blade angle show significant differences in the degree of correlation. Best correlation is obtained near the design operating conditions. Increasing either the Mach number or the blade sweep (via propeller designs, SR-2, SR-1M, and SR-3) degrades the degree of correlation for the fixed blade angle comparisons. This degradation of correlation can be attributed to some degree to the above noted problems.

3. Selection of the most appropriate aerodynamic modeling features and airfoil data bases which yielded the best correlation with the test data varied with each type of propeller design, and to some extent with the type of comparison being made (i.e., Mach number variation, fixed blade angle, etc.). As a result, the application of the analysis to propeller designs for which no

test data exists should be made with care, and the absolute level of the predictions viewed with discretion.

4. The results obtained illustrated a tendency to degrade in the level of correlation with increasing blade sweep at the design Mach number (0.8) as the advance ratio was varied. For this condition, the variation in advance ratio also represented variation in the tip Mach number. Since the effect of increasing blade sweep is to alleviate compressibility effects, this result may indicate that the analysis (lifting-line) has been extended in application beyond an acceptable limit.

5. The analysis can be used for performance trending. However, the prediction of the occurence of peak efficiency as a function of blade angle and advance ratio is not sufficient for final design work. In addition, any significant change in propeller design was shown to have significant impact on the ability to correlate with test results for a given set of modeling options. This implies that trending predictions across propeller designs should be viewed carefully in terms of absolute levels.

Coaxial Propeller Performance

1. The correlation obtained at low speed using the analysis in the coaxial mode of operation at fixed blade angle was generally acceptable when the blade angle was low enough to avoid stalled operation of the blade sections. The actual correlations varied from over- to under-prediction of the power coefficient with increasing advance ratio and good correlation for the thrust predictions. The correlation on the propeller efficiency was within four efficiency points for the lower blade angle conditions. Differences between test and theory are believed to be partially due to inaccuracies in the blade angle and pitch distribution measurements and airfoil characteristics.

2. The correlations obtained for the high speed coaxial propeller, run at fixed blade angle, indicated an over-prediction of both thrust and power levels for all advance ratios. Comparisons of test and predicted efficiencies show an under-prediction at lower advance ratio and an over-prediction at higher advance ratio. On a front to rear propeller basis, the proportioning of front and rear loading is shown to trend correctly with increasing advance ratio. Again, the differences between test and theory may be attributable to all of the problems noted above, with the exception of low aspect ratio and sweep.

Wind Tunnel Effects

The use of the analysis to analyze the effect of wind tunnel configuration was demonstrated. The results indicate that the effects of the wind tunnel influence can be predicted using the analysis. Decreasing the tunnel size was shown to affect the propeller performance in a consistent manner and predict the onset of choked flow at the nacelle for too small a tunnel diameter. The predicted results were also shown to be propeller loading dependent. Although no test results were available for direct correlation, this aspect of the analysis may prove to be a useful tool for evaluation of propeller/tunnel configurations in advance of the testing procedure and to provide estimates of the tunnel effects on the propeller results to correct the performance to free air conditions.

Recommendations

Based on the results obtained under this investigation and the remarks noted above, the following recommendations are presented.

1. The use of the lifting-line propeller portion of the analysis should be limited to initial trending analysis. The sensitivity of the results to the aerodynamic modeling features and the questionable application of lifting-line theory to the highly three dimensional flow problems associated with the high speed propeller configurations result in predictions where the absolute level must be suspect. The degree of accuracy needed for current design work is too high for this type of analysis since efficiencies of one half of a point can be significant in terms of the life-cycle cost of a new design.

2. When using the analysis for trending applications, the results obtained should be viewed with care at the higher Mach number and tip speed conditions which result in transonic and supersonic tip speeds. This is due to the sensitivity of the results to both the aerodynamic model and the need for accurate airfoil characteristics.

REFERENCES

1. Rohrbach, C. and Metzger, F. B.: The Prop-Fan - A New Look in Propulsors. AIAA paper No. 75-1208.

2. Rohrbach, C.: A Report on the Aerodynamic Design and Wind Tunnel Test of a Prop-Fan Model. AIAA paper No. 76-667.

3. Sullivan, J. P.: The Effect of Blade Sweep on Propeller Performance. AIAA paper No. 77-716.

4. Anderson, O. L.: Calculation of Internal Viscous Flows in Axisymmetric Ducts at Moderate to High Reynolds Numbers, Int. J. of Computers and Fluids, Vol. 8, No. 4, December 1980, pp. 391-411.

5. Anderson, O. L.: User's manual for a Finite-Difference Calculation of Turbulent Swirling Compressible flow in Axisymmetric Ducts with Struts and Slot Cooled Walls USAAMRDL-TR-74-50, May 1974.

6. Goldstein, S.: On the Vortex Theory of Screw Propellers, Proceedings of the Royal Society of London, Vol. A 123, No. A 792, 1929.

7. Theodorsen, Theodore: Theory of Propellers, First Edition, New York, McGraw-Hill Book Company, Inc., 1948.

8. Lock, C. N. H.: The Application of Goldstein's Theory to the Practical Design of Airscrews, ARC R&M No. 1377, Aeronautical Research Committee, Great Britain, 1931.

9. Brady, W. G. and P. Crimi: Representation of Propeller Wakes by Systems of Finite Core Vortices, CAL Report No. BB-1665-S-2, Cornell Aeronautical Laboratory, Inc., Buffalo, New York, February 1965.

10. Gartshore, I. S.: An Application of Vortex Theory to Propellers Operating at Zero Advance Ratio, McGill University, Mechanical Engineering Research Laboratories Technical Note 66-3, June 1966.

11. Erickson, J. C., Jr.: A Continuous Vortex Sheet Representation of Deformed Wakes of Hovering Propellers, Proc. of 3rd CAL/AVLABS Symposium 18-20, June 1969.

12. Gartshore, I. S.: Modifications and Applications of a Simple Vortex Wake Method for Predicting the Performance of a Propeller in Static Thrust. Canadair Report RAA-240-103, July 1969.

13. Erickson, J. C., Jr., R. M. Ladden, H. V. Borst, and D. E. Ordway: A Theory for VTOL Propeller Operation in a Static Condition, USAAVLABS TR65-69, October 1965.

14. Clark, David R., and A. C. Leiper: The Free Wake Analysis - A Method for the Prediction of Helicopter Rotor Hovering Performance, United Aircraft Corporation, Silorsky Aircraft Division; Proceedings of the 25th Annual National Forum of the American Helicopter Society, Paper No. 321, May 1969.

15. Landgrebe, Anton J.: An Analytical Method for Predicting Rotor Wake Geometry, Journal of the American Helicopter Society, Vol. 14, No. 4, October 1969, pp. 20-32.

16. Landgrebe, A. J.: The Wake Geometry of a Hovering Helicopter Rotor and Its Influence on Rotor Performance, Journal of the American Helicopter Society, Vol. 17, No. 4, October 1972. (Also preprint No. 620, 28th Annual National Forum of the American Helicopter Society, May 1972.)

17. Ladden, R. M. (Part I), D. C. Gilmore (Part II): Advanced V/STOL Propeller Technology. Volume II Static Thrust Prediction Method Development, AFFDL-TR-71-88 Volume II. Air Force Flight Dynamics Laboratory V/STOL Division, Air Force Systems Command, Wright Patterson Air Force Base, September 1971.

18. Landgrebe, A. J. and T. A. Egolf: Rotorcraft Wake Analysis for the Prediction of Induced Velocities. USAAMRDL Technical Report 75-45, Eustis Directorate, USAAMRDL, Fort Eustis, VA., January 1976.

19. Landgrebe, A. J., and T. A. Egolf: Prediction of Helicopter Induced Flow Velocities Using the Rotorcraft Wake Analysis, Proceedings of the 32nd Annual National Forum of the American Helicopter Society, May 1976.

20. Landgrebe, A. J., and M. C. Cheney: Rotor Wakes - Key to Performance Prediction, AGARD-CP-AAA, AGARD Conference Proceedings No. 111 on Aerodynamics of Rotary Wings, Fluid Dynamics Panel Specialists Meeting, September 1972. (Also, paper presented at the Symposium on Status on Testing and Modeling Techniques for V/STOL Aircraft, Mideast Region of the American Helicopter Society, October 1972.)

21. Swavely, Craig E.: A Smoke Study of the Motion of the Vortices from the Tips of a Two-Bladed Model Helicopter Rotor in Hovering Flight, Masters Thesis, Georgia Institute of Technology, Atlanta, Georgia, December 1958.

22. Lehman, August F.: Model Studies of Helicopter Rotor Flow Patterns, Oceanics, Inc.; USAAVLABS Technical Report 68-17, U.S. Army Aviation Material Laboratories, Fort Eustis, Virginia, April 1968, AD 671670.

23. Landgrebe, A. J. and E. D. Bellinger: An Investigation of the Quantitative Applicability of Model Helicopter Rotor Wake Patterns Obtained from a Water Tunnel, United Aircraft Research Laboratories; USAAMRDL Technical Report 71-69, Eustis Directorate, U.S. Army Air Mobility Research and Development Laboratory, Fort Eustis, Virginia, December 1971, AD739946.

24. Gray, Robin B.: On the Motion of the Helical Vortex Shed from a Single-Bladed Hovering Model Helicopter Rotor and Its Application to the Calculation of the Spanwise Aerodynamic Loading, Princeton University Aeronautical Engineering Department, Report No. 313, Princeton University, September 1955.

25. Gray, Robin, B.: An Aerodynamic Analysis of a Single-Bladed Rotor in Hovering and Low Speed Forward Flight as Determined from Smoke Studies of the Vorticity Distribution in the Wake. Princeton University Aeronautical Engineering Department, Report No. 356, Princeton University, Princeton, New Jersey, September 1956.

26. Landgrebe, A. J.: An Analytical and Experimental Investigation of Helicopter Rotor Hover Performance and Wake Geometry Characteristics, United Aircraft Research Laboratories; USAAMRDL Technical Report 71-24, Eustis Directorate, U.S. Army Air Mobility Research and Development Laboratory, Fort Eustis, Virginia, June 1971, AD728835.

27. Landgrebe, A. J. and B. V. Johnson: Measurement of Model Helicopter Rotor Flow Velocities with a Laser Doppler Velocimeter. Journal of the American Helicopter Society, Vol 19, No. 3, July 1974.

28. Jenney, D. S., J. R. Olson, and A. J. Landgrebe: A Reassessment of Rotor Hovering Performance Prediction Methods. Paper No. 100 of Proceedings of the 23rd Annual National Forum of the American Helicopter Society, May 1967.

29. Peracchio, A.: Discussion of the Lifting Line Theory of Propellers. Hamilton Standard, Division of United Aircraft, HSIR 2451, April 1966.

30. Segal, R. M.: Investigation of the Hovering Performance of Multiple Rotors In and Out of Ground Effect. Sikorsky Aircraft Report SER-50382, September 1964.

31. Wilson, J. C.: Test of a Hovering Model Rotor and a 1/34-Scale Sikorsky Compound Helicopter. United Aircraft Research Laboratories Report UAR-0276, May 1959.

32. Cheney, M. C., Jr.: Experimental Investigation of the Hovering Performance of a Coaxial Rigid Rotor. United Aircraft Research Laboratories Report F410533-1, January 1967.

33. Bellinger, E. D.: Experimental Investigation of Effects of Blade Section Camber and Planform Taper on Rotor Hover Performance, United Aircraft Research Laboratories, USAAMRDL Technical Report 72-4, Eustis Directorate, U.S. Army Air Mobility Research and Development Laboratory, Fort Eustis, Virginia, March 1972, AD743232.

34. Wu, C. H.: A General Theory of Three-Dimensional Flow in Subsonic and Supersonic Turbomachines of Axial, Radial, and Mixed Types. NACA TN 2604, 1952.

35. Marsh, H.: A Digital Computer Program for Through Flow Fluid Mechanics in an Arbitrary Turbomachine Using a Matrix Method. Aero. Res. Council R&M, No. 3509, 1968.

36. Smith, L. H.: The Radial Equilibrium Equation for Turbomachinery. Journal of Eng. for Power, Trans. ASME, Series A, Vol. 88, No. 1, January 1966, pp. 1-12.

37. Novak, D. A.: Streamline Curvature Computing Procedures for Fluid Mechanics. Journal Engineering for Power, Trans., ASME, October 1967.

38. Anderson, O. L.: Finite Difference Solution for Turbulent Swirling Compressible Flow in Axisymmetric Ducts with Struts. NASA CR-2365, February 1974.

39. Anderson, O. L.: A Comparison of Theory and Experiment for Incompressible, Turbulent, Swirling Flows. AIAA 10th Aerospace Sciences Meeting, San Diego, California, January 17-19, 1972.

40. Johnson, I. A. and R. O. Bullock: Aerodynamic Design of Axial Flow Compressors. NASA SP 36, 1965.

41. Borst, H. V.: Summary of Propeller Design Procedures and Data; Eustis Directorate, U.S. Army Air Mobility Research and Development Laboratory. USAAMRDL TR 73-34A. November 1973.

42. Evaard, J. C.: Distribution on Wave Drag and Lift in the Vicinity of Wing Tips at Supersonic Speeds. NACA TN 1382.

43. Jones, R. T. and D. Cohen: High Speed Aerodynamics and Jet Propulsion, Volume VII Aerodynamic Components of Aircraft at High Speeds, Section A: Aerodynamics of Wings at High Speeds, Princeton University Press, Princeton, New Jersey, 1957.

44. Black, D. M.: Cascade Corrections to Isolated Airfoil Data. Internal Correspondence, Hamilton Standard, AR1401, October 8, 1974.

45. Wislicenus, G. F.: Fluid Mechanics of Turbomachinery. McGraw-Hill Book Co., Inc., 1947.

46. Manoni, L. R. and H. D. Taylor: Two-Dimensional Transonic Tests of Sixteen NACA 16-Series Sections. UAC Report R-25744-10, January 24, 1955.

47. Sand, E., Douglas A. Elliot, Jr., Henry V. Borst: Summary of Propeller Design Procedures and Data. Vol. III, Hub, Actuator, and Control Designs, USAAMRDL Technical Report 73-34C, November 1973.

48. Abbot, I. H. and A. E. Von Doenhoff: Theory of Wing Sections. Dover Pub., 1959.

49. Mellor, G. L.: A Combined Theoretical and Empirical Method of Axial Compressor Cascade Prediction, Report No. 9, DYNALYSIS OF PRINCETON, May 1970.

50. Mellor, G. L.: An Analysis of Axial Compressor Cascade Aerodynamics, Part I, ASME Trans., Vol. 81, Series D, No. 3, pp. 362-379, 1959. Errata, ASME Trans., Vol. 84, Series D, No. 2, pp. 619-621, 1962.

51. Mellor, G. L.: An Analysis of Axial Compressor Cascade Aerodynamics, Part II, ASME Trans., Vol. 81, Series D, No. 3, pp. 379-386, 1959.

52. Herrig, L. J., J. C. Emery and J. R. Erwin: Systematic Two-Dimensional Cascade Tests of NACA 65-Series Compressor Blades at Low Speeds, NACA RML 51 G 31, 1951.

53. Anderson, O. L. and D. E. Edwards: Extensions to an Analysis of Turbulent Swirling Compressible Flow in Axisymmetric Ducts, UTRC R81-914720-18, NASA Contract NAS3-21853, February 1981.

54. Kober, H.: Dictionary of Conformal Representations. Dover Publications, Inc., 1957.

55. Williams, J. C.: Viscous Compressible and Incompressible Flow in Slender Channels. AIAA J., Vol. 1, pp. 186-195, 1963.

56. Hinze, J. O.: Turbulence. McGraw-Hill Book Company, New York, 1959.

57. H. Schlicting: Boundary Layer Theory, 6th Edn. McGraw-Hill, New York, 1968.

58. van Driest, E. R.: On Turbulent Flow Near a Wall. Jr. of Aero. Sci., Vol. 28, No. 11 1956.

59. Clauser, E.: The Turbulent Boundary Layer. Advanced Mathematics, Vol. 4, pp. 1-51, 1956.

60. Coles, D. E.: The Law of the Wake in the Turbulent Boundary Layer. J. Fluid Mech., Vol. 1, pp. 161-260, 1956.

61. Holman, J. P.: Experimental Methods for Engineers. McGraw-Hill Book Co., New York, 1966.

62. Keller, H. G.: A New Difference Scheme for Parabolic Problems, Numcerical Solution of Partial Differential Equations - II SYNSPADE, 1970.

63. Keller, H. B.: Accurate Difference Methods for Linear Ordinary Differential Systems Subject to Linear Constraints. SIAM J. Numerical Analysis, Vol. 6, No. 1, 1969.

64. Varah, J. M.: On the Solution of Block-Tridiagonal Systems Arising From Certain Finite Difference Equations. Math. of Computation, Vol. 26, No. 120. 1972.

65. Barber, T. J., P. Raghuraman, and O. Anderson: Evaluation of an Analysis for Axisymmetric Internal Flows in Turbomachinery Ducts, Flow in Primary Non-Rotating Passages in Turbomachines, ASME Winter Annual Meeting, December 1979.

66. Shapiro, A. H.: The Dynamics and Thermodynamics of Compressible Fluid Flow, Volume I, Ronald Press Co., New York, 1953.

67. South, J. C. Jr.; and Jameson, A.: Relaxation Solutions for Inviscid Axisymmetric Transonic Flow Over Blunt or Pointed Bodies. AIAA Computational Fluid Dynamics Conference (Palm Springs, CA, July 1973, p. 8-17).

68. Keller, J. D. and J. C. South, Jr: RAXBOD: A Fortran Program for Inviscid Transonic Flow over Axisymmetric Bodies. NASA TM X-72831, February 1976.

69. ***NASA Test Results***

70. ***Tullahoma***

71. ***Modane***

72. Gilman, J. Jr.: Wind-Tunnel Tests and Analysis of Two 10-foot-diameter Six-Blade Dual-Rotating Tractor Propellers Differing in Pitch Distribution, NACA TN-1634, June 1948.

73. Walker, J. H. and R. M. Reynolds: Investigation of the NACA 4-(5)(05)-037 Six- and Eight-Blade, Dual-Rotation Propellers at Positive and Negative Thrust at Mach Numbers up to 0.90, Including Some Aerodynamic Characteristics of the NACA 4-(5)(05)-041 Two- and Four-Bladed, Single-Rotation Propellers, NACA RM-A54G13, October 1954.

APPENDIX A

COORDINATE TRANSFORMATION RELATIONSHIPS FOR VARIOUS QUANTITIES IN THE ANALYSIS

Unit Vector Review

This appendix assumes that the reader is familiar with vector properties, however a quick overview of the properties of unit vectors in 3-dimensions is given as an introduction because they are used throughout this appendix.

Given a three-dimensional vector $\overline{V}$, whose orthogonal unit directions are $\overline{i}_1$, $\overline{i}_2$, and $\overline{i}_3$, respectively,

$$\overline{V} = V_1\overline{i}_1 + V_2\overline{i}_2 + V_3\overline{i}_3$$

then the unit vector for this vector is

$$\overline{i}_v = \alpha_{v_1}\overline{i}_1 + \alpha_{v_2}\overline{i}_2 + \alpha_{v_3}\overline{i}_3$$

whose direction cosines are

$$\alpha_{v_1} = V_1/V$$

$$\alpha_{v_2} = V_2/V$$

$$\alpha_{v_3} = V_3/V$$

where

$$V = \left(V_1^2 + V_2^2 + V_3^2\right)^{1/2}$$

such that

$$\overline{V} = V\overline{i}_v$$

The dot product of two unit vectors $\bar{i}_x$ and $\bar{i}_y$ is then,

$$\bar{i}_x \cdot \bar{i}_y = \alpha_{x_1}\alpha_{y_1} + \alpha_{x_2}\alpha_{y_2} + \alpha_{x_3}\alpha_{y_3}$$

The cross product of the same two vectors is then

$$\bar{i}_x \times \bar{i}_y = \beta_1\bar{i}_1 + \beta_2\bar{i}_2 + \beta_3\bar{i}_3$$

where

$$\beta_1 = \alpha_{x_2}\alpha_{y_3} - \alpha_{x_3}\alpha_{y_2}$$

$$\beta_2 = \alpha_{x_3}\alpha_{y_1} - \alpha_{x_1}\alpha_{y_3}$$

$$\beta_3 = \alpha_{x_1}\alpha_{y_2} - \alpha_{x_2}\alpha_{y_1}$$

Note that the cross product of orthogonal unit vectors is a unit vector in itself.

Input Chordwise Unit Vectors

In the input coordinate system, (x,y,z) the input unit chordwise vector from figure 42 is:

$$\bar{i}_{c_I} = \cos\theta \bar{i}_y + \sin\theta \bar{i}_z$$

where θ is the local input blade angle including built-in pitch.

For a swept blade, a point (A) along the blade reference line (1/4 chordline) is displaced in the x, y plane by an angle δ as seen in figure 42, thus the input unit chordwise vector becomes

$$\bar{i}_{c_I} = \alpha_{c_{I_r}} \bar{i}_r + \alpha_{c_{I_\phi}} \bar{i}_\phi + \alpha_{c_{I_z}} \bar{i}_z$$

in the cylindrical coordinate system (r, ϕ, z) where the input chordwise direction cosines in the cylindrical coordinate system are:

$$\alpha_{c_{I_r}} = \cos\theta \sin\delta$$

$$\alpha_{c_{I_\phi}} = \cos\theta \cos\delta$$

$$\alpha_{c_{I_z}} = \sin\theta$$

Input Thickness Unit Vector

In the input coordinate system, the input unit thickness vector is

$$\bar{i}_{T_I} = -\sin\theta \bar{i}_y + \cos\theta \bar{i}_z$$

From figure 42, in a manner similar to that of the input chordwise unit vector, the input thickness unit vector in the cylindrical coordinate system is found to be:

$$\bar{i}_{T_I} = \alpha_{T_{I_r}} \bar{i}_r + \alpha_{T_{I_\phi}} \bar{i}_\phi + \alpha_{T_{I_z}} \bar{i}_z$$

where the direction cosines are:

$$\alpha_{T_{I_r}} = -\sin\theta \sin\delta$$

$$\alpha_{T_{I_\phi}} = -\sin\theta \cos\delta$$

$$\alpha_{T_{I_z}} = \cos\theta$$

Spanwise Unit Vector

Consider a segment of the blade reference line centered about point A in figure 43, whose end points are denoted by the subscripts 1 and 2, hub to tip respectively. The unit vector for the spanwise direction at point A, positive from hub to tip, can be approximated by the spanwise unit vector of this segment,

$$\bar{i}_s = \frac{x_2-x_1}{d}\,\bar{i}_x + \frac{y_2-y_1}{d}\,\bar{i}_y + \frac{z_2-z_1}{d}\,\bar{i}_z$$

where

$$d = \left[(x_2-x_1)^2 + (y_2-y_1)^2 + (z_2-z_1)^2\right]^{1/2}$$

In cylindrical coordinates the spanwise unit vector and direction cosines become respectively

$$\bar{i}_s = \alpha_{s_r}\bar{i}_r + \alpha_{s_\phi}\bar{i}_\phi + \alpha_{s_z}\bar{i}_z$$

$$\alpha_{s_r} = (r_2-r_1)\cos\xi/d$$

$$\alpha_{s_\phi} = (r_2+r_1)\sin\xi/d$$

$$\alpha_{s_z} = (z_2-z_1)/d$$

where

$$d = \left[r_1^2 + r_2^2 - 2r_1r_2\cos(2\xi) + (z_2-z_1)^2\right]^{1/2}$$

$$\xi = \frac{1}{2}(\delta_2-\delta_1)$$

Where the following approximations are made for the lag angle and radius at point A.

$$\delta_A = \frac{1}{2}(\delta_2+\delta_1)$$

$$r_A = \frac{1}{2}(r_1+r_2)$$

Normalwise Unit Vector

Since the input chordwise unit vector and the spanwise unit vector both lie in the blade element plane, the normalwise unit vector is just the unit vector of the cross product of the spanwise and input chordwise vector.

$$\bar{i}_n \frac{\bar{i}_s \times \bar{i}_{c_I}}{|\bar{i}_s \times \bar{i}_{c_I}|} = \alpha_{n_r} \bar{i}_r + \alpha_{n_\phi} \bar{i}_\phi + \alpha_{n_z} \bar{i}_z$$

The direction cosines for the normalwise unit vector in the cylindrical coordinate system are

$$\alpha_{n_r} = \frac{1}{\alpha^2} \left(\alpha_{s_\phi} \alpha_{c_{I_z}} - \alpha_{s_z} \alpha_{c_{I_\phi}} \right)$$

$$\alpha_{n_\phi} = \frac{1}{\alpha^2} \left(\alpha_{s_z} \alpha_{c_{I_r}} - \alpha_{s_r} \alpha_{c_{I_z}} \right)$$

$$\alpha_{n_z} = \frac{1}{\alpha^2} \left(\alpha_{s_r} \alpha_{c_{I_\phi}} - \alpha_{s_\phi} \alpha_{c_{I_r}} \right)$$

where

$$\alpha^2 = \left(\alpha_{s_\phi} \alpha_{c_{I_z}} - \alpha_{s_z} \alpha_{c_{I_\phi}} \right)^2 + \left(\alpha_{s_z} \alpha_{c_{I_r}} - \alpha_{s_r} \alpha_{c_{I_z}} \right)^2 + \left(\alpha_{s_r} \alpha_{c_{I_\phi}} - \alpha_{s_\phi} \alpha_{c_{I_r}} \right)^2$$

Chordwise Unit Vector

In the blade element coordinate system the chordwise direction must be normal to the spanwise direction and the normalwise direction to define an orthogonal system, thus the unit chordwise vector is

$$\bar{i}_c = \bar{i}_n \times \bar{i}_s = \alpha_{c_r} \bar{i}_r + \alpha_{c_\phi} \bar{i}_\phi + \alpha_{c_z} \bar{i}_z$$

The direction cosines in the cylindrical coordinate system are then:

$$\alpha_{c_r} = \alpha_{n_\phi} \alpha_{s_z} - \alpha_{n_z} \alpha_{s_\phi}$$

$$\alpha_{c_\phi} = \alpha_{n_z} \alpha_{s_r} - \alpha_{n_r} \alpha_{s_z}$$

$$\alpha_{c_z} = \alpha_{n_r} \alpha_{s_\phi} - \alpha_{n_\phi} \alpha_{s_r}$$

Blade Geometry Quantities in the Blade Element Coordinate System

Because it is necessary to calculate the aerodynamic solution in the blade element coordinate system, the local input blade section properties must be transformed to the blade element system.

The blade element chord length is obtained from the input blade chord by use of the dot product relationship for unit vectors.

$$c = c_I \bar{i}_{c_I} \cdot \bar{i}_c = c_I \left(\alpha_{c_r} \alpha_{c_{I_r}} + \alpha_{c_\phi} \alpha_{c_{I_\phi}} + \alpha_{c_z} \alpha_{c_{I_z}} \right)$$

And in a similar manner the blade element thickness is found to be

$$t = t_I \left(\alpha_{n_r} \alpha_{T_{I_r}} + \alpha_{n_\phi} \alpha_{T_{I_\phi}} + \alpha_{n_z} \alpha_{T_{I_z}} \right)$$

Velocity Vectors in the Blade Element Coordinate System

The velocities in the cylindrical coordinate system must be transformed to the blade element system for computational purposes. In the cylindrical coordinate system the velocity at any point is:

$$\bar{V} = V\bar{i}_v = V_r\bar{i}_r + V_\phi\bar{i}_\phi + V_z\bar{i}_z$$

the unit vector and direction cosines are then; respectively,

$$\bar{i}_v = \alpha_{v_r}\bar{i}_r + \alpha_{v_\phi}\bar{i}_\phi + \alpha_{v_z}\bar{i}_z$$

$$\alpha_{v_r} = V_r/V$$

$$\alpha_{v_\phi} = V_\phi/V$$

$$\alpha_{v_z} = V_z/V$$

where

$$V = \left(V_r^2 + V_\phi^2 + V_z^2\right)^{1/2}$$

The blade element velocity components are then obtained by use of the dot product relationships as:

$$V_s = V\bar{i}_v \cdot \bar{i}_s = V\left(\alpha_{v_r}\alpha_{s_r} + \alpha_{v_\phi}\alpha_{s_\phi} + \alpha_{v_z}\alpha_{s_z}\right)$$

$$V_c = V\bar{i}_v \cdot \bar{i}_c = V\left(\alpha_{v_r}\alpha_{c_r} + \alpha_{v_\phi}\alpha_{c_\phi} + \alpha_{v_z}\alpha_{c_z}\right)$$

$$V_n = V\bar{i}_v \cdot \bar{i}_n = V\left(\alpha_{v_r}\alpha_{n_r} + \alpha_{v_\phi}\alpha_{n_\phi} + \alpha_{v_z}\alpha_{n_z}\right)$$

Thus the velocity vector in the blade element coordinate system becomes

$$\bar{V} = V_s\bar{i}_s + V_c\bar{i}_c + V_n\bar{i}_n$$

whose direction cosines are the respective bracketed quantities in the velocity component relationships above.

Force Vectors

Once the blade forces per unit area have been found in the blade element coordinate systems, they must be transformed to the cylindrical coordinate system to obtain thrust and torque.

The blade force per unit area and direction cosines are respectively

$$\bar{i}_F = \alpha_{F_s}\bar{i}_s + \alpha_{F_c}\bar{i}_c + \alpha_{F_n}\bar{i}_n$$

$$\alpha_{F_s} = F_s/F$$

$$\alpha_{F_c} = F_c/F$$

$$\alpha_{F_n} = F_n/F$$

where

$$F = \left(F_s^2 + F_c^2 + F_n^2\right)^{1/2}$$

using the dot product relationship the component forces per unit area in the cylindrical coordinate system are found to be

$$F_r = F\bar{i}_F \cdot \bar{i}_r = F\left(\alpha_{F_c}\alpha_{c_r} + \alpha_{F_s}\alpha_{s_r} + \alpha_{F_n}\alpha_{n_r}\right)$$

$$F_\phi = F\bar{i}_f \cdot \bar{i}_\phi = F\left(\alpha_{F_c}\alpha_{c_\phi} + \alpha_{F_s}\alpha_{s_\phi} + \alpha_{F_n}\alpha_{n_\phi}\right)$$

$$F_z = F\bar{i}_f \cdot \bar{i}_\phi = F\left(\alpha_{F_c}\alpha_{c_z} + \alpha_{F_s}\alpha_{s_z} + \alpha_{F_n}\alpha_{n_z}\right)$$

The thrust per unit area is then just

$$T = F_z$$

and the torque per unit area is just

$$Q = rF_\phi$$

APPENDIX B

BIOT-SAVART RELATIONSHIPS FOR THE INDUCED VELOCITY OF A CONSTANT STRENGTH VORTEX SEGMENT

The relationships shown here are for a straight line constant strength vortex segment in cylindrical and cartesian coordinate systems which can then be transformed to any desired coordinate system. Consider a straight line vortex segment in a cylindrical coordinate system with end points $(r,\phi,z)_A$ and $(r,\phi,z)_B$ as shown in figure 49 with a circulation strength Γ. From reference 15, the induced velocity components at a field point P, from the Biot-Savart Law, in a cartesian coordinate system coincident with the cylindrical coordinate system are,

$$v_{i_x} = \frac{\Gamma}{4\pi R} K \left[(y_p-y_A)(z_p-z_B)-(z_p-z_A)(y_p-y_B)\right]$$

$$v_{i_y} = \frac{\Gamma}{4\pi R} K \left[(z_p-z_A)(x_p-x_B)-(x_p-x_A)(z_p-z_B)\right]$$

$$v_{i_z} = \frac{\Gamma}{4\pi R} K \left[(x_p-x_A)(y_p-y_B)-(y_p-y_A)(x_p-x_B)\right]$$

$$K = \frac{AP+BP}{(AP)(BP)} \frac{1}{(AP)(BP)+(x_p-x_A)(x_p-x_B)+(y_p-y_A)(y_p-y_B)+(z_p-z_A)(z_p-z_B)}$$

$$AP = \left[(x_p-x_A)^2 + (y_p-y_A)^2 + (z_p-z_A)^2\right]^{1/2}$$

$$BP = \left[(x_p-x_B)^2 + (y_p-y_B)^2 + (z_p-z_B)^2\right]^{1/2}$$

where all of the distances have been nondimensionalized by the reference length R (propeller radius).

Applying the standard relationships between a cartesian and cylindrical coordinate system,

$$x = r\cos\phi$$

$$y = r\sin\phi$$

$$z = z$$

The induced velocity components, after some algebriac manipulation, in the cylindrical coordinate systems are,

$$V_{i_r} = \Gamma\cdot G\cdot[(z_p-z_A)r_B\sin(\phi_p-\phi_B)-(z_p-z_B)r_A\sin(\phi_p-\phi_A)]=\Gamma\cdot GC_r$$

$$V_{i_\phi} = \Gamma\cdot G\cdot[(z_p-z_A)r_B\cos(\phi_p-\phi_B)-(z_p-z_B)r_A\cos(\phi_p-\phi_A)]=\Gamma\cdot GC_\phi$$

$$V_{i_z} = \Gamma\cdot G\cdot[(r_p-r_A)\sin(\phi_p-\phi_A)-(r_p-r_B)\sin(\phi_p-\phi_B)+r_Ar_B\sin(\phi_A-\phi_B)]=\Gamma\cdot GC_z$$

$$G = \frac{1}{4\pi R}\,\frac{AP + BP}{(AP)(BP)}\,.$$

$$\frac{1}{(AP)(BP)+r_p^2-r_pr_A\cos(\phi_p-\phi_A)-r_pr_B\cos(\phi_p-\phi_B)+r_Ar_B\cos(\phi_A-\phi_B)+(z_p-z_A)(z_p-z_B)}$$

$$AP = [r_p^2-2r_pr_A\cos(\phi_p-\phi_A)+r_A^2+(z_p-z_A)^2]^{1/2}$$

$$BP = [r_p^2-2r_pr_B\cos(\phi_p-\phi_B)+r_B^2+(z_p-z_B)^2]^{1/2}$$

The geometric influence coefficients (GC_r, GC_ϕ, GC_z) can then be transformed to the blade element coordinate system for the field point under consideration.

Thus by the appropriate transformation the induced velocity components in the blade element coordinate system become

$$v_{in} = \Gamma\, GC_n$$

$$v_{ic} = \Gamma\, GC_c$$

$$v_{is} = \Gamma\, GC_s$$

The transformation required for this last step are shown in Appendix A.

APPENDIX C

LIST OF SYMBOLS

a	linearized lift curve slope (per radian), or transformation variable
a_I, b_I	Schwartz-Christoffel parameters
A	cascade correlation parameter or generalized wake contraction limit
A^+	Van Driest constant (26.0)
b	number of blades or cascade correlation parameter for exit deviation angle (deg)
c	airfoil chord (ft)
C	Vector of aerodynamic quantities representing the constant vector in a system of simultaneous linear equations
c_d, C_D	section drag coefficient
$C_{D_{Bo}}$	minimum drag coefficient in the "drag bucket"
$C_{D_{CL2}}$	drag due to lift
$\tilde{C}_{D_{CL2}}$	$= \frac{dC_D}{dC_L^2} (t/c)^{-1/3}$, generalized drag due to lift
C_{D_p}	section wave drag coefficient (equal to minimum drag coefficient minus subsonic minimum drag coefficient)
$\tilde{C}_{D_p}$	$= (C_{D_p}) (t/c)^{-5/3}$, generalized wave drag
C_{d_o}	drag coefficient at zero angle of attack
C_{D_o}	extrapolated minimum drag coefficient from the non- "drag bucket" region
C_{f_r}	wall friction drag coefficient
C_F	combined nonlinear correction term added to matrix constant
C_l, C_L	section lift coefficient

C_{l_d}	design lift coefficient
$C_{l_{d_e}}$	design lift coefficient for a reference airfoil
C_{L_o}	lift coefficient at zero angle of attack
$C_{L_{o_e}}$	lift coefficient at zero angle of attack for a reference airfoil
CL_{max}	maximum lift coefficient
$C_{L\alpha}$	section lift curve slope (per radian)
$\tilde{C}_{L_\alpha}$	$= \frac{dC_L}{d\alpha} (t/c)^{1/3}$, generalized lift curve slope
$C_{L_{\alpha_o}}$	lift curve slope of 2π
c_m	function of Mach number and velocity
c_p	specific heat pressure ($ft^2/sec^2/deg\ R$)
C_{pr}	pressure drag coefficient
c_v	specific heat volume ($ft^2/sec^2/deg\ R$)
C_v	nonlinear correction term added to the linearized velocity (fps)
C_z	axial compressor force coefficient
C_α	nonlinear correction term added to the linearized lift coefficient expression
C_ϕ	nonlinear correction term added to the linearized angle of attack expression (radians), or rotational compressor force coefficient
D	cascade diffusion parameter, or drag force (lb_f or lb_f/ft^2)
e	error

f	force/span (lb_f/ft)
F	compressor force coefficient corrected for the absence of the induced velocity
$F_V(x)$	distribution of noninduced inflow velocity ratio
g	blade gap (ft)
GC	geometric influence coefficient (per ft)
GC*	geometric influence coefficient summed over all blades for all segments of a particular filament (per ft)(equation 4)
$\tilde{GC}$	geometric influence coefficients differenced to relate to the bound circulation (per ft)
h	camber, maximum displacement of profile mean line from chord line, or duct height (ft)
h/t	generalized camber parameter
i	unit direction vector or cascade incidence angle (degrees), or $\sqrt{-1}$
i_{mo}	minimum loss incidence angle (degrees)
i_{oo}	cascade correlation parameter for minimum loss incidence angle (degree)
I	entropy
j	summation indices on propeller position or blade station
k	summation indices on trailing filament number
K	cascade correction factor for isolated airfoil
K_{it}	cascade correlation parameter for minimum loss incidence angle
$K_{1_{r=0}}, K_{2_{r=1}}$	generalized wake transport parameters for extension of the inboard sheet to r = 1
$K_{1_{r=1}}, K_{2_{r=1}}$	generalized wake transport parameters for extension of the inboard sheet to r =1

$K_{\delta_s}, K_{\delta_t}$	cascade correlation parameters for deviation angle
l	summation indices on segment number of a trailing filament
L	lift per unit span (lb_f/ft), or duct wall length, or number of propeller positions
m	summation indices on blade number
M	Mach number or matrix of aerodynamic and geometric influence coefficients for a system of simultaneous linear equations
M_{cr}	critical Mach number
M_σ	cascade correlation parameter for deviation angle
n	cascade correlation parameter for minimum loss incident angle, or normal coordinate (dimensionless)
$n_{C_{D_o}}$	empirical cascade correlation parameter
$n_{D_{D_{B_o}}}$	empirical cascade correlation parameter
N_R	Reynolds number, $r_r \sigma_r U_r/\mu_r$ (dimensionless)
P	static pressure (lb_f/ft^2), or power ($ft\ lb_f/sec$)
P_B	Base Pressure (lb_f/ft^2)
P_o	total pressure (lb_f/ft^2)
Pr_T	turbulent Prandtl number (dimensionless)
qn	heat flux
r	radial coordinate in the cylindrical coordinate system
R	blade tip radius (ft)
$\mathcal{R}$	gas constant ($ft^2/sec^2/deg\ R$)
r_A, r_B, r_C, r_D	radial coordinates of selected generalized wake features nondimensionalized by the blade radius

s	streamwise coordinate (dimensionless)
t	maximum airfoil thickness (ft)
T	compressor force (lb_f), or temperature (deg R), or thrust (lb_f)
T_o	total temperature (deg R)
t/c	generalized thickness parameter
U	magnitude of velocity, or velocity component (fps)
U_e	total cascade velocity including induced velocities (fps)
U_z	axial cascade velocity component (fps)
U_ϕ	rotational cascade velocity component (fps)
U^+	universal velocity (dimensionless)
v	induced velocity (fps)
V	velocity as defined where used in text (fps)
v_{imom}	momentum induced velocity (fps)
V_t	wake transport velocity (fps)
W	complex coordinates in duct plane (r + iz)
x	coordinate along the pitch axis in the cartesian coordinate system
y	chordwise coordinate in the cartesian coordinate system
Y^+	universal distance
z	axial coordinate in the cylindrical and cartesian coordinate system
Z	axial distance, z/r_r (dimensionless)
Z_{Bm}	cascade minimum loss

w	compressor momentum induced velocity (fps)
α	angle of attack or cascade flow angle or swirl angle to axis (deg)
α_e	angle between U_e and axial direction (deg)
α_i	cascade incidence angle (deg)
α_{min}	angle of attack for $C_{D_{Bo}}$ (deg)
α_{max}	angle of attack for CL_{max} (deg)
α_s	cascade stagger angle (deg)
α_o	angle of attack for zero lift (deg)

Subscripts

B	due to bound vortex
c	blade element chordwise direction
fr	due to skin friction force
H	hub conditions
i	of a praticular inflow station
i,j,p	summation indices
n	blade element normalwise direction, or in the direction of the normal
pr	due to pressure force
r	reference conditions, based on structural sea level atmospheric conditions for all thermodynamic quantities. The reference r_r is the inlet outer radius, and the velocity is the mean inlet velocity.
s	blade element spanwise direction, or in the streamwise direction
T	tip condition

Tip	blade tip
TR	due to trailing wake
w	wall conditions
0	freestream value, or stagnation conditions
1	inlet of the blade row
2	exit of the blade row
∞	freestream or edge of boundary layer

Superscripts

ν	iteration number
-	mean or average quantity or indicates vector
α_{2c}	corrected exit flow angle due to back pressure (deg)
α_{20}	angle of attack for C_{D_o} (deg)
α^*	metal angle of blade camberline at trailing edge relative to the stagger angle (deg)
β	flow swirl angle (deg)
γ	ratio of specific heats or boundary layer thickness (ft)
Γ	circulation of vortex segment (ft^2/sec)
δ^*	boundary layer displacement thickness (ft)
δ_o	flow deviation angle from the metal angle
δ_{oo}	cascade correlation parameters for deviation angle (deg)
Δ	boundary layer thickness, δ/r_r (dimensionless)
Δ^*	boundary layer displacement thickness, δ^*/r_r (dimensionless)
ε	empirical correction factor for lift curve slope
ζ	$= (M^2-1)\ (t/c)^{-2/3}$, generalized Mach number

η	transformed normal coordinate (dimensionless)
Θ	geometric blade pitch angle or blade pitch angle of streamline to axis (deg)
θ^*	boundary layer momentum thickness (ft)
Θ_B	local geometric blade pitch angle in the blade element coordinate system (rad)
κ	von Karman constant (0.41)
λ	generalized wake contraction parameter for the tip vortex or thermal conductivity (lb/sec/deg R)
μ	viscosity (slugs/ft/sec)
Π	pressure ratio, p/p_r
ρ	density ($slugs/ft^3$)
$\tau_{ns}, \tau_{n\phi}$	stress components
τ^+	stress, τ/τ_w (dimensionless)
ϕ	reference coordinate in the cylindrical coordinate system (rad), or inflow angle (rad)
ϕ_B	blade dissipation function, rate of dissipation of energy of the propeller boundary layer
ϕ_c	effective camber angle (deg)
$\phi(d)$	empirical curve fit relationship
χ	Clauser constant (0.016) (dimensionless) or transformation function
ψ	stream function (slugs/ft)
ψ_w	wake age or wake azimuth position (deg or rad) - see section entitled "Generalized Wake Model"
Ω	propeller rotational speed (rad/sec)

ΔC_{D_o}	twice C_{D_o}
$\Delta C_{D_{B_o}}$	twice $C_{D_{B_o}}$
Δi	twice the minimum loss incidence angle (deg)
Δ_{α_o}	cascade correction for zero angle of attack
Δ_{α_o}	angle of attack for $\Delta C_{D_{B_o}}$ (deg)
Δ_{α_2}	angle of attack for $\Delta C_{D_{B_o}}$ (deg)

MODELING FEATURES			MACH NUMBER 0.6				MACH NUMBER 0.7				MACH NUMBER 0.8			
			AIRFOIL NUMBER				AIRFOIL NUMBER				AIRFOIL NUMBER			
SR-1M AREA RULED SPINNER			23		24		23		24		23		24	
CASCADE DATA	COMPRESSIBLE WAKE	TIP LOSS	η_A	β	η_A	β	η_A	β	η_A	β	η_A	β	η_A	β
NO	NO	NO	.8059	58.79	.8205	57.96	.8039	58.30	.8281	57.66	.7754	57.78	.8079	57.13
NO	YES	NO	.8059	58.79	.8205	57.96	.8039	58.30	.8281	57.66	.8106	56.57	.8430	56.51
NO	NO	YES	.8059	58.79	.8205	57.96	.8039	58.30	.8281	57.66	.7531	58.38	.7856	57.83
NO	YES	YES	.8059	58.79	.8205	57.96	.8039	58.30	.8281	57.66	.7901	57.23	.8205	57.35
YES	NO	NO	.8059	59.22	.8061	58.48	.8094	58.69	.8166	58.14	.7910	58.10	.7938	57.58
YES	YES	NO	.8059	59.22	.8061	58.48	.8094	58.69	.8166	58.14	.8243	56.79	.8298	56.89
YES	NO	YES	.8059	59.22	.8061	58.48	.8094	58.69	.8166	58.14	.7694	58.78	.7634	58.44
YES	YES	YES	.8059	59.22	.8061	58.48	.8094	58.69	.8166	58.14	.8035	57.52	.8021	57.89
SR-2 AREA RULED SPINNER														
NO	NO	NO	.8129	58.54	.8262	58.05	.8011	57.86	.8148	57.69	.7526	58.08	.7723	57.38
NO	YES	NO	.8129	58.54	.8262	58.05	.8011	57.86	.8148	57.69	.7993	56.72	.8218	56.37
NO	NO	YES	.8129	58.54	.8262	58.05	.8011	57.86	.8148	57.69	.7219	58.51	.7538	57.90
NO	YES	YES	.8129	58.54	.8262	58.05	.8011	57.86	.8148	57.69	.7821	57.08	.8107	56.86
YES	NO	NO	.8133	59.00	.8150	58.52	.8064	58.20	.8012	58.13	.7683	58.41	.7575	57.79
YES	YES	NO	.8133	59.00	.8150	58.52	.8064	58.20	.8012	58.13	.8095	56.98	.8063	56.73
YES	NO	YES	.8133	59.00	.8150	58.52	.8064	58.20	.8012	58.13	.7361	58.89	.7357	58.41
YES	YES	YES	.8133	59.00	.8150	58.52	.8064	58.20	.8012	58.13	.7917	57.38	.7930	57.30
SR-3 AREA RULED SPINNER														
NO	NO	NO	.8061	60.58	.8284	59.80	.7927	60.41	.8225	59.61	.7678	60.19	.8168	59.41
NO	YES	NO	.8061	60.58	.8284	59.80	.8078	60.31	.8344	59.38	.7798	60.08	.8256	59.43
NO	NO	YES	.8061	60.58	.8284	59.80	.7928	60.41	.8226	59.61	.7496	61.23	.7904	60.20
NO	YES	YES	.8061	60.58	.8284	59.80	.8078	60.31	.8343	59.37	.7884	60.56	.7437	61.17
YES	NO	NO	.8117	61.41	.8087	60.62	.8061	61.16	.8052	60.36	.7960	60.81	.8023	60.11
YES	YES	NO	.8117	61.41	.8087	60.62	.8211	61.09	.8160	60.13	.8083	60.63	.8097	60.04
YES	NO	YES	.8117	61.41	.8087	60.62	.8063	61.16	.8052	60.36	.7780	62.22	.7641	61.07
YES	YES	YES	.8117	61.41	.8087	60.62	.8211	61.09	.8158	60.13	.7694	62.04	.7664	61.37

Table I. Predicted Propeller Performance Results - Mach Number Variation Study, $J = 3.07$, $C_P = 1.7$

MODELING FEATURES			ADVANCE RATIO 2.8				ADVANCE RATIO 3.0				ADVANCE RATIO 3.2			
			AIRFOIL NUMBER				AIRFOIL NUMBER				AIRFOIL NUMBER			
SR-1M AREA RULED SPINNER			23		24		23		24		23		24	
CASCADE DATA	COMPRESSIBLE WAKE	TIP LOSS	η_A	β	η_A	β	η_A	β	η_A	β	η_A	β	η_A	β
NO	NO	NO	.7851	53.95	.8150	53.10	.7754	57.78	.8079	57.13	.7617	59.78	.7950	59.22
NO	YES	NO	.8178	52.41	.8587	52.22	.8106	56.57	.8430	56.51	.7926	58.96	.8255	58.85
NO	NO	YES	.7613	54.53	.7902	53.91	.7531	58.38	.7856	57.83	.7417	60.35	.7735	59.82
NO	YES	YES	.7882	53.25	.8302	53.40	.7901	57.23	.8205	57.35	.7774	59.38	.8107	59.36
YES	NO	NO	.8019	54.17	.8036	53.42	.7910	58.10	.7938	57.58	.7787	60.15	.7772	59.75
YES	YES	NO	.8328	52.53	.8491	52.44	.8243	56.79	.8298	56.89	.8058	59.28	.8097	59.33
YES	NO	YES	.7782	54.81	.7750	54.34	.7694	58.78	.7634	58.44	.7584	60.82	.7474	60.51
YES	YES	YES	.8021	53.42	.8149	53.78	.8035	57.52	.8021	57.89	.7914	59.73	.7892	59.93
SR-2 AREA RULED SPINNER														
NO	NO	NO	.7564	54.42	.7719	53.34	.7526	58.08	.7723	57.38	.7404	59.93	.7646	59.45
NO	YES	NO	.7942	52.80	.8205	51.94	.7993	56.72	.8218	56.37	.7838	58.52	.8157	58.45
NO	NO	YES	.7226	55.04	.7518	53.98	.7219	58.51	.7538	57.90	.7187	60.23	.7519	59.83
NO	YES	YES	.7588	53.51	.7996	52.85	.7821	57.08	.8107	56.86	.7776	58.70	.8099	58.70
YES	NO	NO	.7731	54.67	.7624	53.59	.7683	58.41	.7575	57.79	.7552	60.32	.7468	59.96
YES	YES	NO	.8060	52.96	.8097	52.11	.8095	56.98	.8063	56.73	.7951	58.81	.7981	58.90
YES	NO	YES	.7367	55.34	.7366	54.32	.7361	58.89	.7357	58.41	.7330	60.65	.7313	60.40
YES	YES	YES	.7684	53.74	.7846	53.15	.7917	57.38	.7930	57.30	.7880	59.01	.7909	59.19
SR-3 AREA RULED SPINNER														
NO	NO	NO	.7897	56.28	.8458	55.41	.7678	60.19	.8168	59.41	.7497	62.27	.7967	61.48
NO	YES	NO	.8124	55.97	.8681	55.12	.7798	60.08	.8256	59.43	.7566	62.22	.8003	61.60
NO	NO	YES	.7781	57.25	.8206	56.33	.7496	61.23	.7904	60.20	.7308	63.24	.7722	62.12
NO	YES	YES	.7764	57.26	.8248	56.61	.7437	61.17	.7884	60.54	.7295	62.96	.7737	62.36
YES	NO	NO	.8189	56.69	.8367	55.92	.7960	60.81	.8023	60.11	.7789	63.03	.7770	62.29
YES	YES	NO	.8411	56.26	.8598	55.52	.8083	60.63	.8097	60.04	.7817	63.04	.7796	62.36
YES	NO	YES	.8079	57.93	.8055	57.02	.7780	63.22	.7641	61.07	.7595	64.34	.7432	63.06
YES	YES	YES	.8036	57.88	.8065	57.25	.7694	62.04	.7664	61.37	.7516	64.02	.7512	63.27

Table II. Predicted Propeller Performance - Advance Ratio Variation Study, M = 0.8, 100% Design Power Loading

MODELING FEATURES			ADVANCE RATIO 2.8				ADVANCE RATIO 3.0				ADVANCE RATIO 3.2			
			AIRFOIL NUMBER				AIRFOIL NUMBER				AIRFOIL NUMBER			
SR-1 CONIC SPINNER			23		24		23		24		23		24	
CASCADE DATA	COMPRESSIBLE WAKE	TIP LOSS	η_A	β	η_A	β	η_A	β	η_A	β	η_A	β	η_A	β
NO	NO	NO	.7828	54.59	.8123	54.09	.7595	58.28	.7981	58.10	.7392	60.26	.7798	60.16
NO	YES	NO	.8062	53.99	.8316	53.99	.7780	57.94	.8075	58.18	.7515	60.11	.7891	60.26
NO	NO	YES	.7504	55.01	.7907	54.71	.7280	58.74	.7745	58.72	.7107	60.69	.7587	60.70
NO	YES	YES	.7740	54.60	.8079	54.86	.7495	58.48	.7873	58.85	.7313	60.47	.7756	60.71
YES	NO	NO	.7933	54.85	.8002	54.46	.7695	58.64	.7784	58.63	.7500	60.68	.7561	60.78
YES	YES	NO	.8150	54.15	.8188	54.30	.7874	58.20	.7908	58.64	.7621	60.48	.7715	60.83
YES	NO	YES	.7602	55.35	.7739	55.19	.7381	59.16	.7477	59.38	.7213	61.19	.7274	61.44
YES	YES	YES	.7821	54.82	.7910	55.29	.7589	58.81	.7655	59.45	.7423	60.89	.7519	61.35
SR-1M CONIC SPINNER														
NO	NO	NO	.8105	53.67	.8356	52.84	.7966	57.58	.8213	56.98	.7808	59.61	.8076	59.11
NO	YES	NO	.8420	52.26	.8748	52.04	.8298	56.47	.8547	56.41	.8088	58.85	.8372	58.76
NO	NO	YES	.7872	54.25	.8109	53.69	.7743	58.19	.7987	57.71	.7603	60.19	.7855	59.71
NO	YES	YES	.8130	53.13	.8457	53.24	.8086	57.13	.8326	57.27	.7923	59.30	.8215	59.29
YES	NO	NO	.8200	53.89	.8223	53.19	.8051	57.91	.8054	57.45	.7917	59.97	.7869	59.66
YES	YES	NO	.8504	52.38	.8640	52.29	.8377	56.70	.8404	56.81	.8162	59.21	.8188	59.26
YES	NO	YES	.7965	54.53	.7937	54.12	.7837	58.60	.7740	58.32	.7702	60.69	.7572	60.43
YES	YES	YES	.8206	53.27	.8295	53.63	.8165	57.43	.8120	57.81	.8006	59.69	.7992	59.87
SR-1M AREA RULED SPINNER														
NO	NO	NO	.7851	53.95	.8150	53.10	.7754	57.78	.8079	57.13	.7617	59.78	.7950	59.22
NO	YES	NO	.8178	52.41	.8587	52.22	.8106	56.57	.8430	56.51	.7926	58.96	.8255	58.85
NO	NO	YES	.7613	54.53	.7902	53.91	.7531	58.38	.7856	57.83	.7417	60.35	.7735	59.82
NO	YES	YES	.7882	53.25	.8302	53.40	.7901	57.23	.8205	57.35	.7774	59.38	.8107	59.36
YES	NO	NO	.8019	54.17	.8036	53.42	.7910	58.10	.7938	57.58	.7787	60.15	.7772	59.75
YES	YES	NO	.8328	52.53	.8491	52.44	.8243	56.79	.8298	56.89	.8058	59.28	.8097	59.33
YES	NO	YES	.7782	54.81	.7750	54.34	.7694	58.78	.7634	58.44	.7584	60.82	.7474	60.51
YES	YES	YES	.8021	53.42	.8149	53.78	.8035	57.52	.8021	57.89	.7914	59.73	.7892	59.93

Table III. Predicted Propeller Performance Results - Twist and Spinner Variation Study, M = 0.8, 100% Design Power Loading

M_∞=0.6

J	C_T	C_P	η_A	$\Delta\eta$	η
β_{75}=56.0					
2.324	.6295	2.1131	.6923	-.033	.6593
2.534	.5649	1.8960	.7550	-.033	.7220
2.747	.4837	1.6490	.8058	-.033	.7728
2.956	.3892	1.3614	.8451	-.033	.8121
3.168	.2818	1.0262	.8699	-.033	.8369
3.488	.1056	.4447	.8283	-.033	.7953
β_{75}=58.0					
2.747	.5804	2.0990	.7596	-.033	.7266
2.956	.5043	1.8541	.8040	-.033	.7710
3.168	.4153	1.5655	.8404	-.033	.8074
3.488	.2631	1.0535	.8711	-.033	.8381
3.840	.0784	.3903	.7713	-.033	.7383
β_{75}=59.3					
2.747	.6376	2.4008	.7295	-.033	.6965
2.956	.5709	2.1818	.7735	-.033	.7405
3.168	.4938	1.9228	.8136	-.033	.7806
3.488	.3583	1.4607	.8556	-.033	.8226
3.840	.1911	.8515	.8618	-.033	.8288
β_{75}=60.4					
2.747	.6772	2.6558	.7005	-.033	.6675
2.956	.6208	2.4558	.7472	-.033	.7142
3.168	.5526	2.2234	.7874	-.033	.7544
3.488	.4330	1.8059	.8363	-.033	.8033
3.840	.2808	1.2478	.8641	-.033	.8311
4.224	.0971	.5268	.7786	-.033	.7456

M_∞=0.8

J	C_T	C_P	η_A	$\Delta\eta$	η
β_{75}=58.0					
2.745	.5533	2.2559	.6733	-.033	.6403
3.020	.4800	1.9383	.7479	-.033	.7149
3.294	.3790	1.5621	.7992	-.033	.7662
3.570	.2535	1.0966	.8253	-.033	.7923
3.842	.1082	.5522	.7528	-.033	.7198
β_{75}=59.3					
2.745	.5971	2.5592	.6404	-.033	.6074
3.020	.5397	2.2740	.7168	-.033	.6838
3.294	.4586	1.9454	.7765	-.033	.7435
3.570	.3518	1.5334	.8190	-.033	.7860
3.842	.2260	1.0423	.8331	-.033	.8001
4.118	.0787	.4657	.6959	-.033	.6629
β_{75}=60.4					
2.745	.6236	2.8119	.6088	-.033	.5758
3.020	.5826	2.5531	.6891	-.033	.6561
3.294	.5164	2.2618	.7521	-.033	.7191
3.570	.4257	1.8986	.8005	-.033	.7675
3.842	.3175	1.4596	.8357	-.033	.8027
4.118	.1874	.9324	.8277	-.033	.7947

Table IVa. Performance Map Predictions, SR-2, Modeling Option 1

M_∞=0.6

J	C_T	C_P	η_A	$\Delta\eta$	η
		β_{75}=56.0			
2.324	.6797	2.2697	.6960	-.033	.6630
2.534	.6199	2.0576	.7634	-.033	.7304
2.747	.5332	1.7911	.8178	-.033	.7848
2.956	.4294	1.4865	.8539	-.033	.8209
3.168	.3104	1.1213	.8770	-.033	.8440
3.488	.1077	.4627	.8119	-.033	.7789
		β_{75}=58.0			
2.747	.6333	2.2572	.7707	-.033	.7377
2.956	.5517	1.9940	.8179	-.033	.7849
3.168	.4518	1.6849	.8495	-.033	.8165
3.488	.2814	1.1233	.8738	-.033	.8408
3.840	.0692	.3677	.7227	-.033	.6897
		β_{75}=59.3			
2.747	.6897	2.5651	.7386	-.033	.7056
2.956	.6211	2.3332	.7869	-.033	.7539
3.168	.5355	2.0533	.8262	-.033	.7932
3.488	.3857	1.5554	.8649	-.033	.8319
3.840	.1936	.8706	.8539	-.033	.8209

M_∞=0.8

J	C_T	C_P	η_A	$\Delta\eta$	η
		β_{75}=58.0			
2.745	.6456	2.5570	.6931	-.033	.6601
3.020	.5452	2.1097	.7804	-.033	.7474
3.294	.4259	1.6866	.8318	-.033	.7988
3.570	.2789	1.1782	.8451	-.033	.8121
3.842	.1109	.7691	.5540	-.033	.5210
		β_{75}=59.3			
2.745	.6762	2.8050	.6617	-.033	.6287
3.020	.6065	2.4532	.7466	-.033	.7136
3.294	.5060	2.0594	.8093	-.033	.7763
3.570	.3891	1.6517	.8410	-.033	.8080
3.842	.2427	1.0966	.8503	-.033	.8173
4.118	.0712	.4273	.6862	-.033	.6532
		β_{75}=60.4			
2.745	.6958	2.9872	.6394	-.033	.6064
3.020	.6487	2.7118	.7224	-.033	.6894
3.294	.5648	2.3599	.7884	-.033	.7554
3.570	.4696	2.0322	.8250	-.033	.7920
3.842	.3433	1.5447	.8539	-.033	.8209
4.118	.1929	.9437	.8418	-.033	.8088

Table IVb. Performance Map Predictions, SR-2, Modeling Option 2

M_∞=0.6

J	C_T	C_P	η_A	$\Delta\eta$	η
β_{75}=55.0					
2.534	.5631	1.9533	.7305	-.033	.6975
2.747	.3947	1.3227	.8197	-.033	.7867
2.956	.2950	1.0279	.8484	-.033	.8154
3.168	.1849	.6877	.8518	-.033	.8188
3.488	.0034	.0996	.1191	-.033	.0861
β_{75}=57.0					
2.747	.4910	1.7332	.7782	-.033	.7452
2.956	.4100	1.4797	.8191	-.033	.7861
3.168	.3156	1.1825	.8455	-.033	.8125
3.488	.1588	.6601	.8391	-.033	.8061
β_{75}=58.0					
2.747	.5326	1.9357	.7558	-.033	.7228
2.956	.4600	1.7036	.7982	-.033	.7652
3.168	.3751	1.4296	.8312	-.033	.7982
3.488	.2299	.9421	.8512	-.033	.8182
3.840	.0535	.3092	.6644	-.033	.6314

M_∞=0.8

J	C_T	C_P	η_A	$\Delta\eta$	η
β_{75}=56.0					
2.745	.5550	2.0358	.7483	-.033	.7153
3.020	.4362	1.6140	.8162	-.033	.7832
3.294	.2768	1.0811	.8434	-.033	.8104
3.570	.0909	.4472	.7257	-.033	.6927
3.842	-.1241	-.2992	1.5936	-.033	1.5606
β_{75}=57.0					
2.745	.5983	2.2669	.7245	-.033	.6915
3.020	.4964	1.8726	.8006	-.033	.7676
3.294	.3575	1.3950	.8442	-.033	.8112
3.570	.1899	.8148	.8320	-.033	.7990
3.842	-.0055	.1192	-.1772	-.033	-.2102
β_{75}=58.0					
2.745	.6333	2.4785	.7014	-.033	.6684
3.020	.5403	2.0843	.7829	-.033	.7499
3.294	.4273	1.6914	.8322	-.033	.7992
3.570	.2806	1.1739	.8533	-.033	.8203
3.842	.1061	.5346	.7625	-.033	.7295
4.118	-.0772	-.1530	2.0778	-.033	2.0448

Table IVc. Performance Map Predictions, SR-2, Modeling Option 3

M_∞=0.6

J	C_T	C_P	η_A	$\Delta\eta$	η
β_{75}=59.3					
2.747	.6304	2.3996	.7217	-.031	.6907
2.956	.5670	2.1830	.7678	-.031	.7368
3.168	.4965	1.9524	.8056	-.031	.7746
3.488	.3806	1.5532	.8547	-.031	.8237
3.840	.2338	1.0269	.8743	-.031	.8433
4.224	.0550	.3370	.6894	-.031	.6584
β_{75}=60.4					
2.747	.6615	2.6465	.6866	-.031	.6556
2.956	.6117	2.4584	.7355	-.031	.7045
3.168	.5524	2.2461	.7791	-.031	.7481
3.488	.4488	1.8836	.8311	-.031	.8001
3.840	.3175	1.4087	.8655	-.031	.8345
4.224	.1546	.7783	.8390	-.031	.8080
β_{75}=61.3					
2.747	.6927	2.8503	.6676	-.031	.6366
2.956	.6490	2.6831	.7150	-.031	.6840
3.168	.5934	2.4826	.7572	-.031	.7262
3.488	.4988	2.1486	.8097	-.031	.7787
3.840	.3801	1.7158	.8507	-.031	.8197
4.224	.2311	1.1367	.8588	-.031	.8278
β_{75}=63.1					
2.747	.7321	3.2810	.6129	-.031	.5819
2.956	.7052	3.1410	.6637	-.031	.6327
3.168	.6667	2.9907	.7062	-.031	.6752
3.488	.5916	2.7128	.7607	-.031	.7297
3.840	.4950	2.3451	.8105	-.031	.7795
4.224	.3733	1.8710	.8428	-.031	.8118

M_∞=0.8

J	C_T	C_P	η_A	$\Delta\eta$	η
β_{75}=59.3					
2.745	.6118	2.5491	.6588	-.031	.6278
3.020	.5649	2.3174	.7362	-.031	.7052
3.294	.4846	1.9920	.8013	-.031	.7703
3.570	.3818	1.6072	.8481	-.031	.8171
3.842	.2617	1.1601	.8667	-.031	.8357
4.118	.1245	.6319	.8113	-.031	.7803
β_{75}=60.4					
2.745	.6342	2.7832	.6255	-.031	.5945
3.020	.6085	2.6031	.7060	-.031	.6750
3.294	.5418	2.3205	.7691	-.031	.7381
3.570	.4524	1.9652	.8218	-.031	.7908
3.842	.3499	1.5705	.8560	-.031	.8250
4.118	.2271	1.0919	.8565	-.031	.8255
4.533	.0221	.2416	.4146	-.031	.3836
β_{75}=63.1					
2.745	.6730	3.3588	.5500	-.031	.5190
3.020	.6805	3.2806	.6264	-.031	.5954
3.294	.6558	3.1232	.6917	-.031	.6607
3.570	.5986	2.8674	.7453	-.031	.7143
3.842	.5255	2.5534	.7907	-.031	.7597
4.118	.4414	2.2041	.8247	-.031	.7937
4.553	.2906	1.5670	.8444	-.031	.8134
4.991	.0960	.6898	.6946	-.031	.6636
β_{75}=64.0					
2.745	.6756	3.5406	.5238	-.031	.4928
3.294	.6815	3.3828	.6636	-.031	.6326
3.570	.6391	3.1700	.7197	-.031	.6887
3.842	.5765	2.8942	.7653	-.031	.7343
4.118	.5016	2.5732	.8027	-.031	.7717

Table Va. Performance Map Predictions, SR-1M, Modeling Option 1

M_∞=0.6

J	C_T	C_P	η_A	$\Delta\eta$	η
β_{75}=59.3					
2.747	.5988	2.2269	.7387	-.031	.7077
2.956	.5404	2.0451	.7811	-.031	.7501
3.168	.4725	1.8336	.8164	-.031	.7854
3.488	.3554	1.4533	.8530	-.031	.8220
3.840	.2091	.9378	.8562	-.031	.8252
4.224	.0311	.2554	.5144	-.031	.4834
β_{75}=60.4					
2.747	.6241	2.4331	.7046	-.031	.6736
2.956	.5811	2.2834	.7523	-.031	.7213
3.168	.5253	2.0994	.7927	-.031	.7617
3.488	.4221	1.7651	.8341	-.031	.8031
3.840	.2905	1.2997	.8583	-.031	.8273
4.224	.1281	.6775	.7987	-.031	.7677
β_{75}=61.3					
2.747	.6462	2.5998	.6828	-.031	.6518
2.956	.6106	2.4648	.7323	-.031	.7013
3.168	.5592	2.2998	.7703	-.031	.7393
3.488	.4670	1.9949	.8165	-.031	.7855
3.840	.3469	1.5743	.8462	-.031	.8152
4.224	.1987	1.0051	.8351	-.031	.8041

M_∞=0.8

J	C_T	C_P	η_A	$\Delta\eta$	η
β_{75}=59.3					
2.745	.6262	2.4774	.6938	-.031	.6628
3.020	.5749	2.2547	.7700	-.031	.7390
3.294	.4854	1.9344	.8266	-.031	.7956
3.570	.3666	1.5250	.8582	-.031	.8272
3.842	.2446	1.0797	.8704	-.031	.8394
4.118	.1058	.5496	.7927	-.031	.7617
β_{75}=60.4					
2.745	.6434	2.6513	.6661	-.031	.6351
3.020	.6063	2.4813	.7379	-.031	.7069
3.294	.5392	2.2170	.8011	-.031	.7701
3.570	.4412	1.8781	.8387	-.031	.8077
3.842	.3332	1.4784	.8659	-.031	.8349
4.118	.2088	1.0005	.8594	-.031	.8284
β_{75}=63.1					
2.745	.6650	3.0616	.5962	-.031	.5652
3.020	.6591	2.9936	.6649	-.031	.6339
3.294	.6308	2.8525	.7284	-.031	.6974
3.570	.5855	2.6979	.7748	-.031	.7438
3.842	.5070	2.3951	.8133	-.031	.7823
4.118	.4162	2.0406	.8399	-.031	.8089
4.553	.2599	1.3947	.8484	-.031	.8174
4.991	.0630	.5119	.6142	-.031	.5832

Table Vb. Performance Map Predictions, SR-1M, Modeling Option 2

M_∞=0.6

J	C_T	C_P	η_A	$\Delta\eta$	η
		β_{75}=56.7			
2.747	.5037	1.7352	.7974	-.031	.7664
2.956	.4237	1.5003	.8348	-.031	.8038
3.168	.3348	1.2309	.8617	-.031	.8307
3.488	.1869	.7532	.8655	-.031	.8345
3.840	.0050	.1162	.1652	-.031	.1342
		β_{75}=57.5			
2.747	.5367	1.8931	.7788	-.031	.7478
2.956	.4635	1.6729	.8190	-.031	.7880
3.168	.3809	1.4209	.8492	-.031	.8182
3.488	.2423	.9716	.8698	-.031	.8388
3.840	.0717	.3733	.7376	-.031	.7066
		β_{75}=58.8			
2.747	.5804	2.1561	.7395	-.031	.7085
2.956	.5222	1.9677	.7845	-.031	.7535
3.168	.4540	1.7543	.8199	-.031	.7889
3.488	.3372	1.3649	.8617	-.031	.8307
3.840	.1851	.8268	.8597	-.031	.8287
		β_{75}=59.6			
2.747	.6084	2.2985	.7271	-.031	.6961
2.956	.5537	2.1217	.7714	-.031	.7404
3.168	.4892	1.9165	.8087	-.031	.7777
3.488	.3760	1.5470	.8478	-.031	.8168
3.840	.2340	1.0461	.8590	-.031	.8280
4.224	.0602	.3800	.6692	-.031	.6382

M_∞=0.8

J	C_T	C_P	η_A	$\Delta\eta$	η
		β_{75}=56.5			
2.745	.5475	1.9608	.7665	-.031	.7355
3.020	.4600	1.6644	.8347	-.031	.8037
3.294	.3125	1.1735	.8772	-.031	.8462
3.570	.1585	.6573	.8609	-.031	.8299
3.842	-.0051	.0771	-.2540	-.031	-.2850
		β_{75}=57.8			
2.745	.5547	2.0734	.7344	-.031	.7034
3.020	.4893	1.8403	.8030	-.031	.7720
3.294	.3670	1.4192	.8518	-.031	.8208
3.570	.2547	1.0370	.8768	-.031	.8458
3.842	.1097	.5201	.8104	-.031	.7794
4.118	-.0446	-.0668	2.7494	-.031	2.7184
		β_{75}=60.4			
2.745	.6350	2.6213	.6650	-.031	.6340
3.020	.5999	2.4554	.7378	-.031	.7068
3.294	.5306	2.1881	.7988	-.031	.7678
3.570	.4335	1.8506	.8363	-.031	.8053
3.842	.3310	1.4678	.8664	-.031	.8354
4.118	.1934	.9402	.8471	-.031	.8161
4.553	-.0069	.1121	-.2801	-.031	-.3111

Table Vc. Performance Map Predictions, SR-1M, Modeling Option 3

M_∞=0.6

J	C_T	C_P	η_A	$\Delta\eta$	η
		β_{75}=59.3			
2.693	.4910	1.7516	.7549	-.02	.7349
2.898	.4345	1.5750	.7995	-.02	.7795
3.106	.3677	1.3725	.8321	-.02	.8121
3.419	.2547	1.0184	.8551	-.02	.8351
3.765	.1112	.5264	.7953	-.02	.7753
		β_{75}=60.4			
2.693	.5201	1.9360	.7235	-.02	.7035
2.898	.4746	1.7807	.7724	-.02	.7524
3.106	.4168	1.5984	.8099	-.02	.7899
3.419	.3156	1.2773	.8448	-.02	.8248
3.765	.1871	.8409	.8377	-.02	.8177
4.142	.0299	.2474	.5006	-.02	.4806
		β_{75}=61.3			
2.693	.5403	2.0970	.6939	-.02	.6739
2.898	.5057	1.9594	.7479	-.02	.7279
3.106	.4565	1.7943	.7902	-.02	.7702
3.419	.3647	1.4978	.8325	-.02	.8125
3.765	.2473	1.1018	.8451	-.02	.8251
4.142	.0998	.5487	.7534	-.02	.7334

M_∞=0.8

J	C_T	C_P	η_A	$\Delta\eta$	η
		β_{75}=59.3			
2.691	.5420	1.9164	.7611	-.02	.7411
2.961	.4525	1.6304	.8218	-.02	.8018
3.229	.3538	1.3298	.8591	-.02	.8391
3.500	.2443	.9825	.8703	-.02	.8503
3.767	.1225	.5584	.8264	-.02	.8064
		β_{75}=60.4			
2.691	.5661	2.0820	.7317	-.02	.7117
2.961	.4928	1.8345	.7954	-.02	.7754
3.229	.4074	1.5668	.8396	-.02	.8196
3.500	.3115	1.2645	.8622	-.02	.8422
3.767	.2041	.8964	.8577	-.02	.8377
4.037	.0805	.4322	.7519	-.02	.7319
		β_{75}=61.3			
2.691	.5859	2.2369	.7048	-.02	.6848
2.961	.5286	2.0258	.7726	-.02	.7526
3.229	.4547	1.7840	.8230	-.02	.8030
3.500	.3594	1.4817	.8490	-.02	.8290
3.767	.2665	1.1678	.8597	-.02	.8397
4.037	.1543	.7518	.8286	-.02	.8086
4.444	-.1391	-.4472	1.3823	-.02	1.3623

Table VIa. Performance Map Predictions, SR-3, Modeling Option 2

M_∞=0.6

J	C_T	C_P	η_A	$\Delta\eta$	η
β_{75}=59.5					
2.693	.5016	1.7842	.7571	-.02	.7371
2.898	.4460	1.6189	.7984	-.02	.7784
3.106	.3821	1.4247	.8330	-.02	.8130
3.419	.2708	1.0781	.8588	-.02	.8388
3.765	.1306	.6013	.8177	-.02	.7977
β_{75}=60.7					
2.693	.5272	1.9690	.7211	-.02	.7011
2.898	.4864	1.8289	.7707	-.02	.7507
3.106	.4312	1.6601	.8068	-.02	.7868
3.419	.3351	1.3556	.8452	-.02	.8252
3.765	.2115	.9402	.8469	-.02	.8269
4.142	.0552	.3532	.6473	-.02	.6273
β_{75}=61.5					
2.693	.5419	2.0962	.6962	-.02	.6762
2.898	.5120	1.9776	.7503	-.02	.7303
3.106	.4631	1.8245	.7884	-.02	.7684
3.419	.3757	1.5445	.8317	-.02	.8117
3.765	.2616	1.1619	.8477	-.02	.8277
4.142	.1170	.6219	.7792	-.02	.7592

M_∞=0.8

J	C_T	C_P	η_A	$\Delta\eta$	η
β_{75}=58.2					
2.691	.5127	1.7450	.7906	-.02	.7706
2.961	.4076	1.4250	.8469	-.02	.8269
3.229	.2948	1.0893	.8739	-.02	.8539
3.500	.1726	.6984	.8650	-.02	.8450
3.767	.0343	.2141	.6035	-.02	.5835
β_{75}=59.4					
2.691	.5454	1.9408	.7562	-.02	.7362
2.961	.4605	1.6623	.8203	-.02	.8003
3.229	.3611	1.3585	.8583	-.02	.8383
3.500	.2548	1.0221	.8725	-.02	.8525
3.767	.1339	.6037	.8355	-.02	.8155
β_{75}=60.2					
2.691	.5607	2.0473	.7370	-.02	.7170
2.961	.4846	1.7948	.7995	-.02	.7795
3.229	.3968	1.5201	.8429	-.02	.8229
3.500	.2995	1.2134	.8639	-.02	.8439
3.767	.1913	.8424	.8554	-.02	.8354
4.037	.0659	.3711	.7169	-.02	.6969

Table VIb. Performance Map Predictions, SR-3, Modeling Option 3

TULLAHOMA TUNNEL MACH NUMBER = 0.8

NUMBER OF BLADES	PROPELLER DIAMETER (ft)	NACELLE DIAMETER (ft)	PROPELLER DIA. / NACELLE DIA.	PROPELLER DIA. / TUNNEL DIA.	NACELLE DIA. / TUNNEL DIA.	BLEED %	C_P	C_T	η	β	J
8	11.000	4.122	2.669	.609	.228	YES	1.695		SOLUTION	CHOKED	
8	9.000	3.373	2.668	.499	.187	NO	1.695	.4703	.7979	57.35	2.88
8	9.000	3.373	2.668	.499	.187	-0.10	1.695	.4741	.8071	57.14	2.88
8	7.465	2.745	2.719	.413	.152	NO	1.695	.4805	.8142	57.16	2.88
8	7.465	2.745	2.719	.413	.152	-0.12	1.695	.4741	.8060	57.10	2.88
8	9.000	3.373	2.668	.499	.187	NO	1.695	.4699	.7973	57.37	2.88
8	9.000	3.373	2.668	.499	.187	NO	1.446	.4140	.8234	56.22	2.88
8	9.000	3.373	2.668	.499	.187	-0.10	1.446	.4180	.8363	55.98	2.88
8	9.000	3.373	2.668	.499	.187	NO	1.446	.4148	.8249	56.17	2.88
8	9.000	3.373	2.668	.499	.187	0.50	1.446	.4245	.8496	55.67	2.88
8	9.000	3.373	2.668	.499	.187	NO	1.446	.4154	.8260	56.13	2.88
8	9.000	3.373	2.668	.499	.187	5.00	1.446	.4291	.8566	55.47	2.88
2	9.000	3.373	2.668	.499	.187	NO	0.319	.0987	.8840	53.99	2.88
2	9.000	3.373	2.668	.499	.187	-0.10	0.319	.0989	.8950	53.84	2.88
2	9.000	3.373	2.668	.499	.187	NO	0.319	.0981	.8840	53.93	2.88
2	9.000	3.373	2.668	.499	.187	0.50	0.319	.1002	.9062	53.62	2.88
2	9.000	3.373	2.668	.499	.187	NO	0.319	.0982	.8852	53.90	2.88
2	9.000	3.373	2.668	.499	.187	2.00	0.319	.1016	.9192	53.36	2.86
8	9.000	3.373	2.668	.499	.187	NO	0.000	-.0260	NA	50.02	2.88
8	9.000	3.373	2.668	.499	.187	-0.10	0.000	-.0224	NA	49.66	2.88
8	9.000	3.373	2.668	.499	.187	0.50	0.000	-.0264	NA	50.02	2.88
8	9.000	3.373	2.668	.499	.187	5.00	0.000	-.0265	NA	50.02	2.88

TULLAHOMA TUNNEL MACH NUMBER = 0.7

8	9.000	3.373	2.668	.499	.187	NO	1.695	.5176	.7788	55.66	2.55
8	9.000	3.373	2.668	.499	.187	-0.50	1.695	.5207	.7842	55.54	2.55

Table VII. Predicted Propeller Performance Results - Wind Tunnel Study

MODANE TUNNEL MACH NUMBER = 0.8

NUMBER OF BLADES	PROPELLER DIAMETER (ft)	NACELLE DIAMETER (ft)	PROPELLER DIA. / NACELLE DIA.	PROPELLER DIA. / TUNNEL DIA.	NACELLE DIA. / TUNNEL DIA.	BLEED %	C_P	C_T	η	β	J
8	11.000	4.122	2.669	.623	.159	NO	1.695	.4436	.8213	58.56	3.14
8	9.000	3.373	2.668	.346	.130	NO	1.695	.4437	.8205	58.51	3.14
8	9.000	3.373	2.668	.346	.130	NO	1.446	.3917	.8505	57.39	3.14
2	9.000	3.373	2.668	.346	.130	NO	0.319	.0919	.9065	55.30	3.14
8	9.000	3.373	2.668	.346	.130	NO	0.000	-.024	NA	51.58	3.14

MODANE TUNNEL MACH NUMBER = 0.7

8	9.000	3.373	2.668	.346	.130	NO	1.695	.4942	.8104	56.8	2.78

MODANE TUNNEL MACH NUMBER = 0.6

8	9.000	3.373	2.668	.346	.130	NO	1.695	.5364	.7636	54.90	2.66

FREE AIR MACH NUMBER = 0.8

8	9.000	3.373	2.668	.000	.000	NO	1.695	.4795	.8130	51.13	2.35
8	9.000	3.373	2.668	.000	.000	NO	1.446	.4245	.8475	55.91	2.80

Table VII. Continued

		FRONT			REAR			TOTAL			
$\beta_{F_{0.75R}}$	J	C_P	C_T	η	C_P	C_T	η	C_P	C_T	η	
55	1.4	.3929	.1525	.5434	.4791	.1802	.5266	.8720	.3327	.5341	*
"	2.0	.5370	.1609	.5993	.6065	.1879	.6196	1.1435	.3488	.6100	*
"	2.4	.5464	.1545	.6786	.5068	.1573	.7449	1.0532	.3118	.7105	
"	2.9	.3637	.1067	.8508	.2524	.0775	.8905	.6161	.1842	.8670	
"	3.2	.2384	.0661	.8872	.0786	.0141	.5740	.3170	.0802	.8095	
"	3.4	.1460	.0348	.8104	-.0534	-.0309	1.9674	.0926	.0039	.1431	
60	1.8	.5175	.1537	.5346	.6213	.1823	.5282	1.1388	.3360	.5310	*
"	2.4	.6943	.1639	.5666	.7846	.1965	.6011	1.4789	.3604	.5848	*
"	3.1	.6664	.1514	.7043	.5806	.1506	.8041	1.2470	.3020	.7507	
"	3.6	.4888	.1147	.8448	.3246	.0801	.8884	.8134	.1948	.8621	
"	4.0	.3235	.0690	.8532	.0810	.0075	.3704	.4045	.0765	.7564	
"	4.4	.1260	.0149	.5203	-.2110	-.0749	1.5619	-.0850	-.0600	3.1058	
65	2.4	.7470	.1529	.4912	.8732	.1884	.5178	1.6202	.3413	.5055	*
"	3.1	.9952	.1663	.5180	1.0582	.2033	.5956	2.0534	.3696	.5579	*
"	3.6	.9942	.1641	.5942	.8933	.1794	.7230	1.8875	.3435	.6551	
"	4.0	.8913	.1509	.6772	.7184	.1495	.8324	1.6097	.3004	.7464	
"	4.6	.6978	.1196	.7884	.4083	.0749	.8438	1.1061	.1945	.8088	
"	5.0	.5424	.0856	.7891	.1467	.0105	.3579	.6891	.0961	.6972	
"	5.4	.3602	.0426	.6386	-.1520	-.0594	2.1103	.2082	-.0168	-.4357	

* SECTION ANGLE OF ATTACK WENT OFF AIRFOIL TABLES AT SOME STATIONS

Table VIII. Predicted Low Speed Coaxial Performance Results

(A) EFFECT OF MACH NUMBER

SPINNER A, 8 BLADES

$\beta_{F_{.75}}$	$\beta_{R_{.75}}$	J	C_{P_F}	C_{P_R}	C_{T_F}	C_{T_R}	η_{F_A}	η_{R_A}	C_{P_T}	C_{T_T}	η_T	
MACH 0.6												
60	58	3.0	1.527	1.733	.3353	.4034	.6589	.6984	3.261	.7387	.6799	
60	58	3.2	1.352	1.467	.3012	.3503	.7127	.7640	2.820	.6515	.7394	
60	58	3.4	1.166	1.188	.2595	.2849	.7572	.8160	2.354	.5444	.7869	
60	58	3.6	.9811	.9060	.2147	.2123	.7876	.8433	1.887	.4270	.8144	
60	58	3.8	.7838	.6113	.1642	.1289	.7969	.8021	1.395	.2931	.7992	
65	62.5	3.5	2.066	2.401	.3606	.4581	.6283	.6868	4.466	.8187	.6598	
65	62.5	4.0	1.778	1.893	.3082	.3676	.6934	.7769	3.671	.6758	.7364	
65	62.5	4.3	1.475	1.386	.2468	.2625	.7356	.8326	2.861	.5093	.7826	
65	62.5	4.6	1.304	1.110	.2110	.2004	.7449	.8311	2.413	.4114	.7845	
65	62.5	4.8	1.128	.8307	.1726	.1330	.7344	.7687	1.959	.3056	.7489	
MACH 0.7												
60	58	3.0	1.488	1.529	.2889	.3196	.5825	.6270	3.017	.6085	.6051	
60	58	3.2	1.315	1.322	.2642	.2867	.6431	.6939	2.637	.5509	.6686	
60	58	3.4	1.120	1.051	.2282	.2304	.6928	.7455	2.171	.4586	.7183	
60	58	3.6	.9204	.7549	.1855	.1586	.7256	.7563	1.675	.3441	.7394	
60	58	3.8	.7081	.4498	.1347	.0722	.7229	.6100	1.158	.2069	.6790	
65	62.5	3.6	2.143	2.388	.3288	.4010	.5524	.6046	4.530	.7298	.5799	
65	62.5	4.0	1.828	1.860	.2900	.3319	.6344	.7135	3.688	.6219	.6743	
65	62.5	4.4	1.478	1.289	.2308	.2263	.6870	.7724	2.767	.4571	.7268	
65	62.5	4.6	1.286	.9877	.1940	.1589	.6936	.7399	2.274	.3529	.7137	
65	62.5	4.8	1.082	.6688	.1510	.0817	.6699	.5864	1.751	.2327	.6380	
MACH 0.8												
60	58	3.2	1.181	1.102	.2155	.2197	.5839	.6379	2.283	.4352	.6100	
60	58	3.4	.8572	.6642	.1518	.1189	.6021	.6086	1.521	.2707	.6050	
60	58	3.6	.6836	.4210	.1124	.0490	.5916	.4188	1.105	.1614	.5257	
60	58	3.8	NEGATIVE THRUST-NO SOLUTION									
60	58	4.0	NEGATIVE THRUST-NO SOLUTION									
65	62.5	3.4	1.905	1.904	.2483	.2805	.4433	.5009	3.809	.5288	.4721	*
65	62.5	3.8	1.761	1.670	.2426	.2646	.5236	.6021	3.431	.5072	.5618	
65	62.5	4.1	1.523	1.311	.2125	.2071	.5721	.6476	2.834	.4196	.6070	
65	62.5	4.3	1.330	1.021	.1815	.1481	.5865	.6236	2.351	.3296	.6026	
65	62.5	4.5	1.118	.7043	.1422	.0716	.5726	.4575	1.822	.2138	.5281	

(B) EFFECT OF SPINNER SHAPE

6 BLADES, MACH 0.7

SPINNER A												
65	64.2	3.2	1.508	1.766	.2934	.3303	.6225	.5984	3.275	.6237	.6095	*
65	64.2	3.6	1.573	1.849	.2929	.3513	.6705	.6840	3.422	.6442	.6778	
65	64.2	4.0	1.573	1.838	.2800	.3372	.7117	.7337	3.411	.6172	.7236	*
65	64.2	4.4	1.383	1.607	.2370	.2883	.7541	.7892	2.990	.5253	.7730	*
65	64.2	4.8	1.077	1.198	.1673	.1980	.7456	.7933	2.275	.3653	.7707	
SPINNER B												
65	64.2	3.2	1.511	1.767	.2952	.3268	.6253	.5920	3.277	.6220	.6074	*
65	64.2	3.6	1.575	1.854	.2954	.3474	.6751	.6746	3.429	.6428	.6748	*
65	64.2	4.0	1.576	1.839	.2833	.3319	.7189	.7216	3.415	.6152	.7203	*
65	64.2	4.4	1.387	1.585	.2417	.2787	.7665	.7735	2.972	.5204	.7702	
65	64.2	4.8	1.085	1.155	.1734	.1838	.7675	.7636	2.240	.3572	.7655	

* OFF AIRFOIL TABLES IN ANGLE OF ATTACK RANGE

Table IX. Predicted Moderate Speed Coaxial Propeller Performance

Figure 1 – Conceptual Model of a High Speed Propeller–Nacelle Configuration

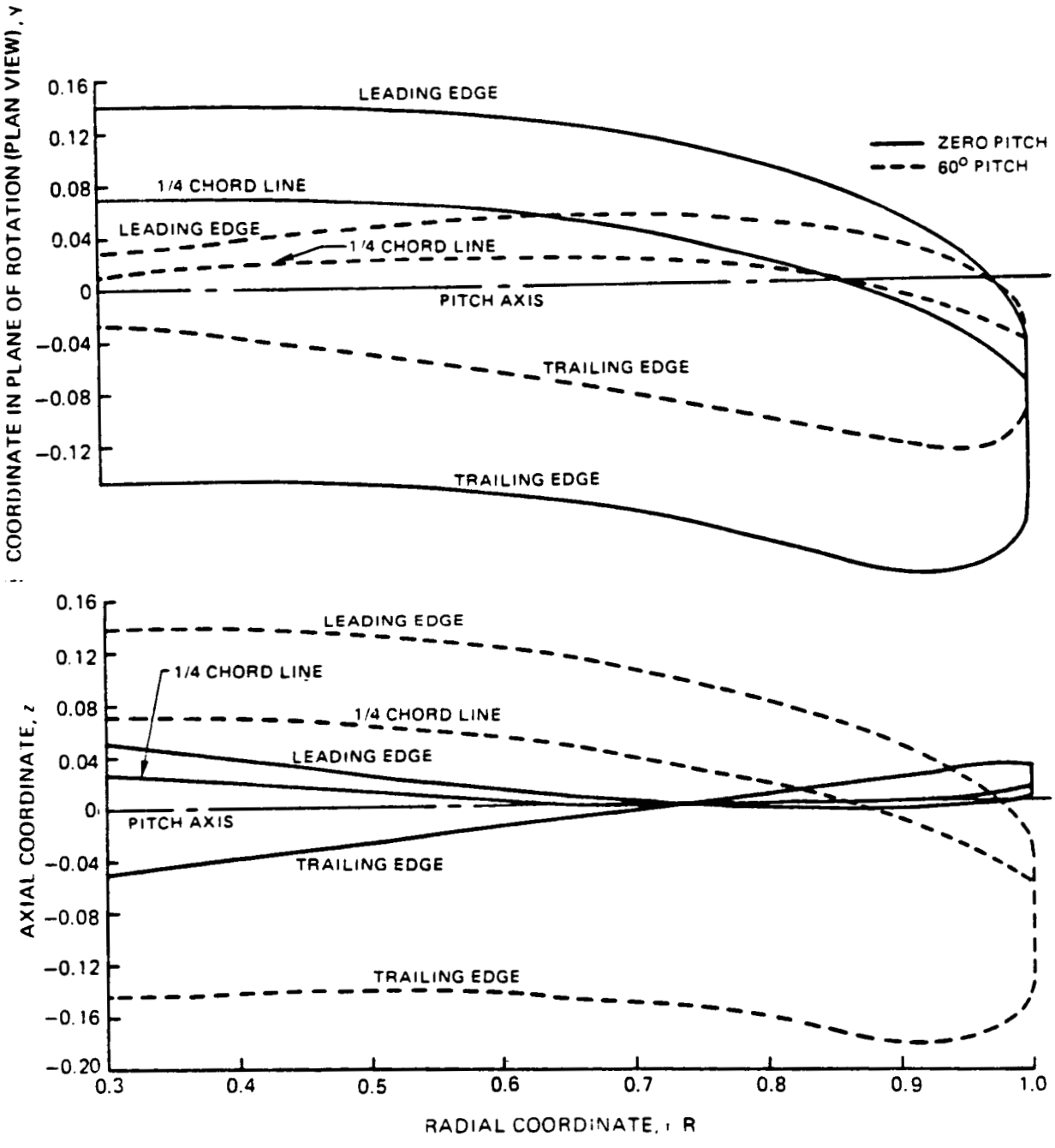

Figure 2. Variation of Blade Geometry of a Model Propeller with Sweep, Axial and Inplane Views at Zero and 60 Deg. Pitch

85-4-90-73

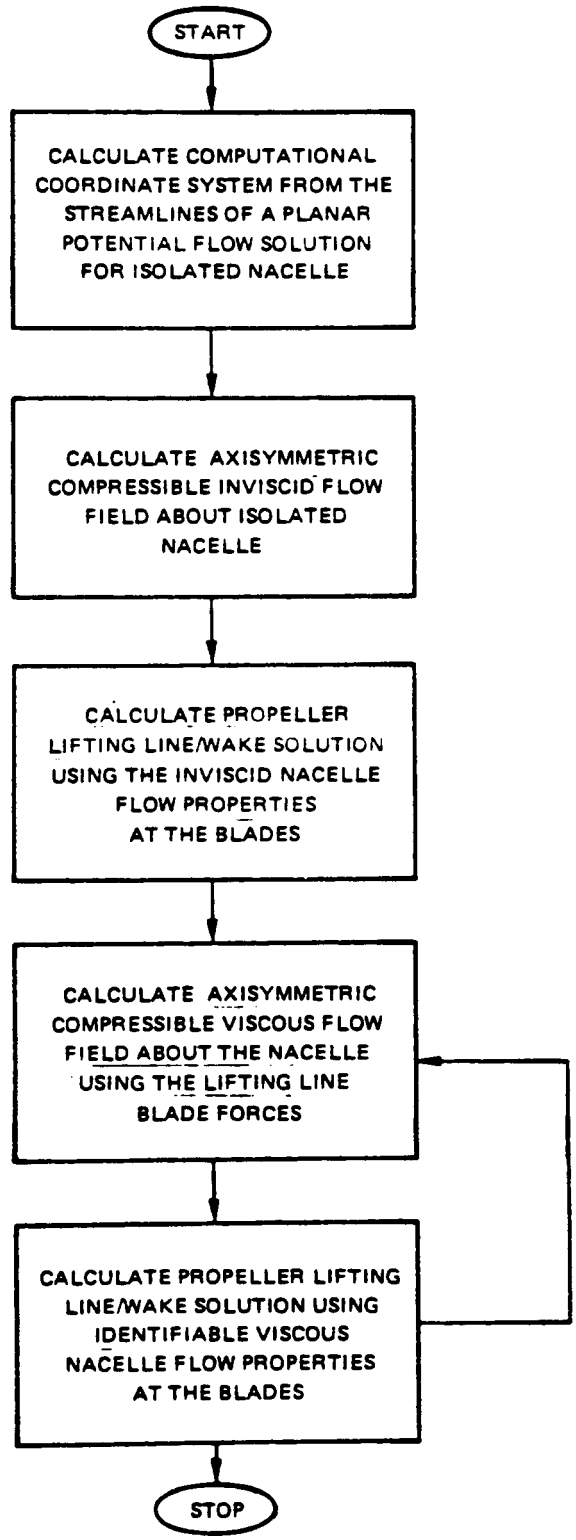

Figure 3. Simplified Structure of Major Program Tasks

85-4-90-72

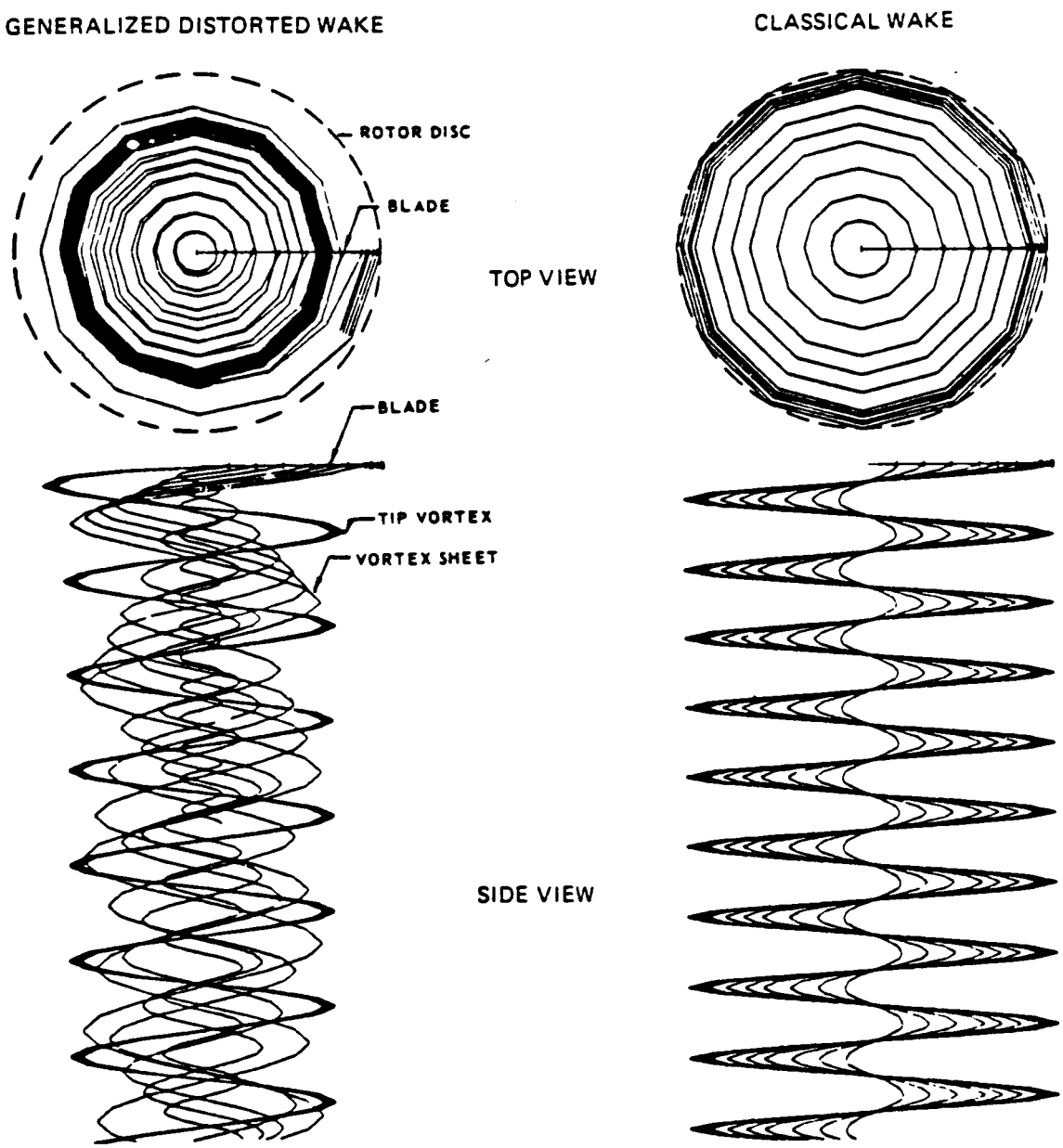

Figure 4. Computer Wake Representation for One Blade of a Hovering Rotor, Classical a Generalized Distorted Wake Models

85-4-

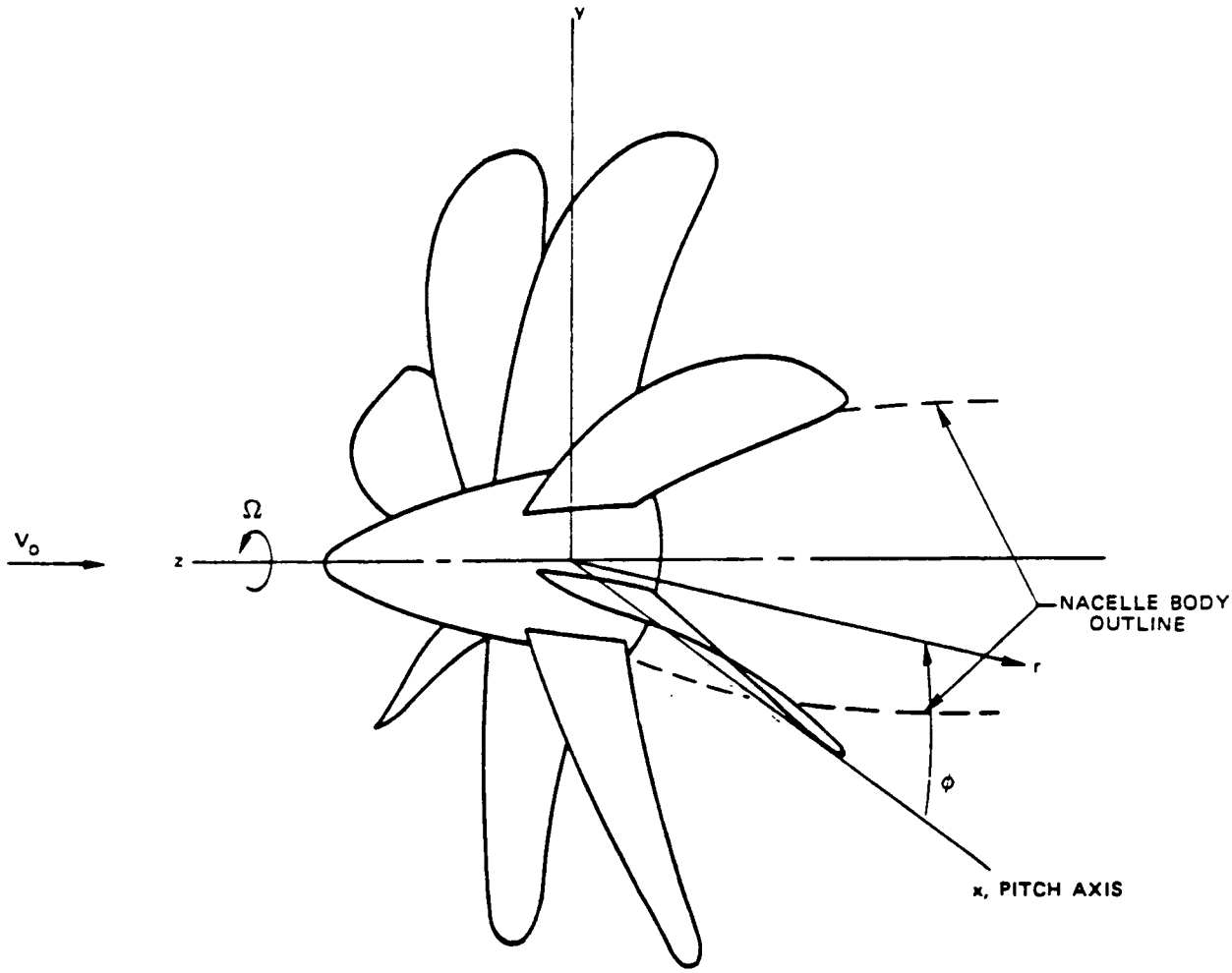

Figure 5. Cylindrical and Cartesian Coordinate Systems for Propeller Geometry

85-4-90-71

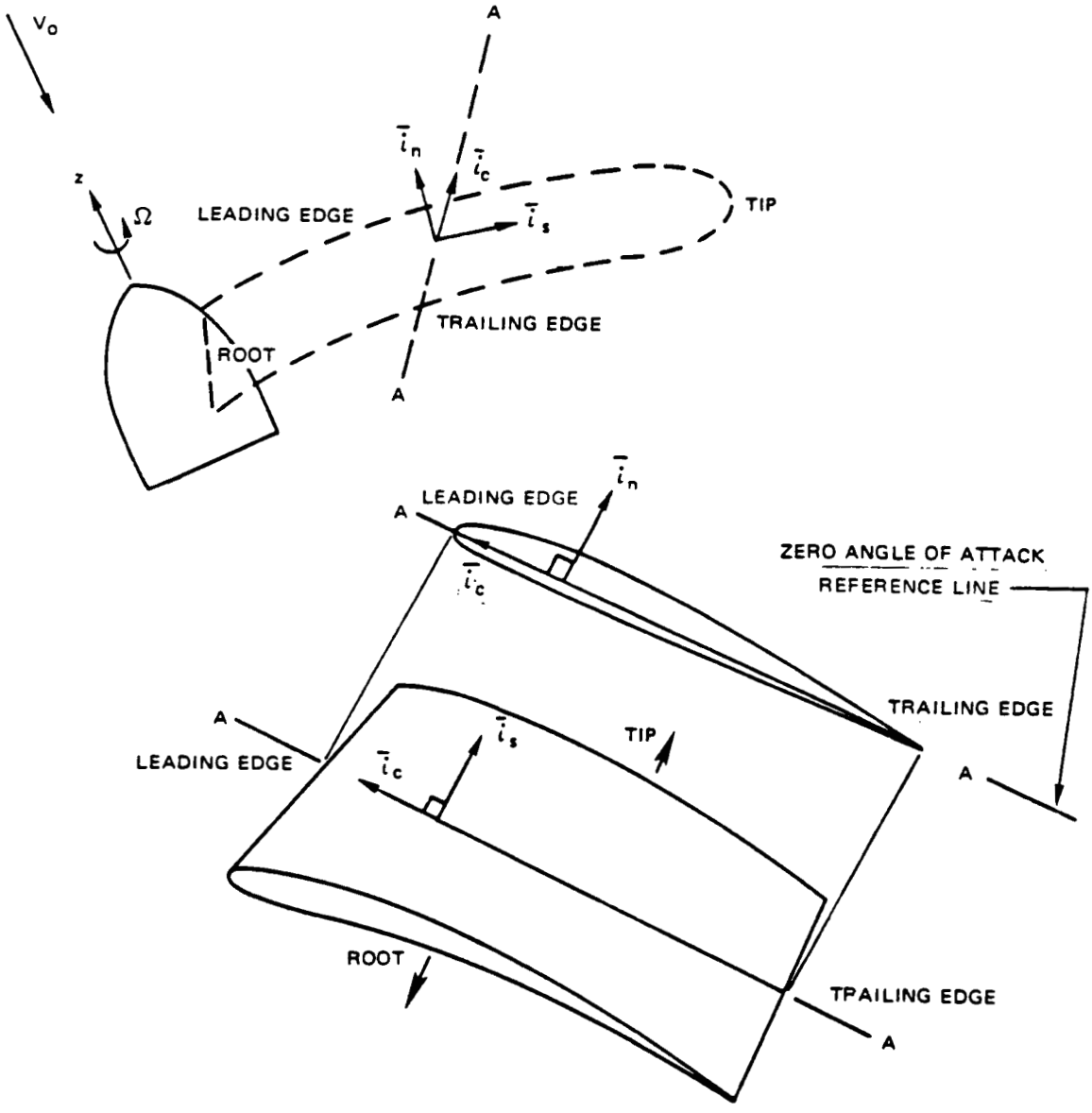

Figure 6. Blade Element Coordinate System

85-4-90

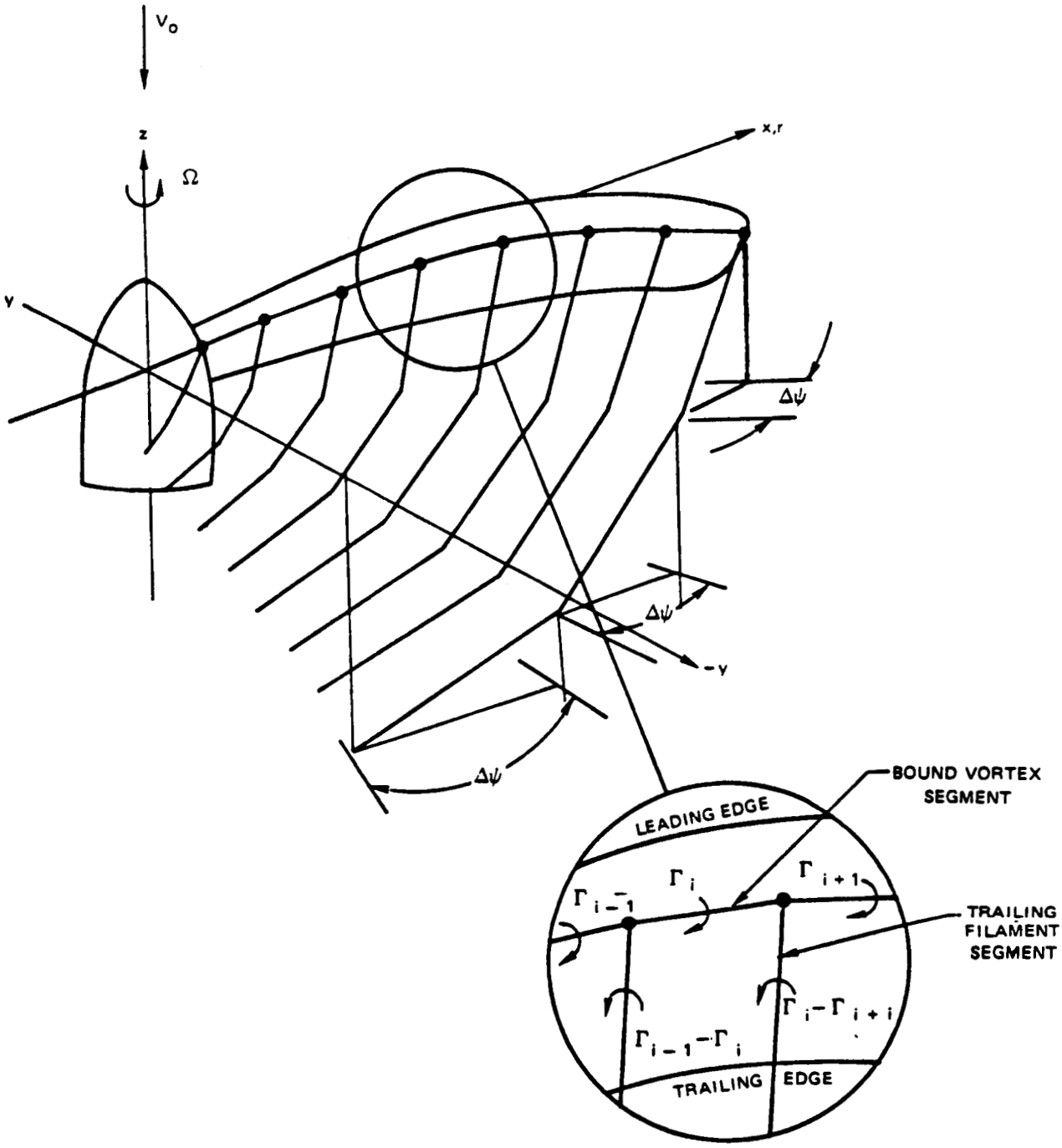

Figure 7. Representation of Propeller Blade and Wake by Bound and Trailing Vortex Segments

85-4-90-69

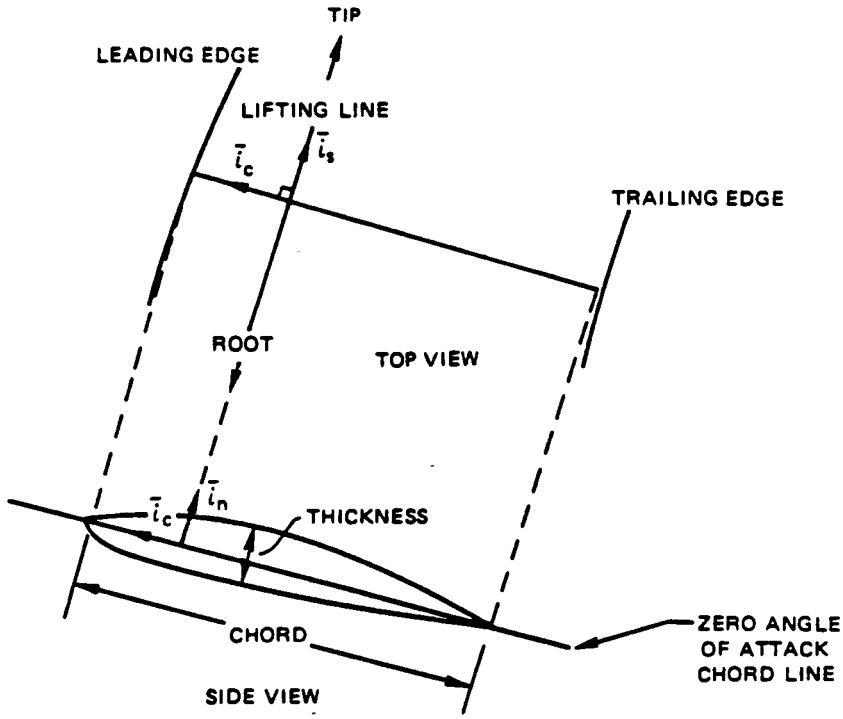

- LOCAL BLADE ELEMENT GEOMETRY

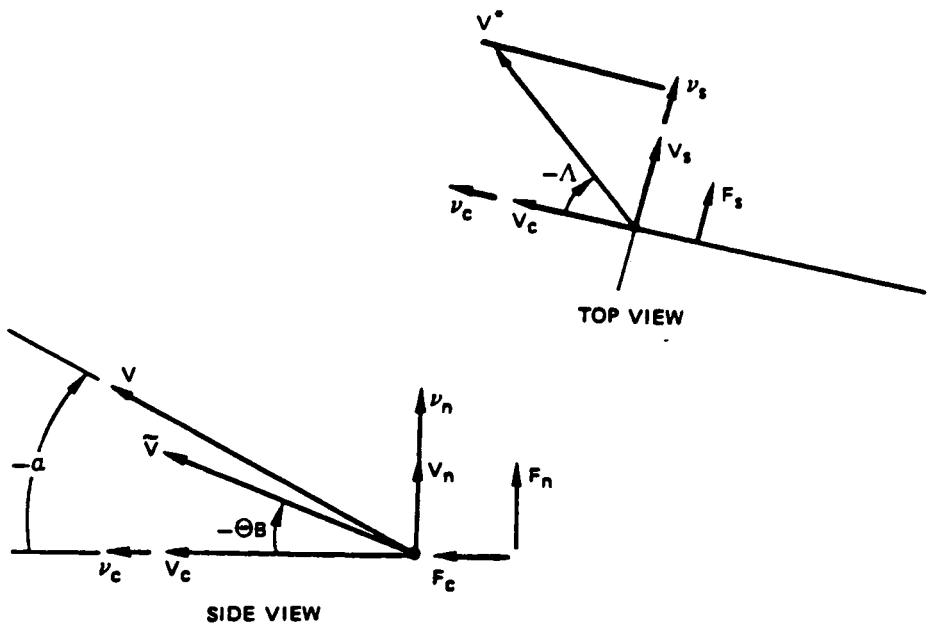

LOCAL BLADE ELEMENT VELOCITY VECTOR AND FORCE DIAGRAM

Figure 8. Aerodynamic Related Quantities in the Local Blade Element Coordinate System

85-4-90-68

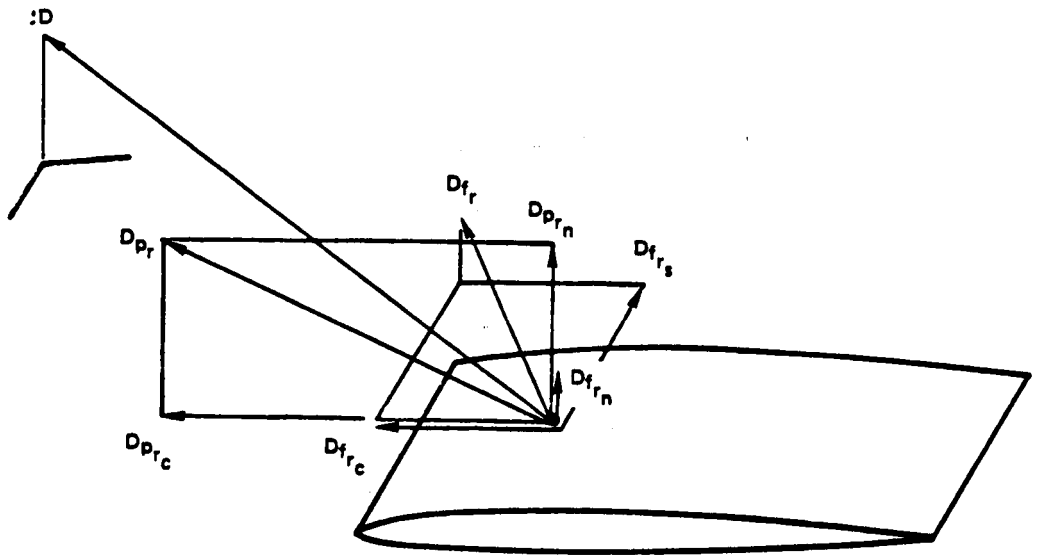

Figure 9. Vector Diagram of Drag Forces in the Blade Element Coordinate System

85-4-90-67

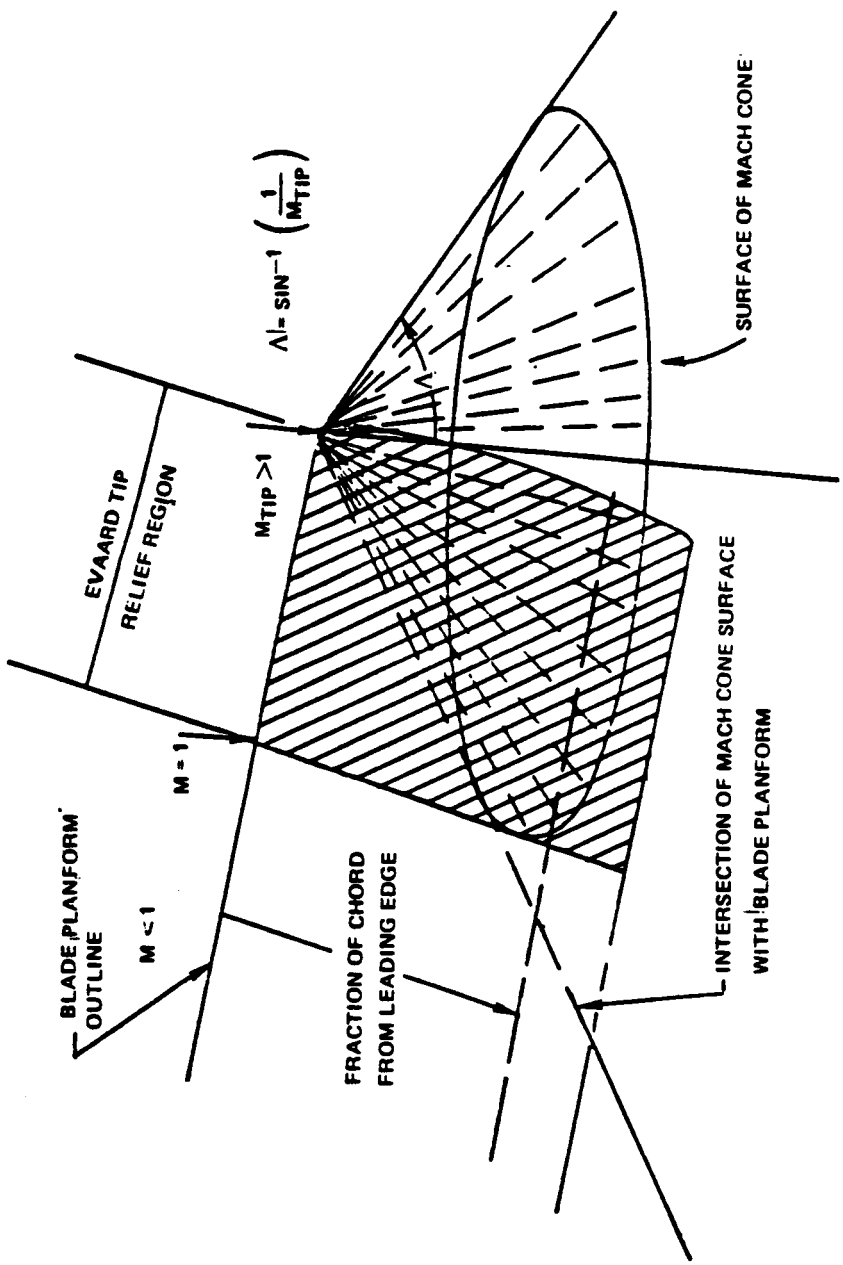

Figure 10. Evaard Tip Relief Region on Propeller Blade

85-4-90-66

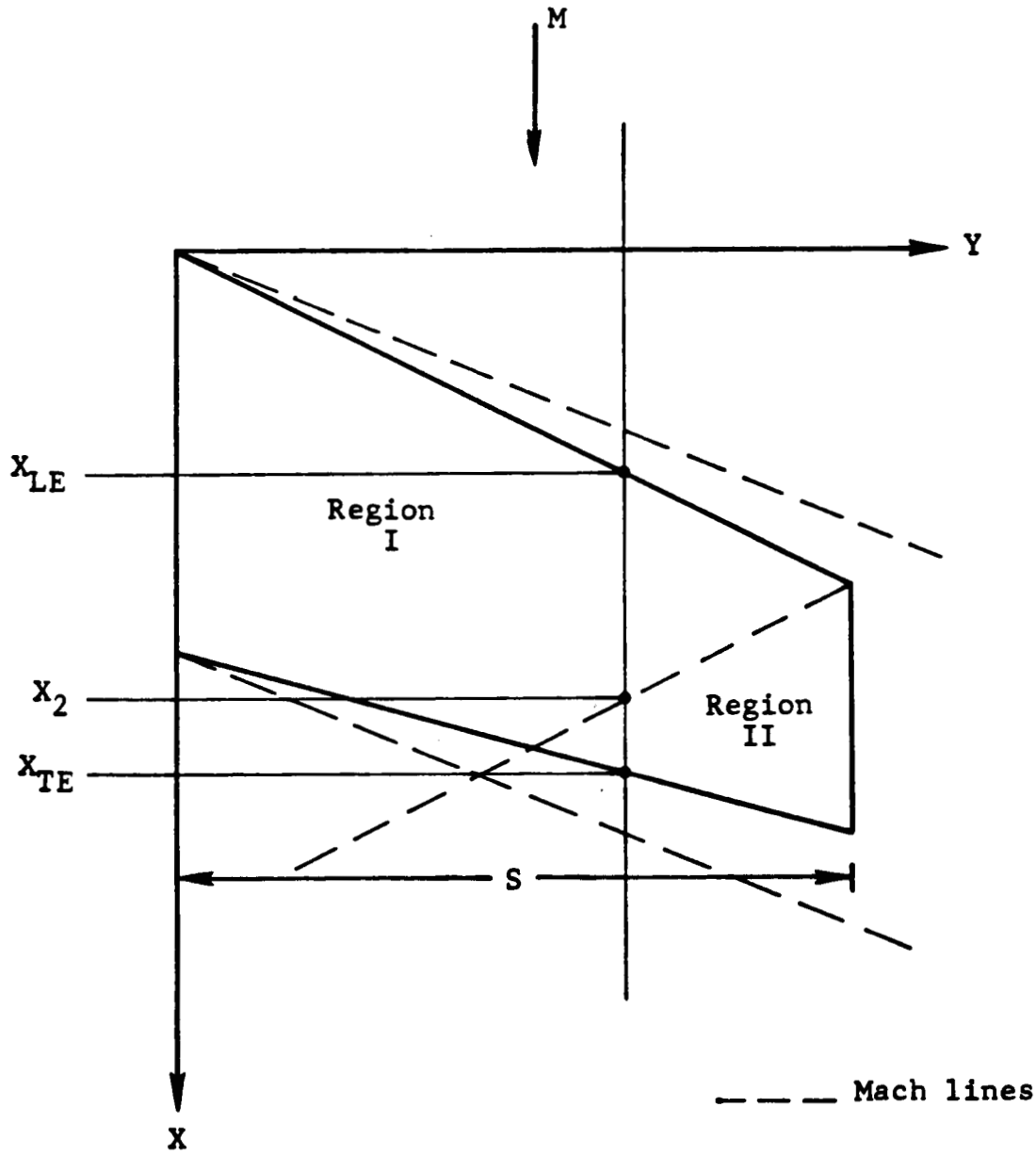

Figure 11. Definition of Surface Regions and Coordinate System for a Swept Wing with Subsonic Leading Edge and Supersonic Trailing Edge

85-4-90-65

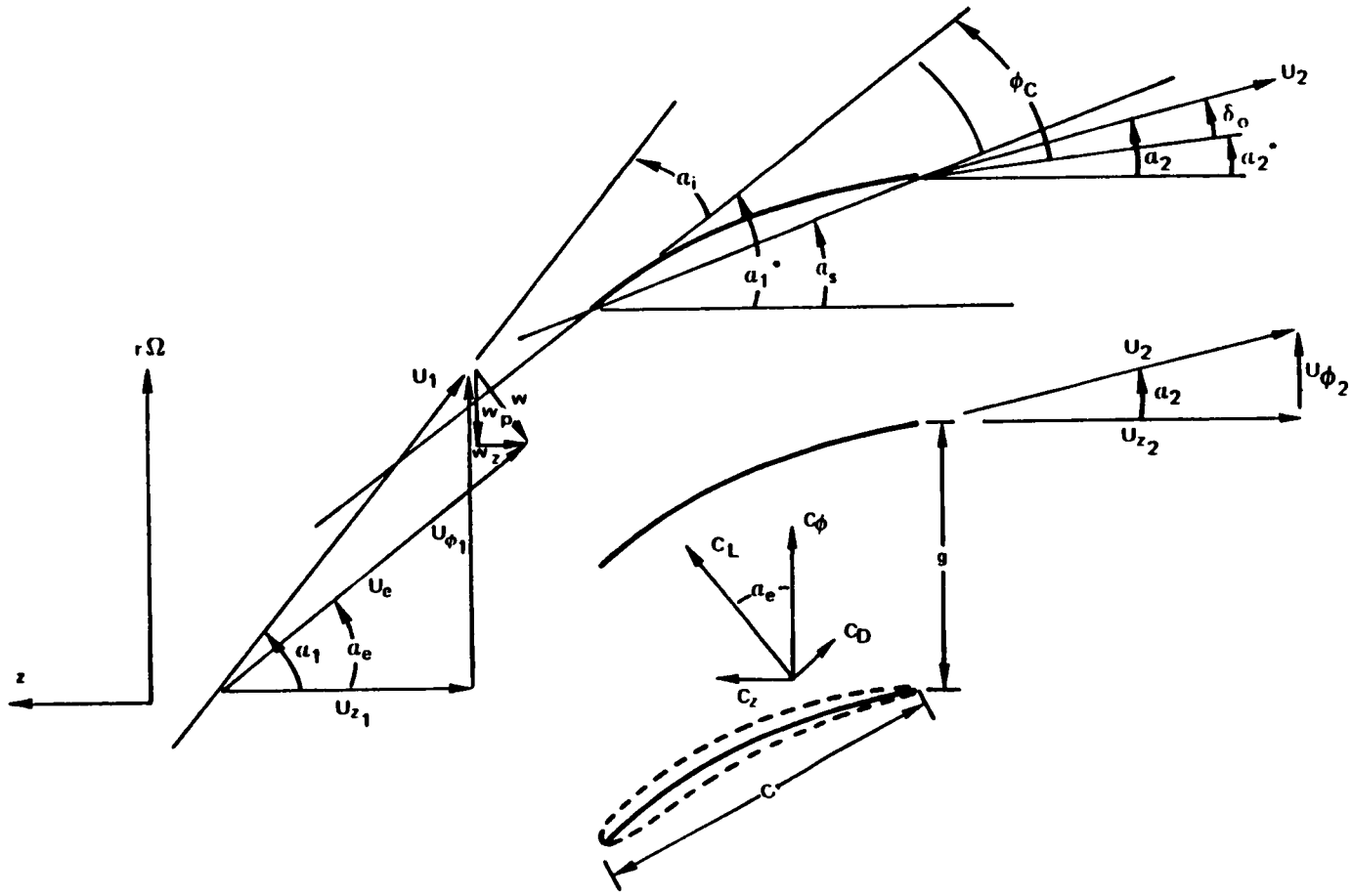

Figure 12. Geometric and Velocity Quantities for the Cascade Airfoil Correlation

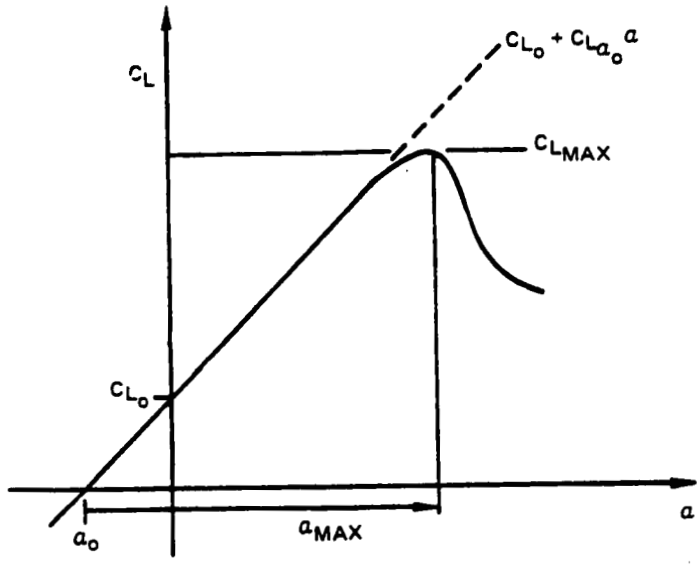

(a) C_L CORRELATION PARAMETERS

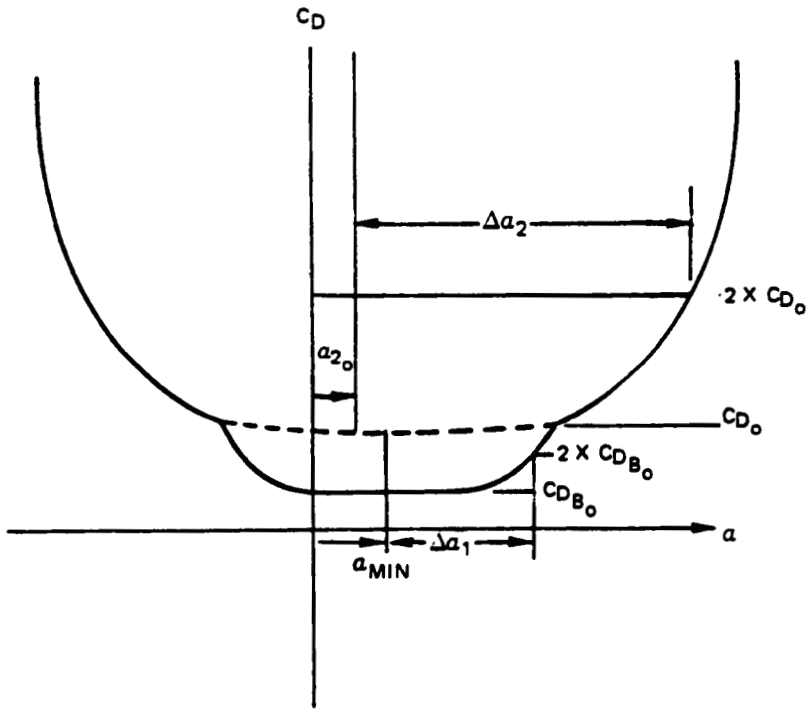

(b) C_D DATA CORRELATION PARAMETERS

Figure 13. C_L and C_D Data Correlation Parameters

85-4-90-63

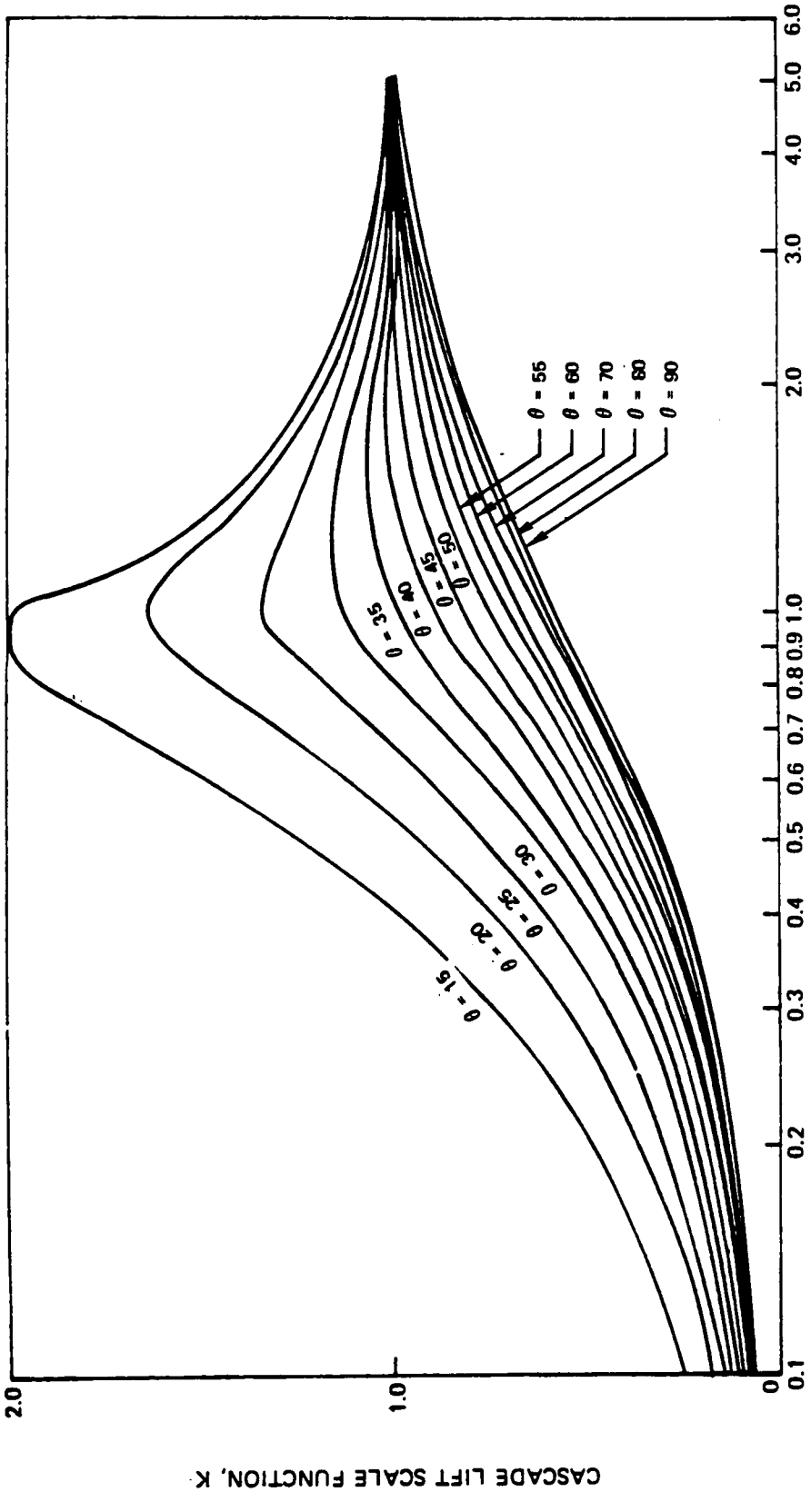

Figure 14. Two Dimensional Cascade Lift Scale Function for Isolated Airfoils

85-4-90-62

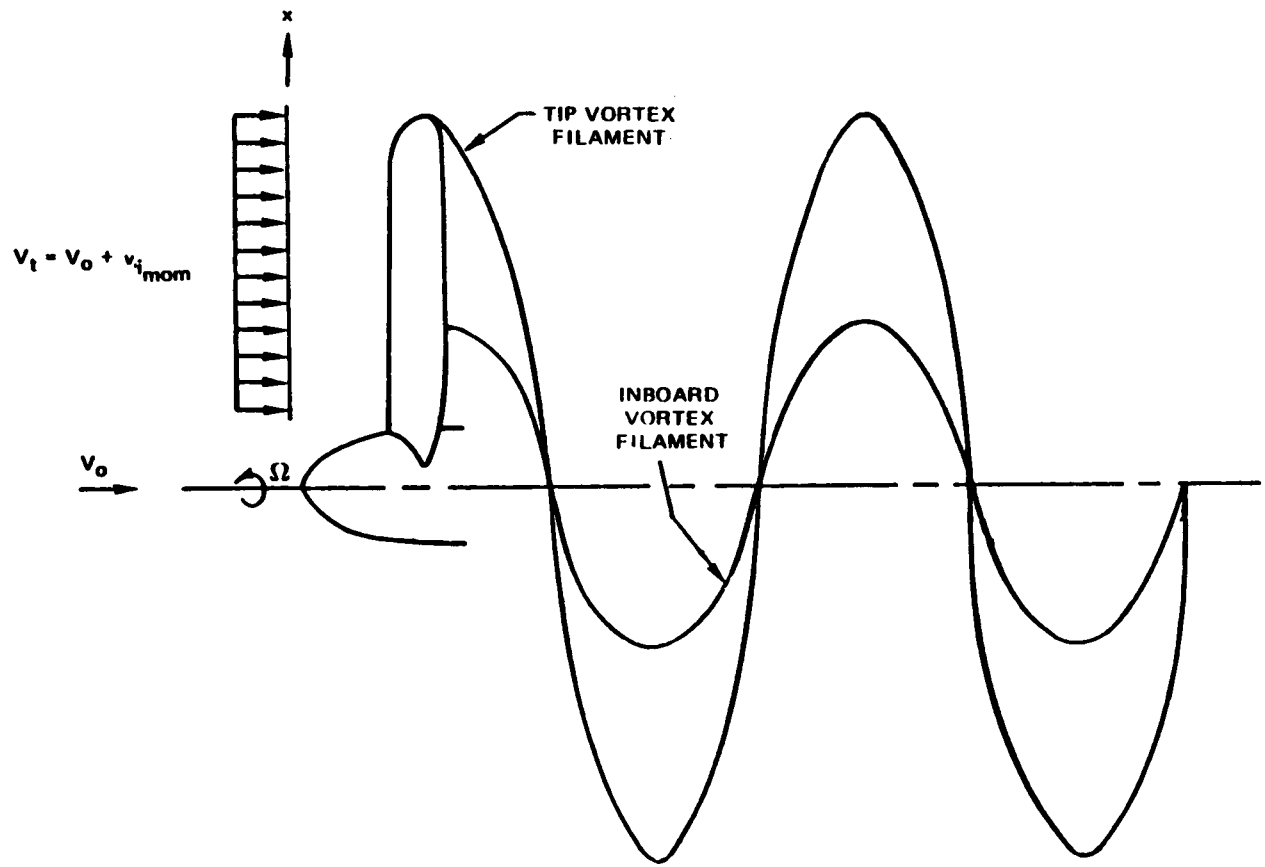

Figure 15. Classical Wake Vortex Model

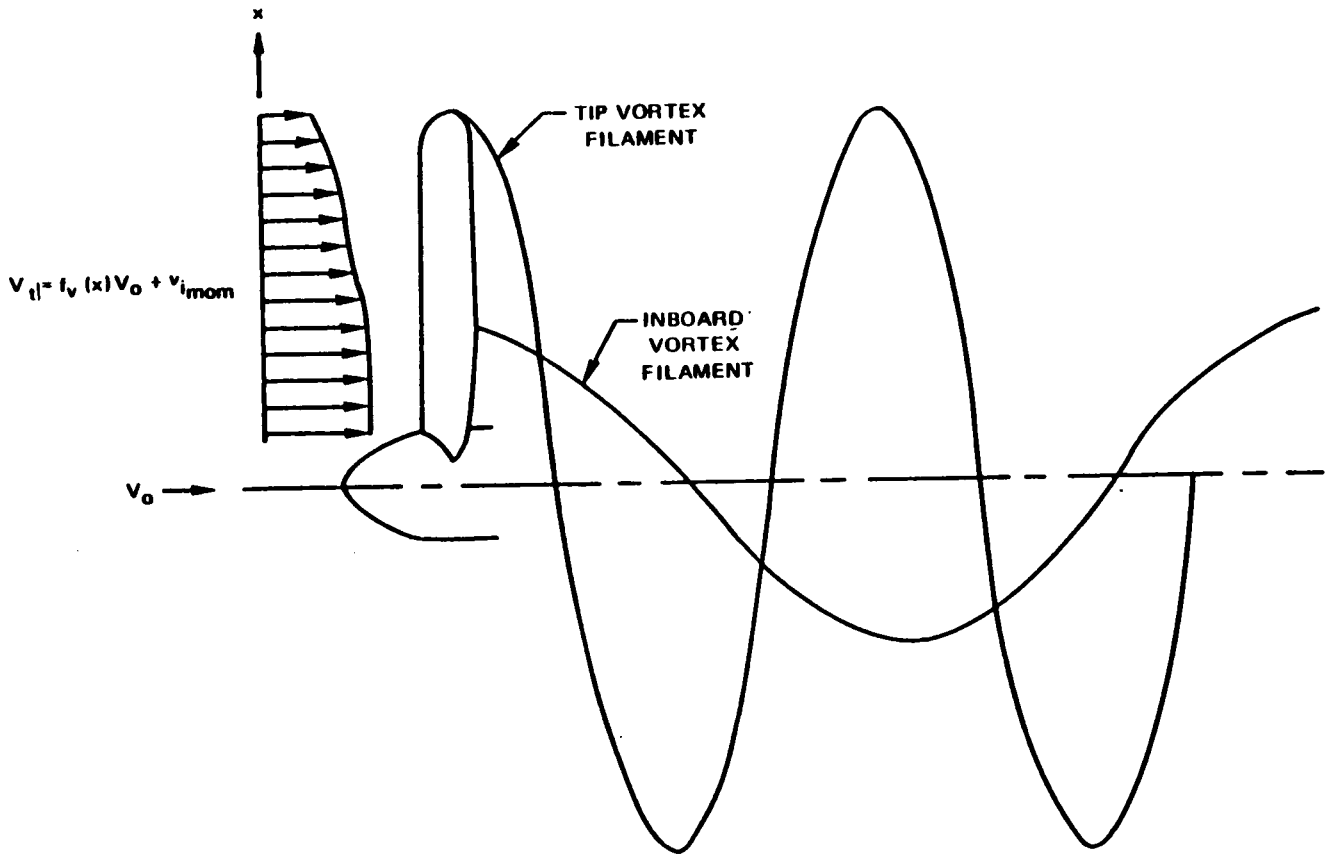

Figure 16. Modified Classical Wake Vortex Model

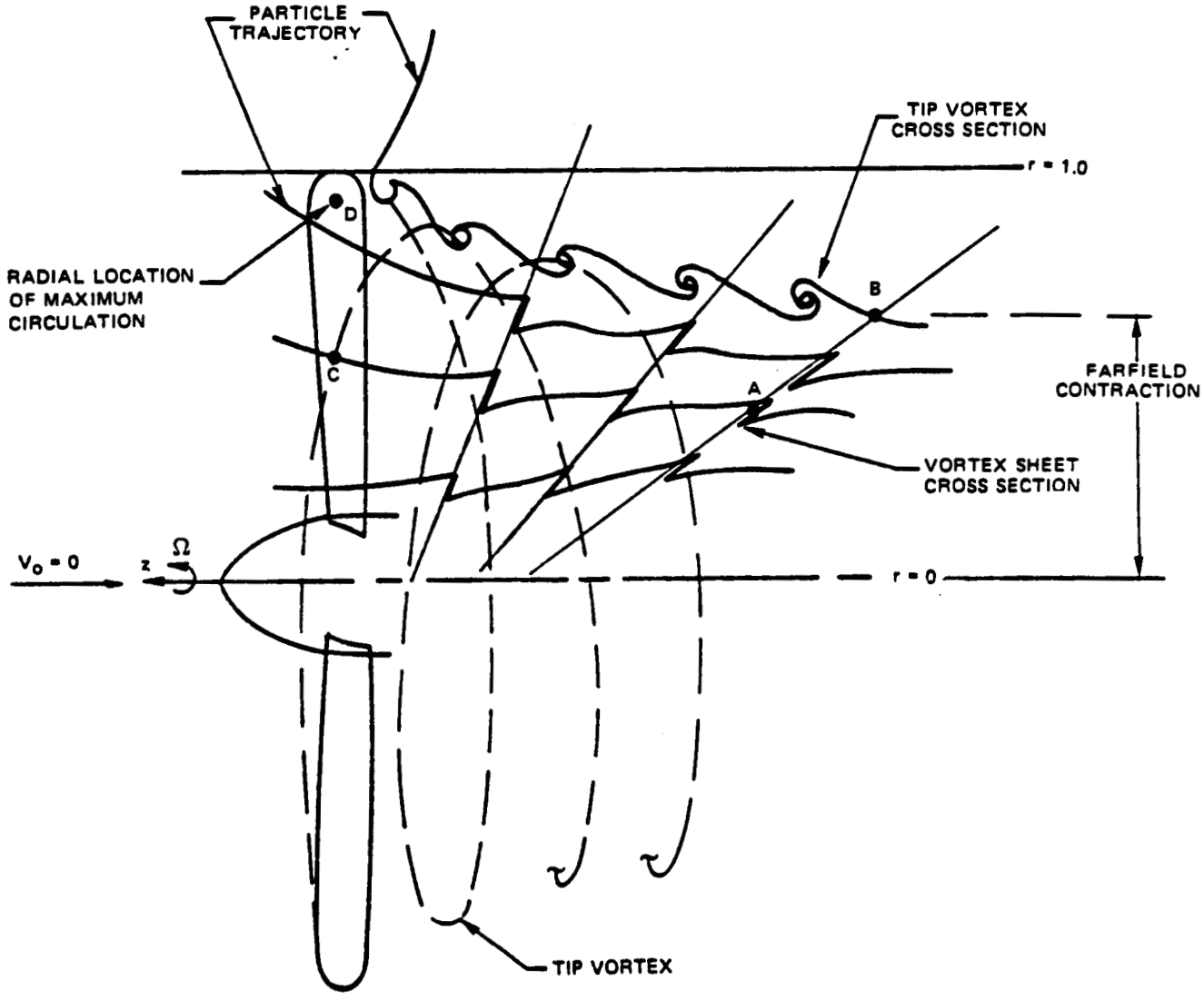

Figure 17. Characteristics of the Generalized Wake Model

85-4-90-59

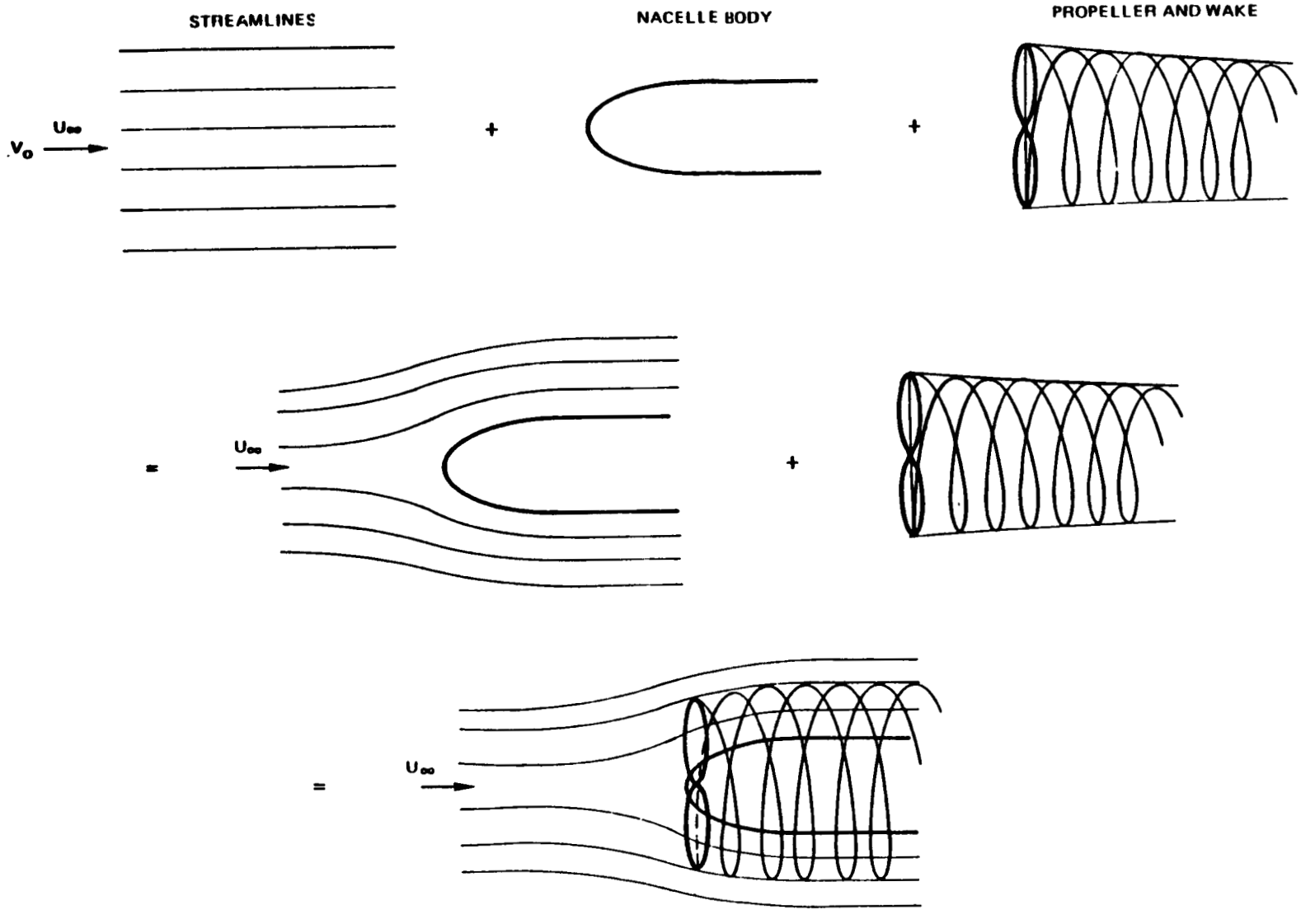

Figure 18. Construction of Propeller Wake with Nacelle Influences by Superposition

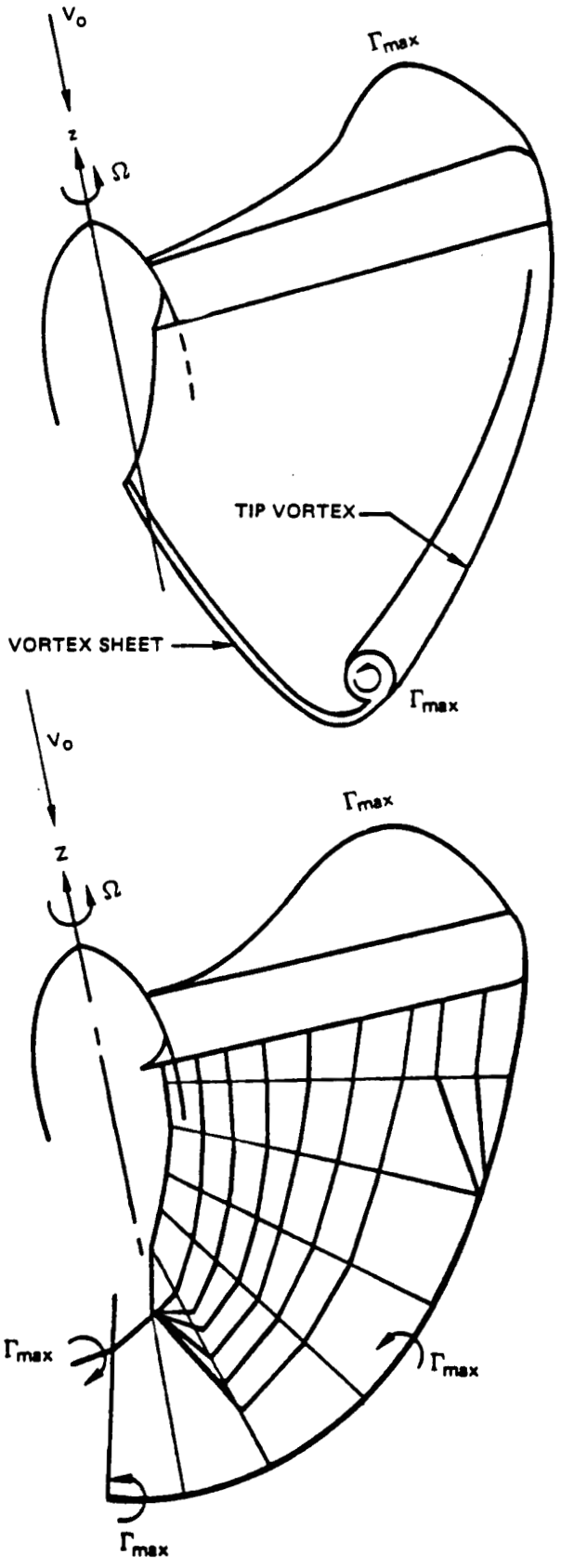

Figure 19. Modeling the Wake Rollup with Discrete Vortices

85-4-90-57

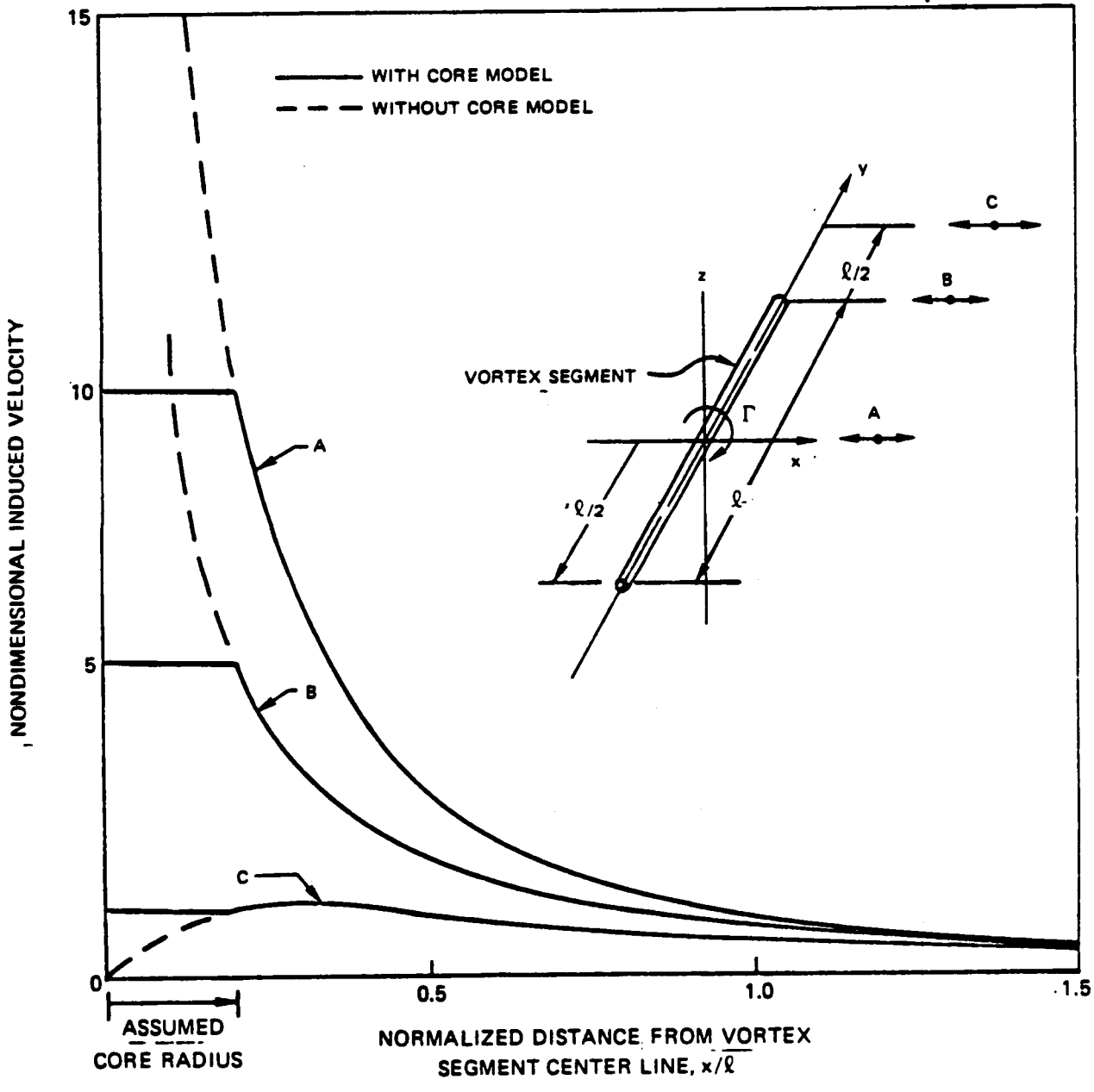

Figure 20. Induced Velocity Variations for Vortex Segment with Finite Core

85-4-90-56

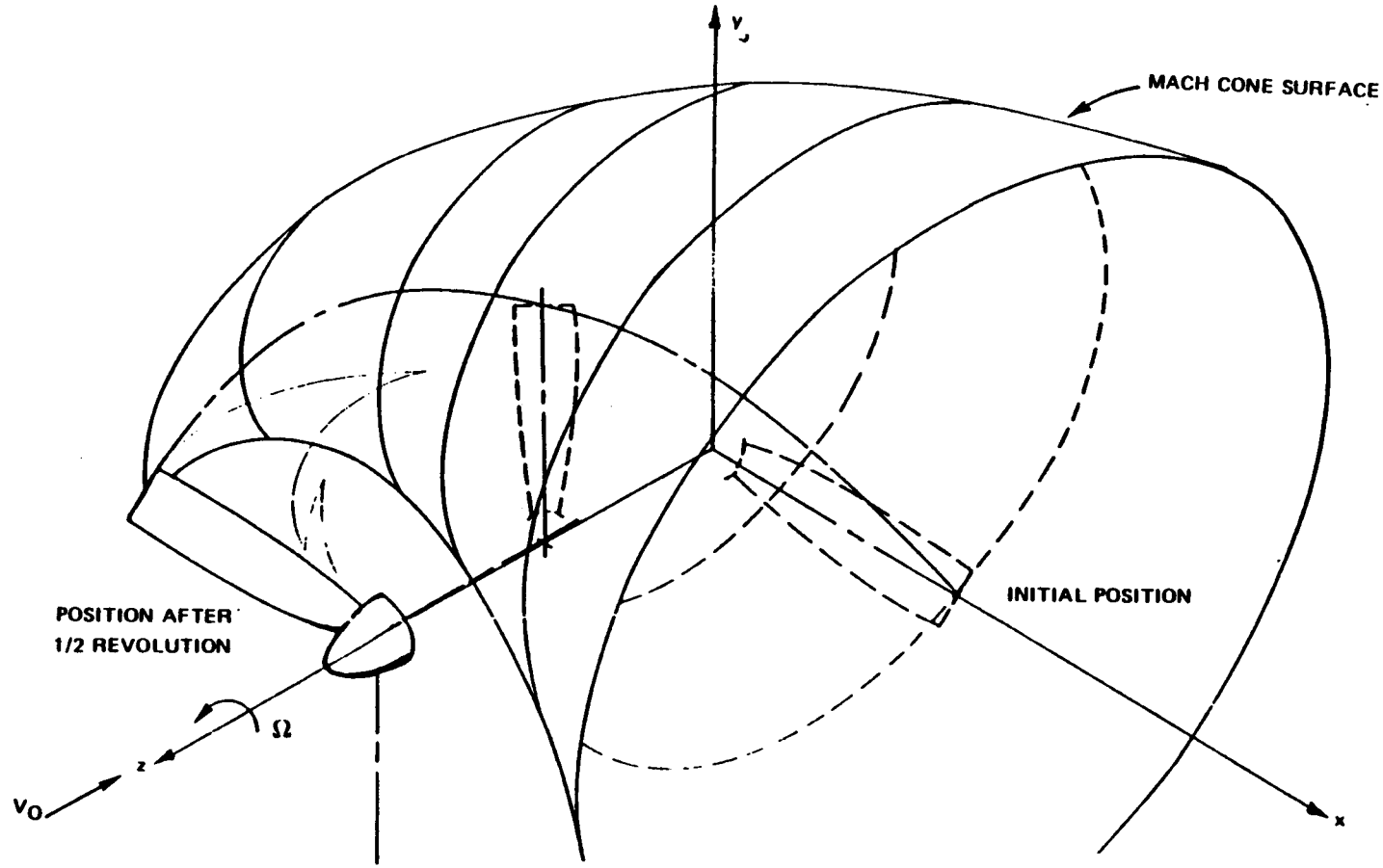

Figure 21. Mach Cone Caused by Propeller Tip Operating at Mach Number Greater than 1.0

85-4-90-55

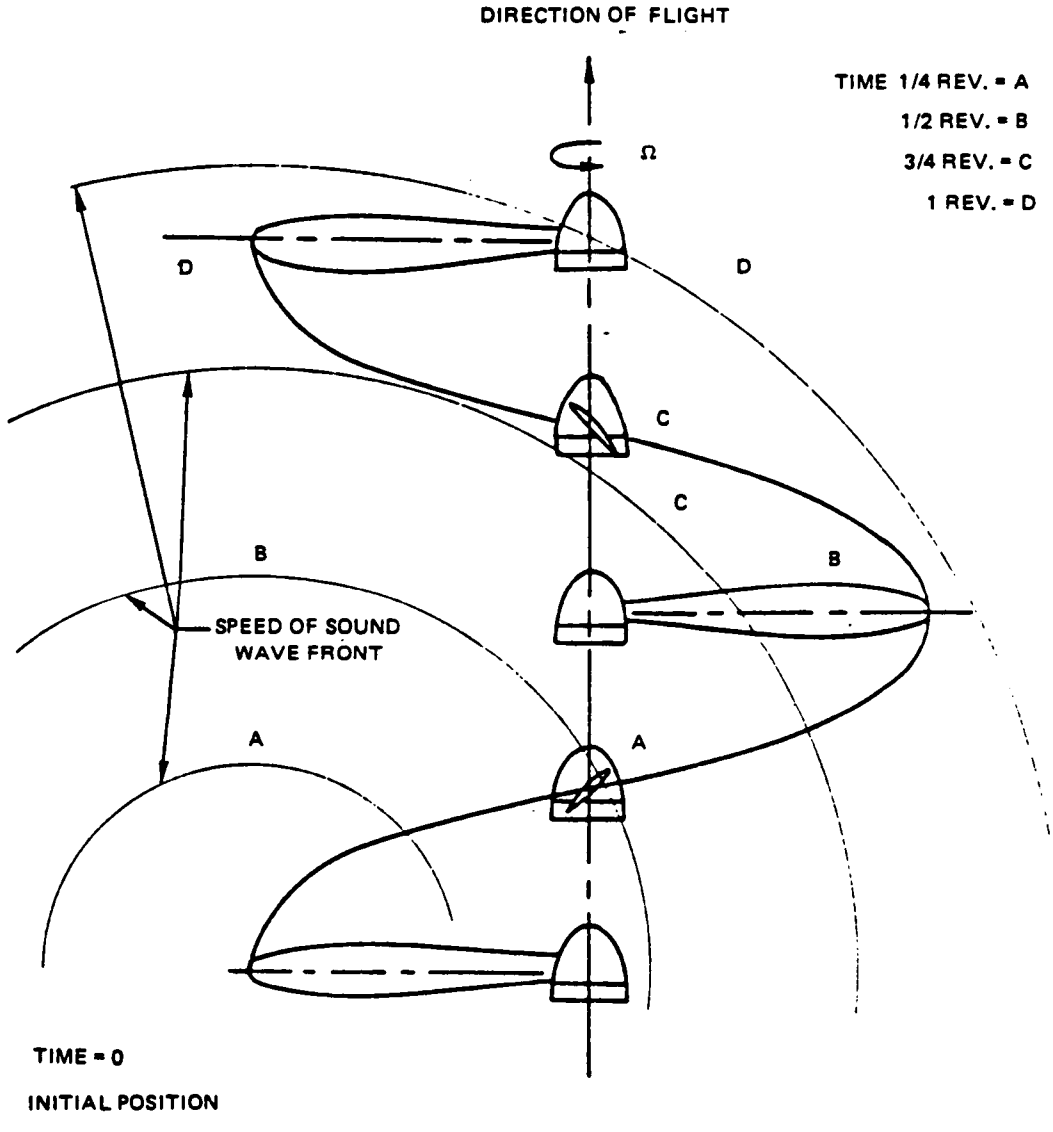

Figure 22. Propeller Vortex Lines and Relative Positions

85-4-90-54

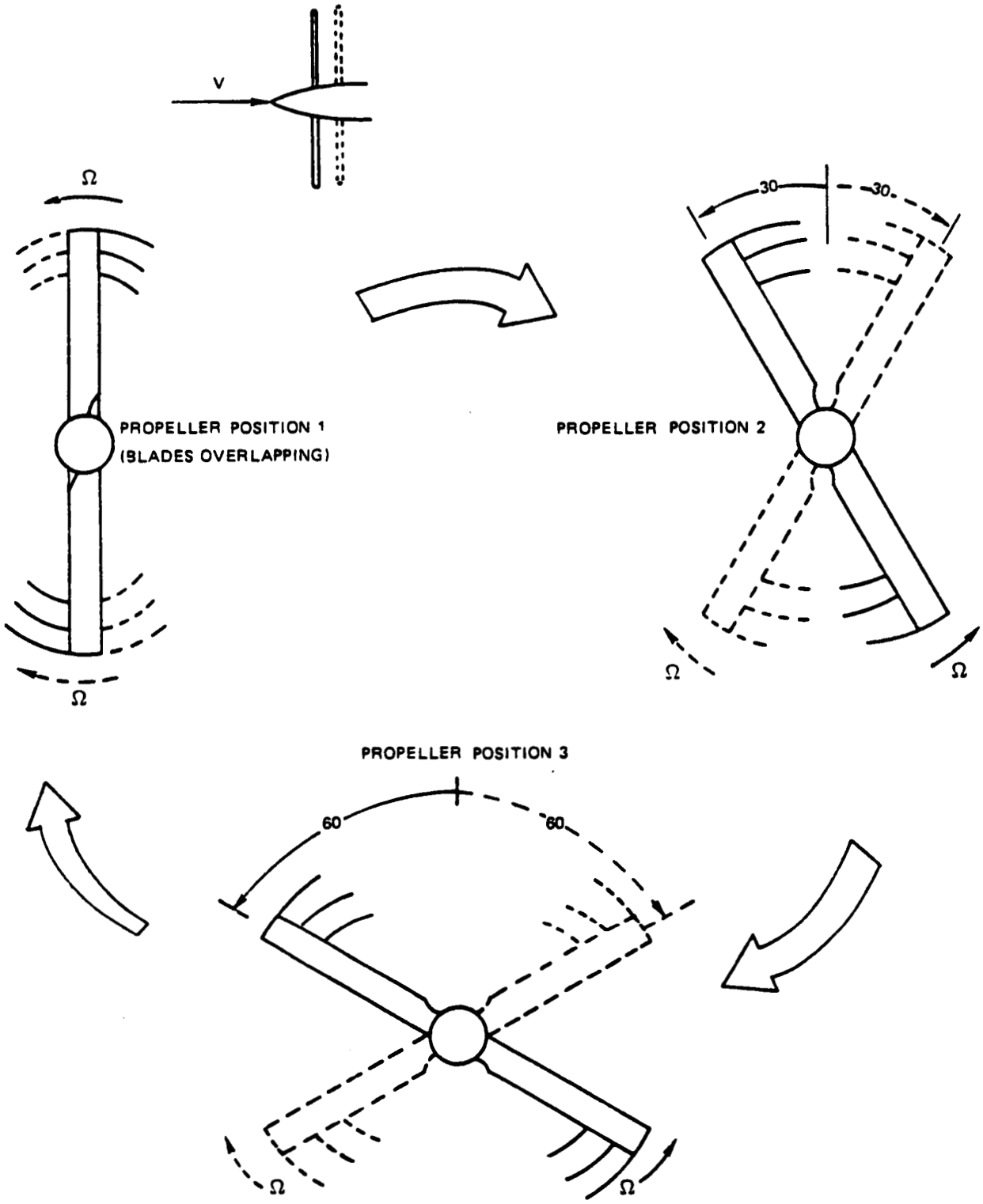

Figure 23. Relative Blade and Wake Geometry for a Two Bladed Propeller for a Azimuth Increment Variation of 30 Degrees

85-4-90-53

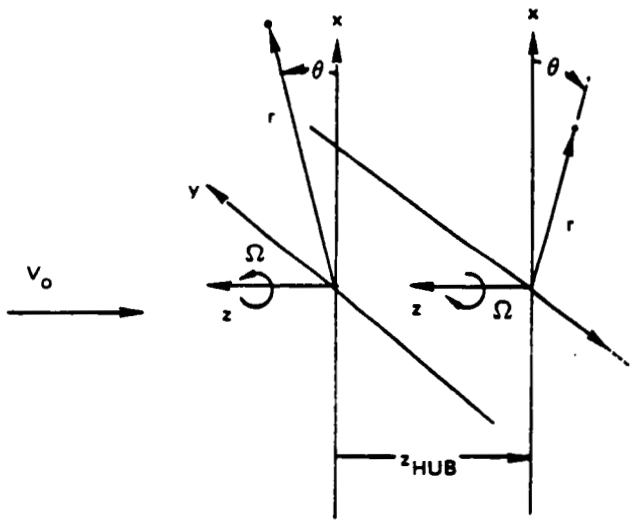

Figure 24. Cylindrical and Cartesian Coordinate Systems for Coaxial Counter Rotating Propeller Configurations

85-4-90-52

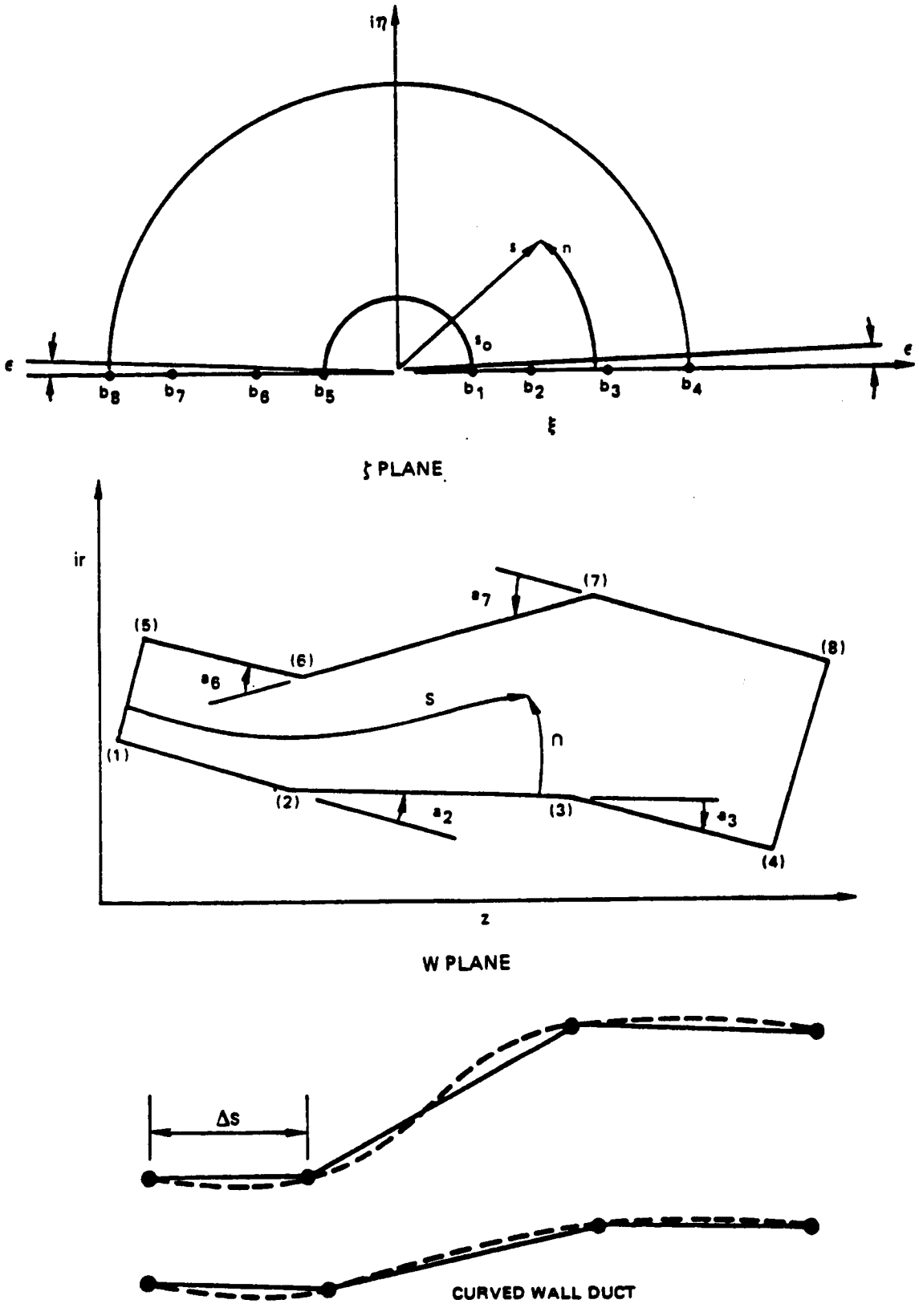

Figure 25. Conformal Mapping of Duct

85-4-90-51

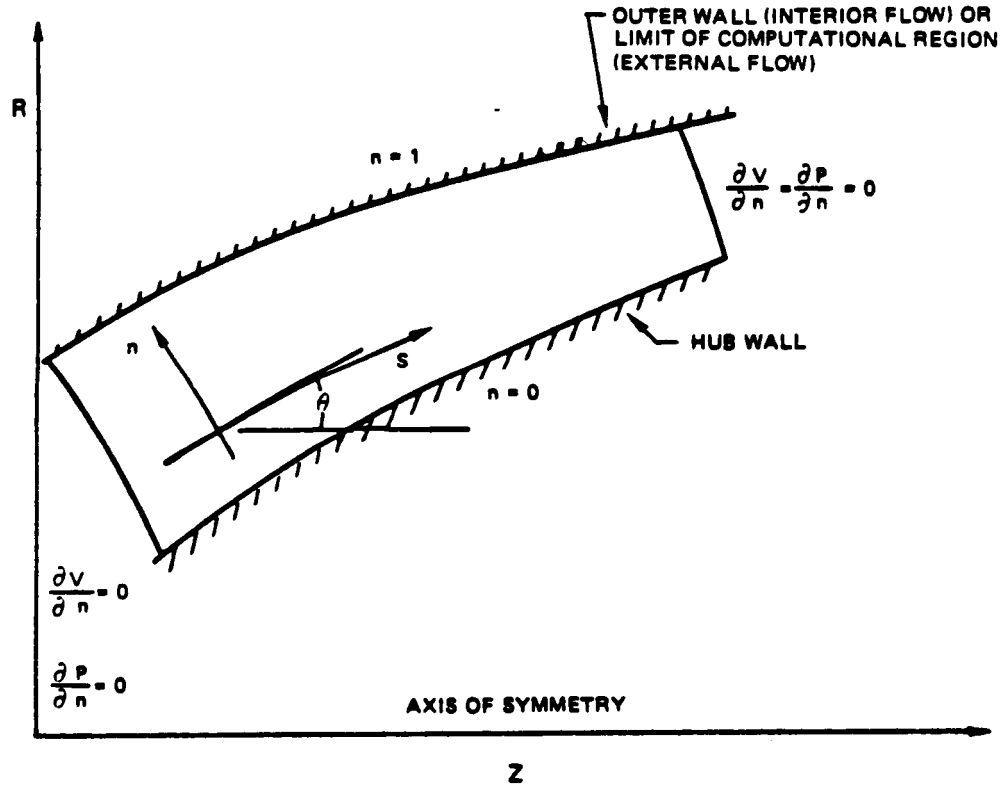

Figure 26. Orthogonal Streamline Coordinate System

85-4-90-49

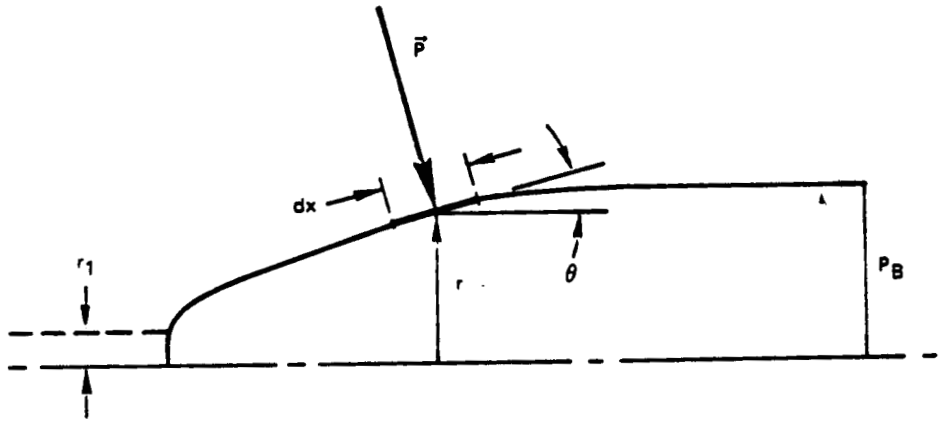

PRESSURE DRAG

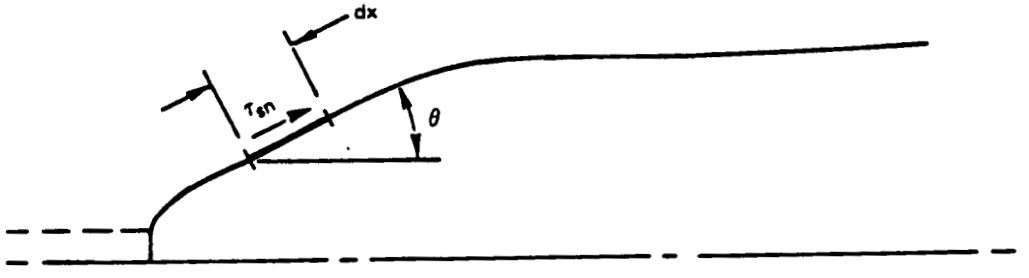

FRICTION DRAG

Figure 27. Nacelle Drag Forces

85-4-90-50

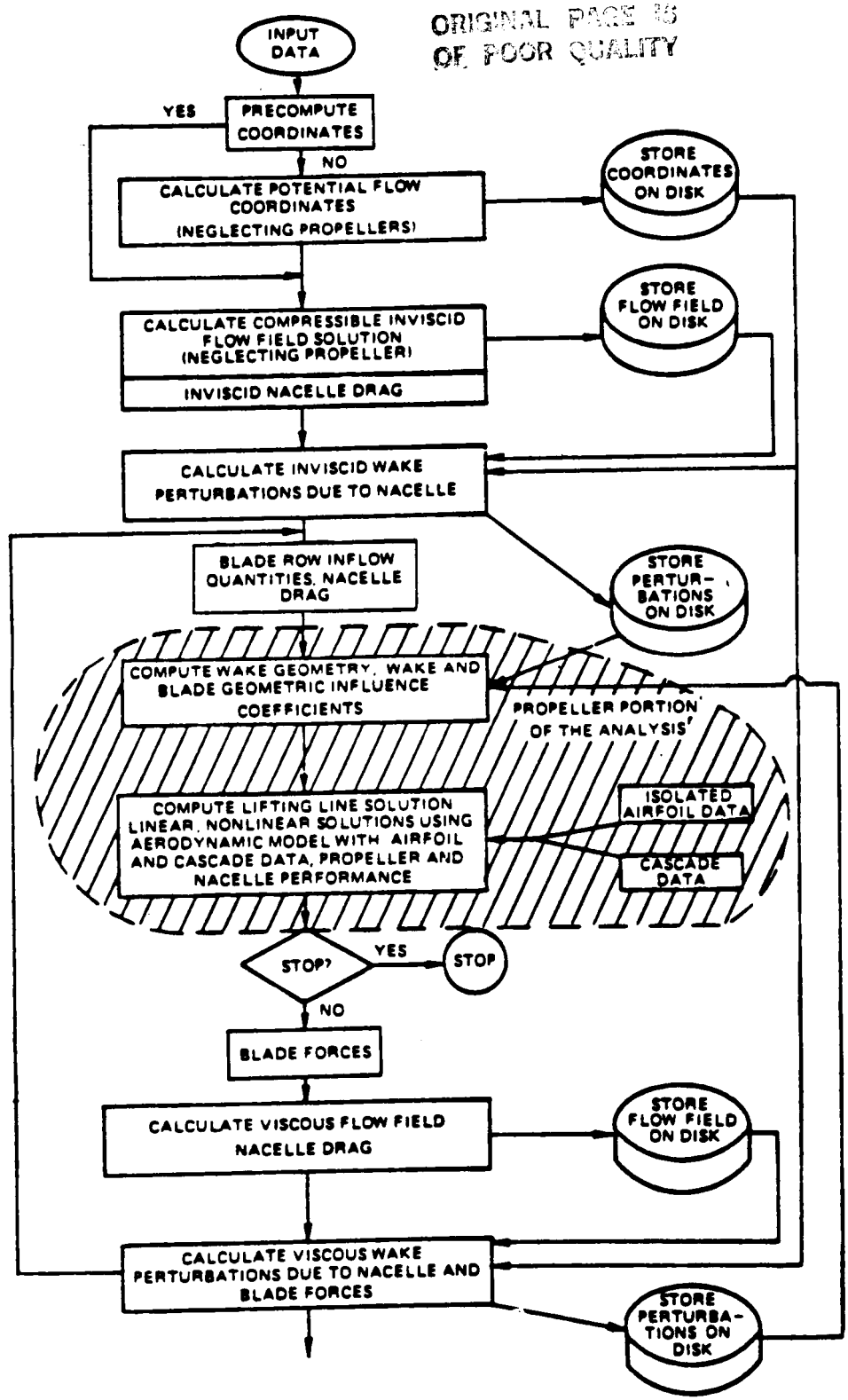

Figure 28. Flow Diagram of the Combined Propeller-Nacelle Analysis

85-4-90-48

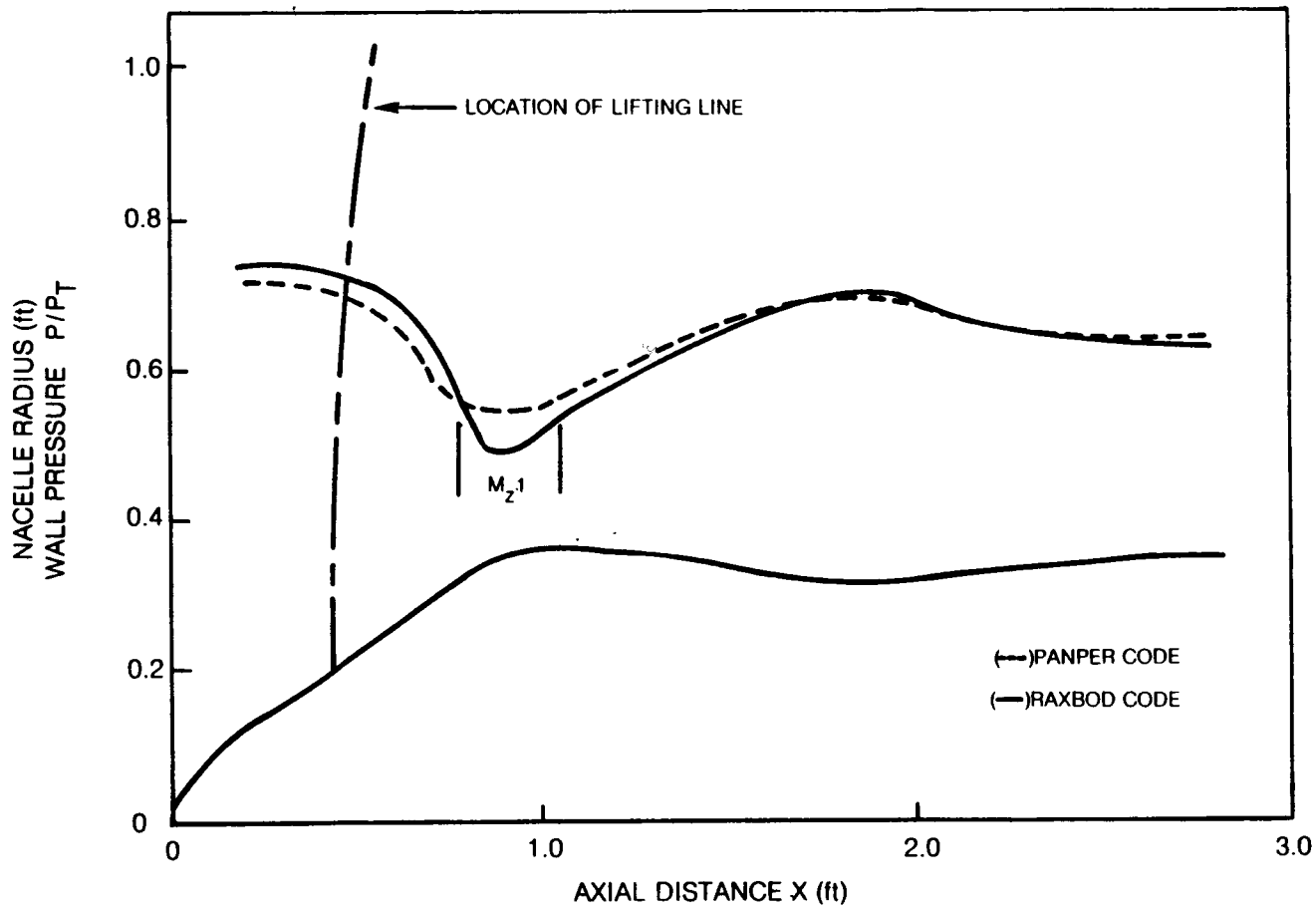

Figure 29 Comparison of Predicted Wall Pressure Distributions For SR-1 Nacelle at M_∞=0.80

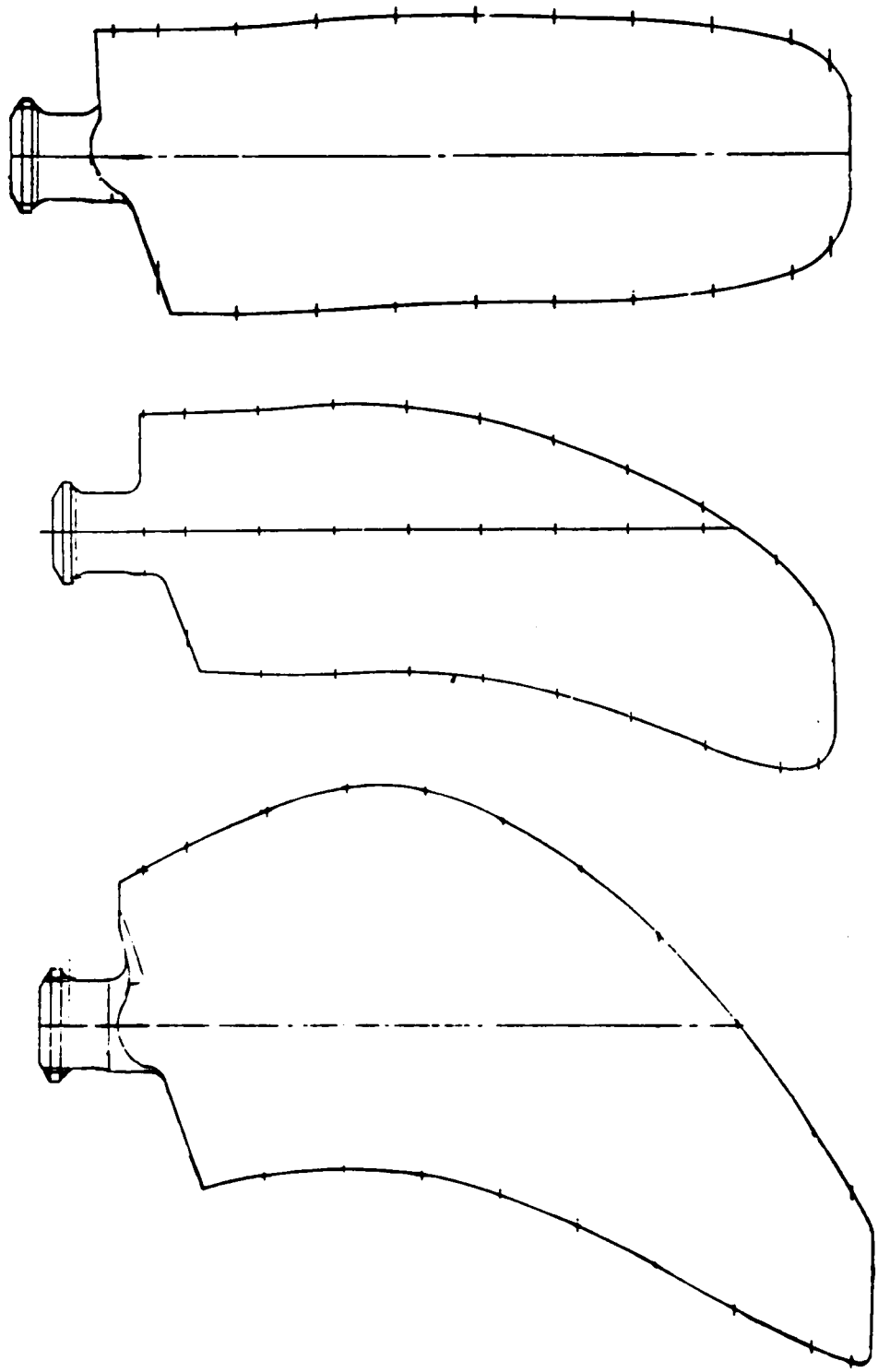

Figure 30. Prop-fan Planforms

85-4-90-78

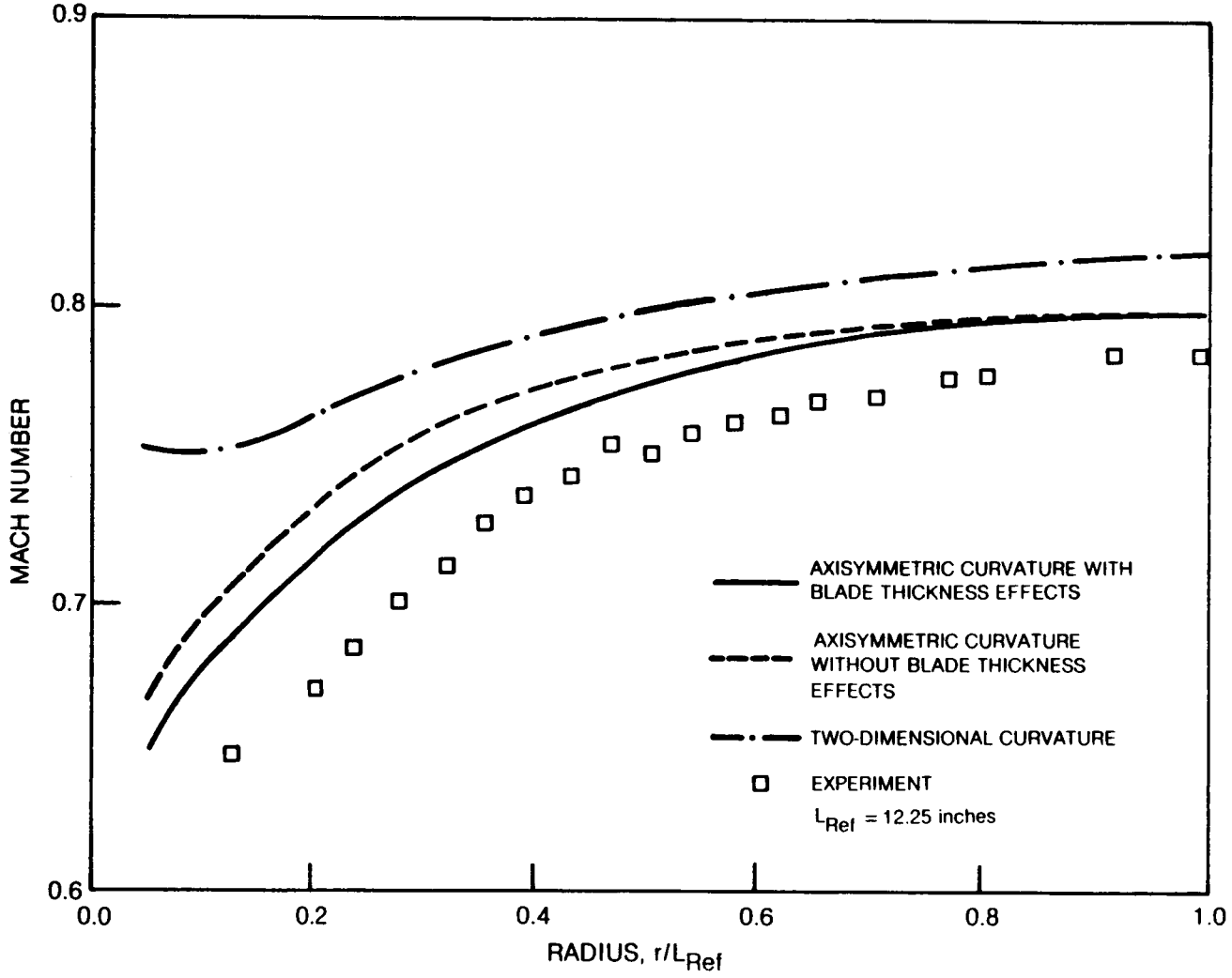

Figure 31 Comparison of Computed Inviscid Mach Number Profile at $Z/L_{Ref}=0.09$ for the SR-3 Nacelle Propeller Configuration at $M_\infty=0.8$ With Test Data.

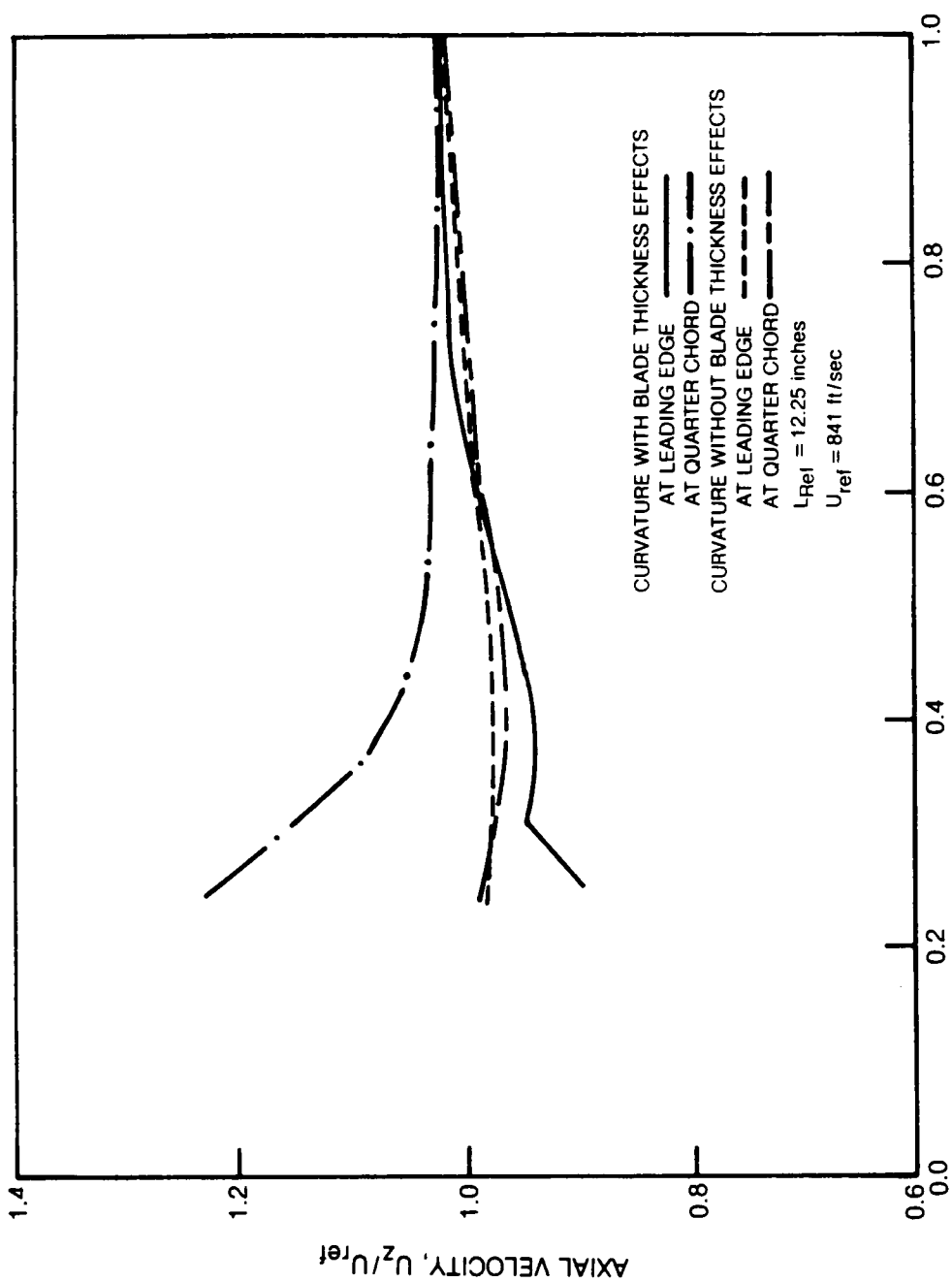

Figure 32. Computed Inviscid Axial Velocity at the Blade Leading Edge and Quarter Chord of the SR-3 Propeller at $M_\infty = 0.8$

84-6-73-4

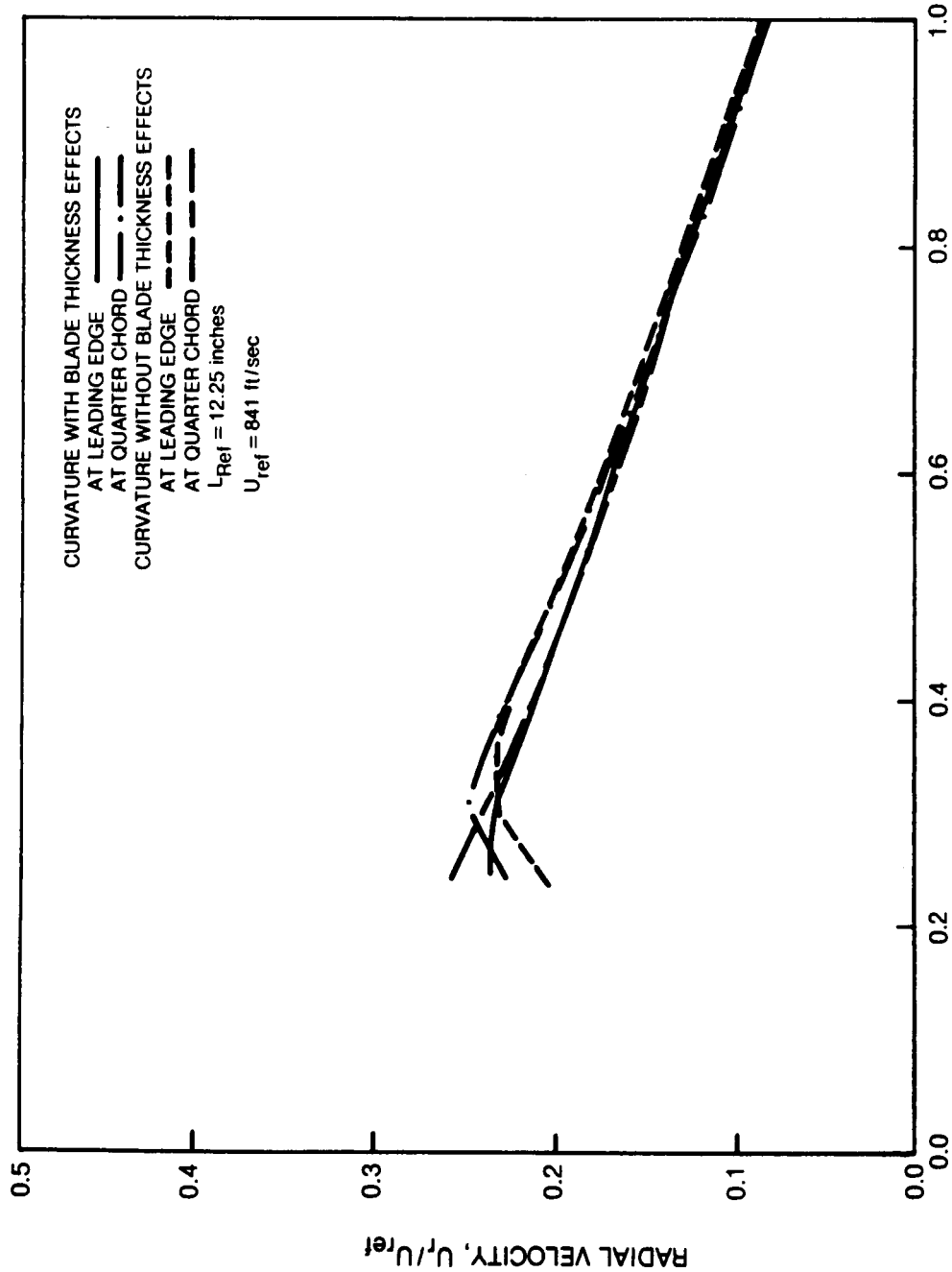

Figure 33. Computed Inviscid Radial Velocity at the Blade Leading Edge and Quarter Chord of the SR-3 Propeller at M_∞=0.8

84-6-73-3

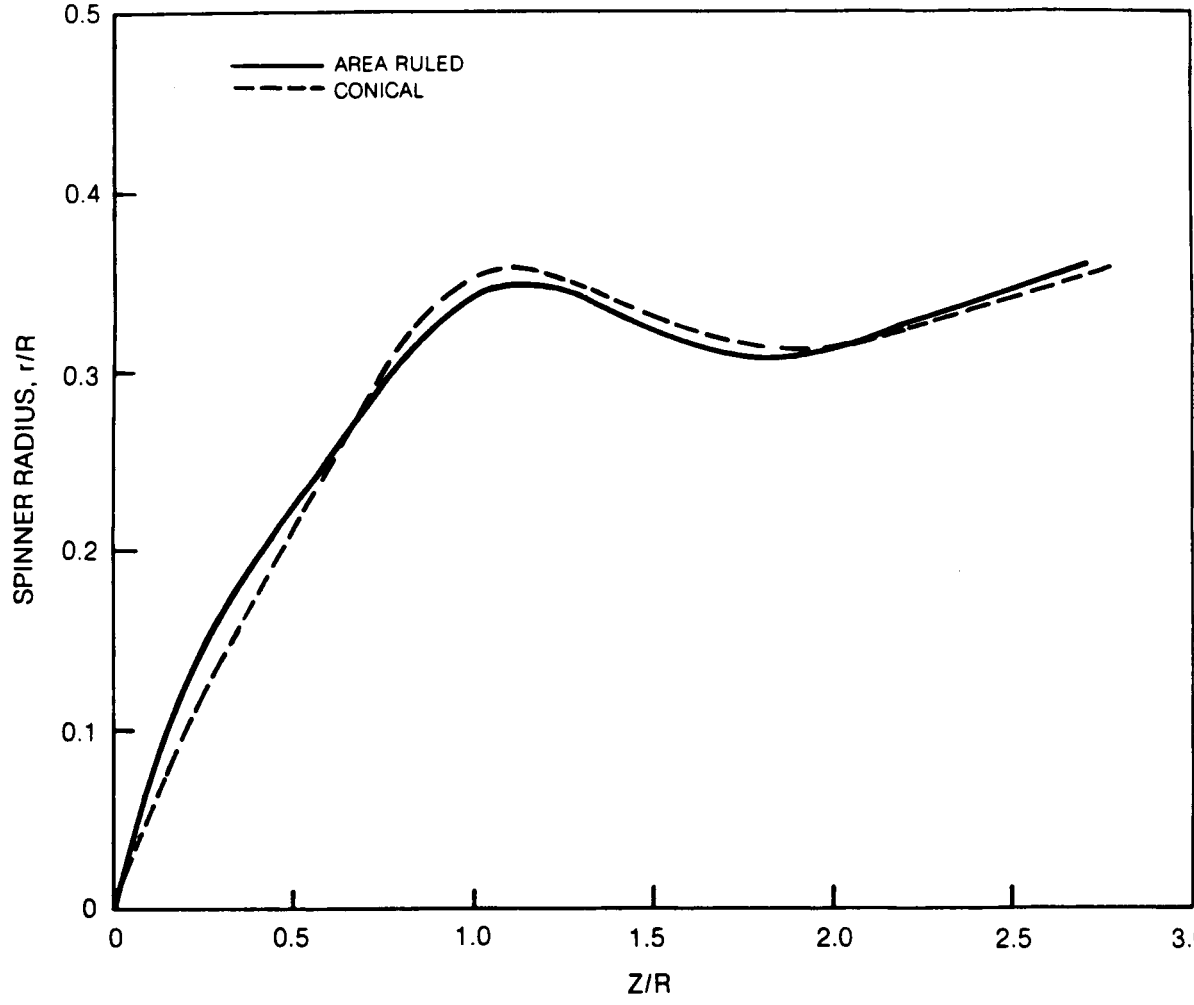

Figure 34. Comparison of Spinner Profiles

85-4-90-75

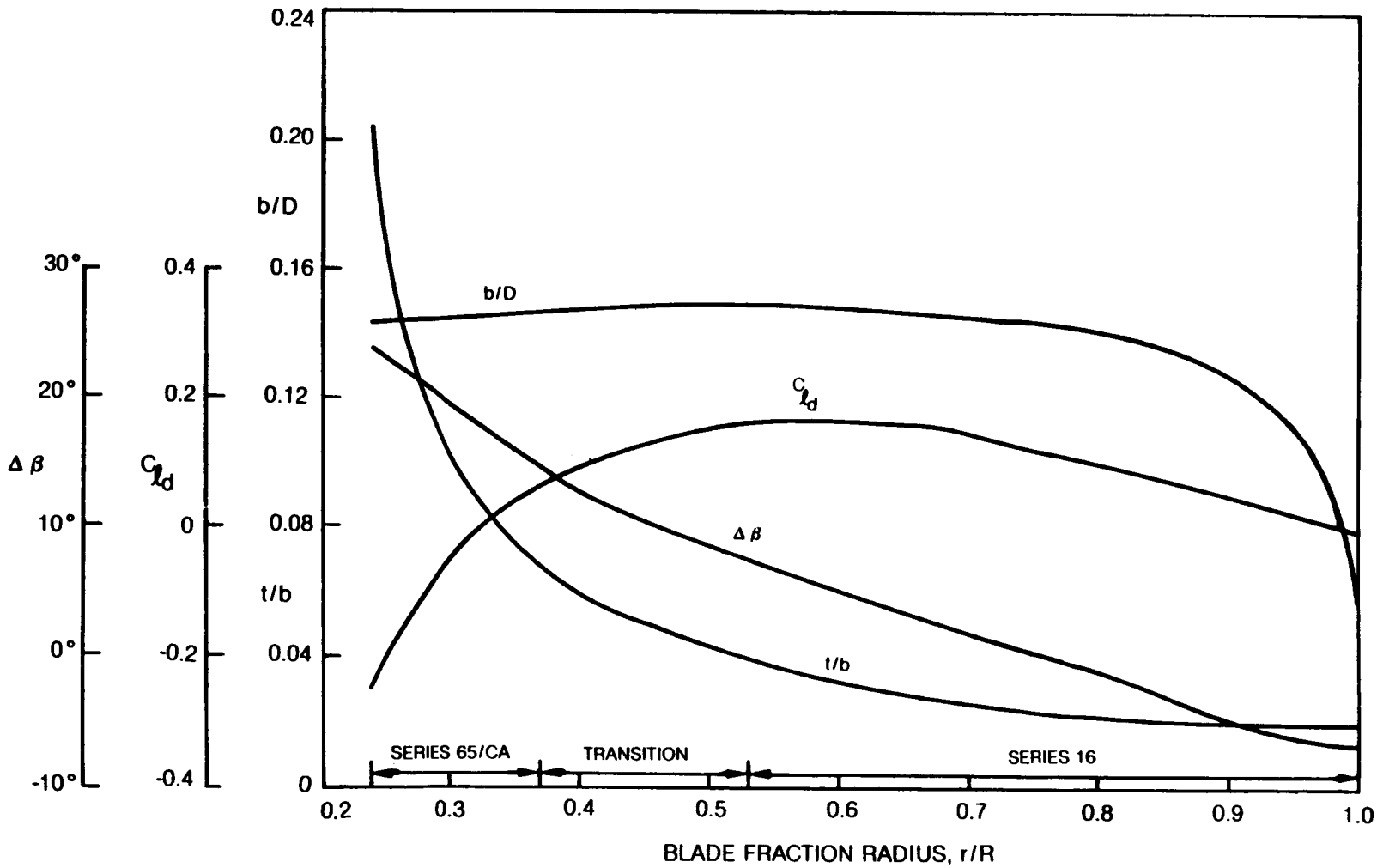

Figure 35 Blade Characteristics for SR-2 Propeller Design

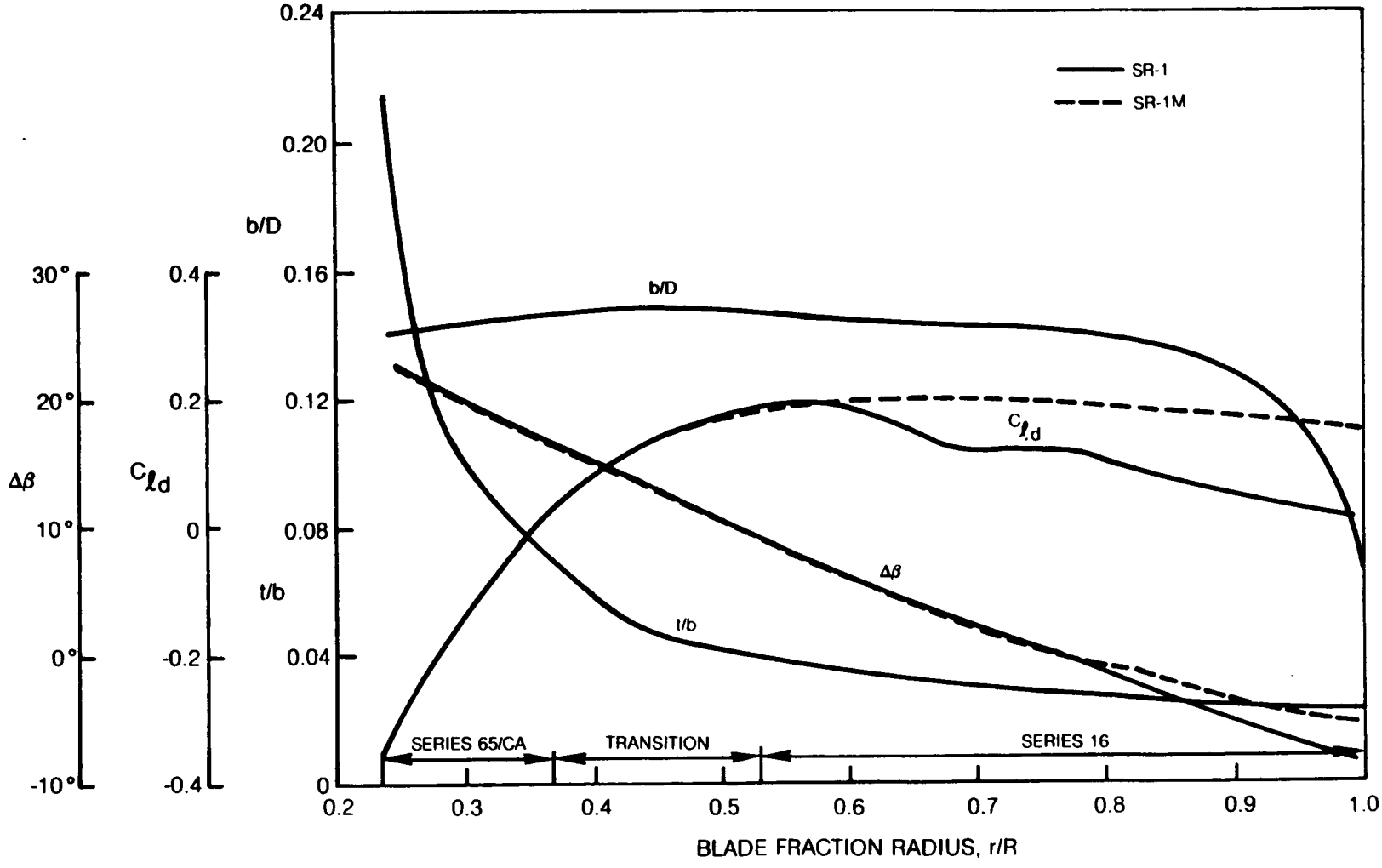

Figure 36. Blade Characteristics for SR-1 and SR-1M Propeller Designs

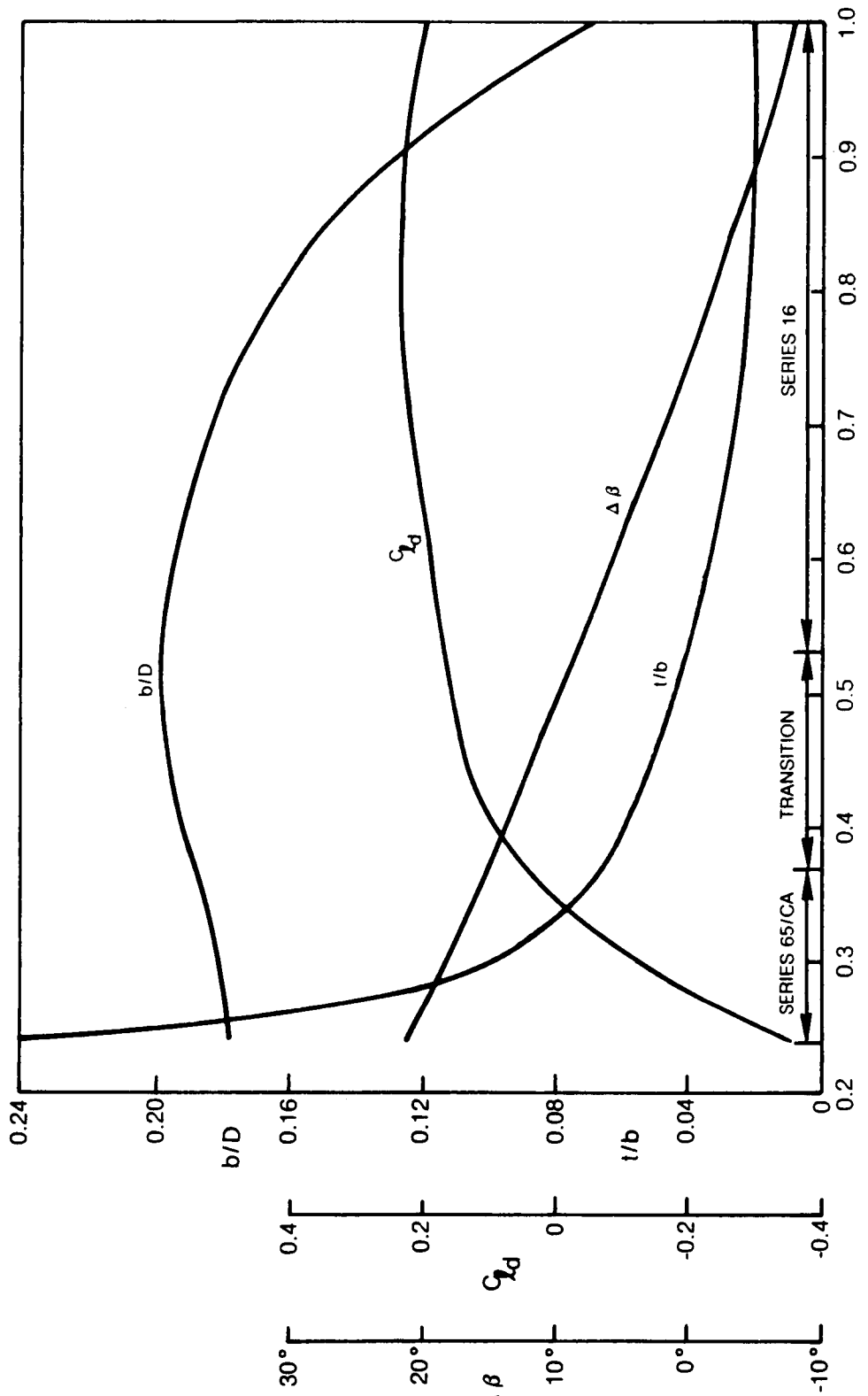

Figure 37 Blade Characteristics for SR-3 Propeller Design

84-6-73-7

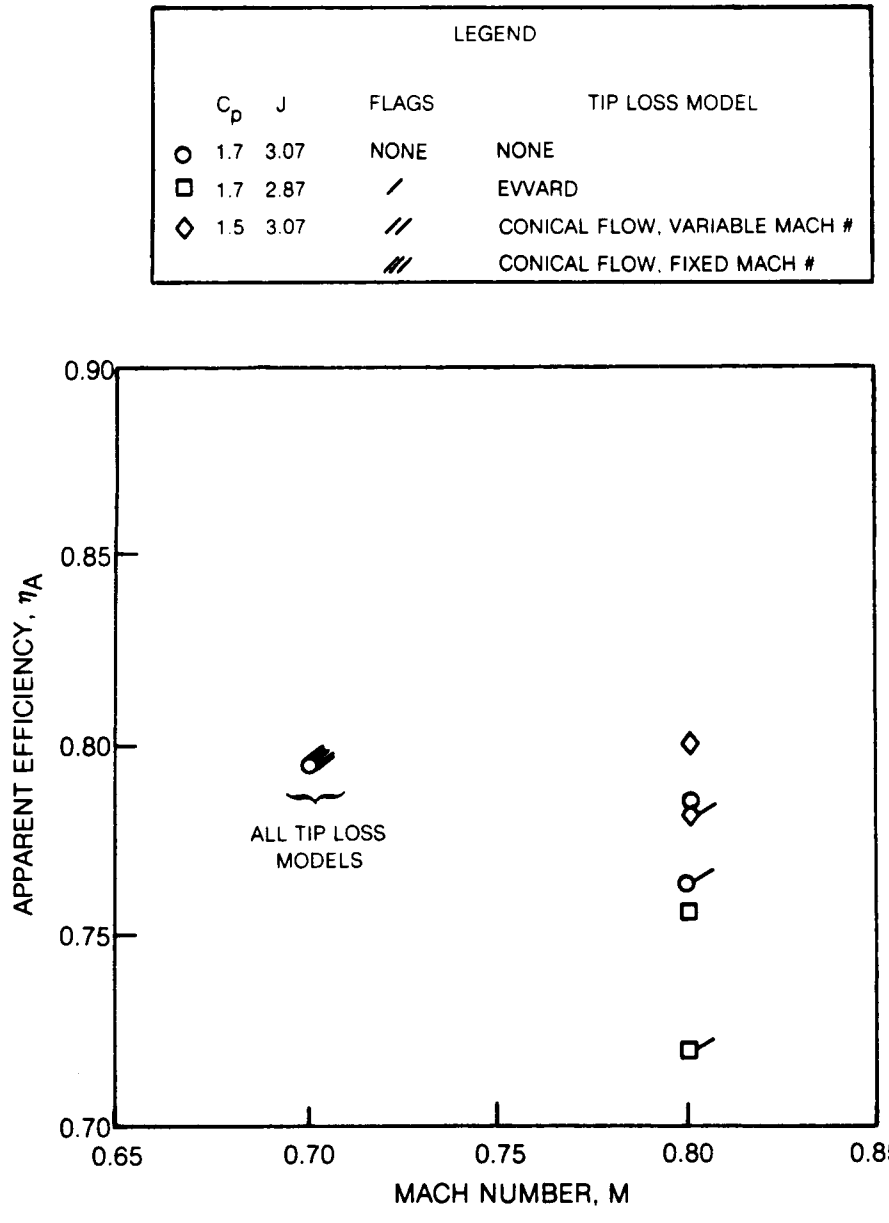

Figure 38 Effect of Compressible Flow Tip Models on Propeller Efficiencies for the SR-2 Propeller, Area Ruled Spinner.

84-6-73-8

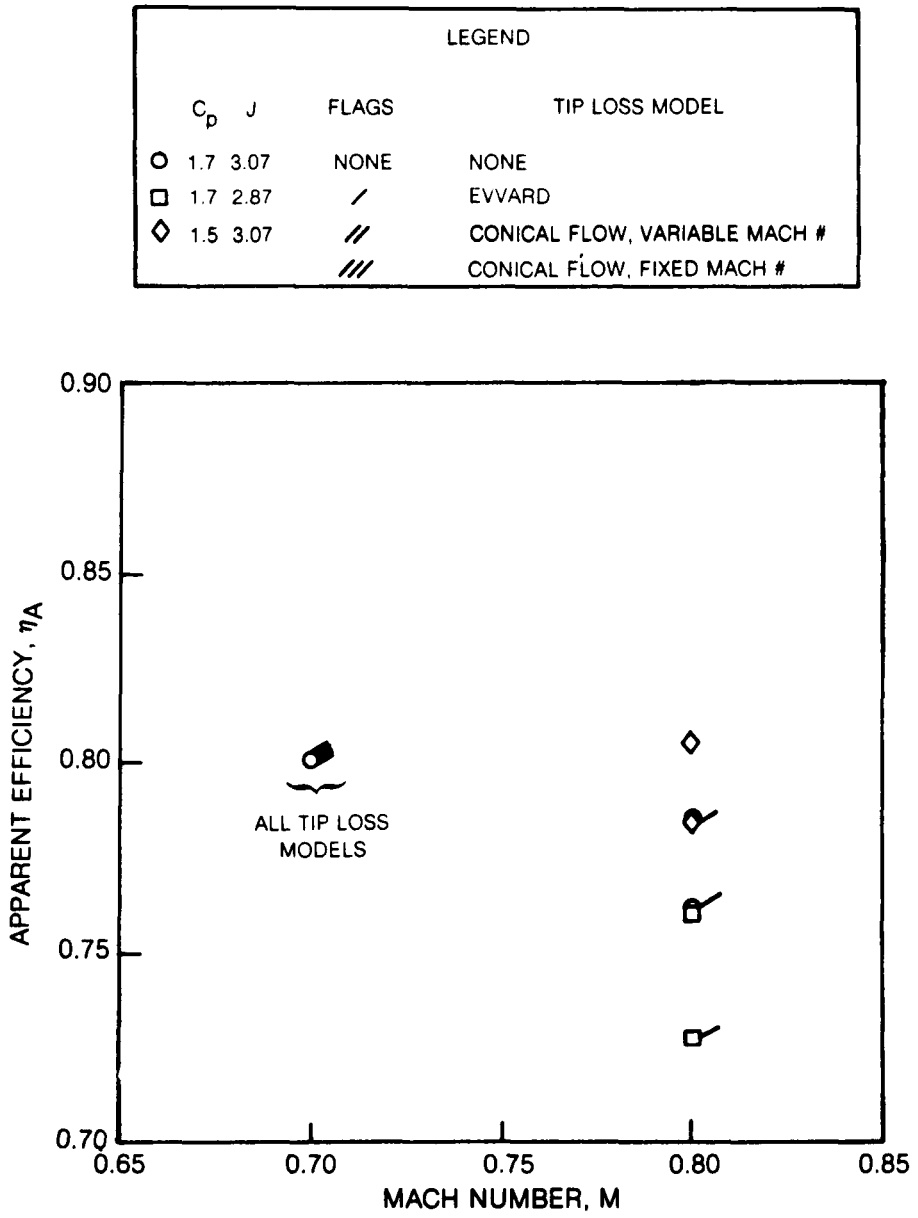

Figure 39 Effect of Compressible Flow Tip Loss Models on Propeller Efficiencies for the SR-1 Propeller, Area Ruled Spinner.

84-6-73-9

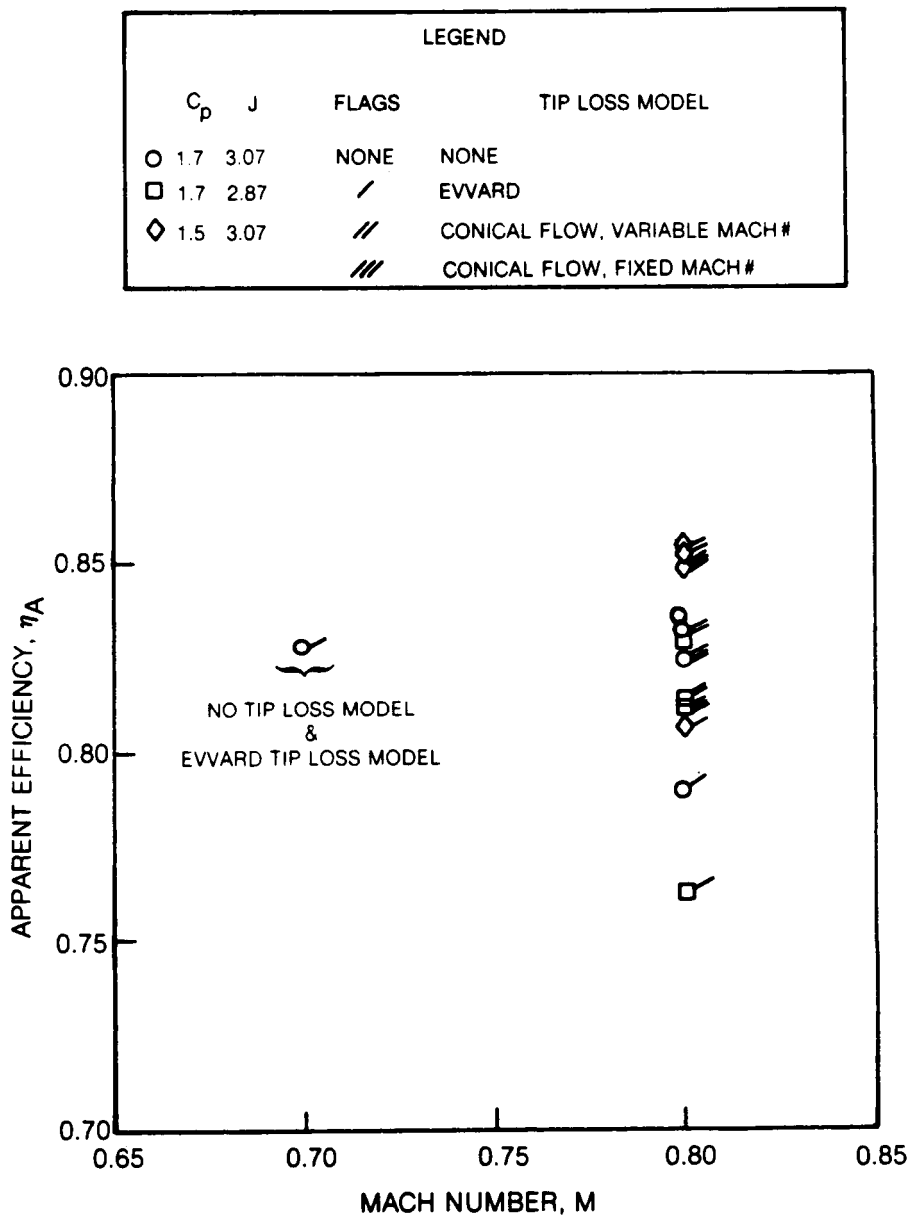

Figure 40 Effect of Compressible Flow Tip Loss Models on Propeller Efficiencies for the SR-3 Propeller, Area Ruled Spinner.

84-6-73-1

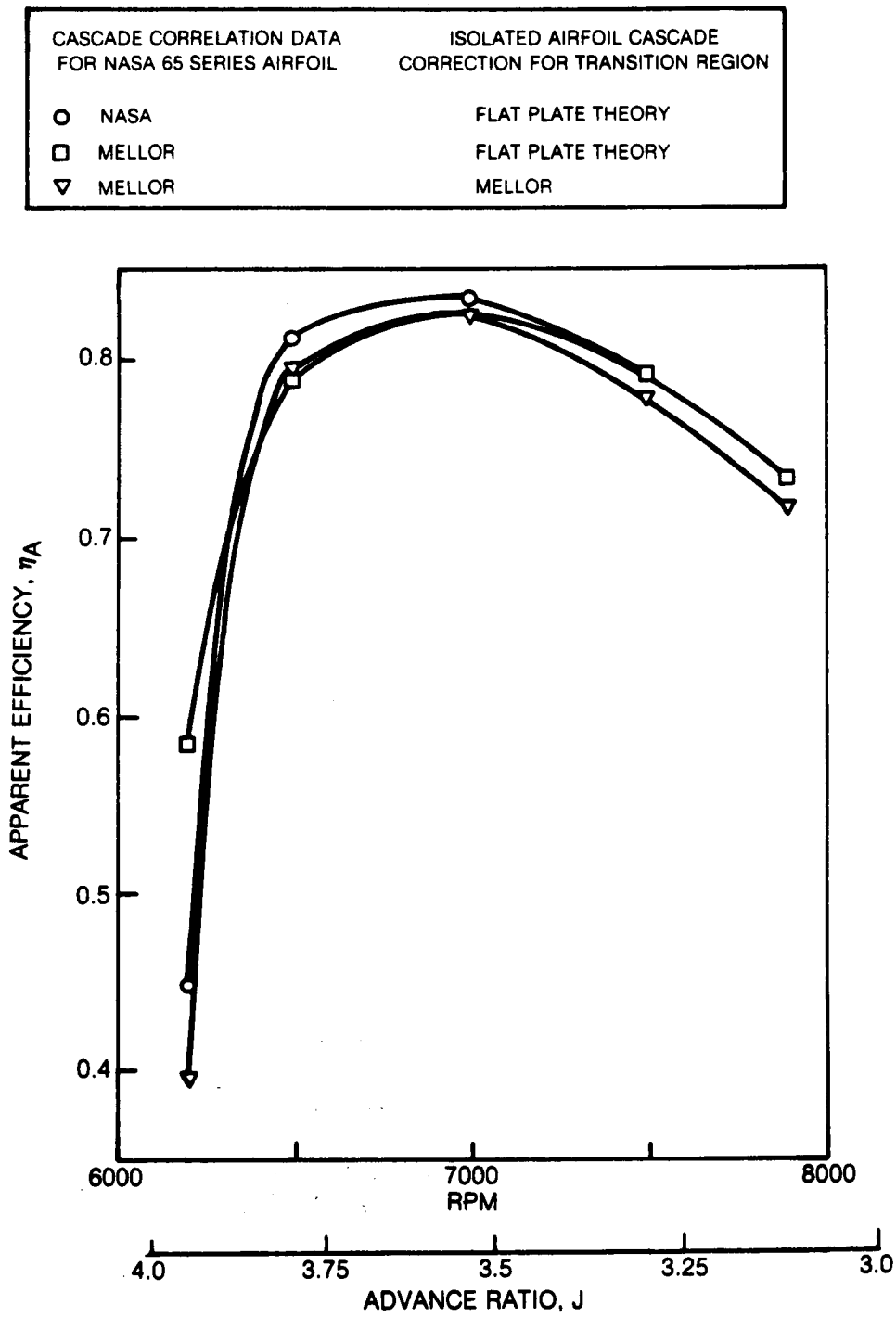

Figure 41. Effect of Cascade Data Correlation Models on SR-1 Propeller Efficiency, Fixed Blade Angle (60.2°), 0.8 Mach Number

84-6-73-11

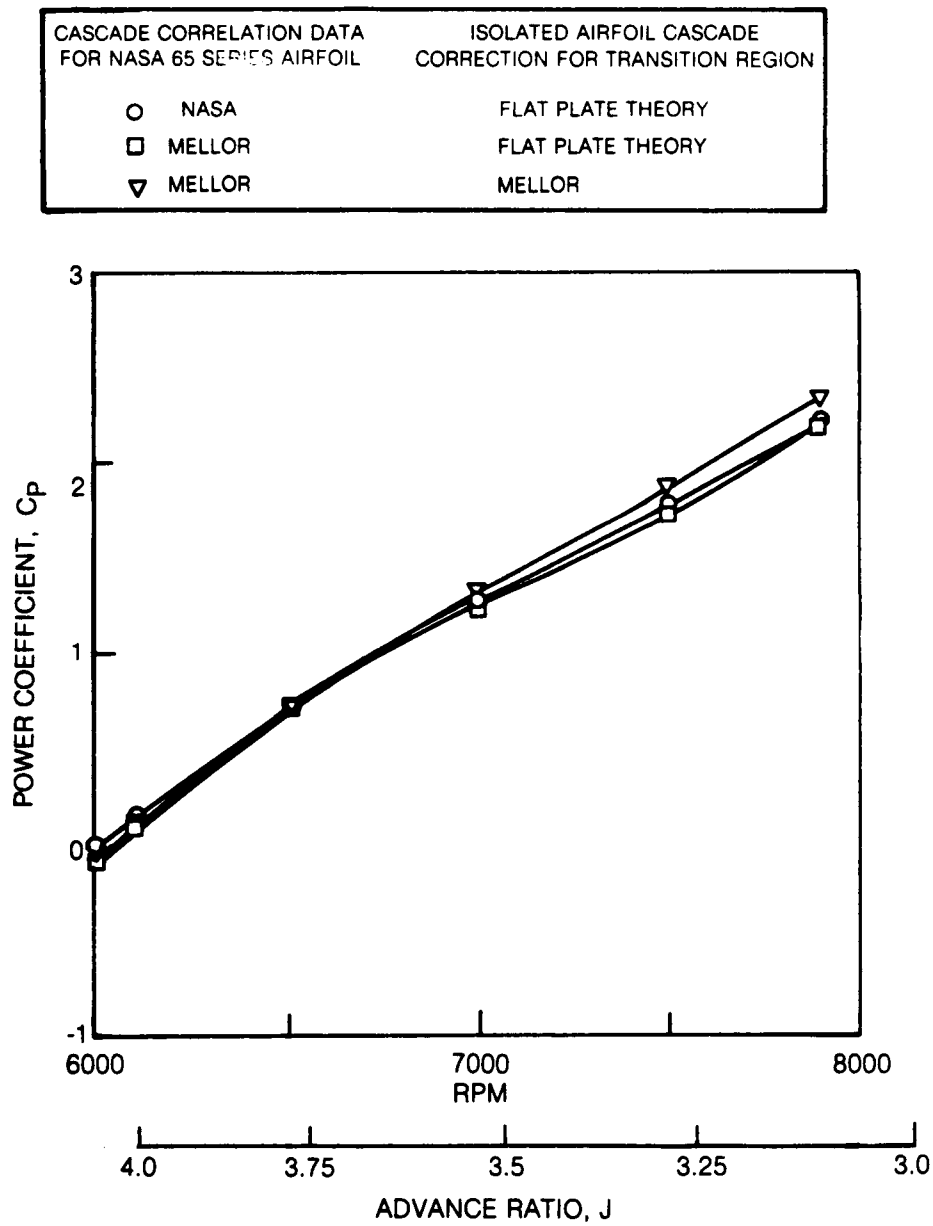

Figure 42 Effect of Cascade Data Correlation Models on SR-1 Propeller Power Coefficient, Fixed Blade Angle (60.2°),0.8 Mach Number

84-6-73-12

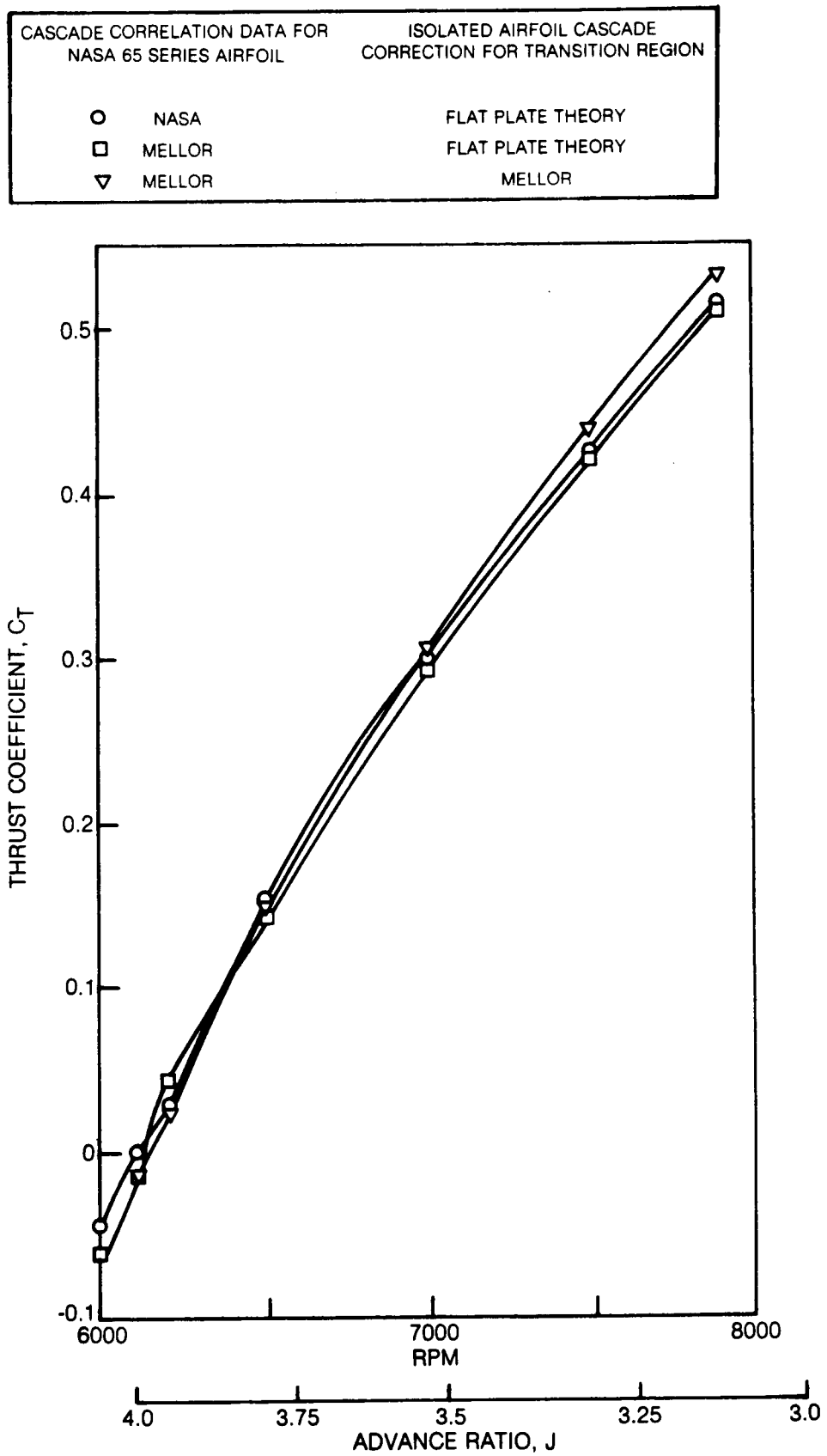

Figure 43 Effect of Cascade Data Correlation Models on SR-1 Propeller Thrust Coefficient, Fixed Blade Angle (60.2°),0.8 Mach Number

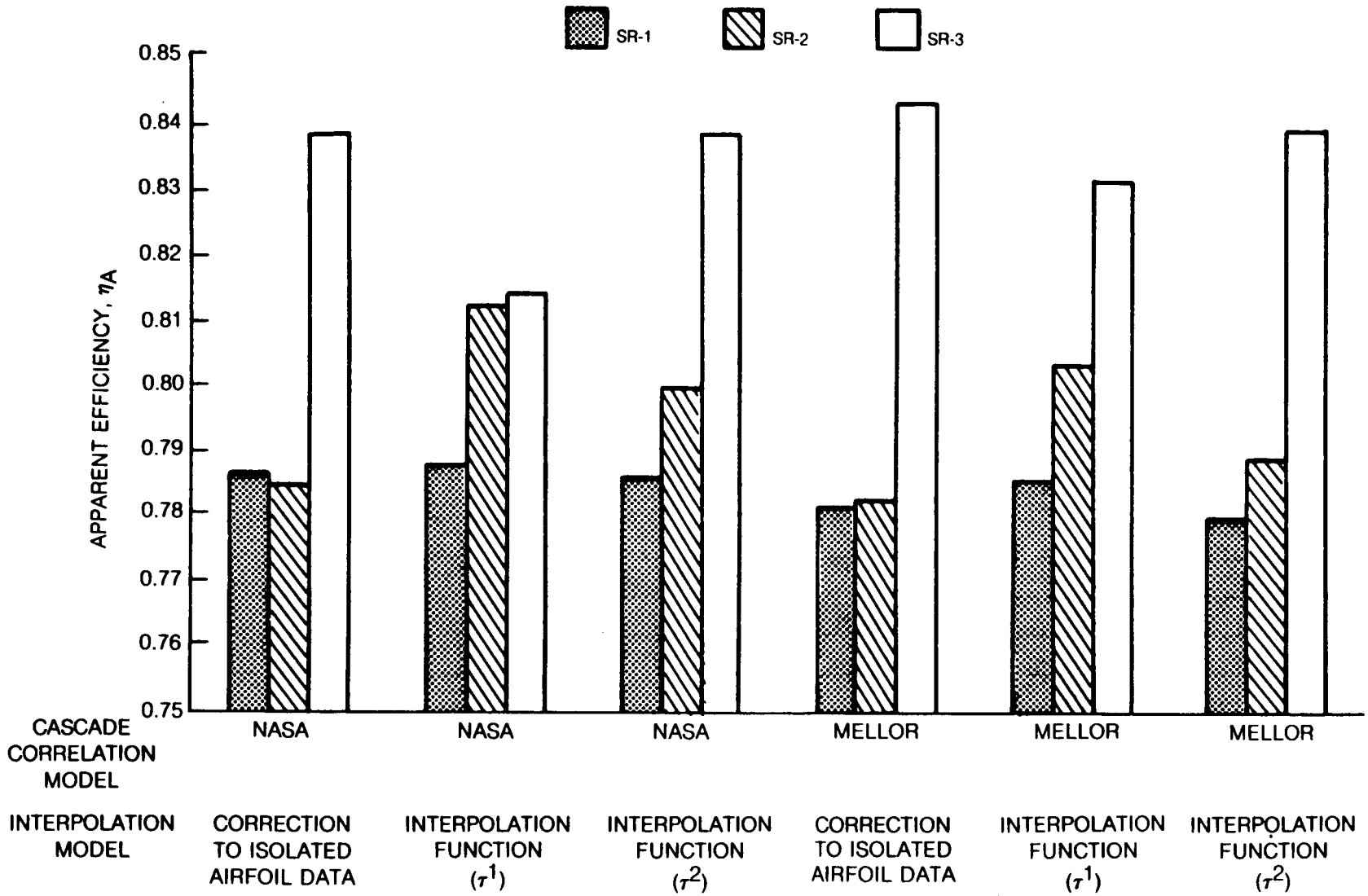

Figure 44 Comparison of Transition Interpolation Models Using the NASA and Mellor Cascade Correlations at Design Point.

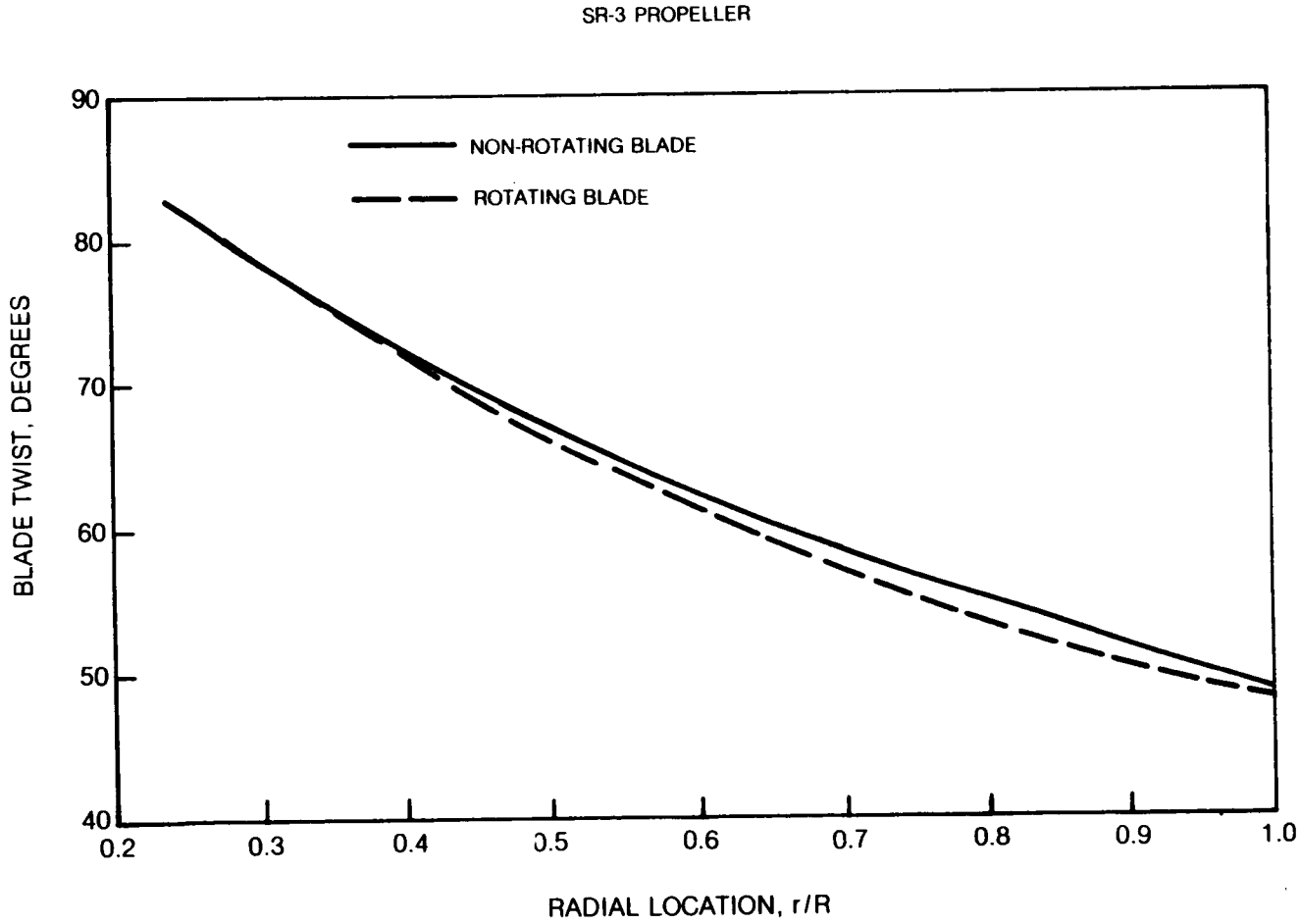

Figure 45 Centrifugal Effect on Blade Twist

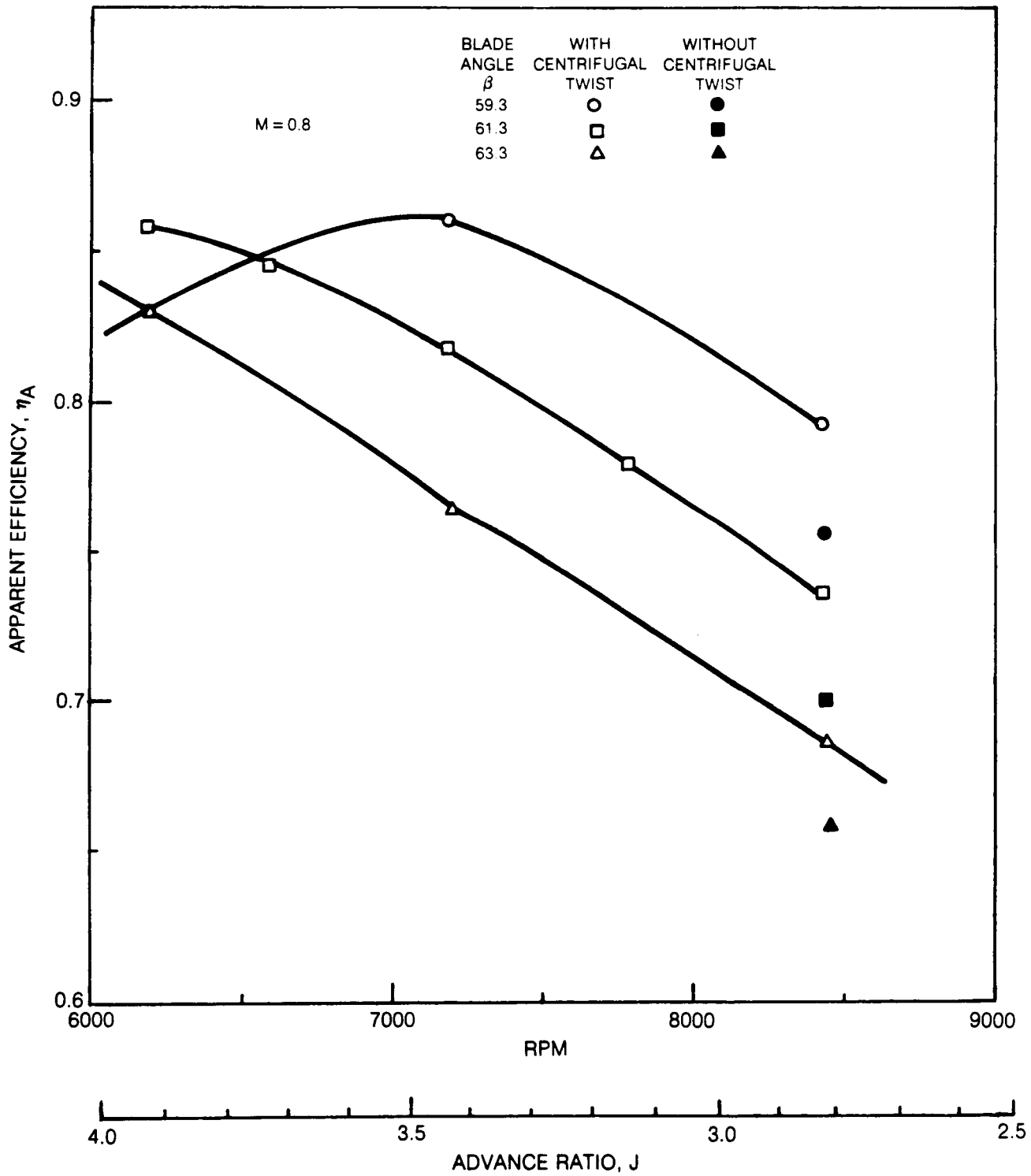

Figure 46. Effect of Centrifugal Twist on Propeller Efficiency — SR-3

84-6-73-16

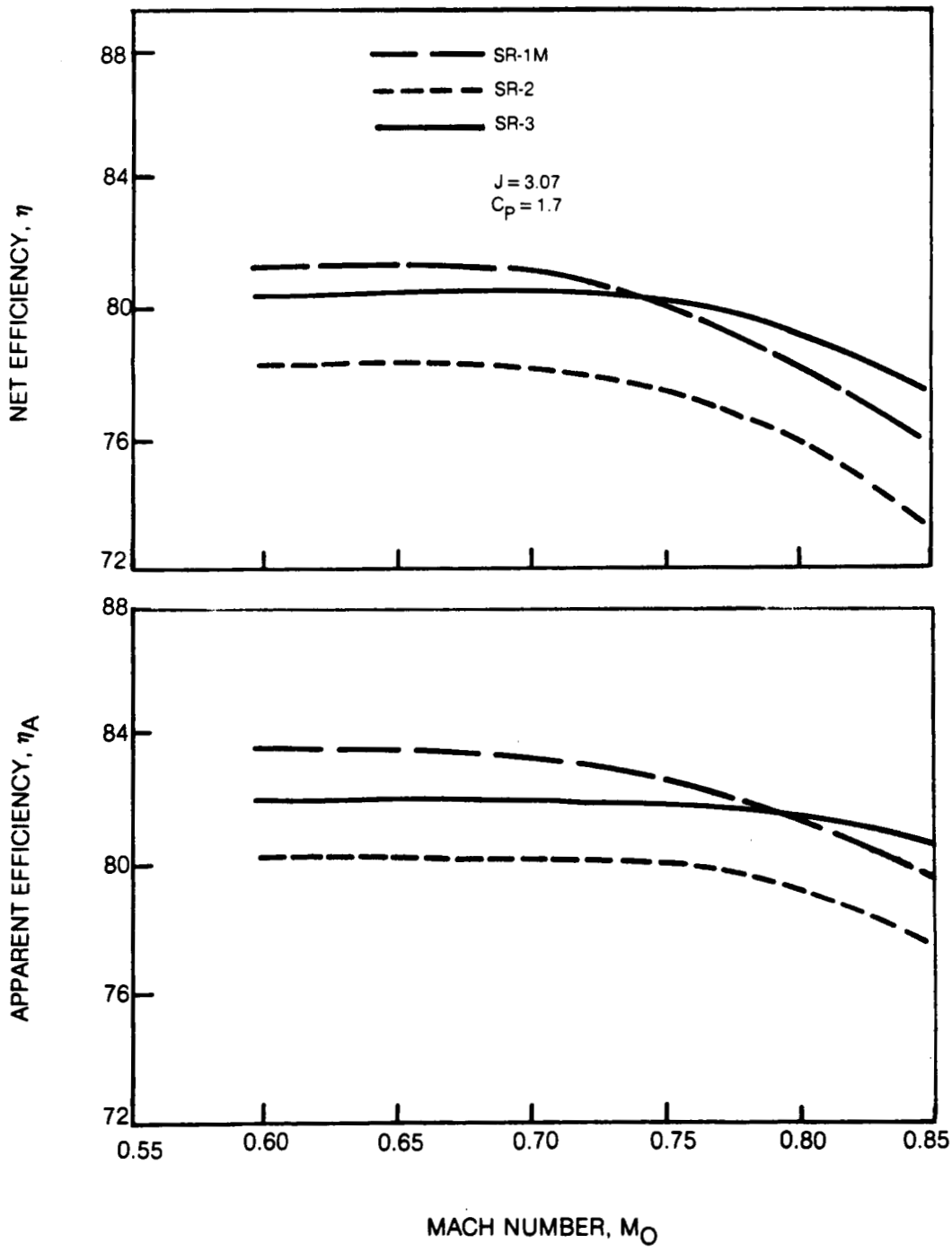

Figure 47 Effect of Sweep and Mach Number at Fixed Advance Ratio—Test Results

84-6-73-17

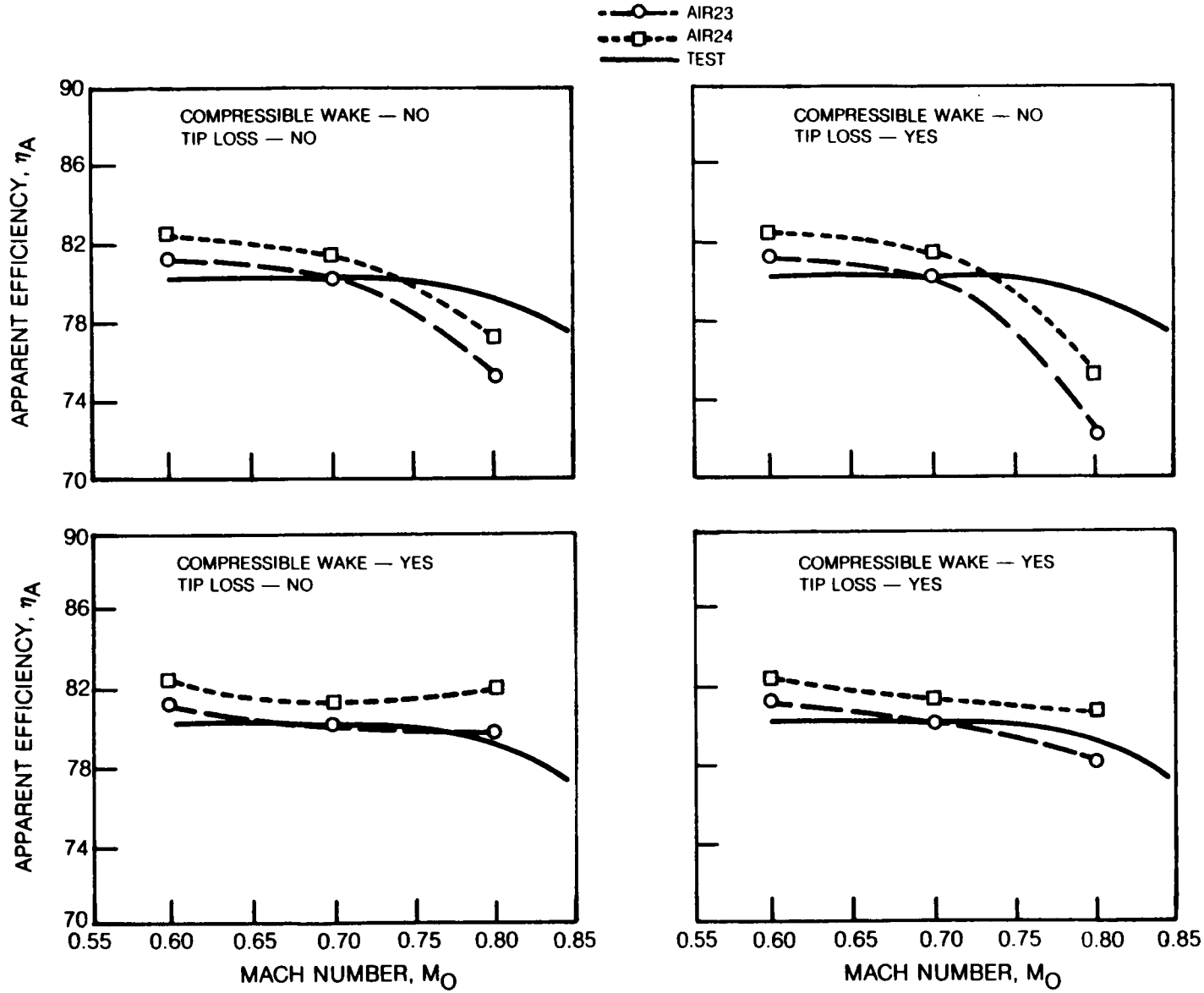

Figure 48. Effect of Airfoil Data Source and Aerodynamic Modeling Features without Cascade Data on SR-2 Propeller with Area Ruled Spinner — Mach Number Variation, $J = 3.07$, $C_p = 1.7$

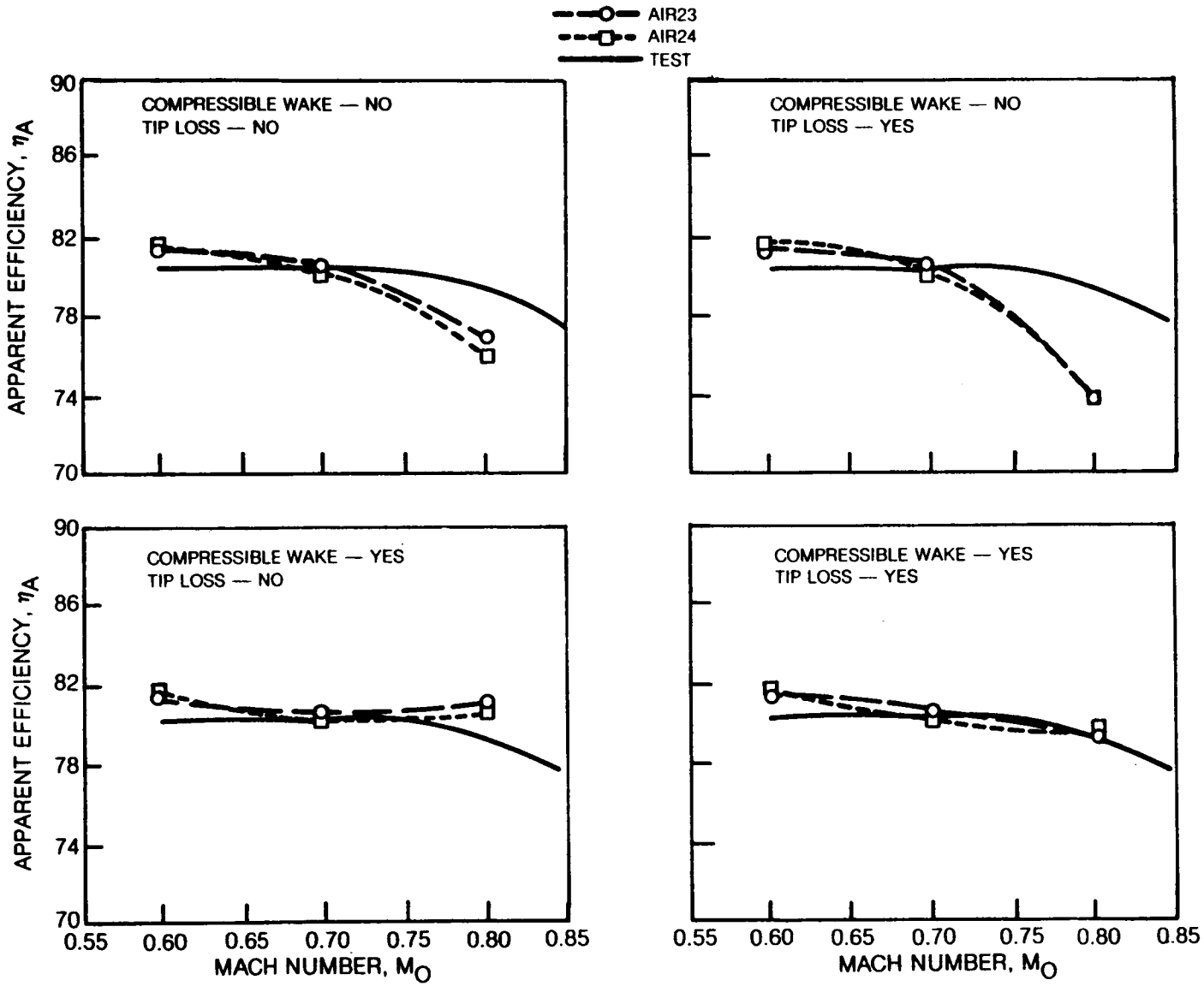

Figure 49. Effect of Airfoil Data Source and Aerodynamic Modeling Features with Cascade Data on SR-2 Propeller with Area Ruled Spinner — Mach Number Variation, $J = 3.07$, $C_p = 1.7$

84-6-73-19

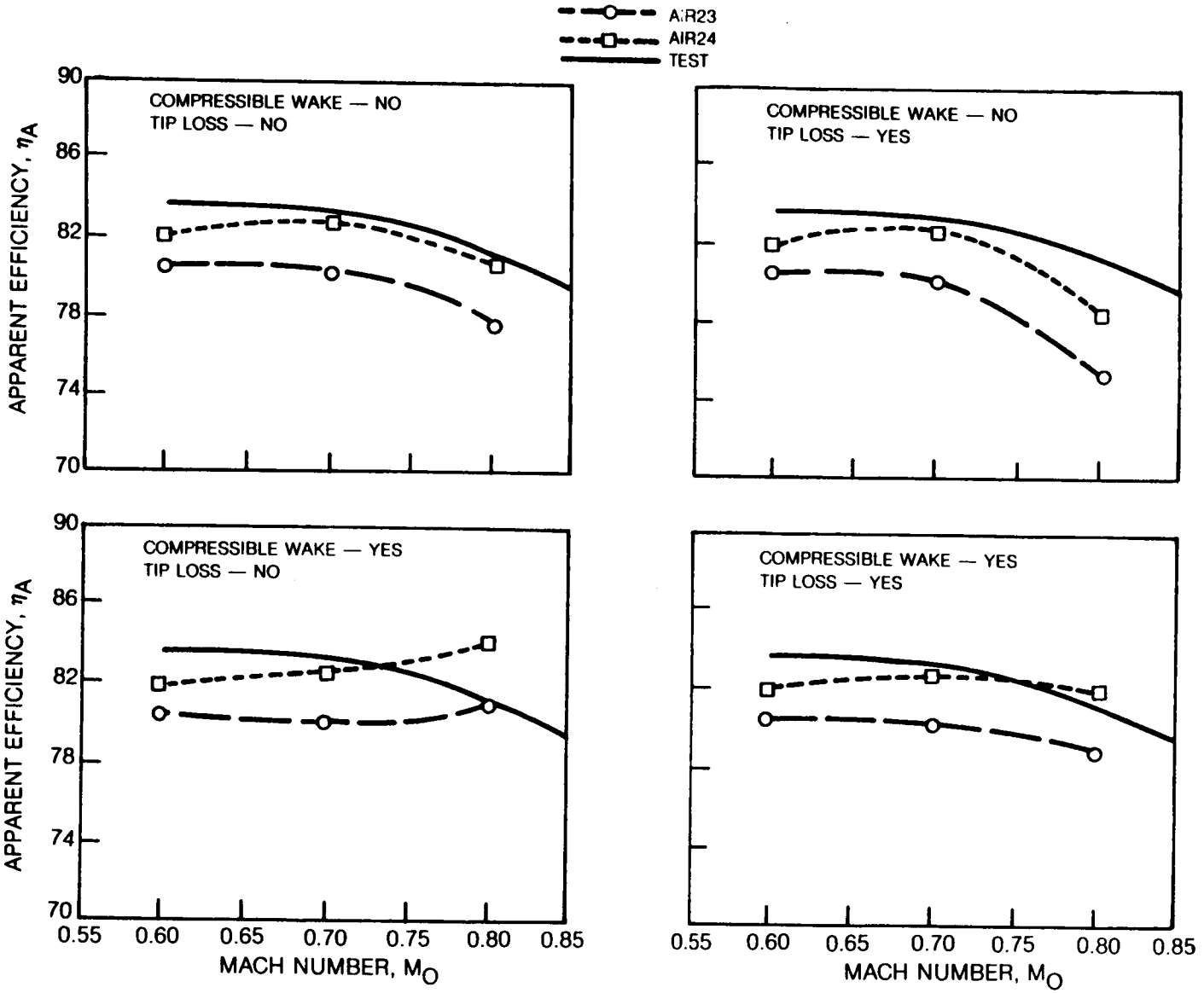

Figure 50. Effect of Airfoil Data Source and Aerodynamic Modeling Features without Cascade Data on SR-1M Propeller with Area Ruled Spinner — Mach Number Variation, $J = 3.07$, $C_p = 1.7$

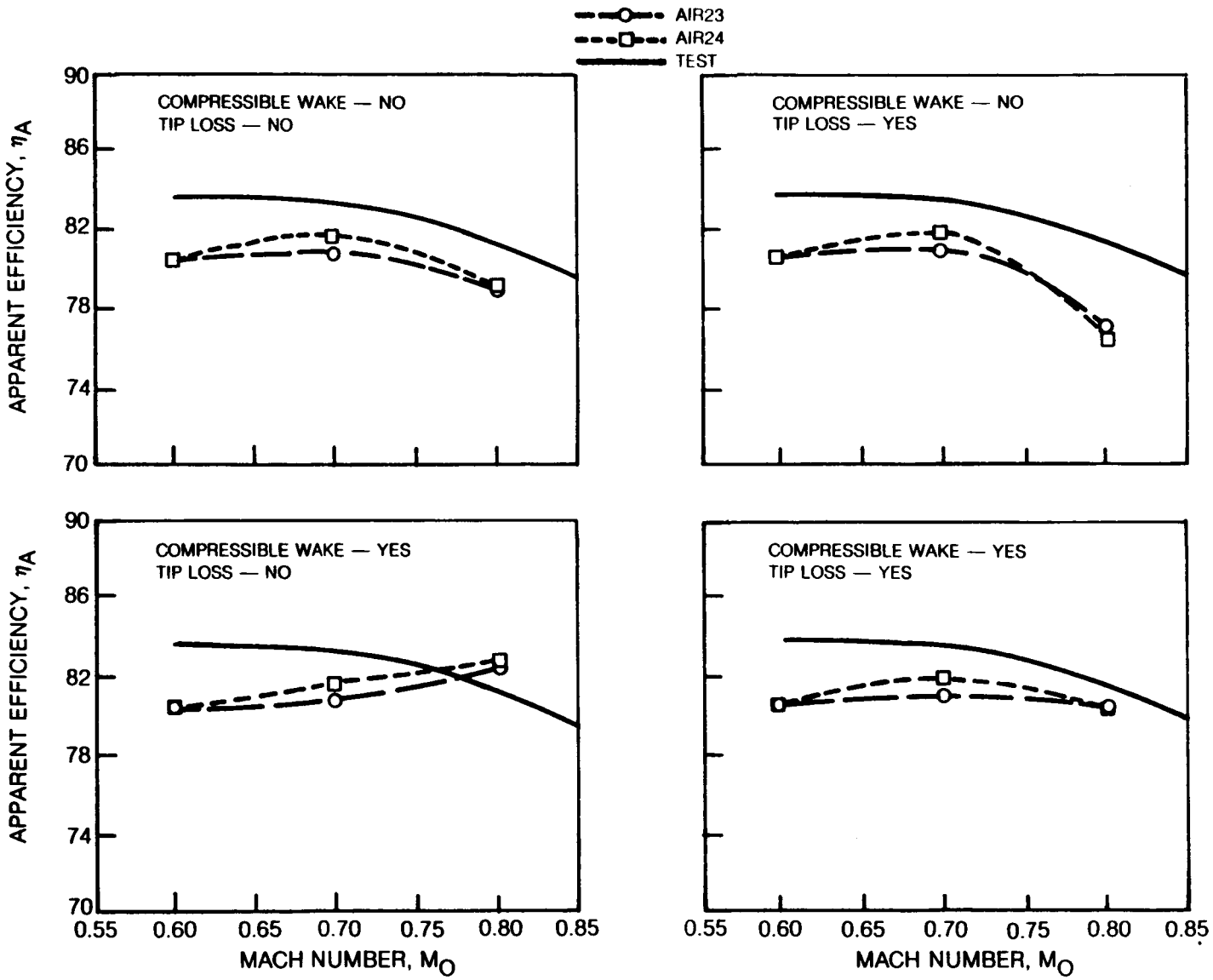

Figure 51. Effect of Airfoil Data Source and Aerodynamic Modeling Features with Cascade Data on SR-1M Propeller with Area Ruled Spinner — Mach Number Variation, J = 3.07, C_p = 1.7

84-A-73-21

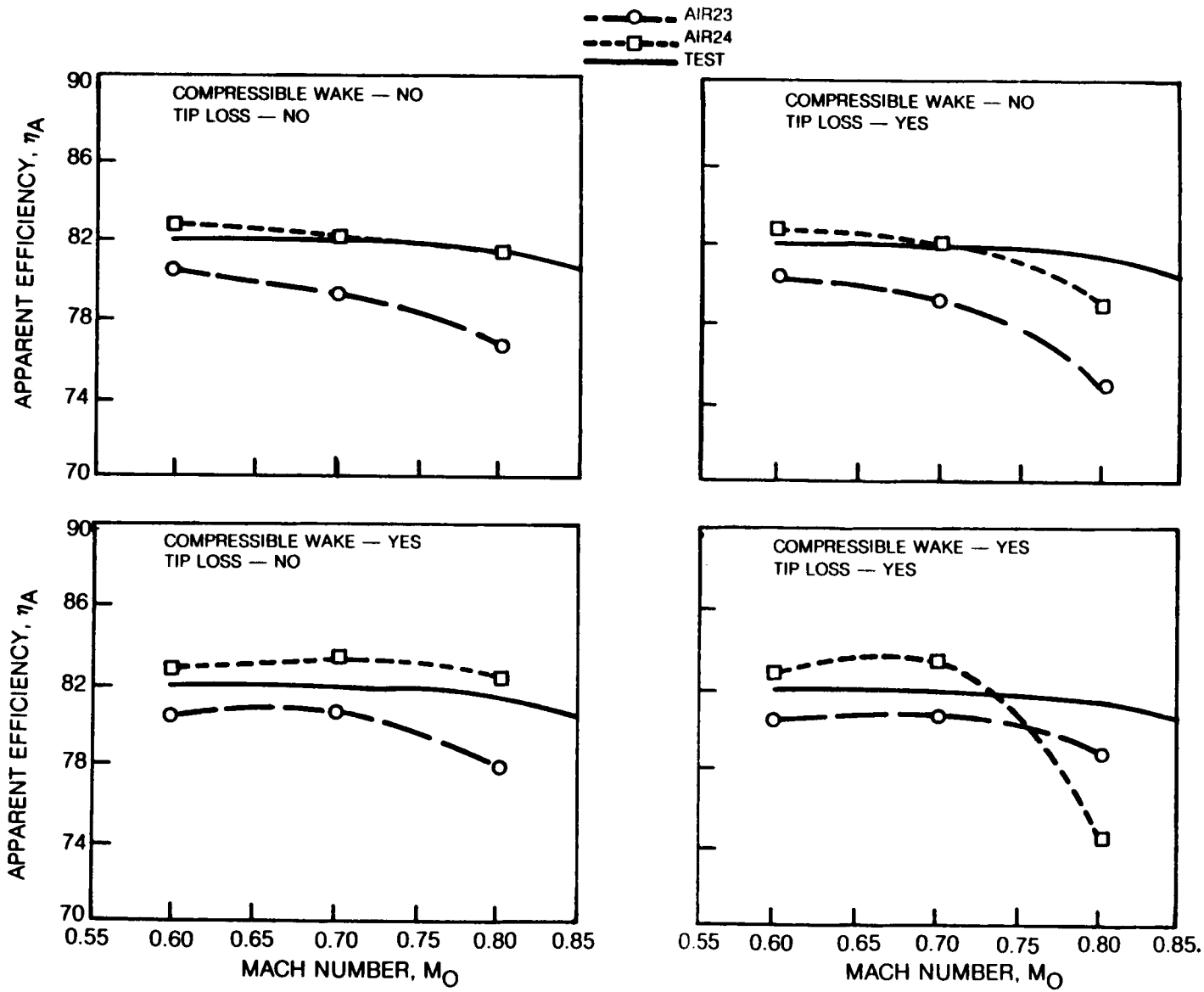

Figure 52. Effect of Airfoil Data Source and Aerodynamic Modeling Features without Cascade Data on SR-3 Propeller with Area Ruled Spinner — Mach Number Variation, $J = 3.07$, $C_p = 1.7$

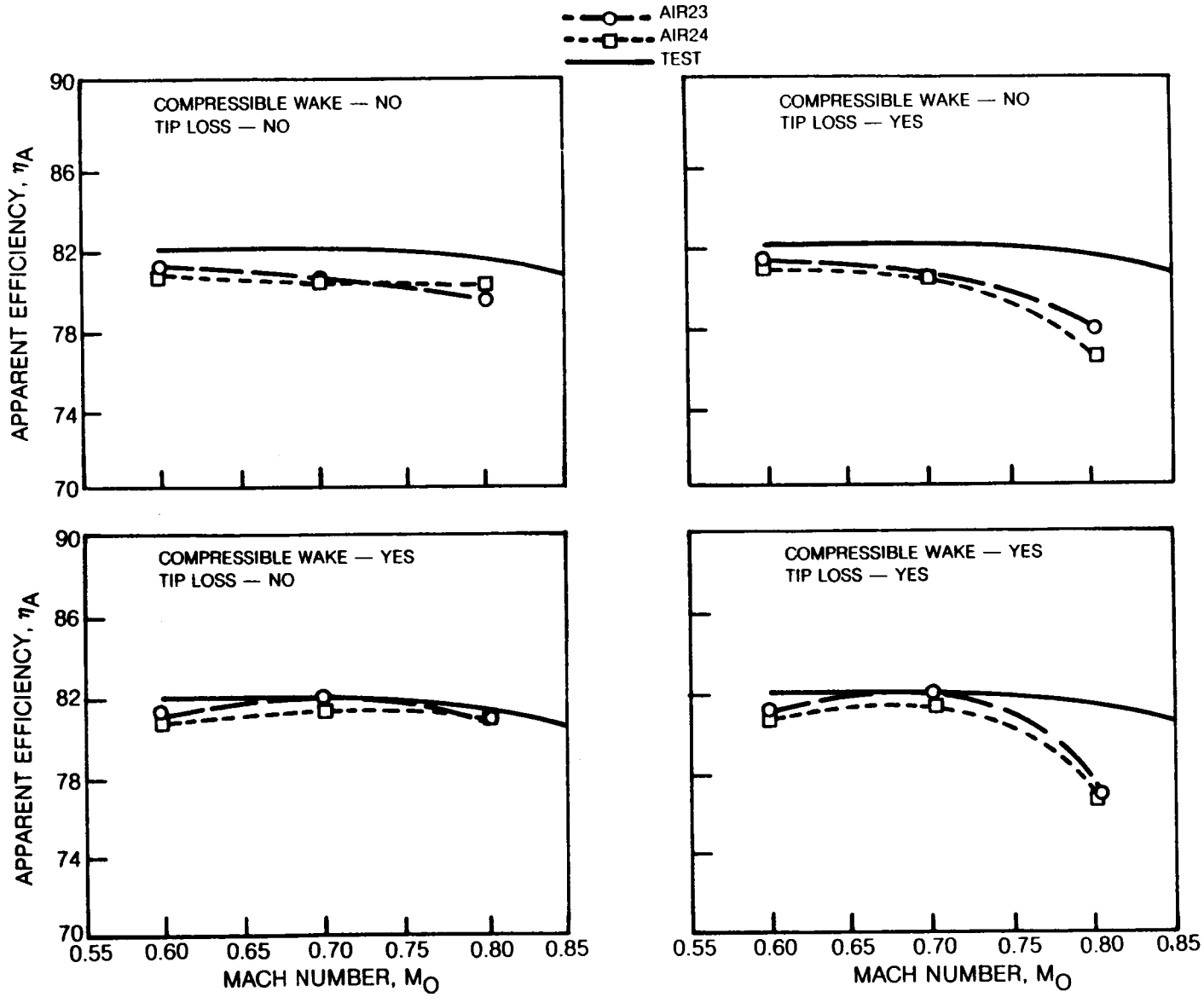

Figure 53. Effect of Airfoil Data Source and Aerodynamic Modeling Features with Cascade Data on SR-3 Propeller with Area Ruled Spinner — Mach Number Variation, J = 3.07, C_p = 1.7

84-6-73-23

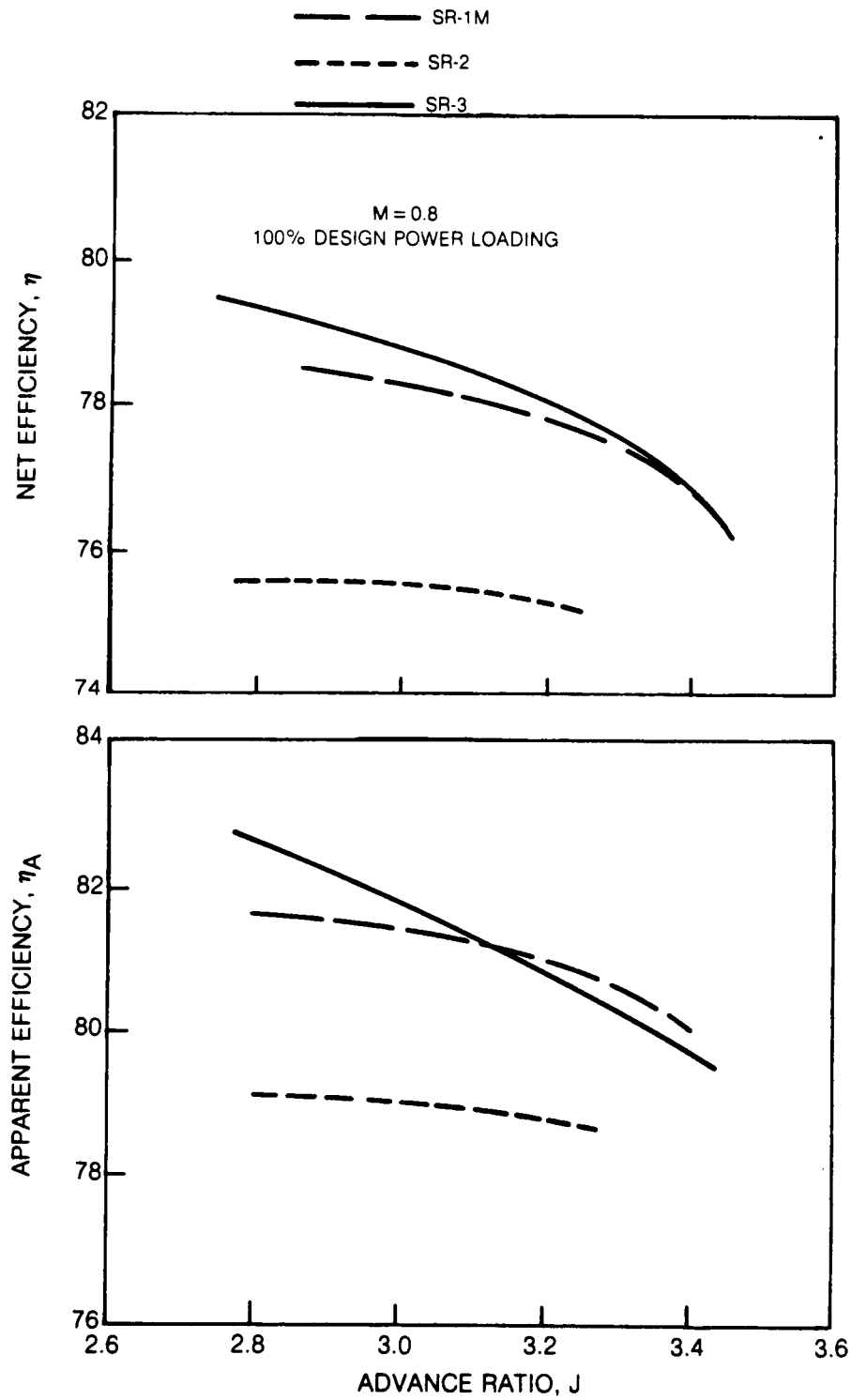

Figure 54 Effect of Sweep and Advance Ratio At Fixed Mach Number — Test Results

84-6-73-24

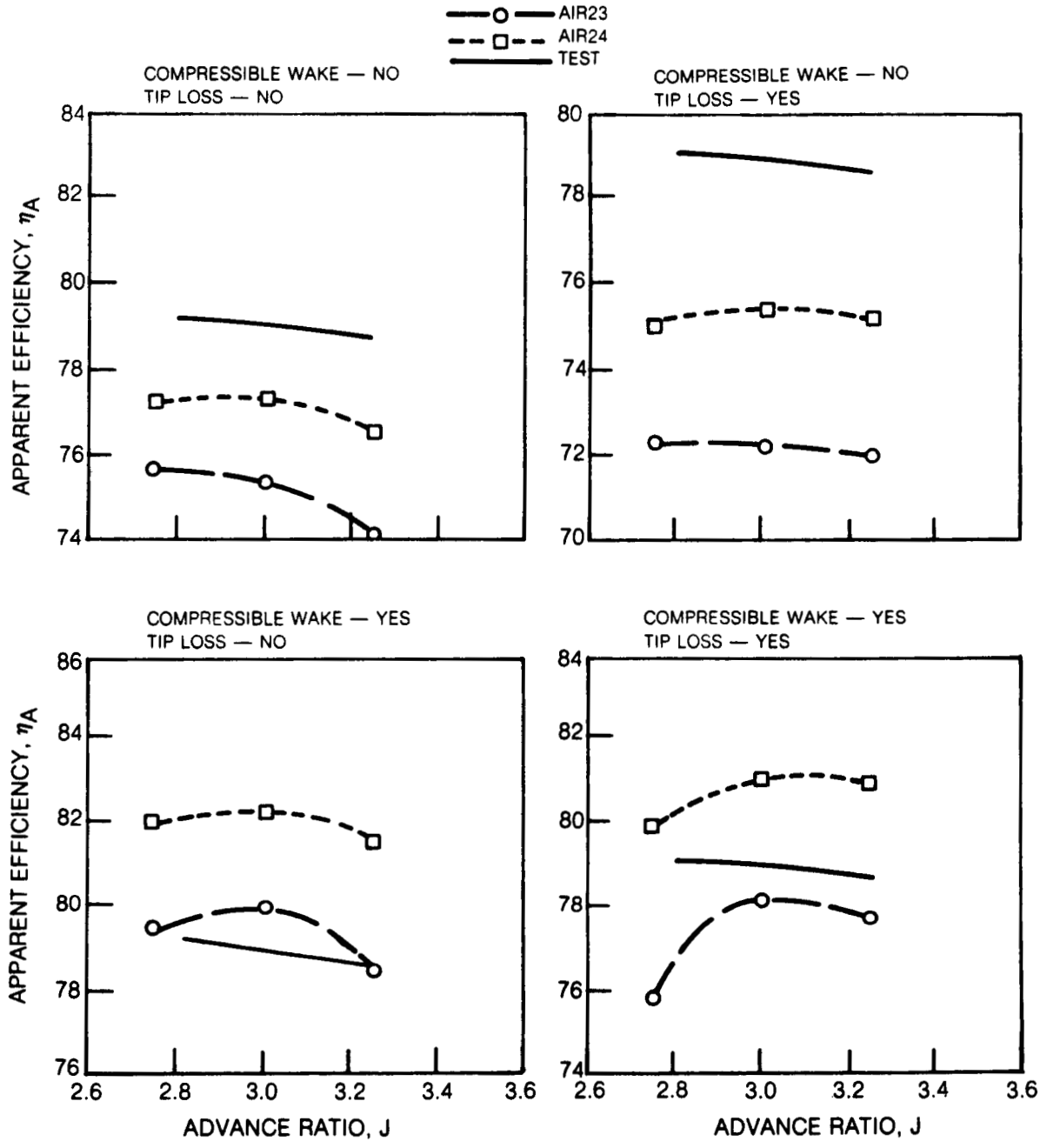

Figure 55. Effect of Airfoil Data Source and Aerodynamic Modeling Features without Cascade Data on SR-2 Propeller with Area Ruled Spinner — Advance Ratio Variation, M = 0.8, 100% Design Power Loading

84-6-73-25

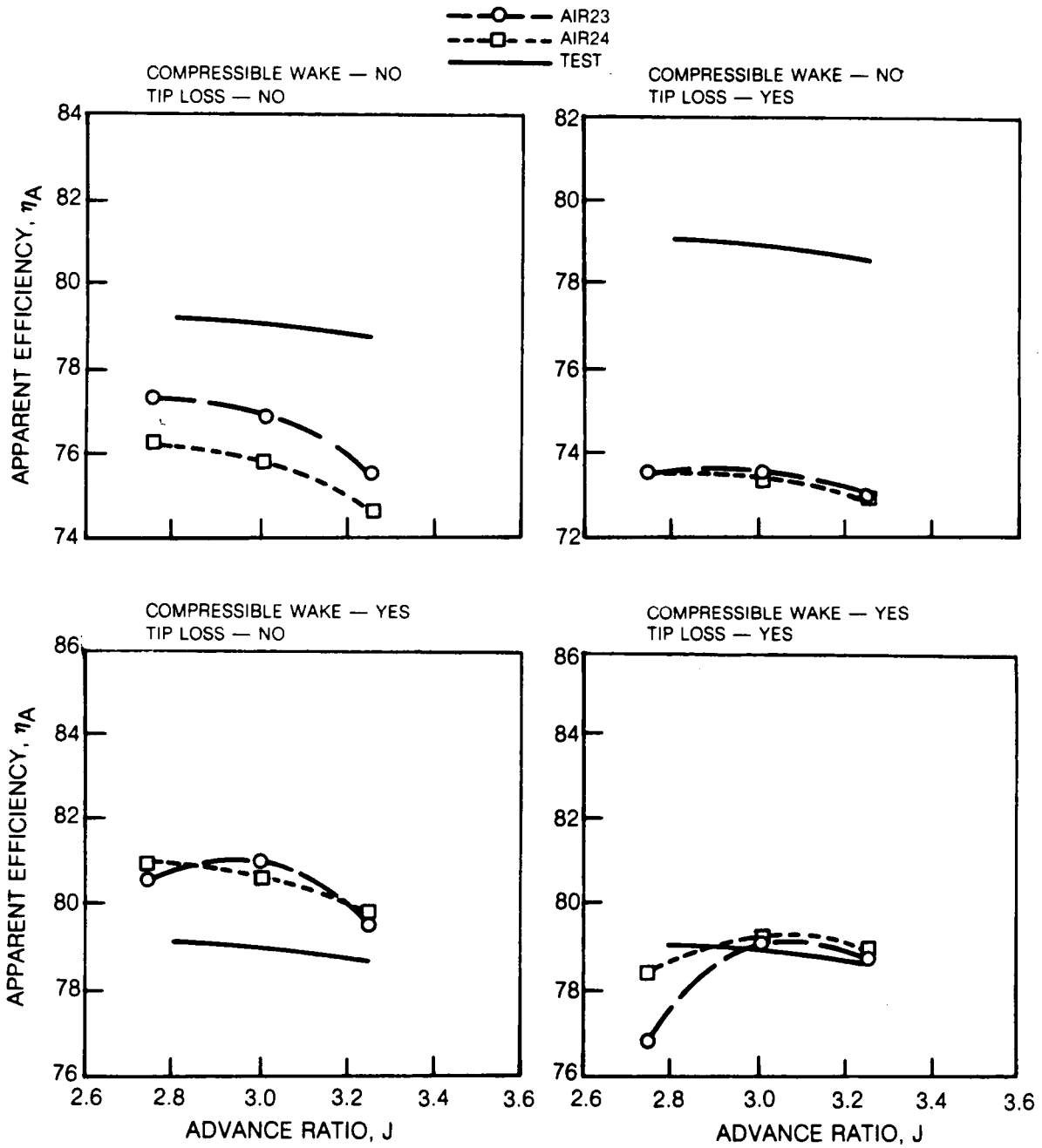

Figure 56. Effect of Airfoil Data Source and Aerodynamic Modeling Features with Cascade Data on SR-2 Propeller with Area Ruled Spinner — Advance Ratio Variation, M = 0.8, 100% Design Power Loading

84-6-73-26

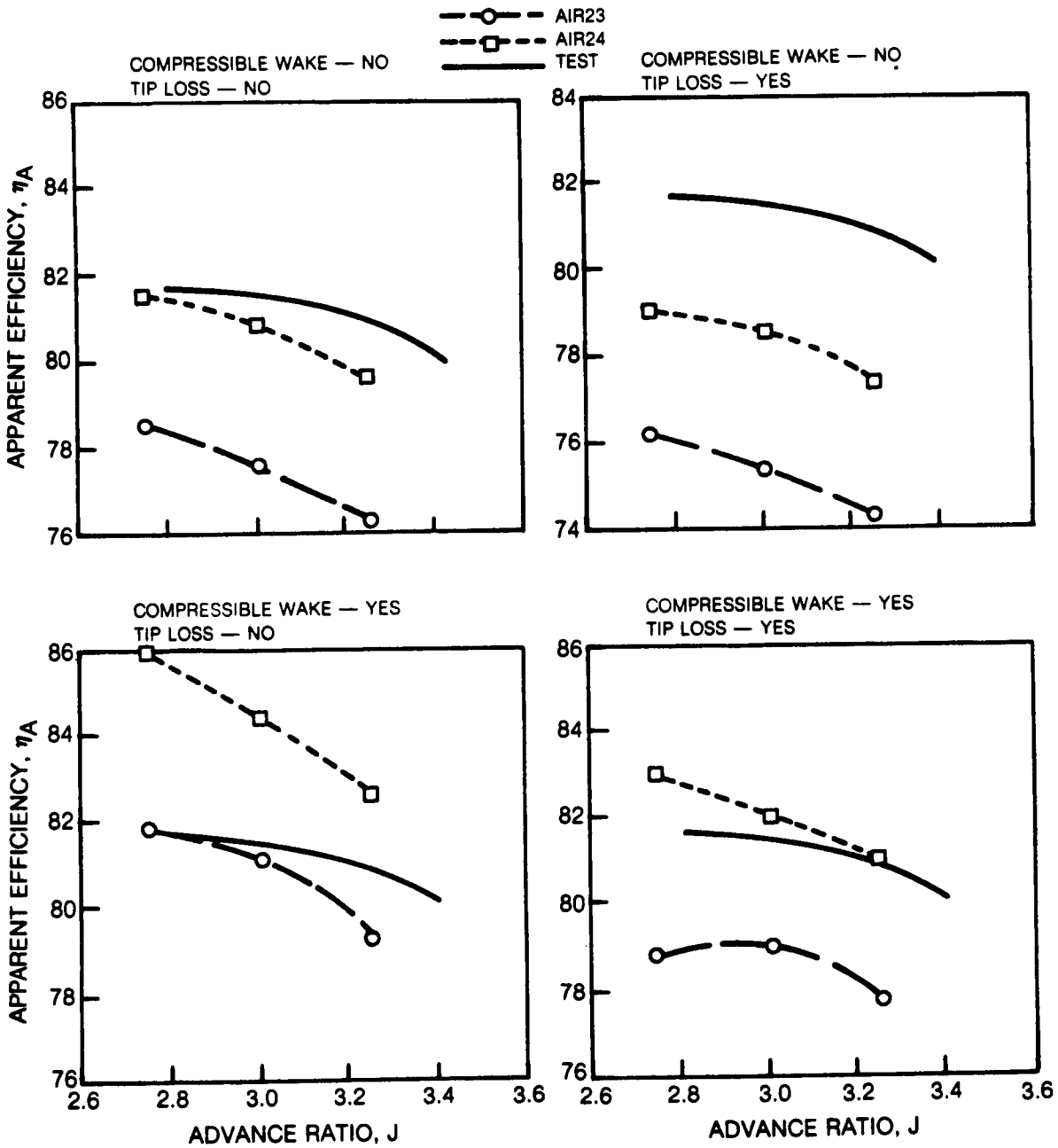

Figure 57. Effect of Airfoil Data Source and Aerodynamic Modeling Features without Cascade Data on SR-1M Propeller with Area Ruled Spinner — Advance Ratio Variation, M = 0.8, 100% Design Power Loading

84-6-73-27

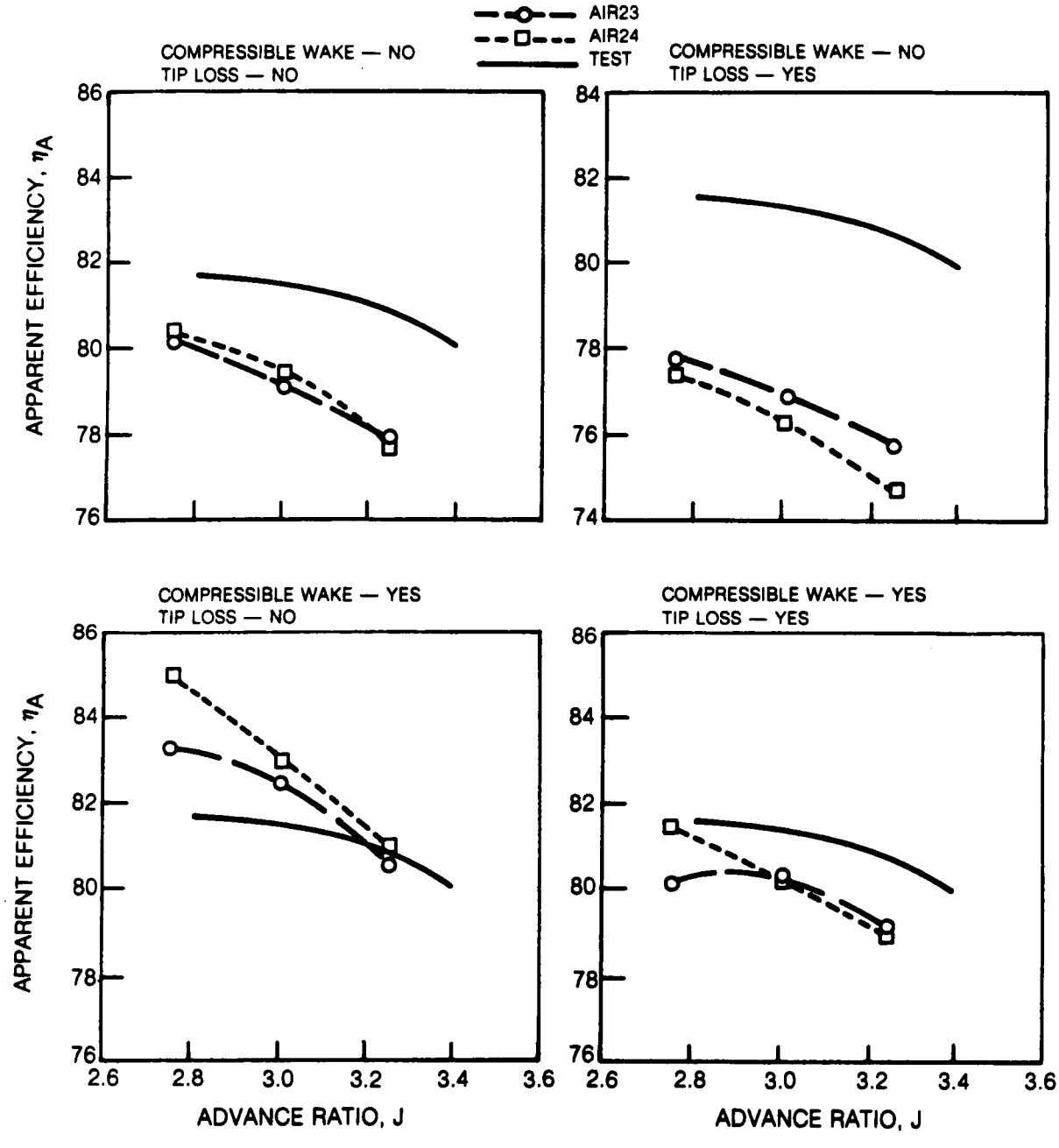

Figure 58. Effect of Airfoil Data Source and Aerodynamic Modeling Features with Cascade Data on SR-1M Propeller with Area Ruled Spinner — Advance Ratio Variation, M = 0.80, 100% Design Power Loading

84-6-73-28

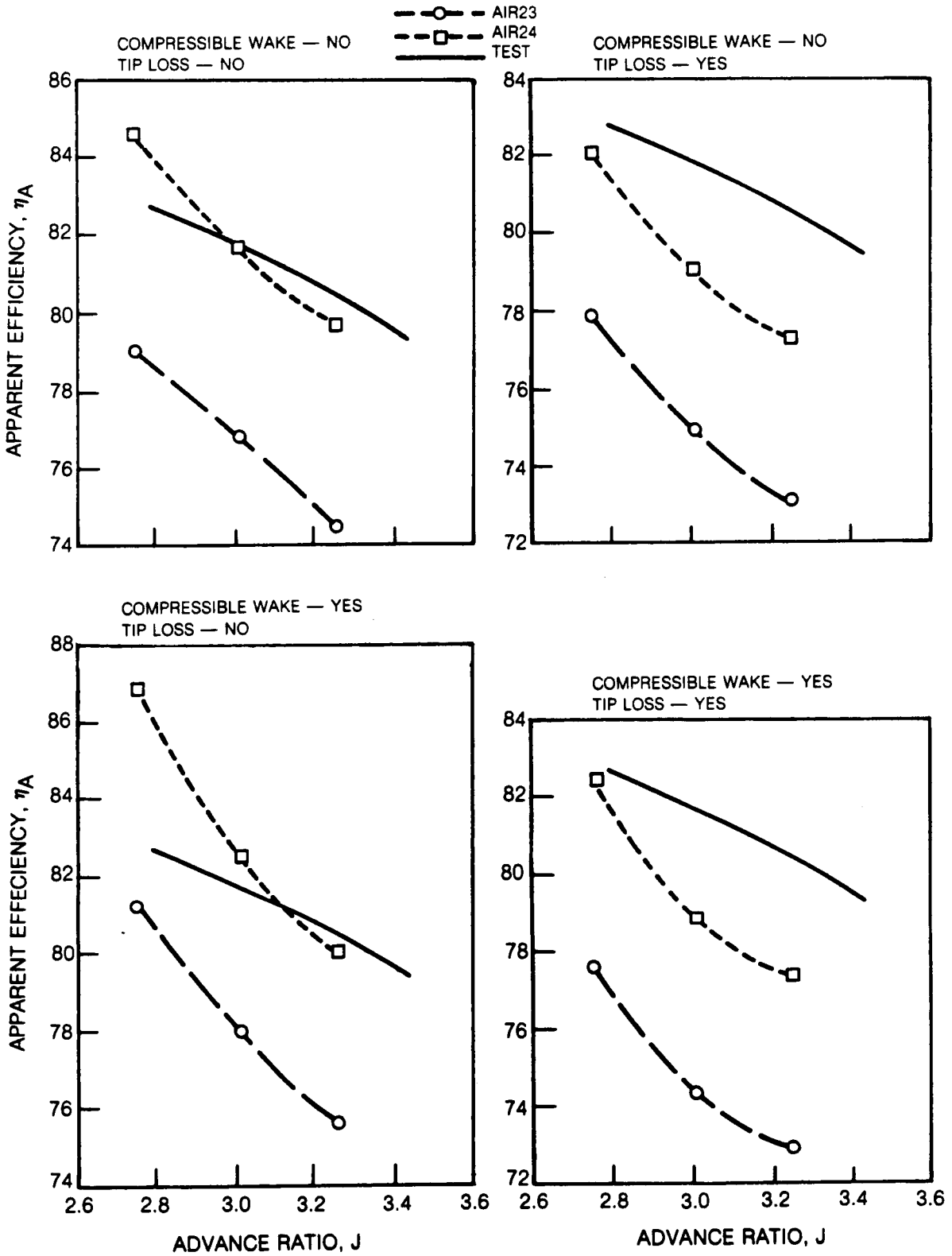

Figure 59. Effect of Airfoil Data Source and Aerodynamic Modeling Features without Cascade Data on SR-3 Propeller with Area Ruled Spinner — Advance Ratio Variation, M = 0.8, 100% Design Power Loading

84-6-73-29

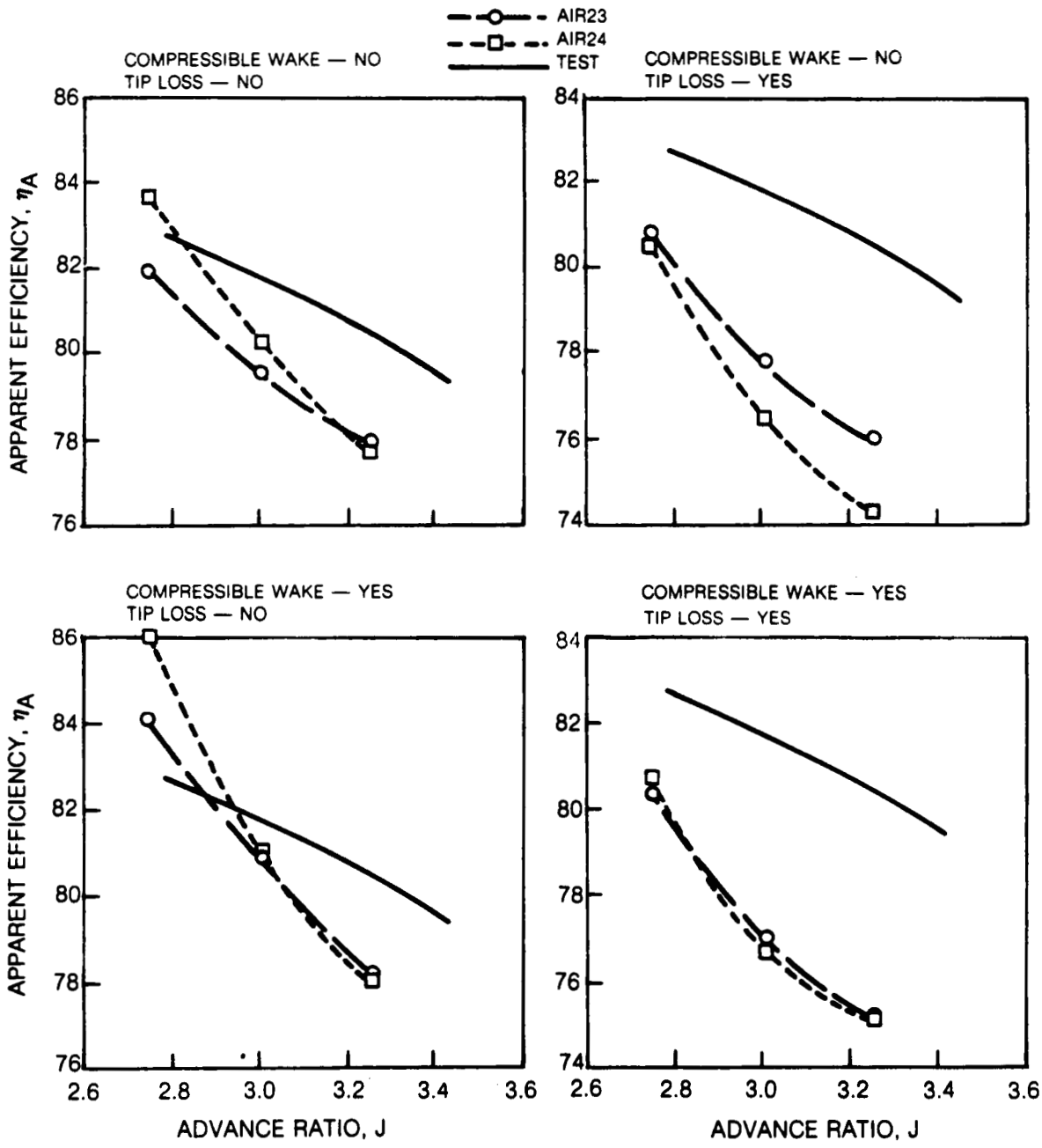

Figure 60. Effect of Airfoil Data Source and Aerodynamic Modeling Features with Cascade Data on SR-3 Propeller with Area Ruled Spinner — Advance Ratio Variation, M = 0.8, 100% Design Power Loading

84-6-73-30

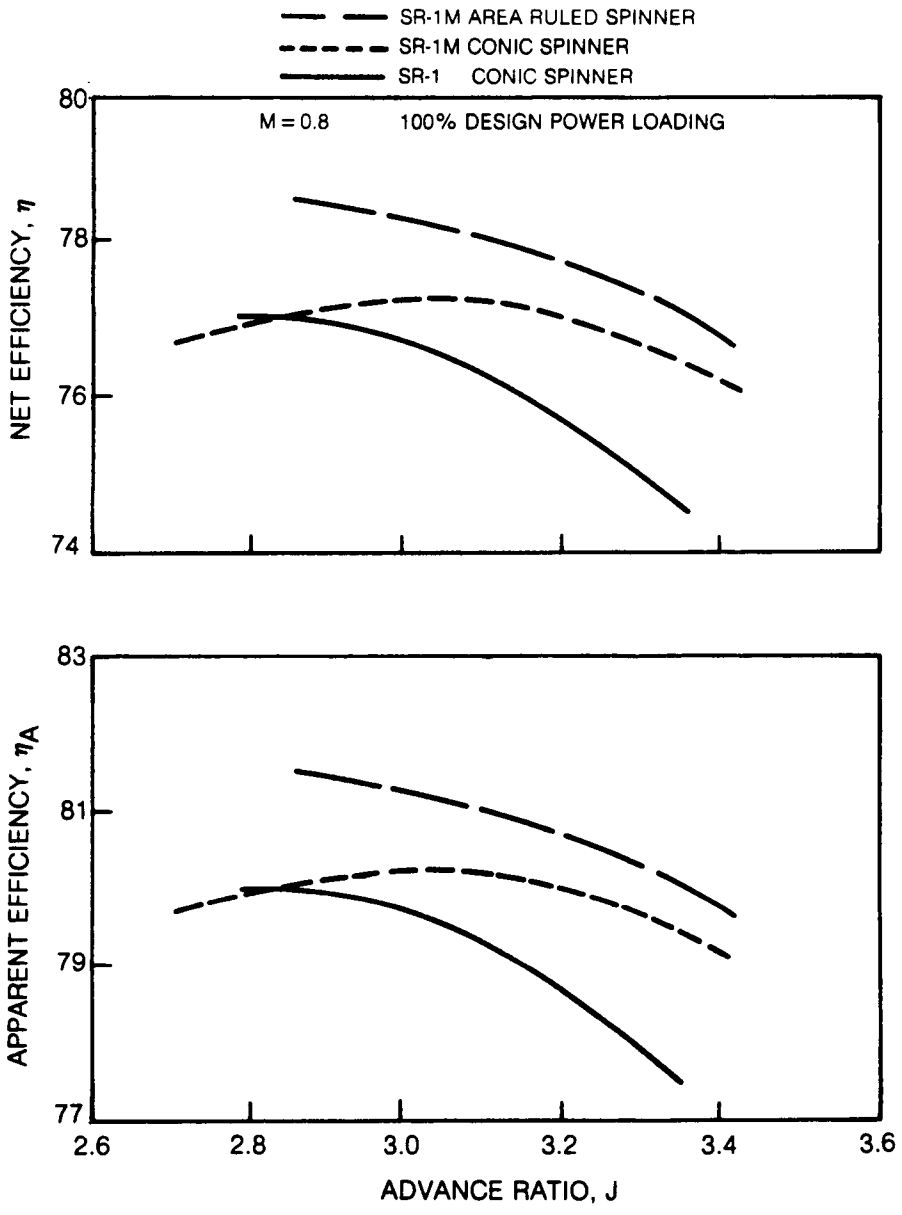

Figure 61. Effect of Twist and Area Ruling — Test Results

84-6-73-31

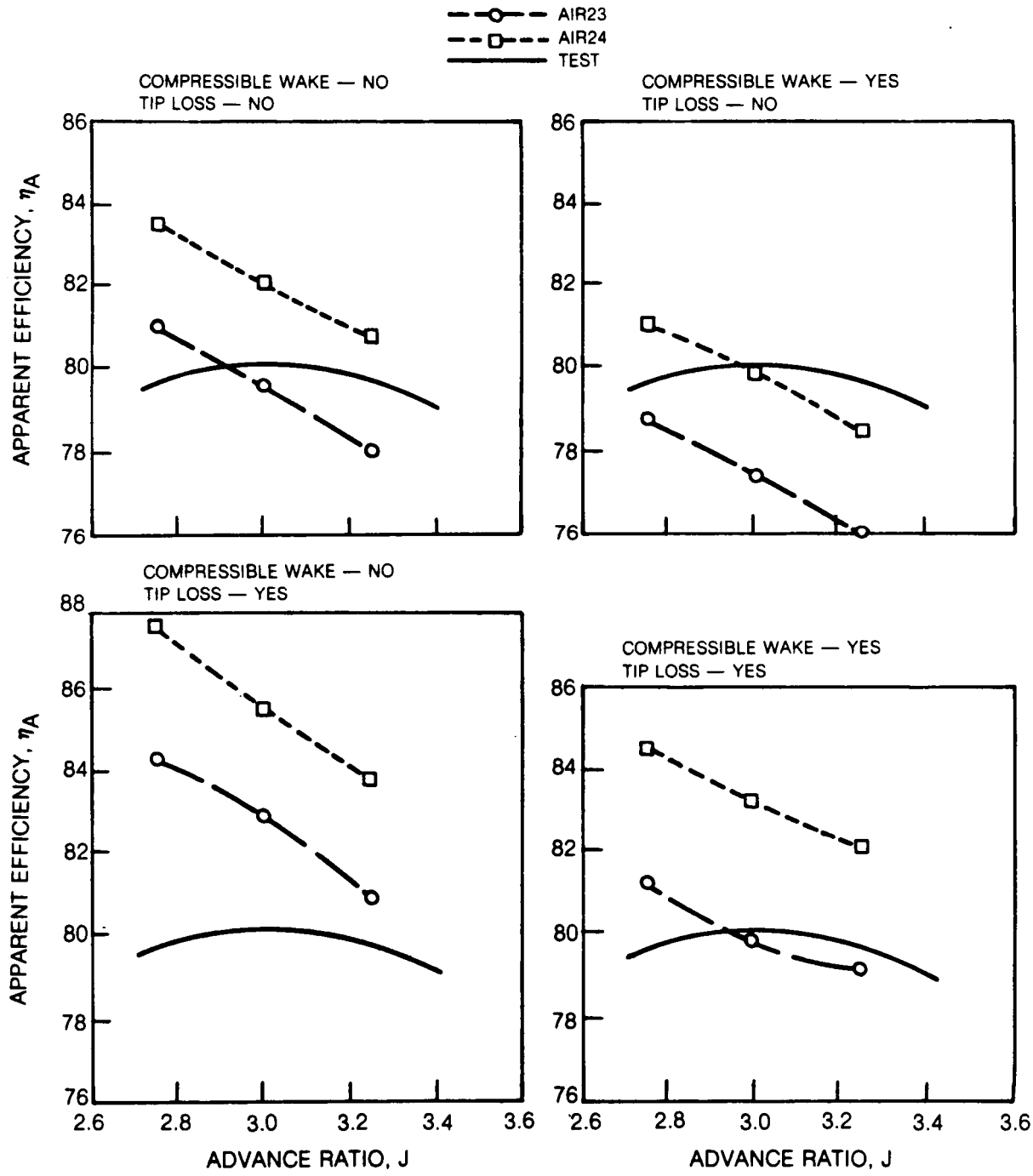

Figure 62. Effect of Airfoil Data Source and Aerodynamic Modeling Features without Cascade Data on SR-1M Propeller with Conic Spinner — Advance Ratio Variation, M = 0.80, 100% Design Power Loading

84-6-73-32

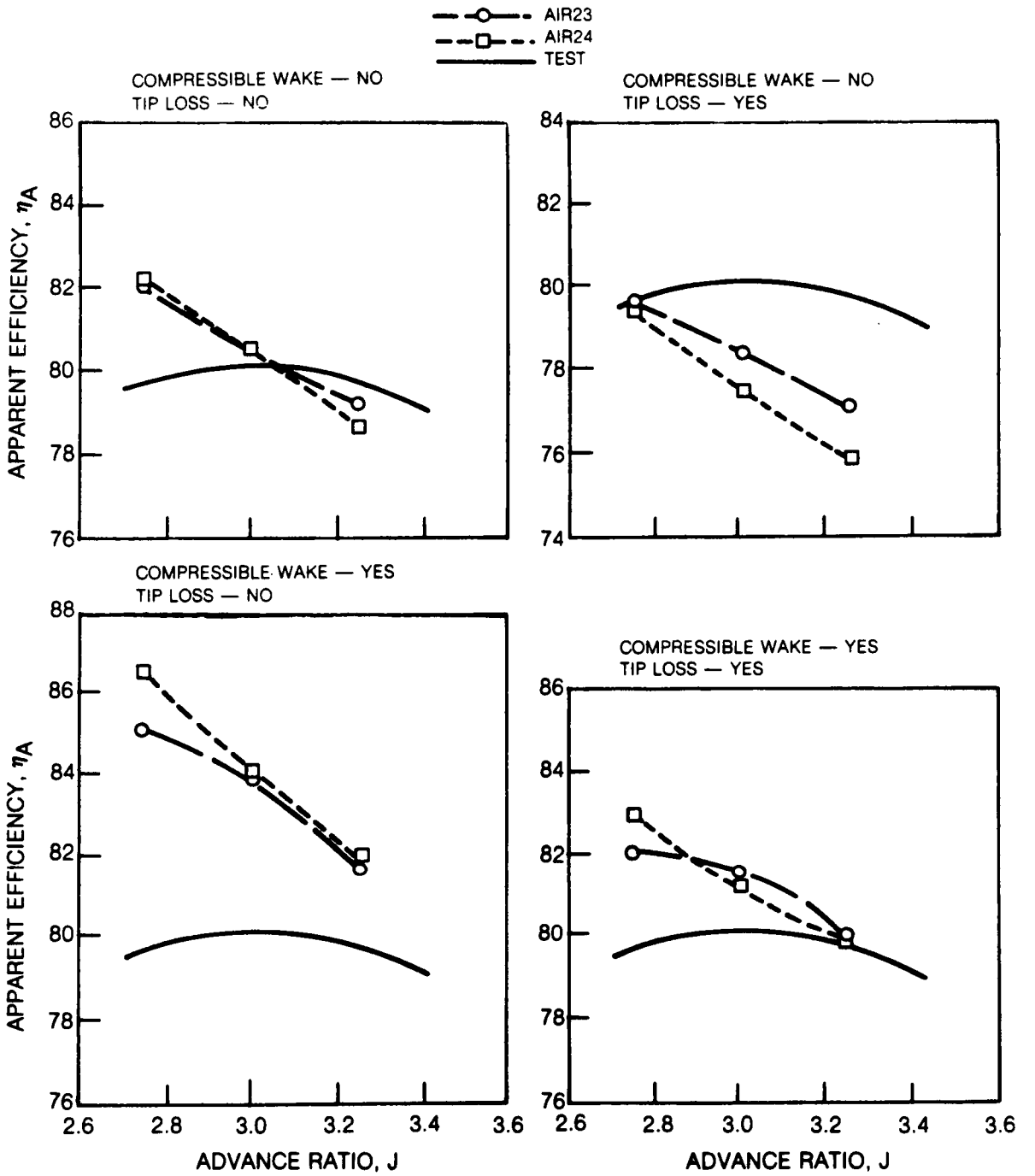

Figure 63. Effect of Airfoil Data Source and Aerodynamic Modeling Features with Cascade Data on SR-1M Propeller with Conic Spinner — Advance Ratio Variation, M = 0.8, 100% Design Power Loading

84-6-73-33

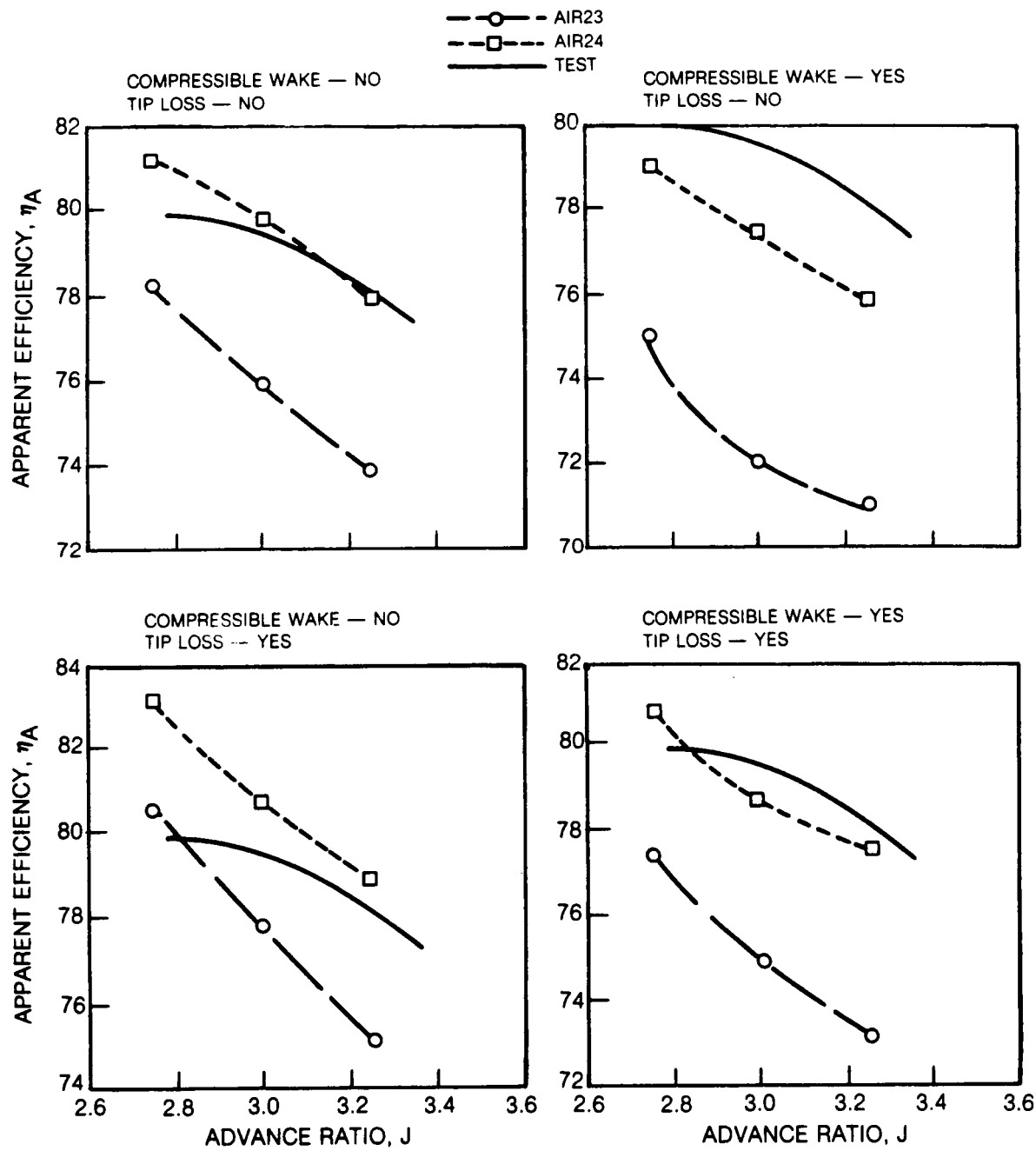

Figure 64. Effect of Airfoil Data Source and Aerodynamic Modeling Features without Cascade Data on SR-1 Propeller with Conic Spinner — Advance Ratio Variation, M = 0.8, 100% Design Power Loading

84-6-73-34

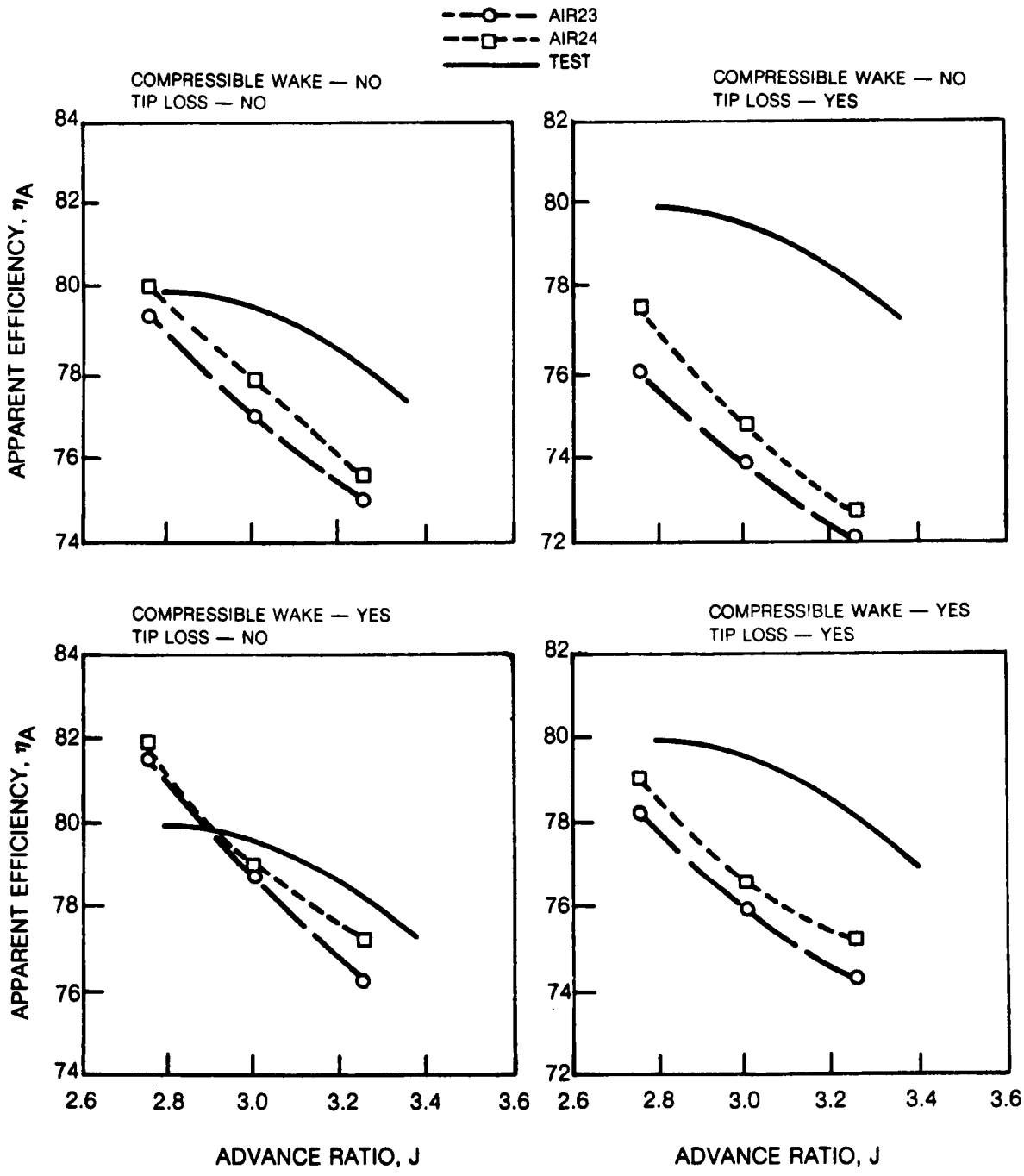

Figure 65. Effect of Airfoil Data Source and Aerodynamic Modeling Features with Cascade Data on SR-1 Propeller with Conic Spinner — Advance Ratio Variation, M = 0.8. 100% Design Power Loading

84-6-73-35

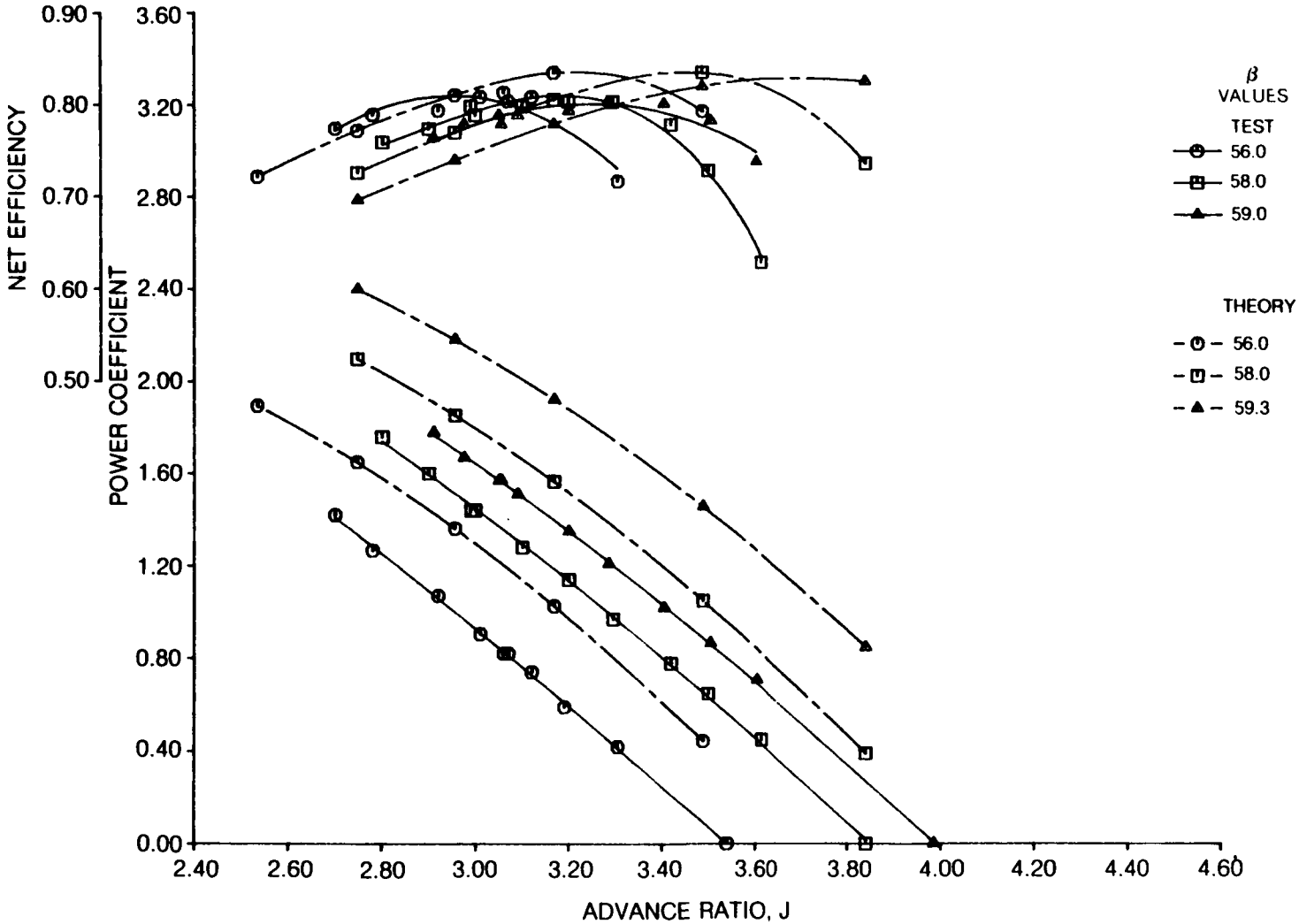

Figure 66a. Comparison of Measured and Predicted SR-2 Propeller Performance, M = 0.6 -Modeling Option 1

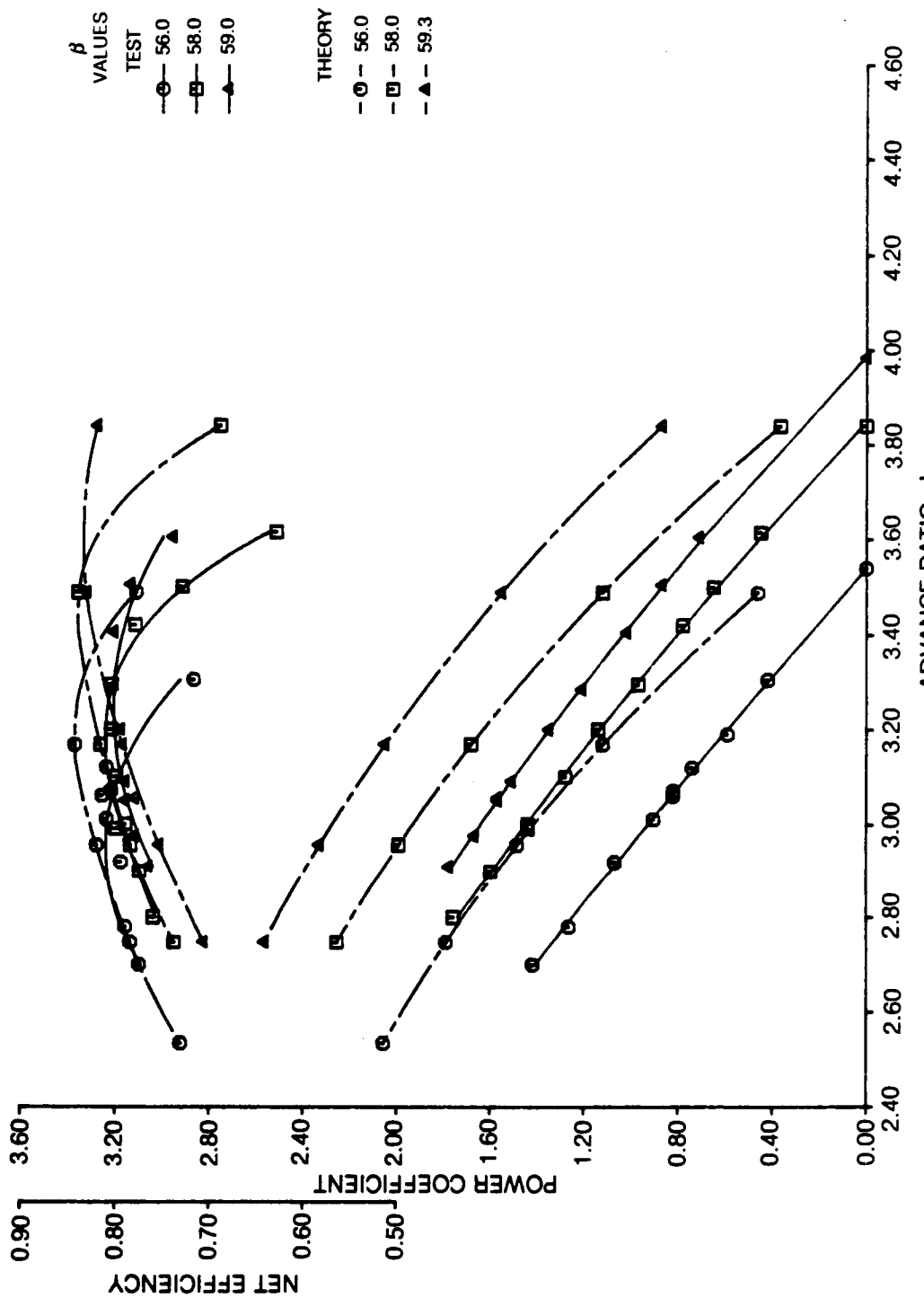

Figure 66b. Comparison of Measured and Predicted SR-2 Propeller Performance, M = 0.6 -Modeling Option 2

85-4-90-2

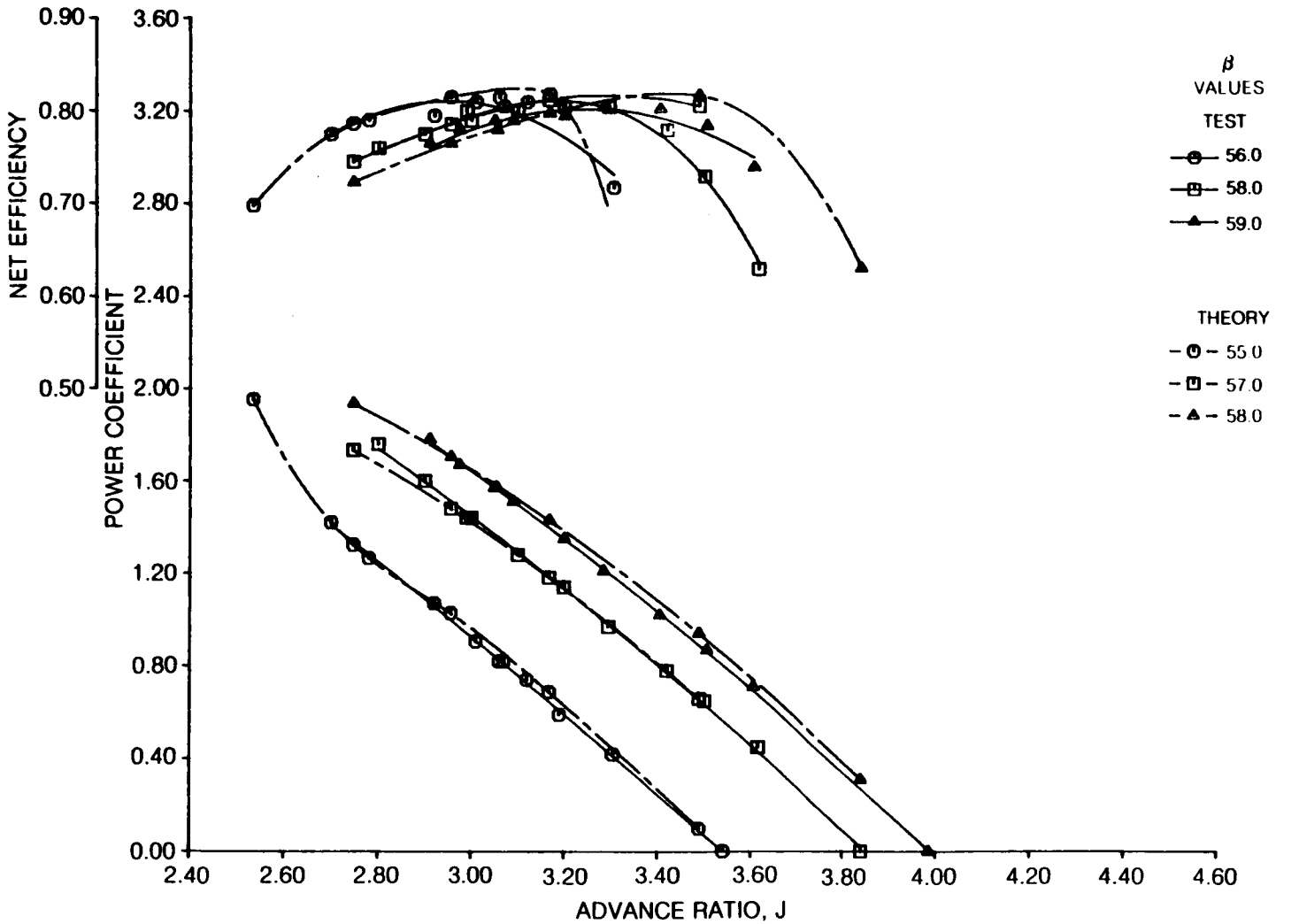

Figure 66c. Comparison of Measured and Predicted SR-2 Propeller Performance, M = 0.6 -Modeling Option 3

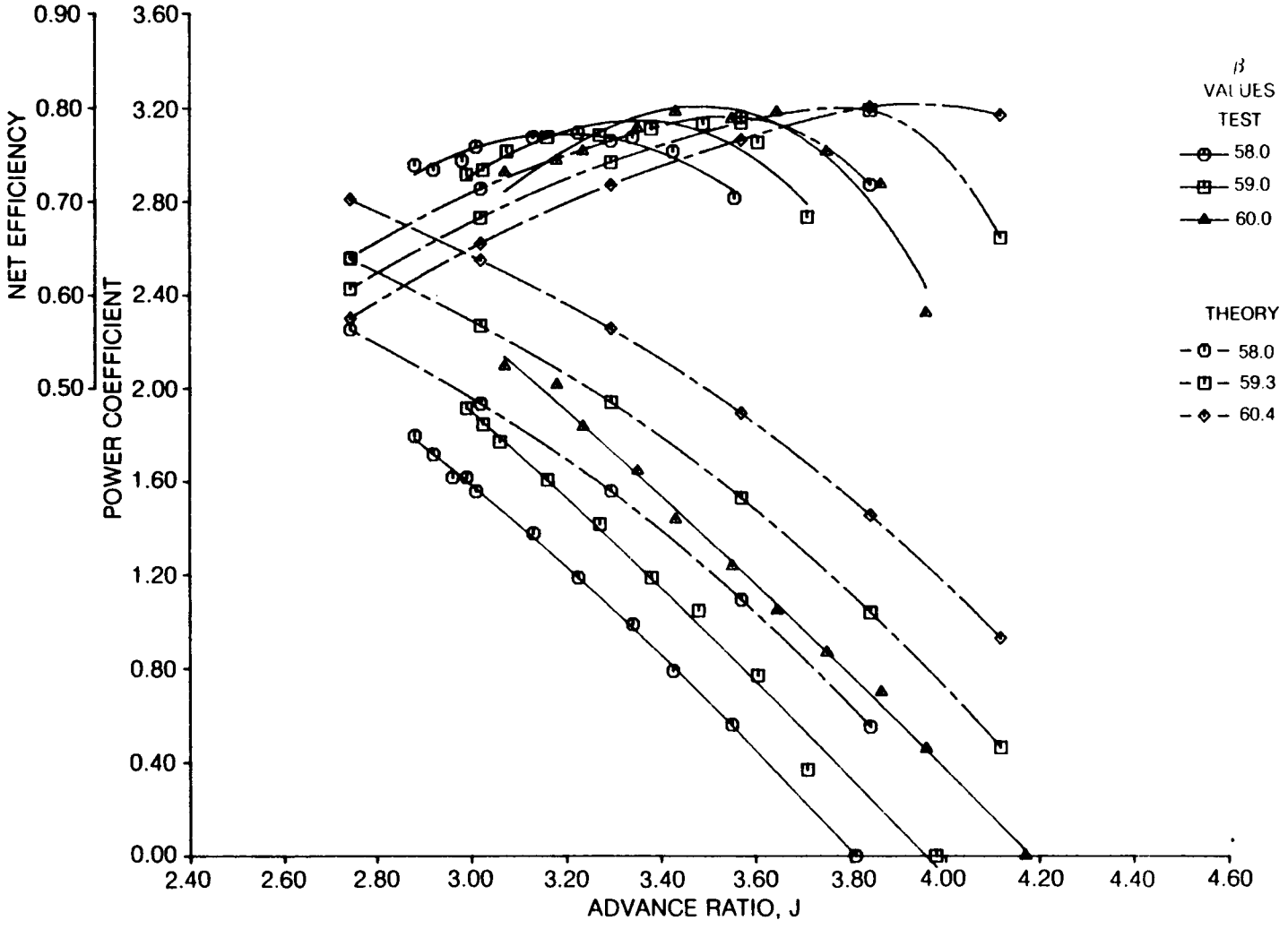

Figure 67a. Comparison of Measured and Predicted SR-2 Propeller Performance, M = 0.8 -Modeling Option 1

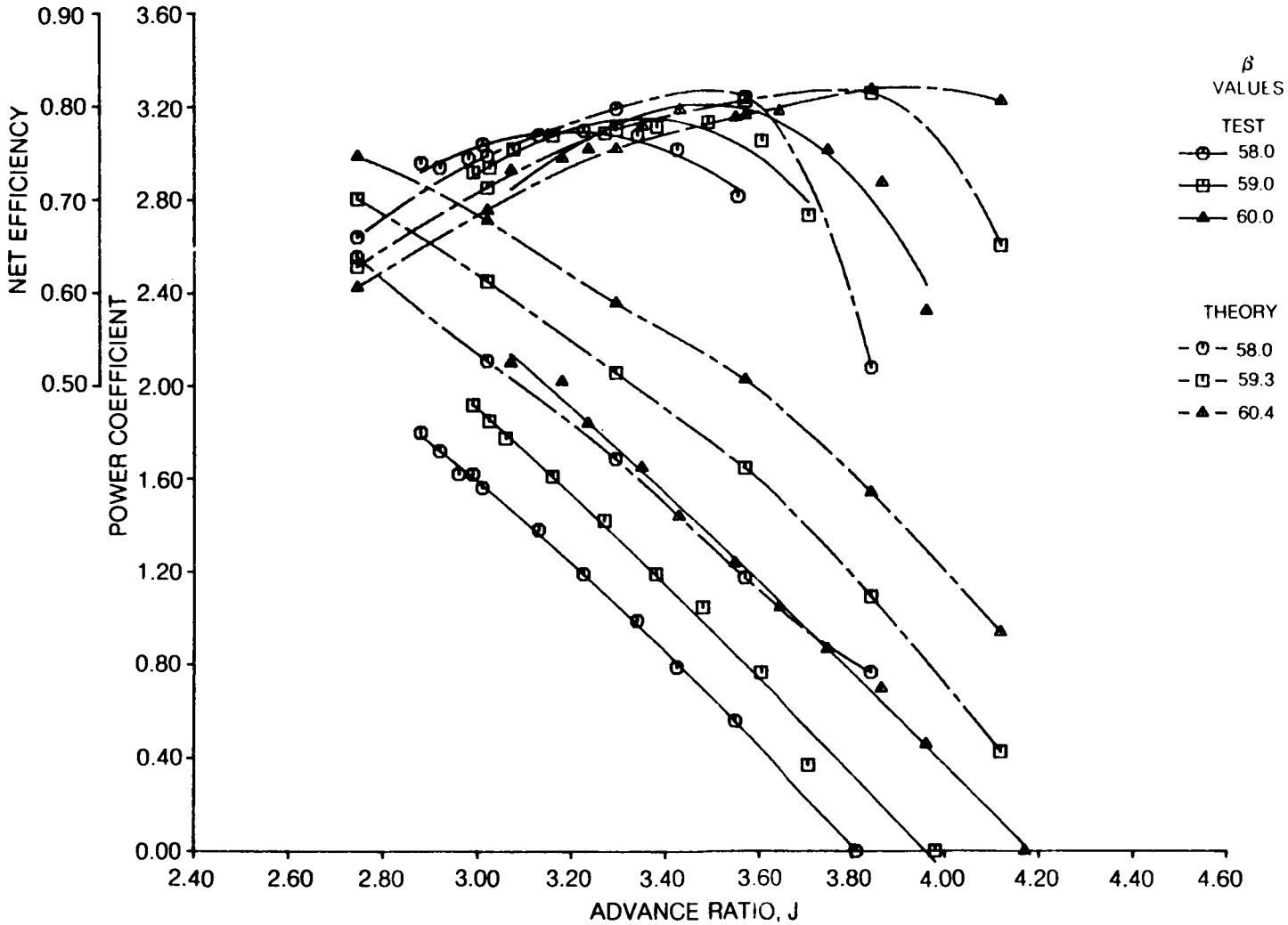

Figure 67b. Comparison of Measured and Predicted SR-2 Propeller Performance, M = 0.8 -Modeling Option 2

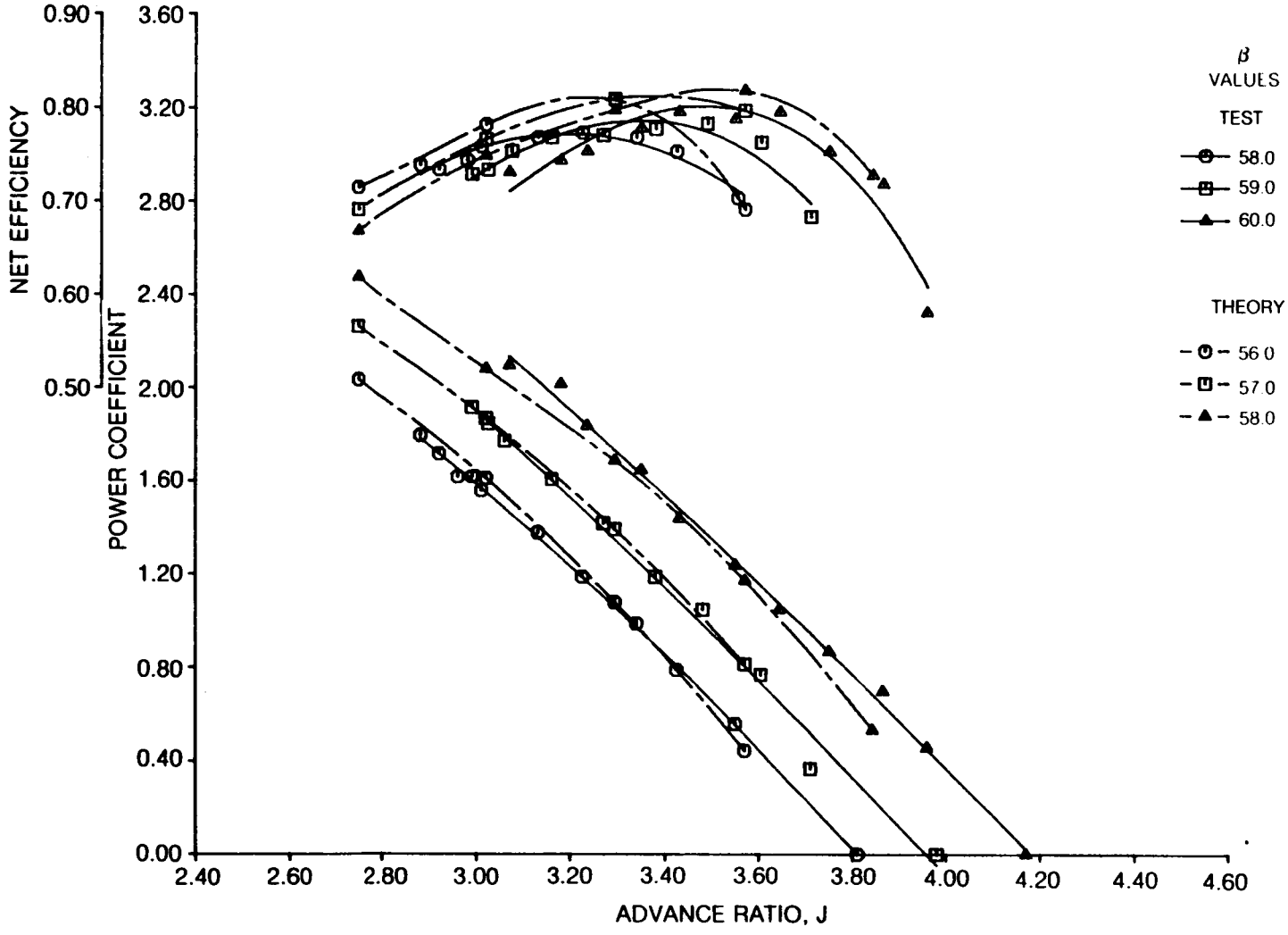

Figure 67c. Comparison of Measured and Predicted SR-2 Propeller Performance, M = 0.8 -Modeling Option 3

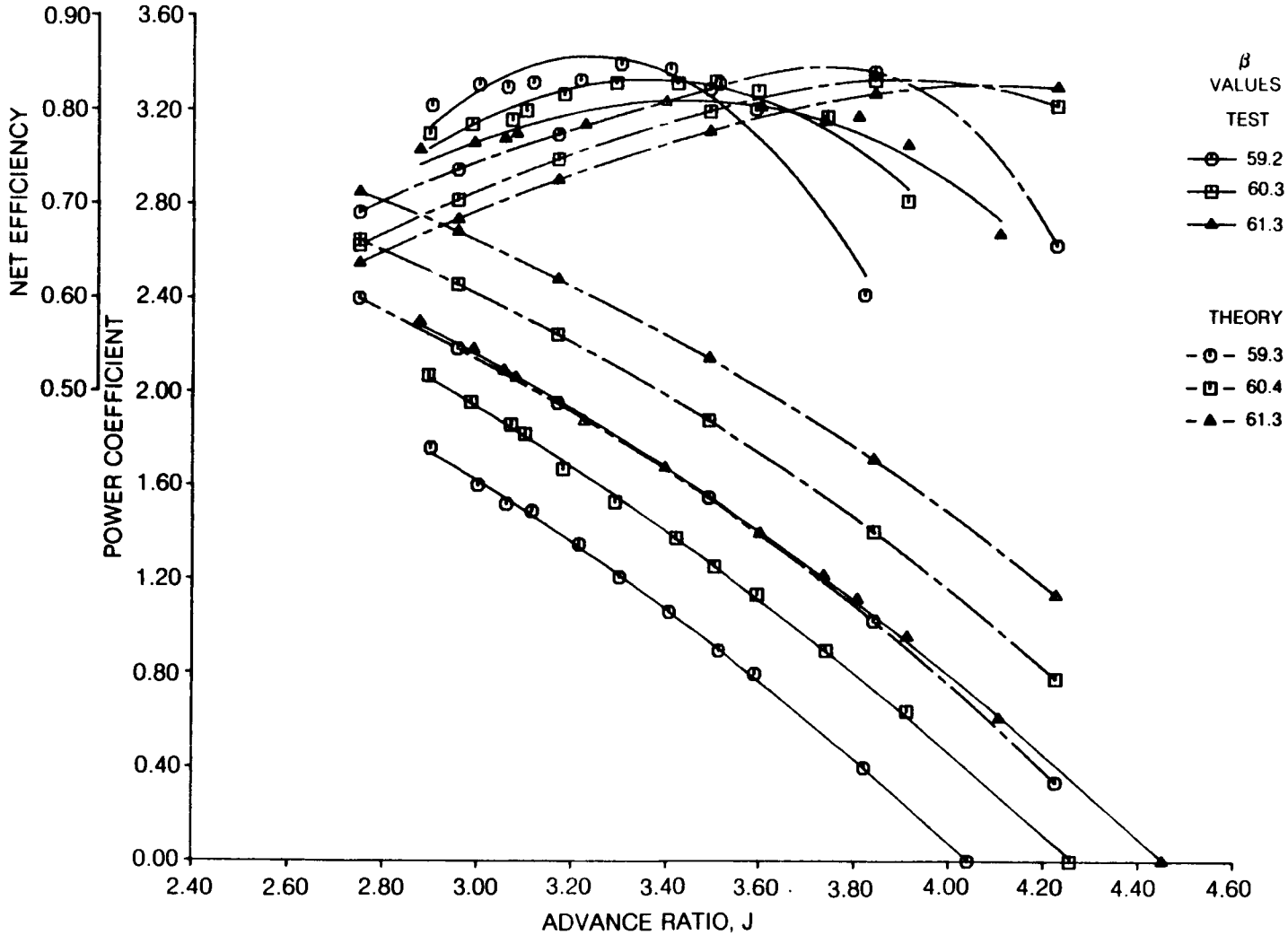

Figure 68a. Comparison of Measured and Predicted SR-1M Propeller Performance M = 0.6 -Modeling Option 1

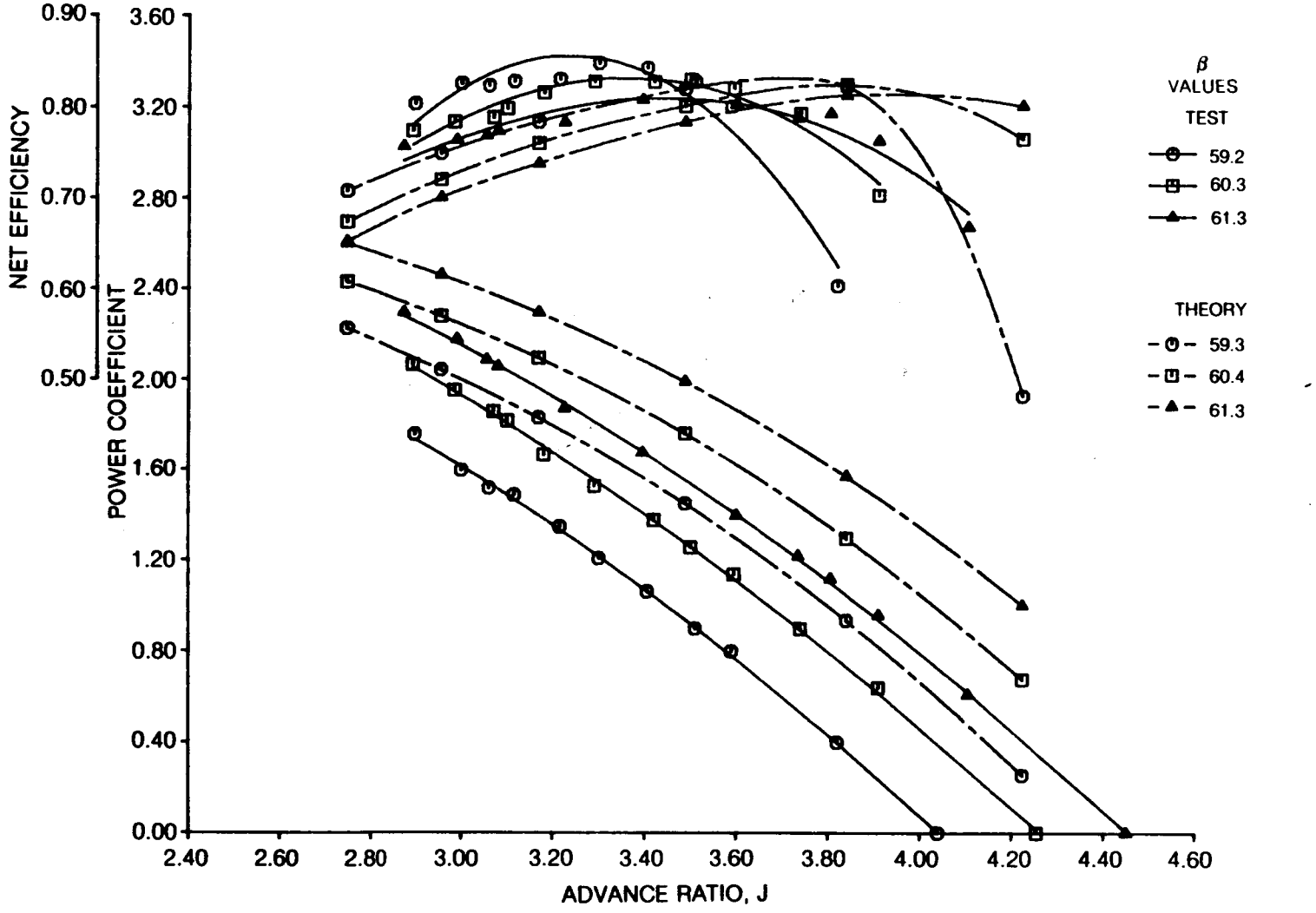

Figure 68b. Comparison of Measured and Predicted SR-1M Propeller Performance M = 0.6 -Modeling Option 2

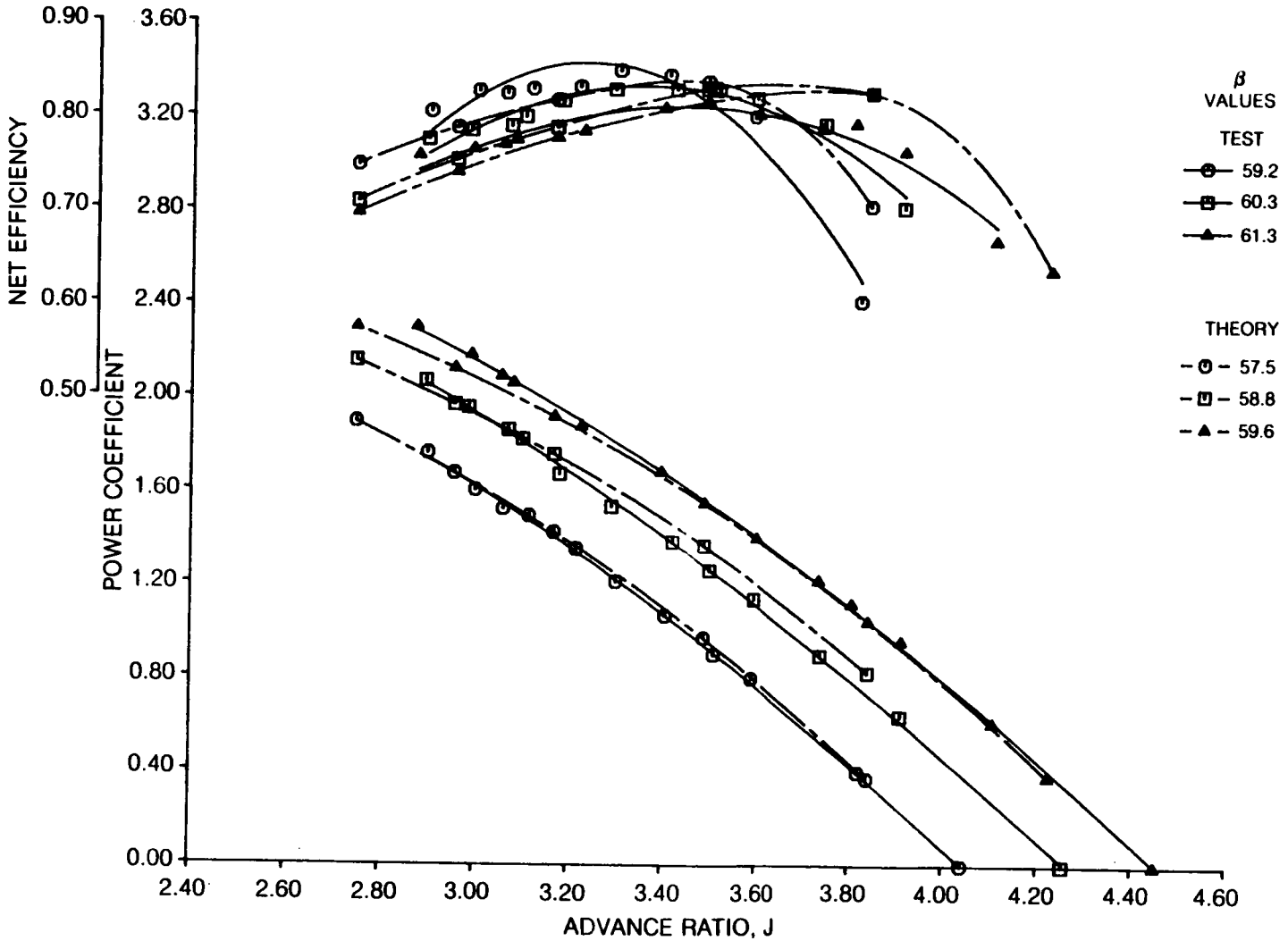

Figure 68c. Comparison of Measured and Predicted SR-1M Propeller Performance, M = 0.6 -Modeling Option 3

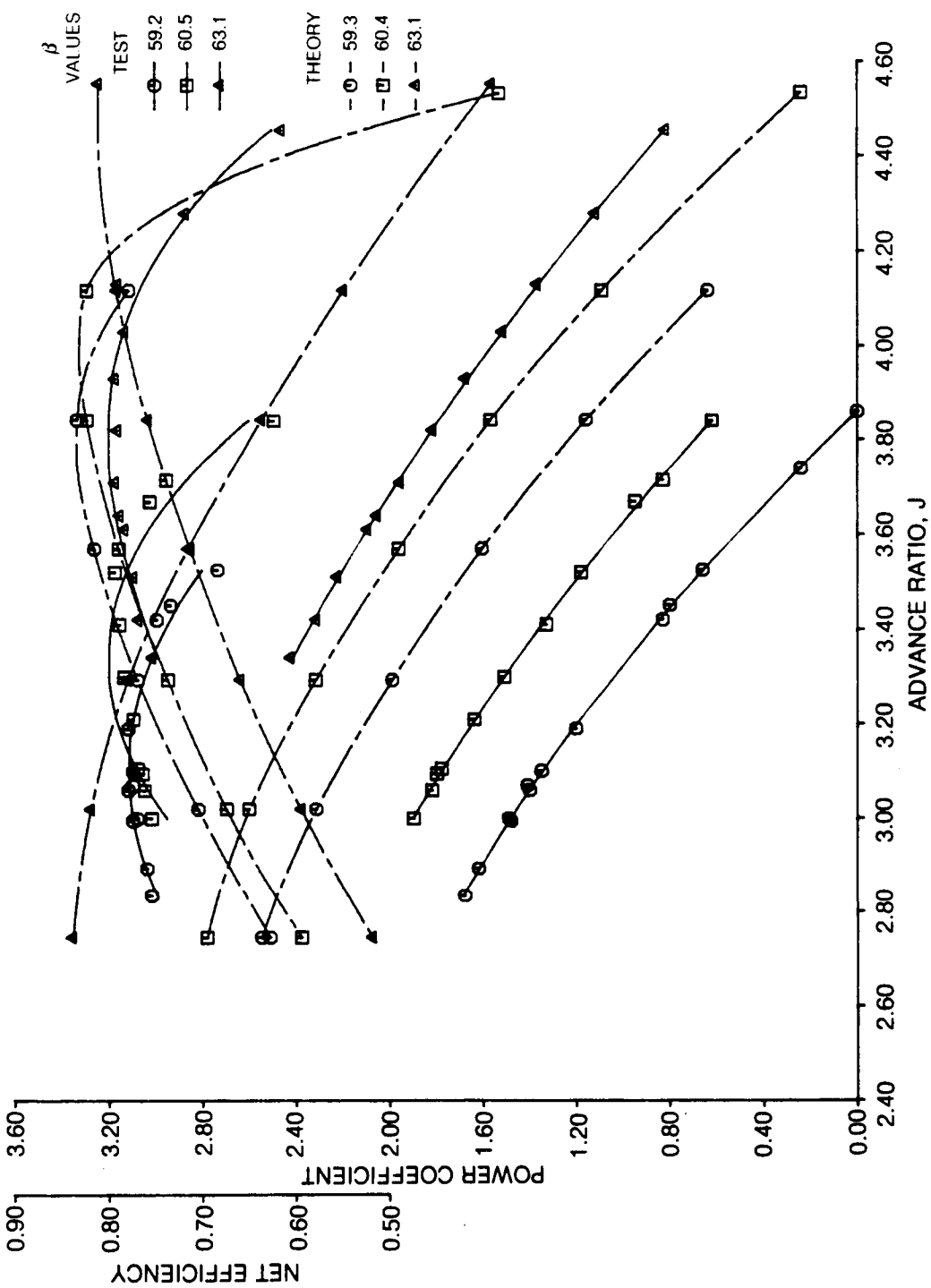

Figure 69a. Comparison of Measured and Predicted SR-1M Propeller Performance, M = 0.8 -Modeling Option 1

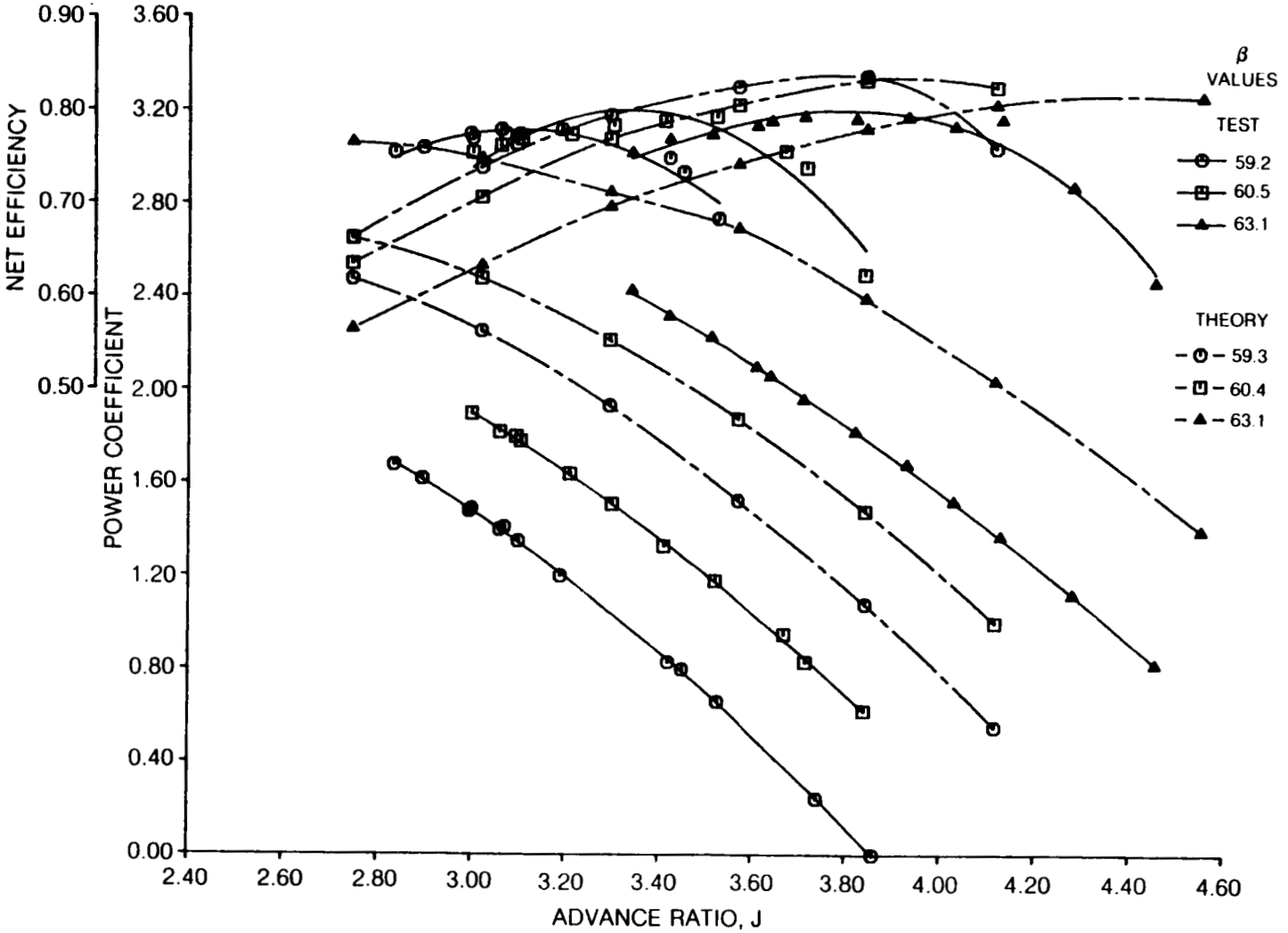

Figure 69b. Comparison of Measured and Predicted SR-1M Propeller Performance, M = 0.8 -Modeling Option 2

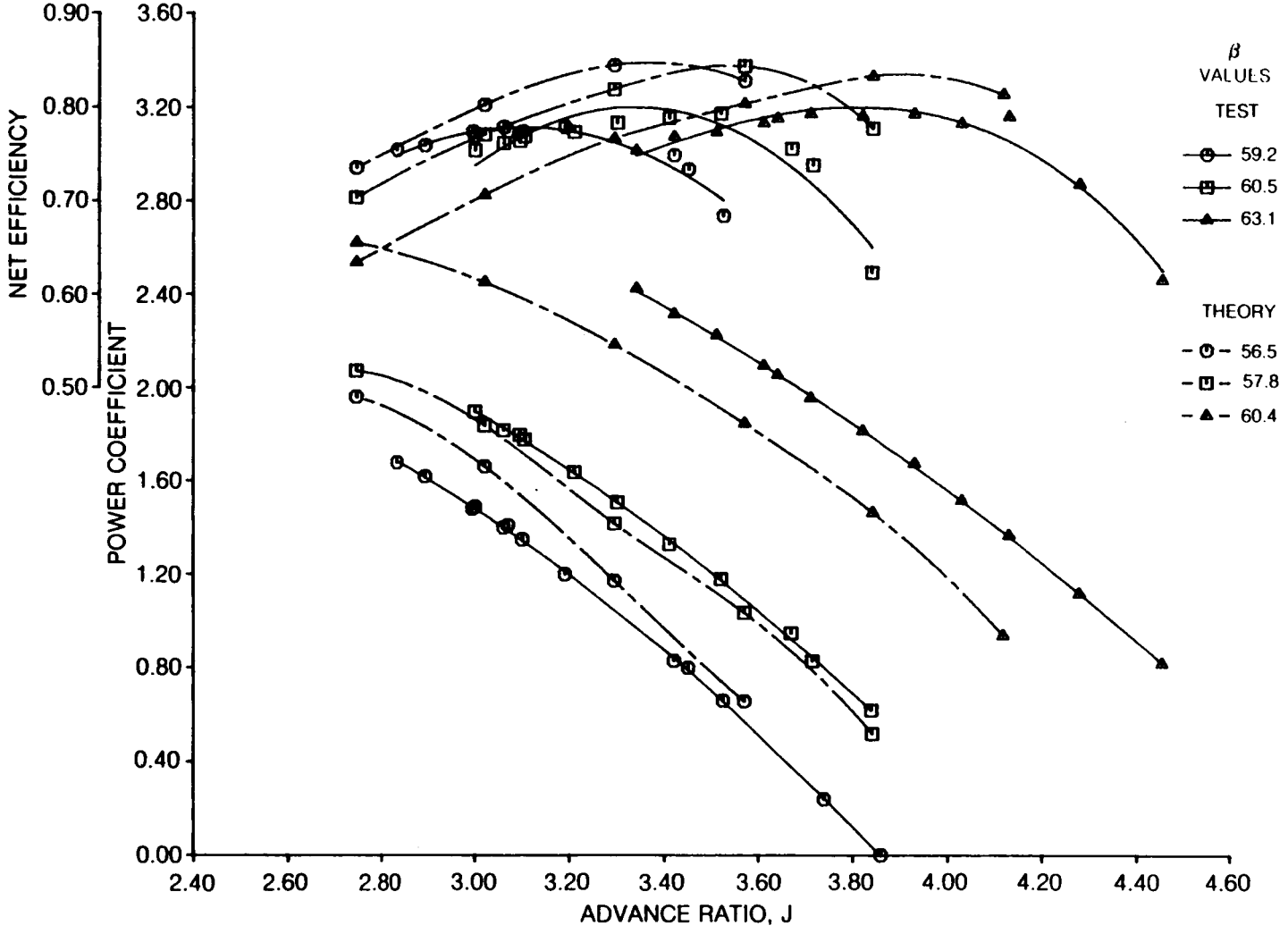

Figure 69c. Comparison of Measured and Predicted SR-1M Propeller Performance, M = 0.8 -Modeling Option 3

86-4-60-17

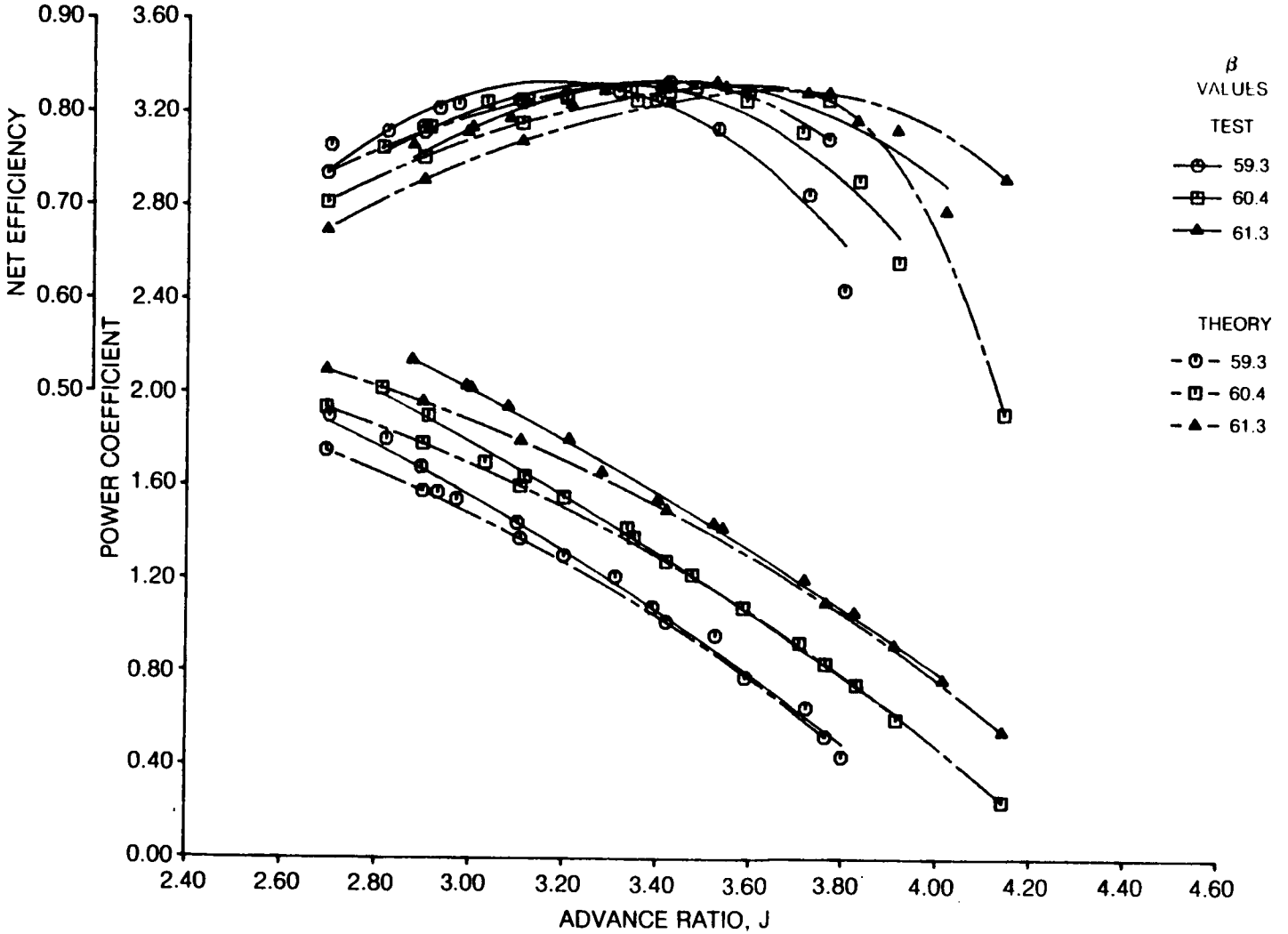

Figure 70a. Comparison of Measured and Predicted SR-3 Propeller Performance, M = 0.6 -Modeling Option 2

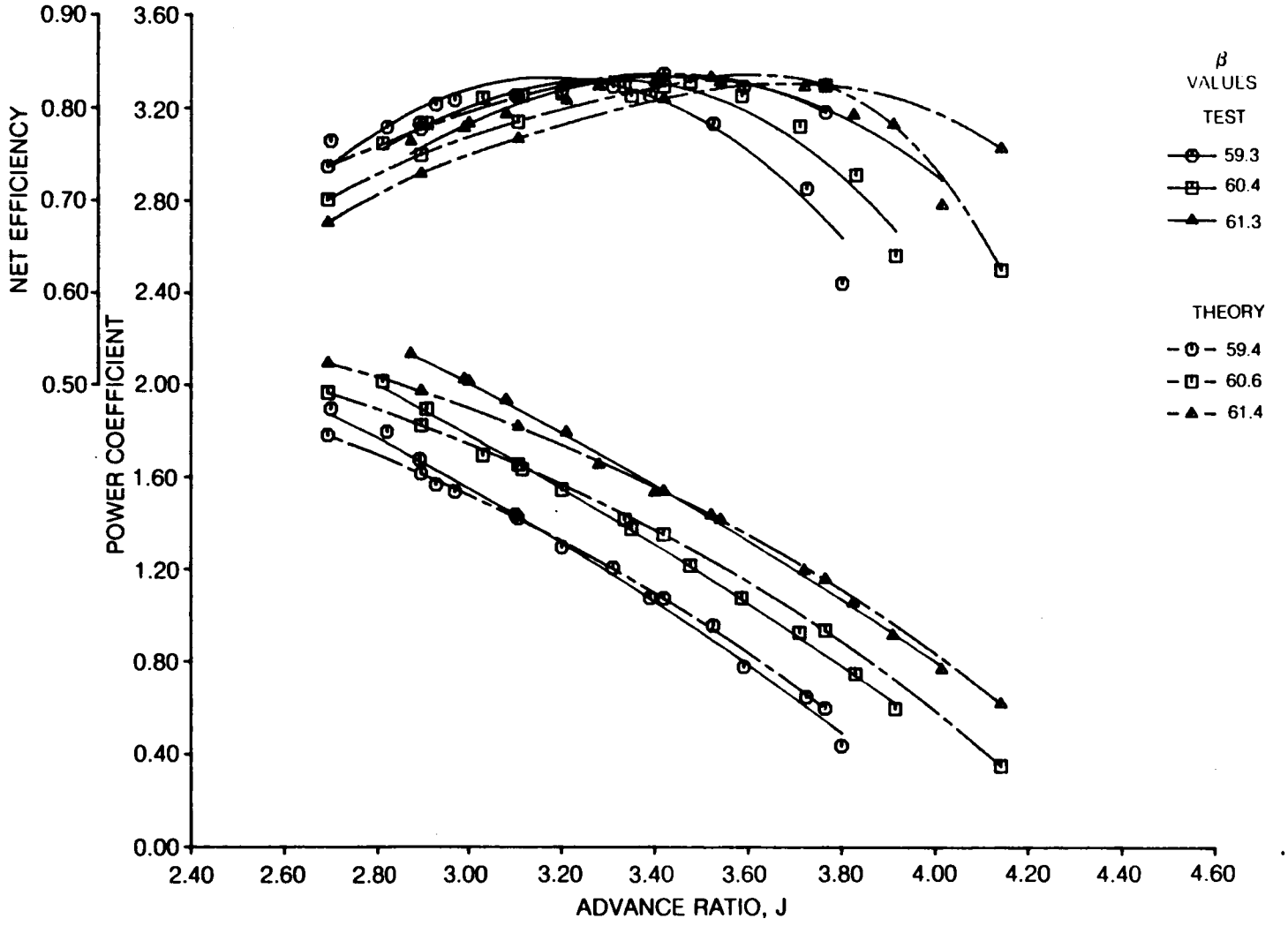

Figure 70b. Comparison of Measured and Predicted SR-3 Propeller Performance, M = 0.6 -Modeling Option 3

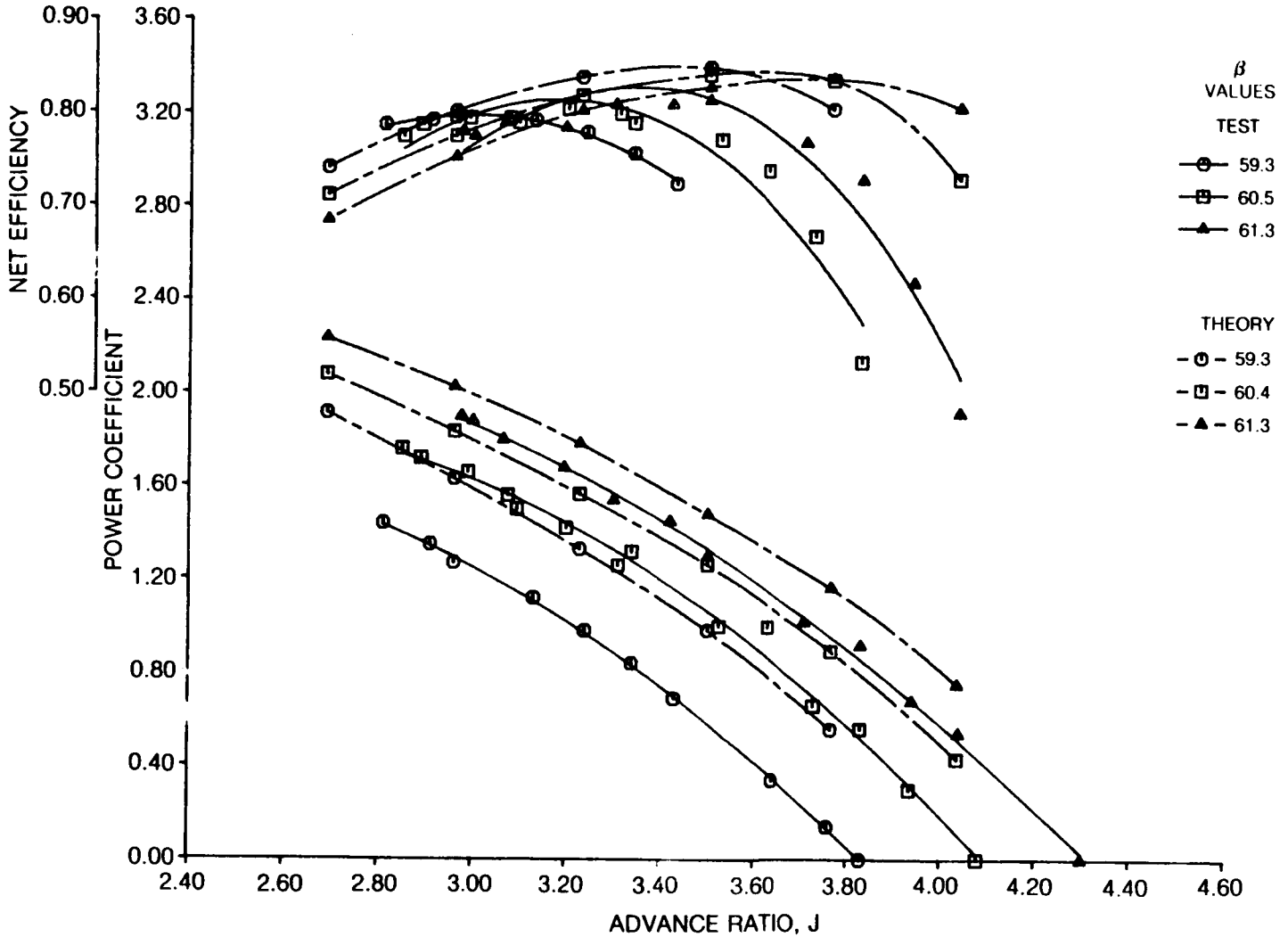

Figure 71a. Comparison of Measured and Predicted SR-3 Propeller Performance, M = 0.8 -Modeling Option 2

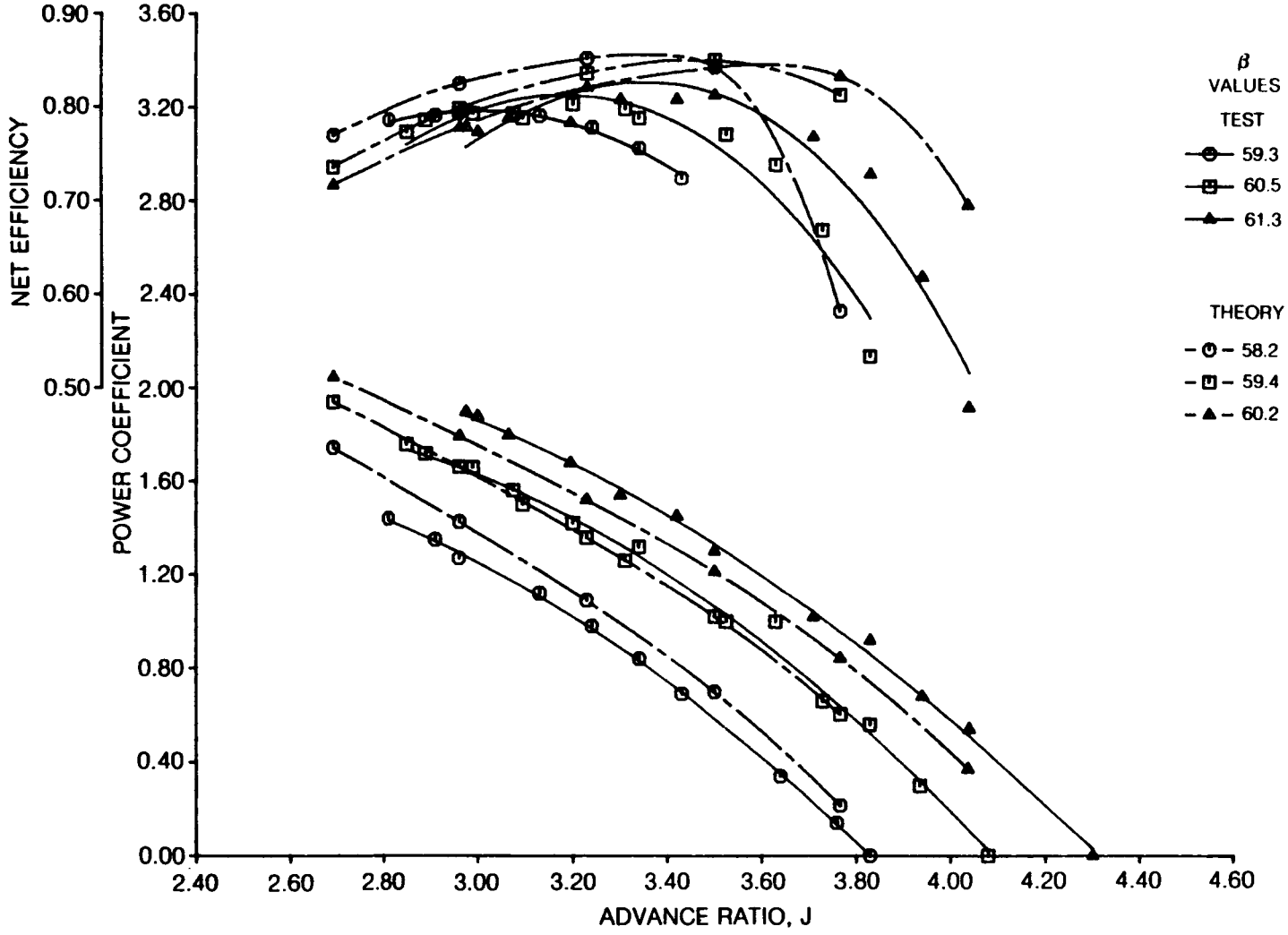

Figure 71b. Comparison of Measured and Predicted SR-3 Propeller Performance, M = 0.8 -Modeling Option 3

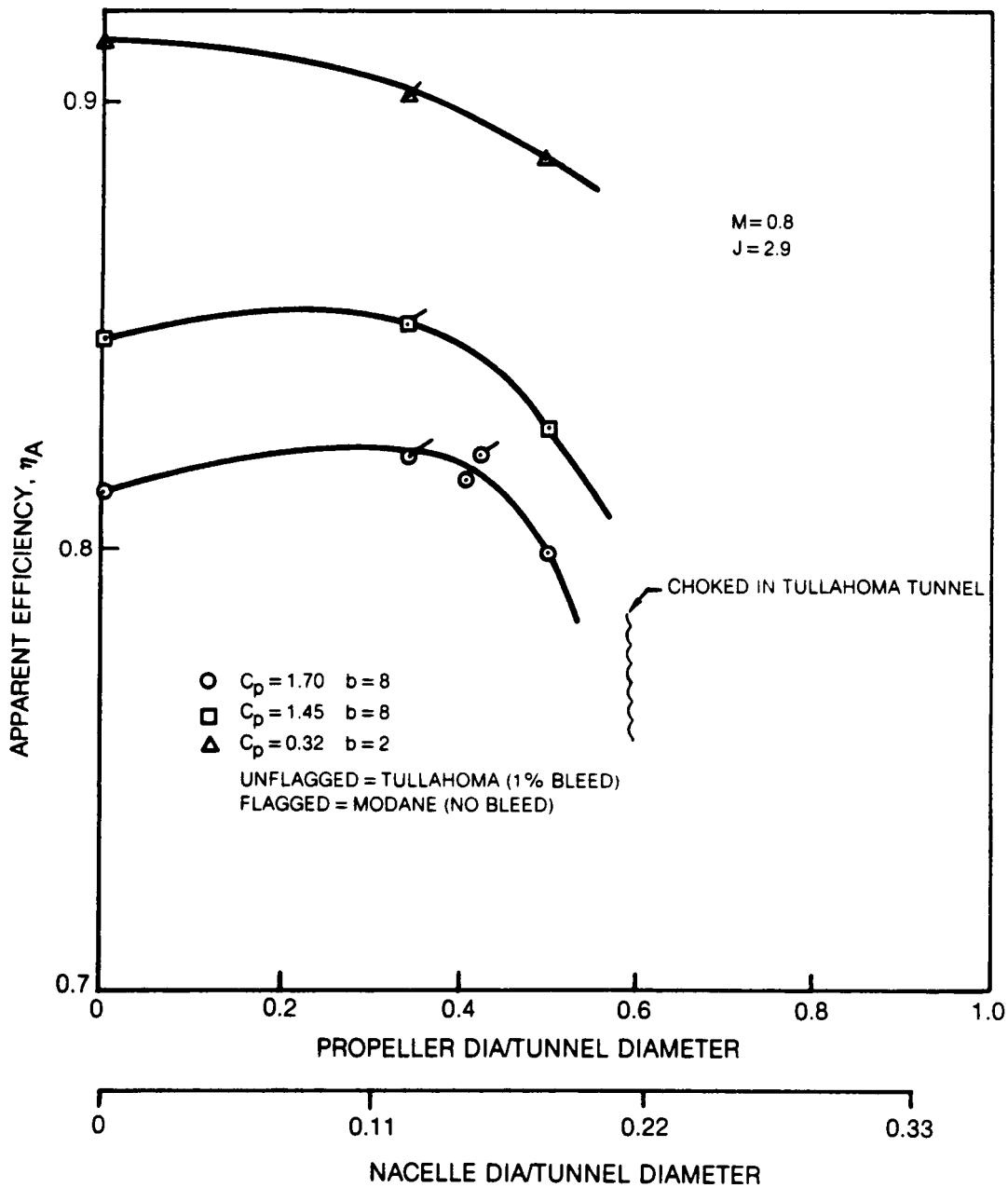

Figure 72. Predicted Effect of Propeller/Tunnel Size on SR-3 Propeller Performance

84-6-73-42

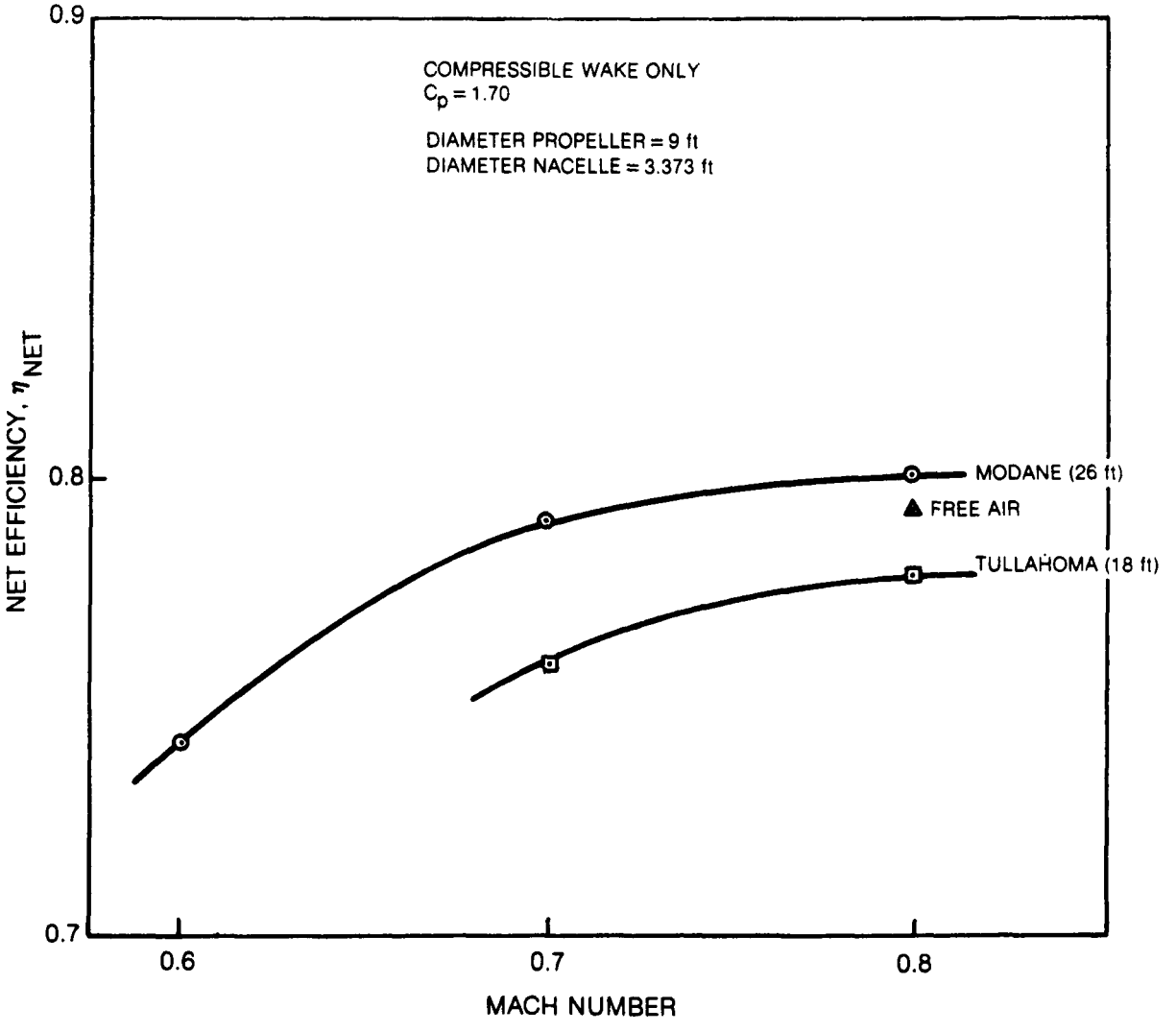

Figure 73. Influence of Tunnel Size on Predicted Propeller Performance for a Fixed Propeller/Nacelle Configuration (SR-3)

84-6-73-43

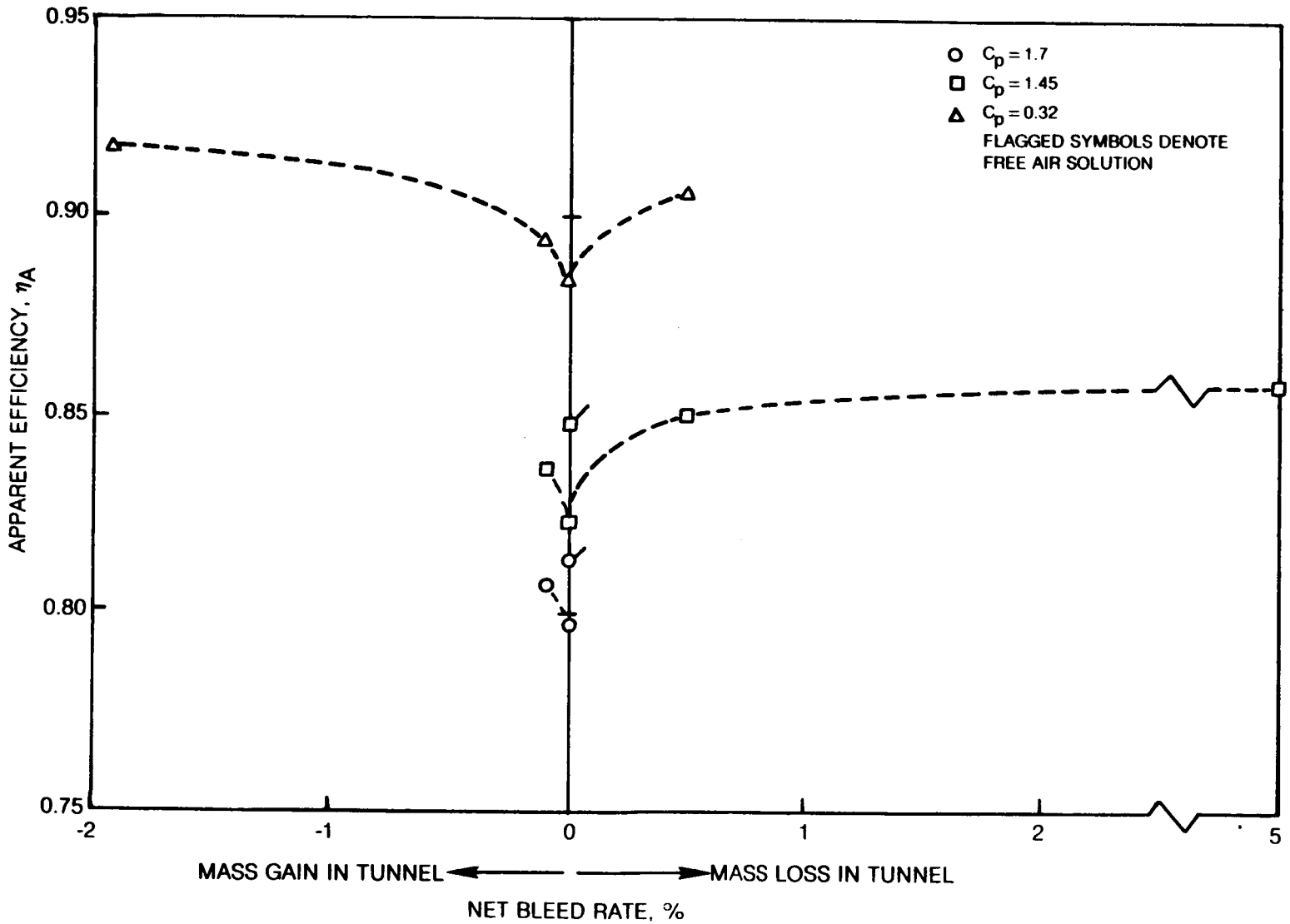

Figure 74. Effect of Tunnel Bleed on Predicted SR-3 Propeller Performance

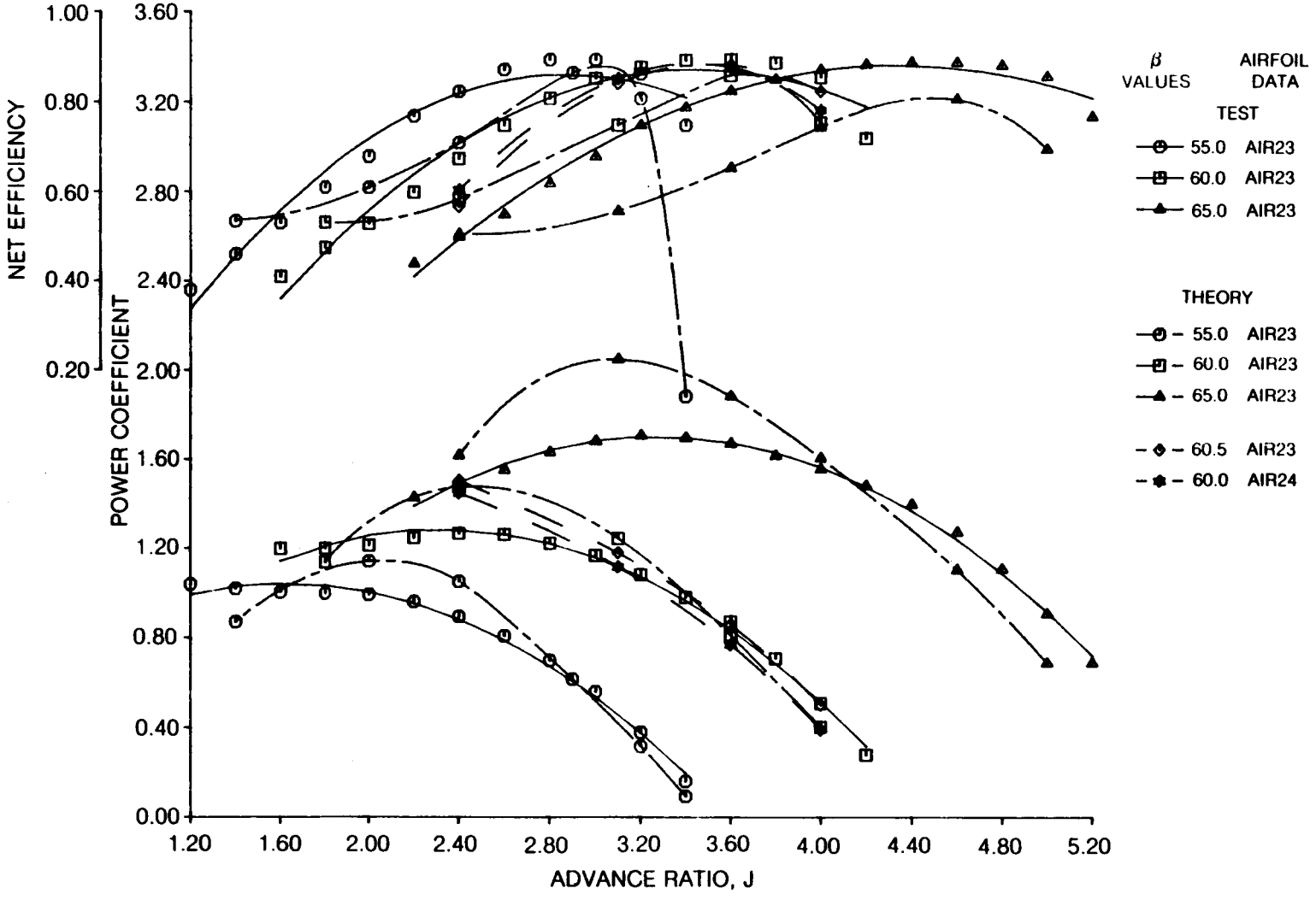

Figure 75. Comparison of Predicted and Measured Power Coefficient for Coaxial Propeller -Low Speed (Ref. 72)

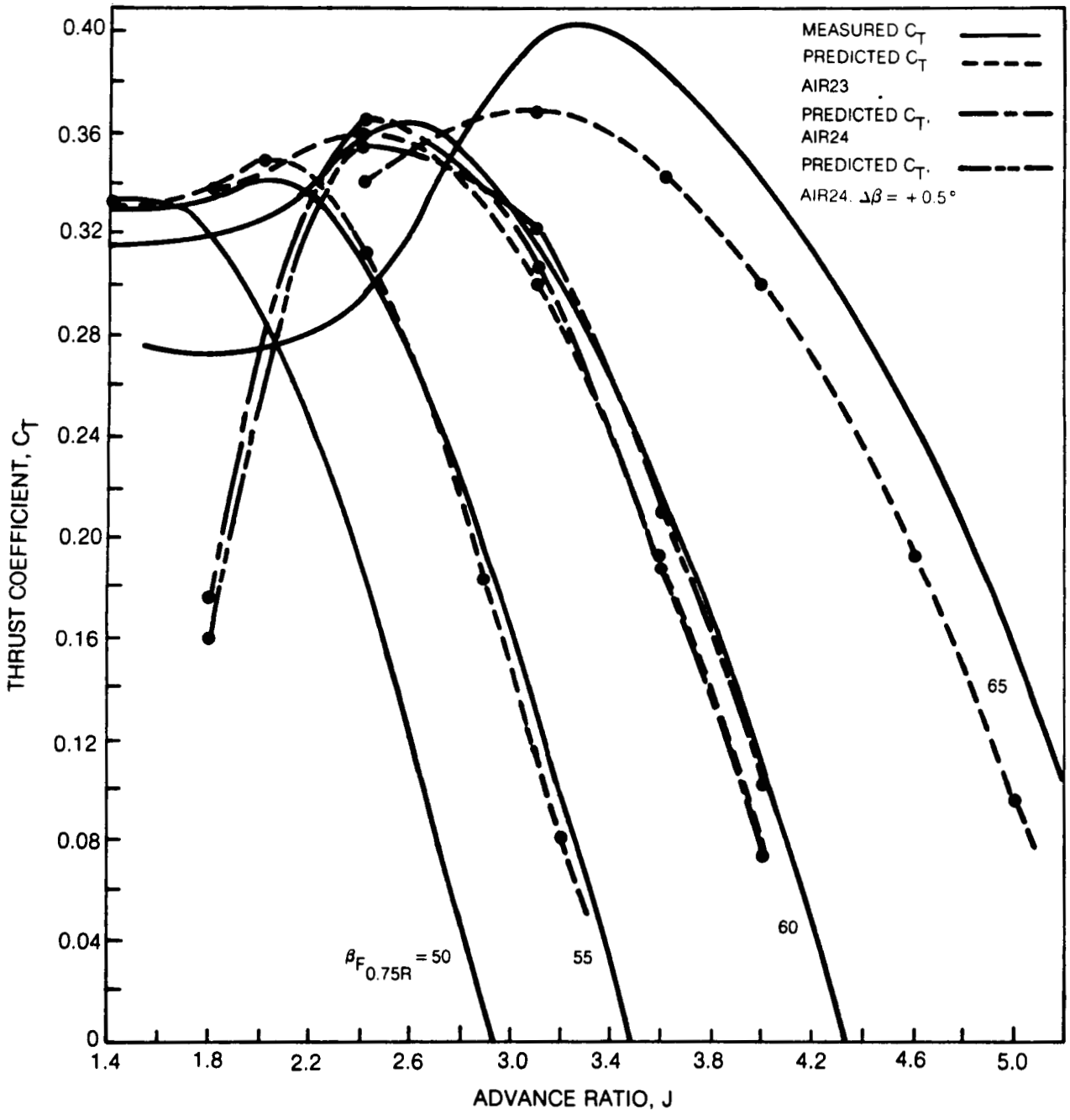

Figure 76. Comparison of Predicted and Measured Thrust Coefficient for Coaxial Propeller — Low Speed (Ref. 72)

84-6-73-46

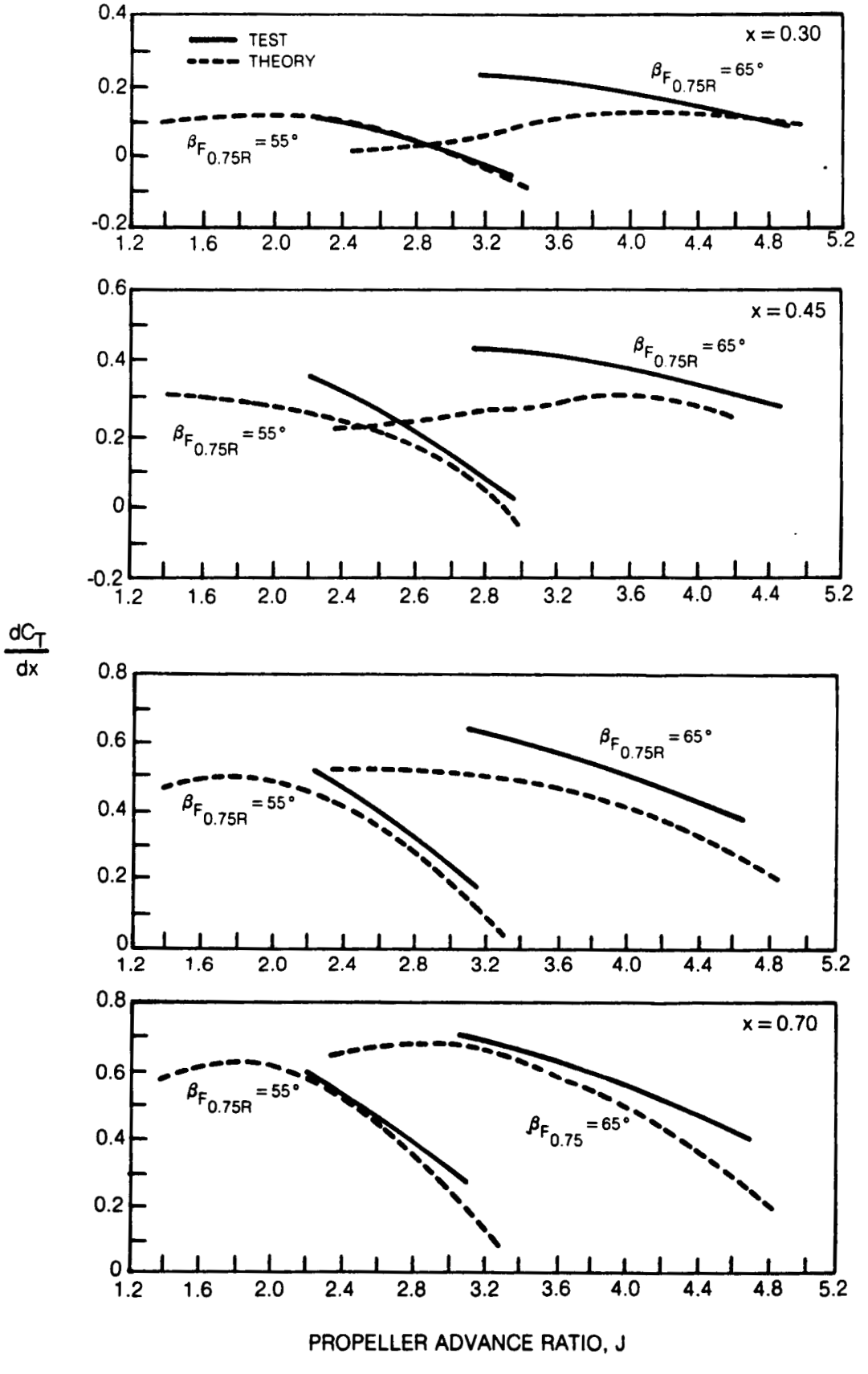

Figure 77. Comparison of Blade Section Differential Thrust — Low Speed (Ref. 72)

84-6-73-47

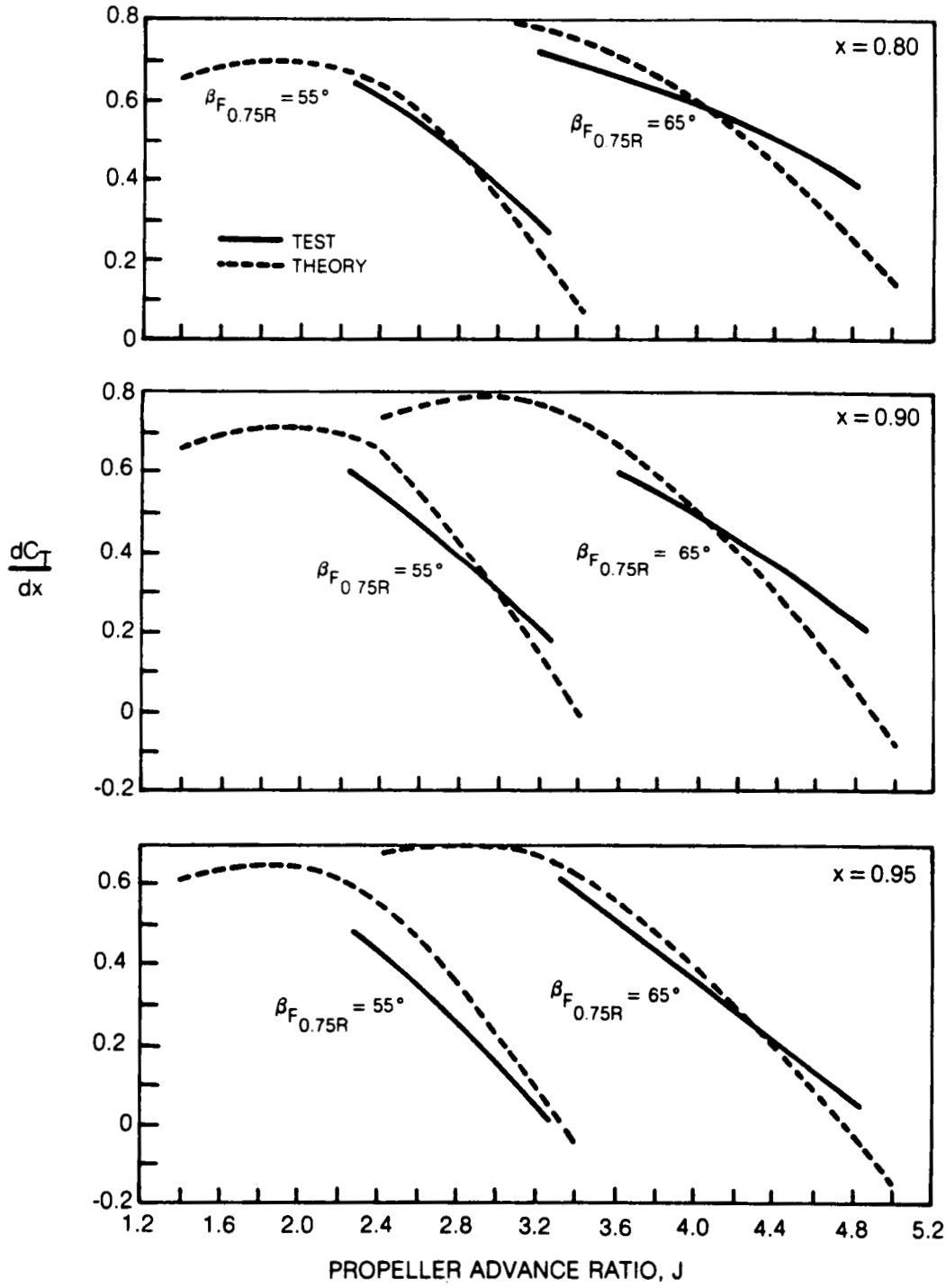

Figure 77. Continued

84-6-73-48

ALL DIMENSIONS IN INCHES
PROPELLER BLADES SHOWN IN DEVELOPED PLAN FORM
SPINNERS ARE CONTOURED TO THE NACA 1-SERIES PROFILE (REF. 12)
PLANFORMS ALINE WITH BLADES WHEN $\beta_F = 65°$ AND $\beta_R = 64.2°$ ($\beta = 60°$ FOR SINGLE)

PLANFORM COORDINATES			
FRONT		REAR	
x_p	y_p	x_p	y_p
3.482	2.890	8.582	3.655
3.720	2.924	8.820	3.695
3.920	2.992	9.220	3.760
4.320	3.167	9.620	3.825
4.720	3.220	10.020	3.860
6.520	3.220	11.420	3.860
6.920	3.317	11.820	3.890
7.320	3.411	12.220	3.950
7.706	3.502	12.806	4.040

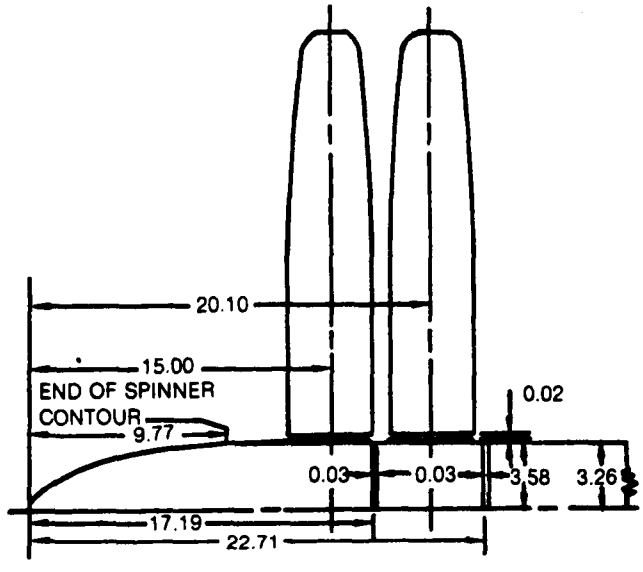

(a) SPINNER A

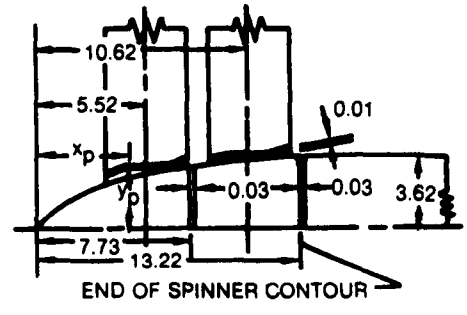

(b) SPINNER B

Figure 78. Spinner Planforms for Moderate Speed Coaxial Propeller Study (Ref. 73)

84-6-73-49

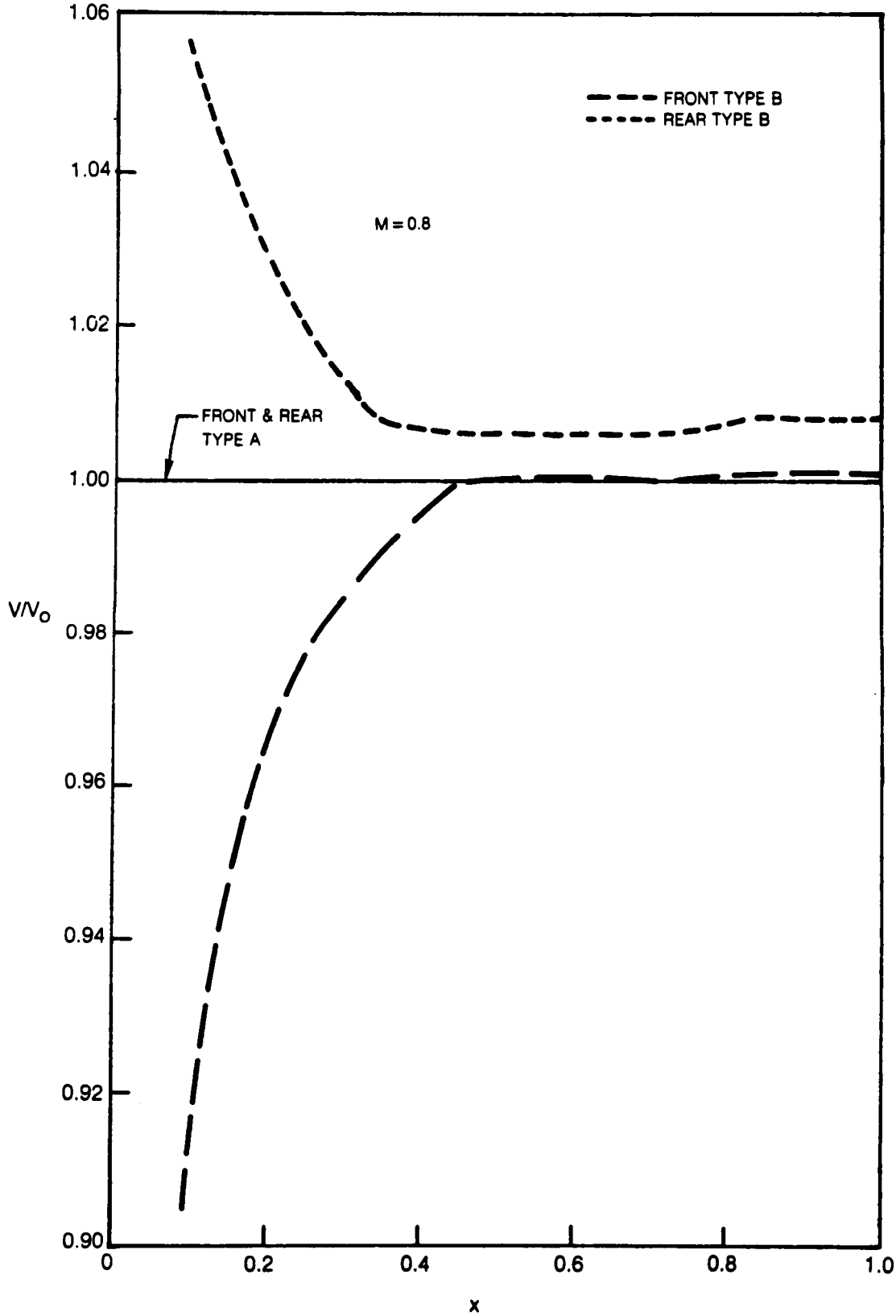

Figure 79. Comparison of Predicted Nacelle Induced Inflow Profiles for Type A & B Nacelles of Ref. 73

84-6-73-50

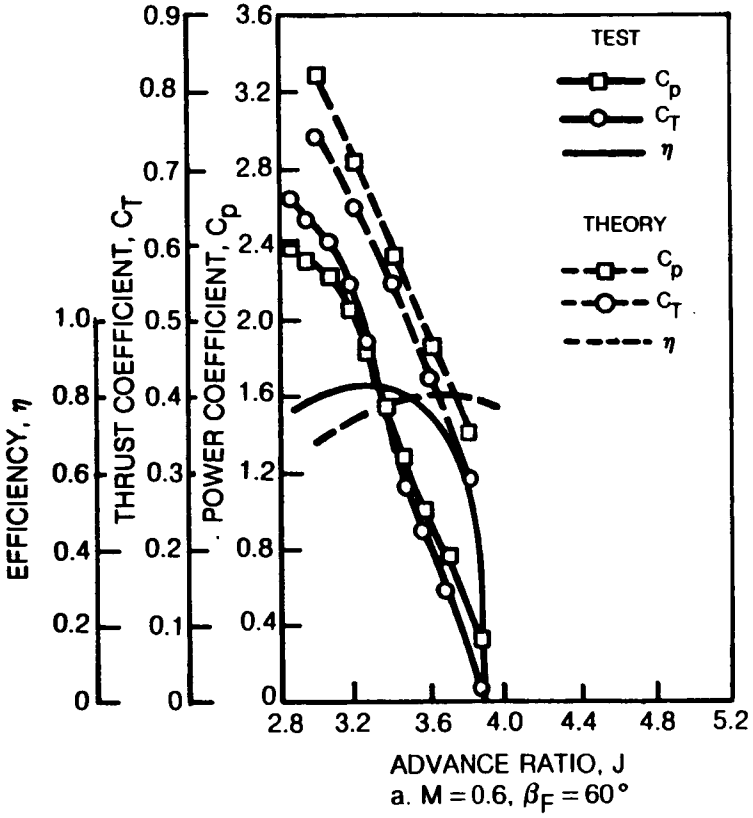

a. M = 0.6, $\beta_F = 60°$

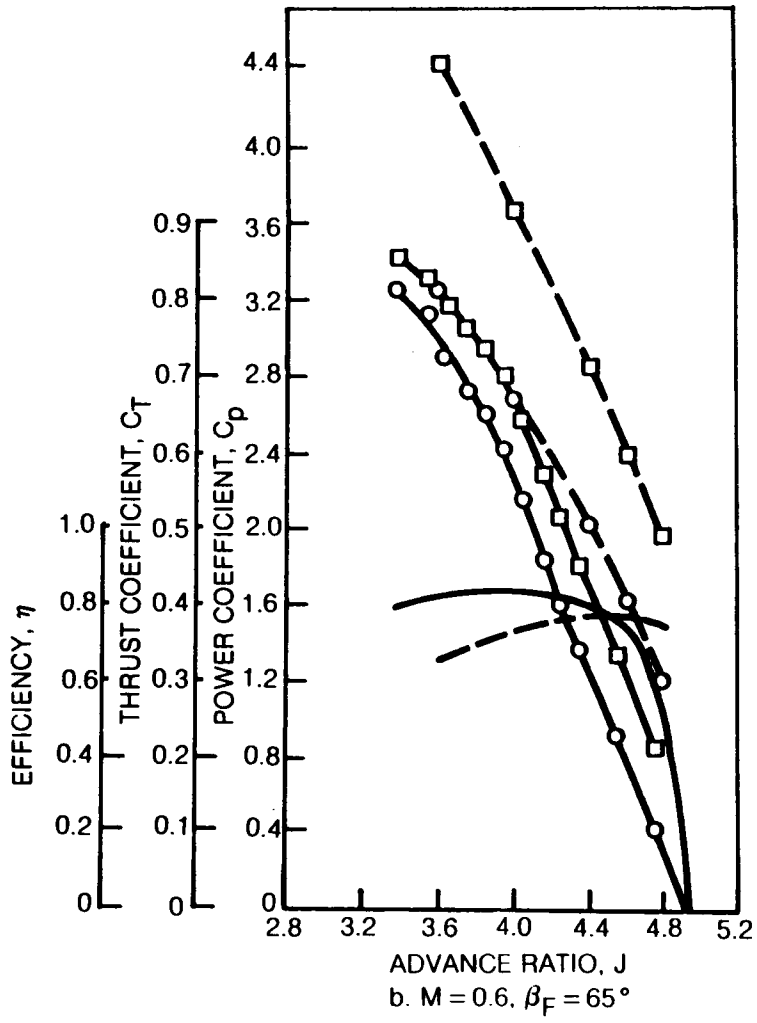

b. M = 0.6, $\beta_F = 65°$

Figure 80 Comparison of Measured and Predicted Coaxial Propeller Performance with Spinner A and Optimum $\Delta\beta$ (Test Data From Fig. 8 of Ref. 73)

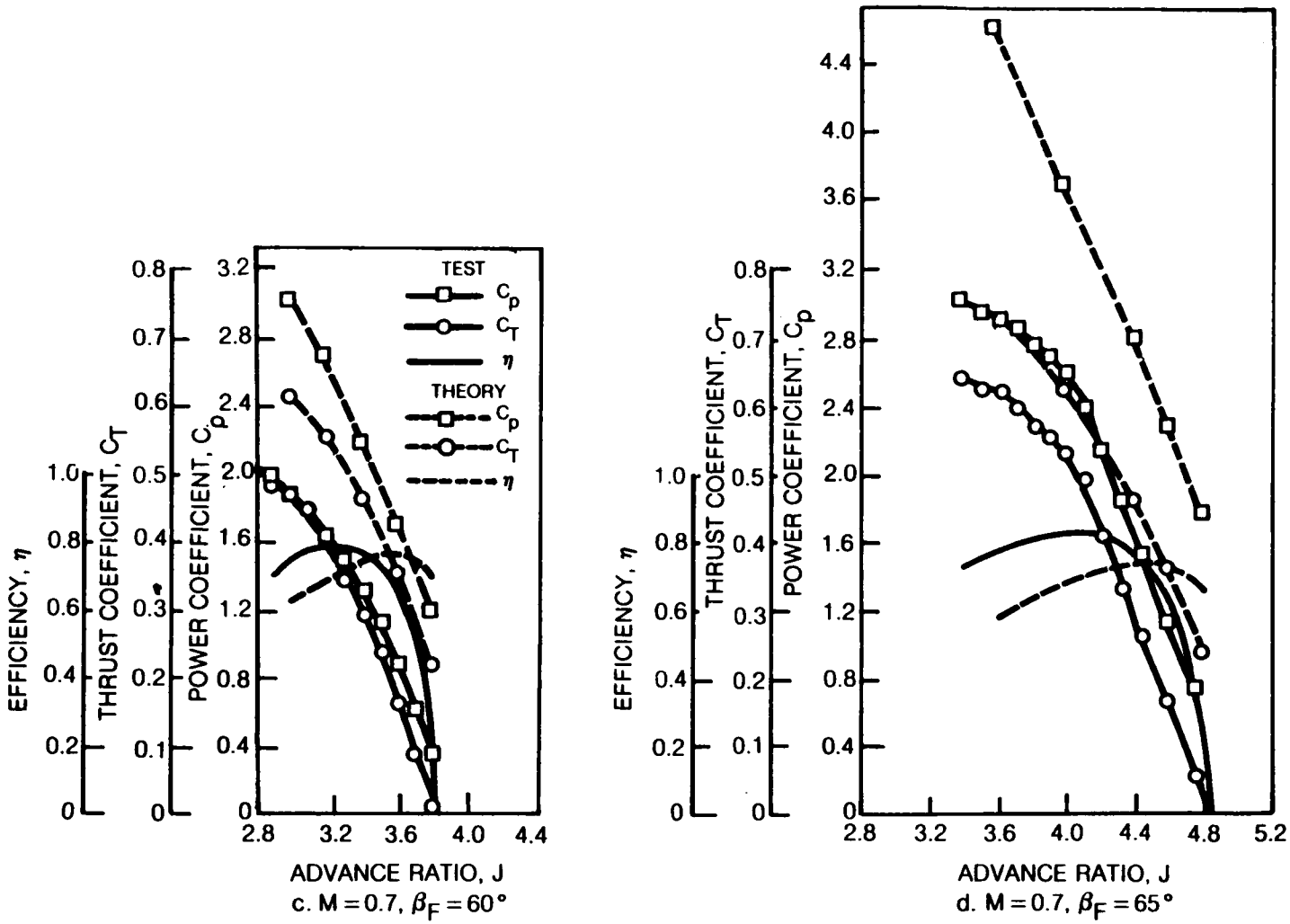

Figure 80 Continued

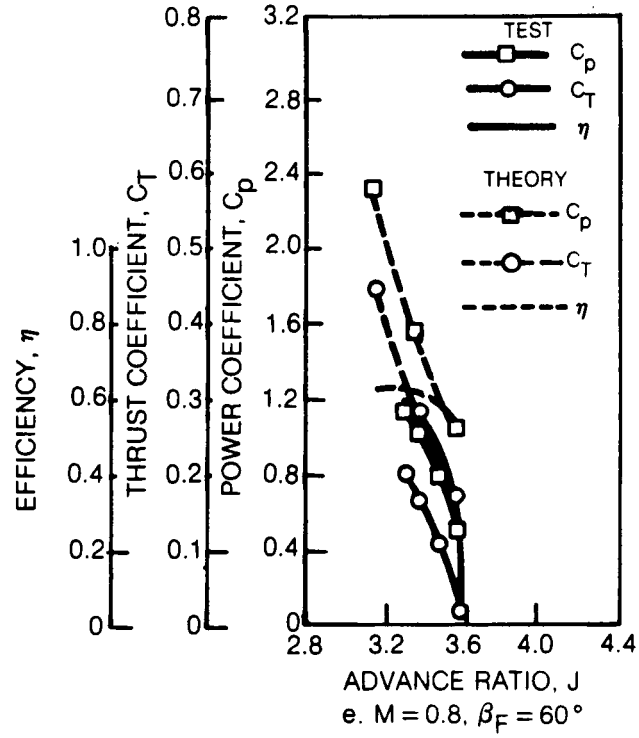

e. M = 0.8, β_F = 60°

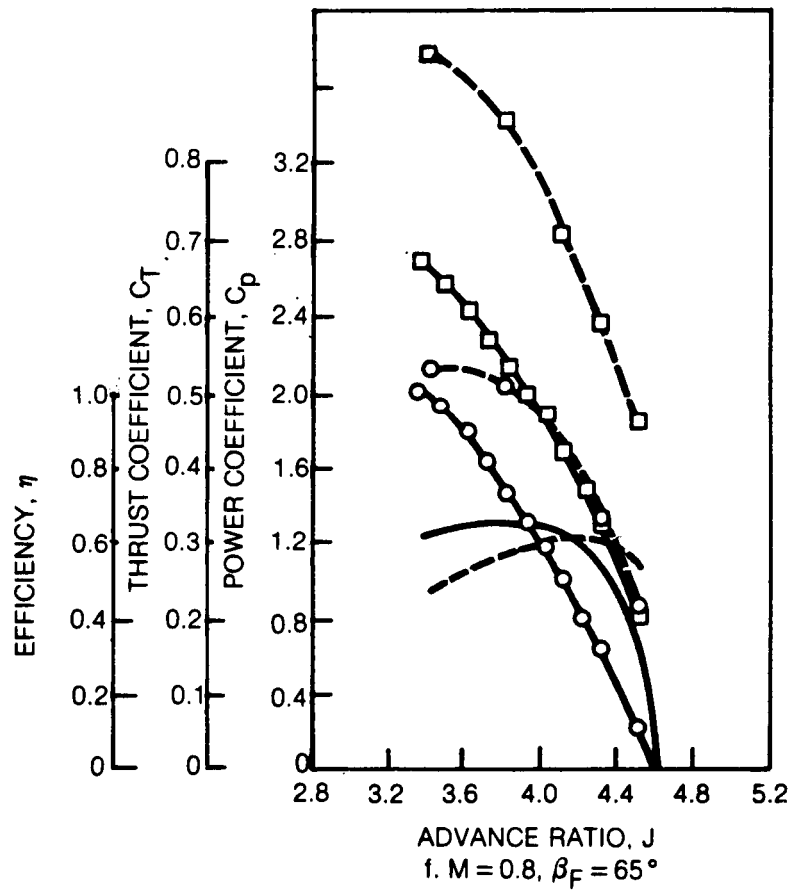

f. M = 0.8, β_F = 65°

Figure 80 Concluded

84-6-73-53

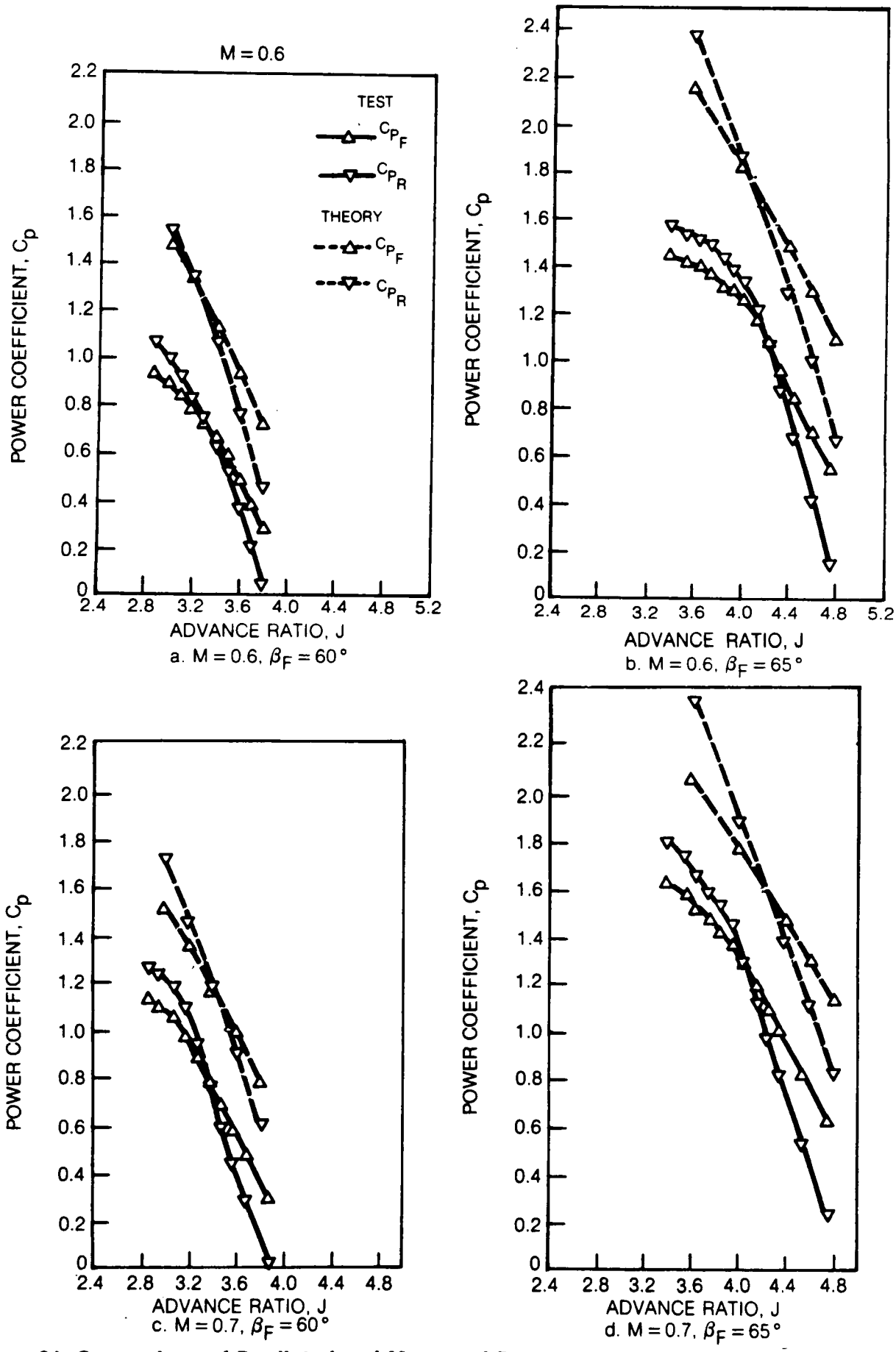

Figure 81 Comparison of Predicted and Measured Power Coefficient Variation Between Front and Rear Propellers, Optimum $\Delta\beta$ (Test Data From Fig. 14 of Ref. 73)

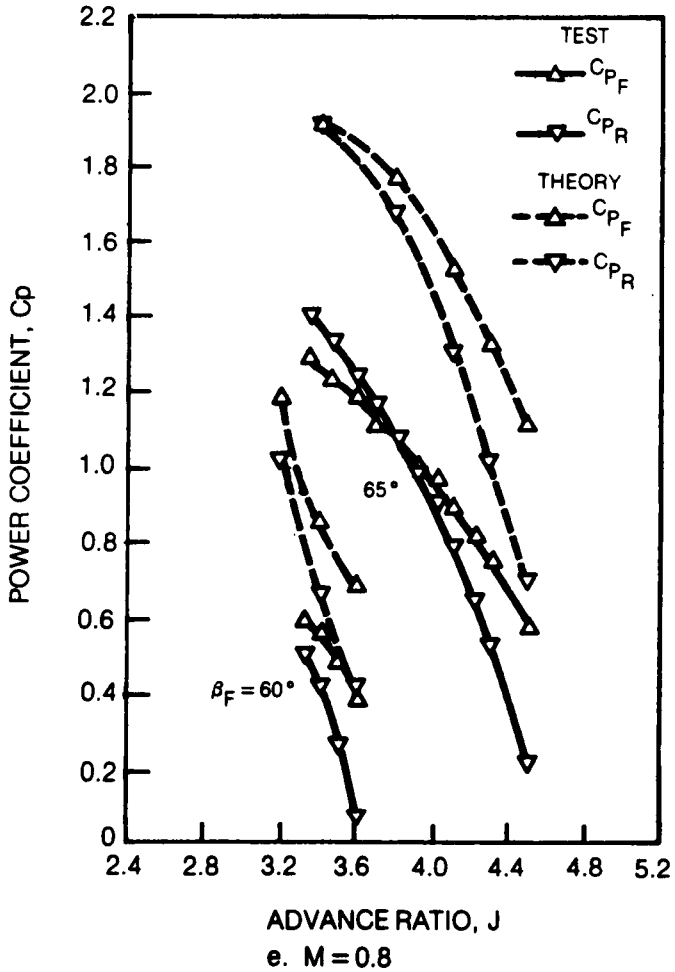

e. M = 0.8

Figure 81 Concluded

84-6-73-55

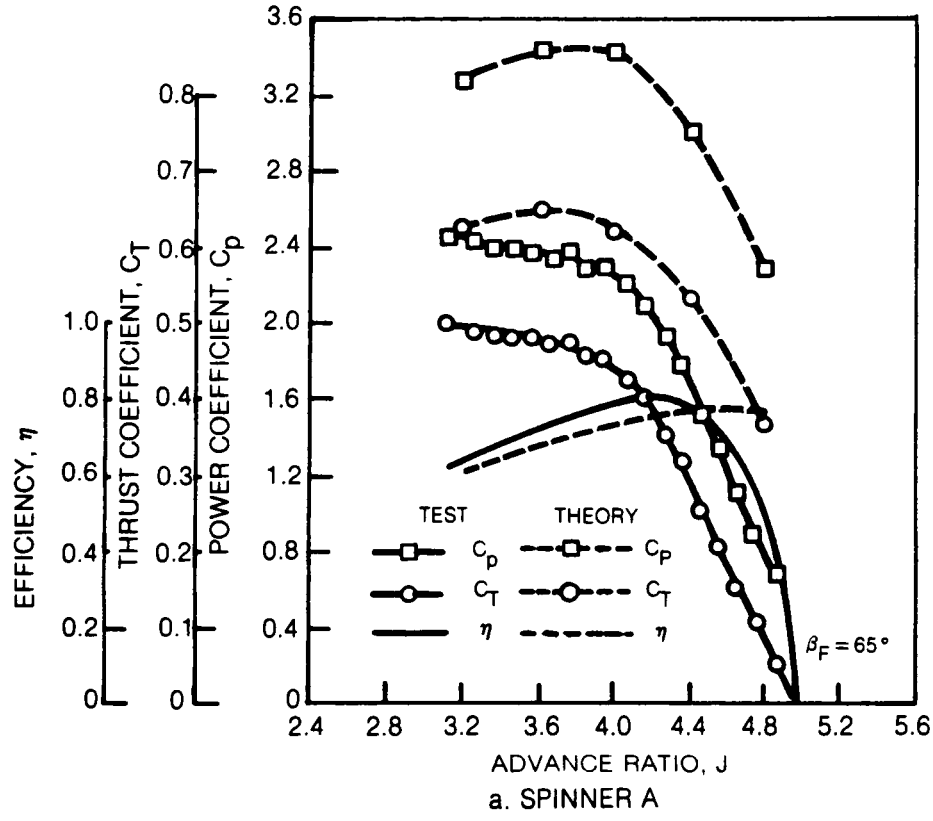

a. SPINNER A

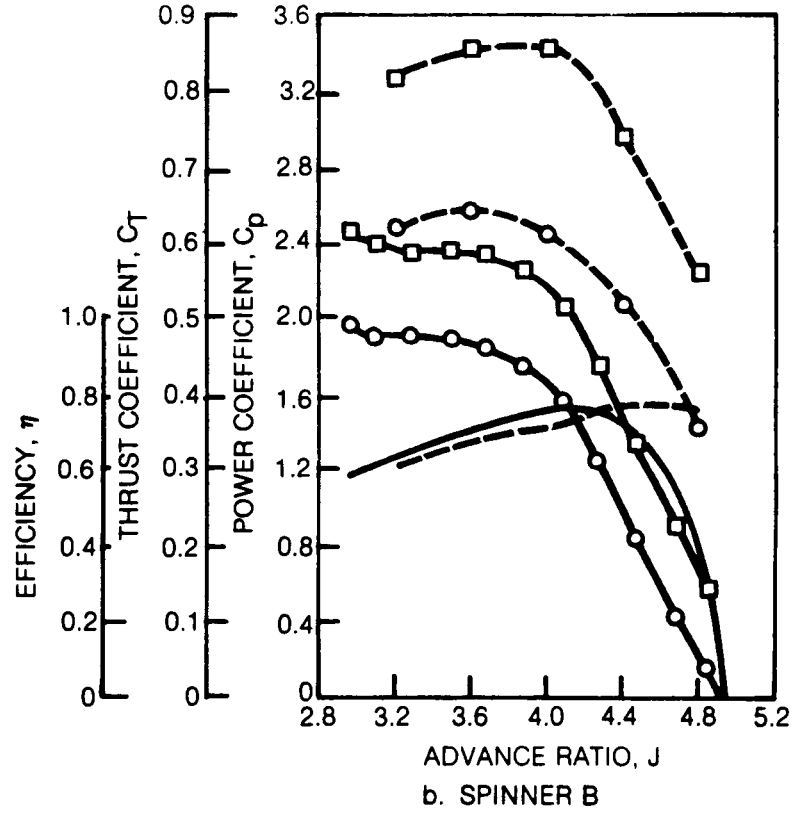

b. SPINNER B

Figure 82. Effect of Spinner Design on the Comparison of Predicted and Measured Propeller Performance, $\Delta\beta = 0.8°$, M = 0.70 (Ref. 73)

84-6-73-56

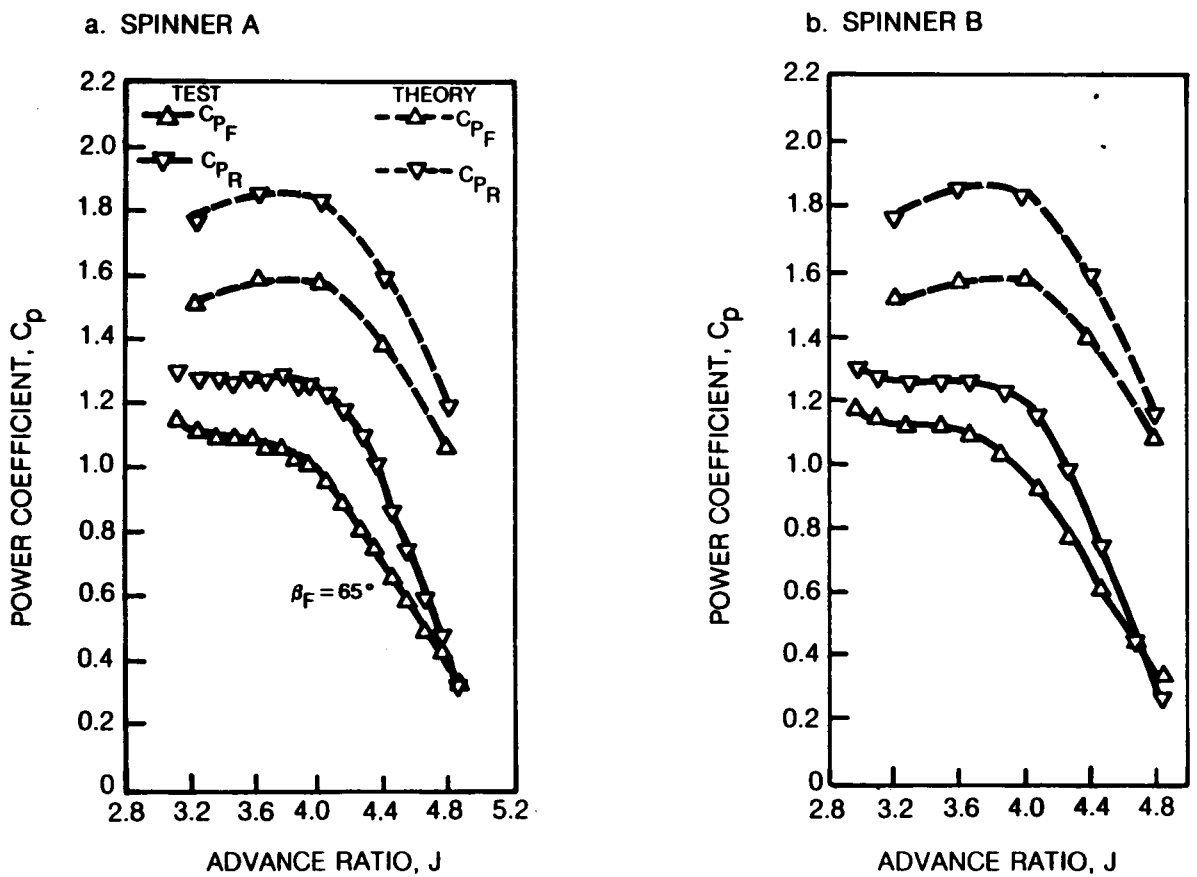

Figure 83. Comparison of Predicted and Measured Power Coefficient Variation Between Front and Rear Propellers, $\Delta\beta = 0.8°$, M = 0.70 (Test Data From Figs. 15, 16 of Ref. 73)

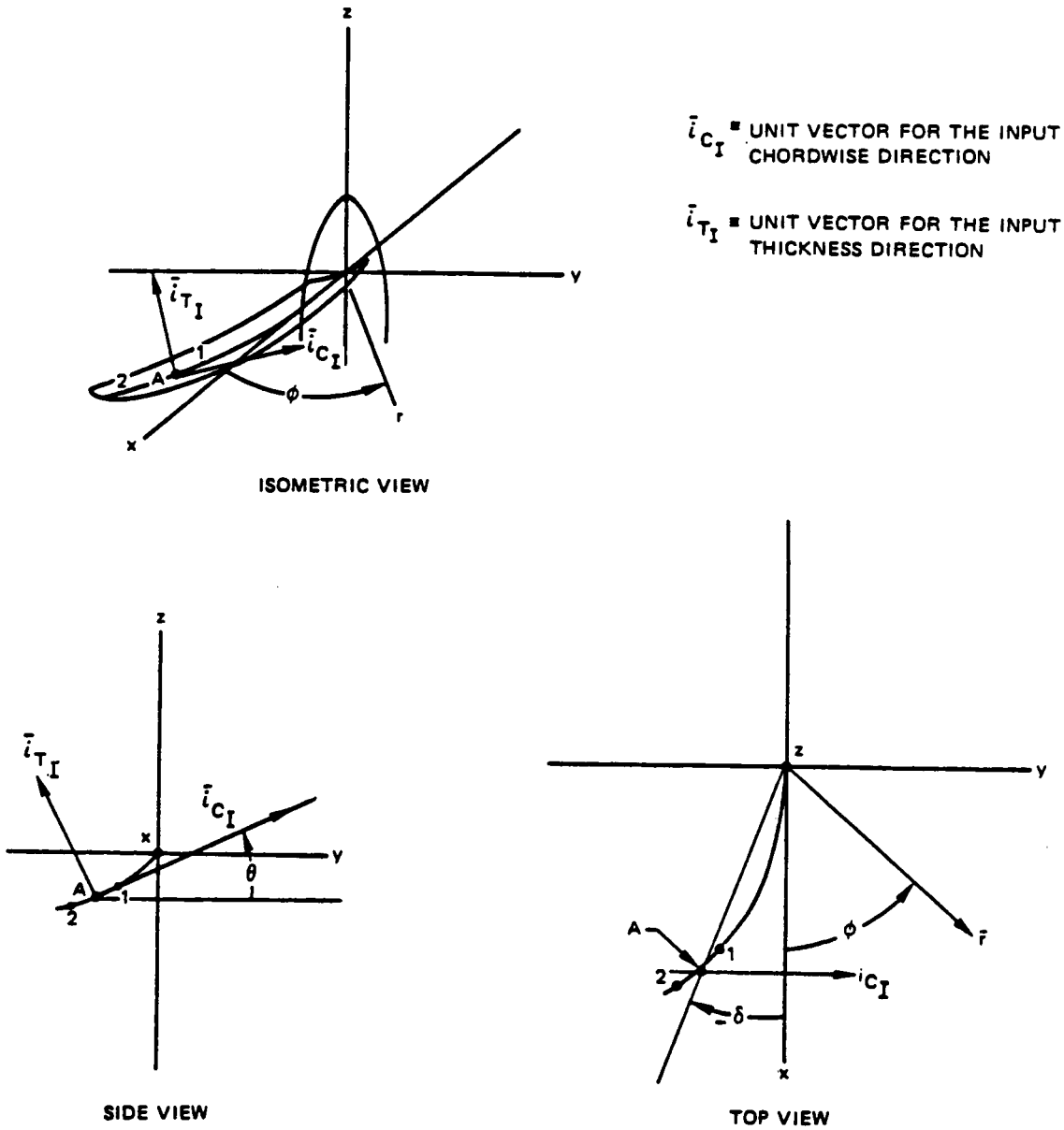

Figure 84. Blade Coordinate Systems

85-4-90-47

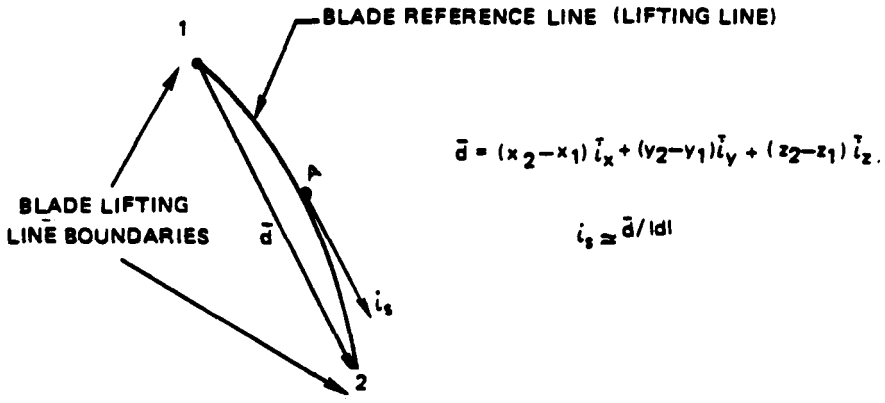

Figure 85. Spanwise Unit Vector

85-4-90-46

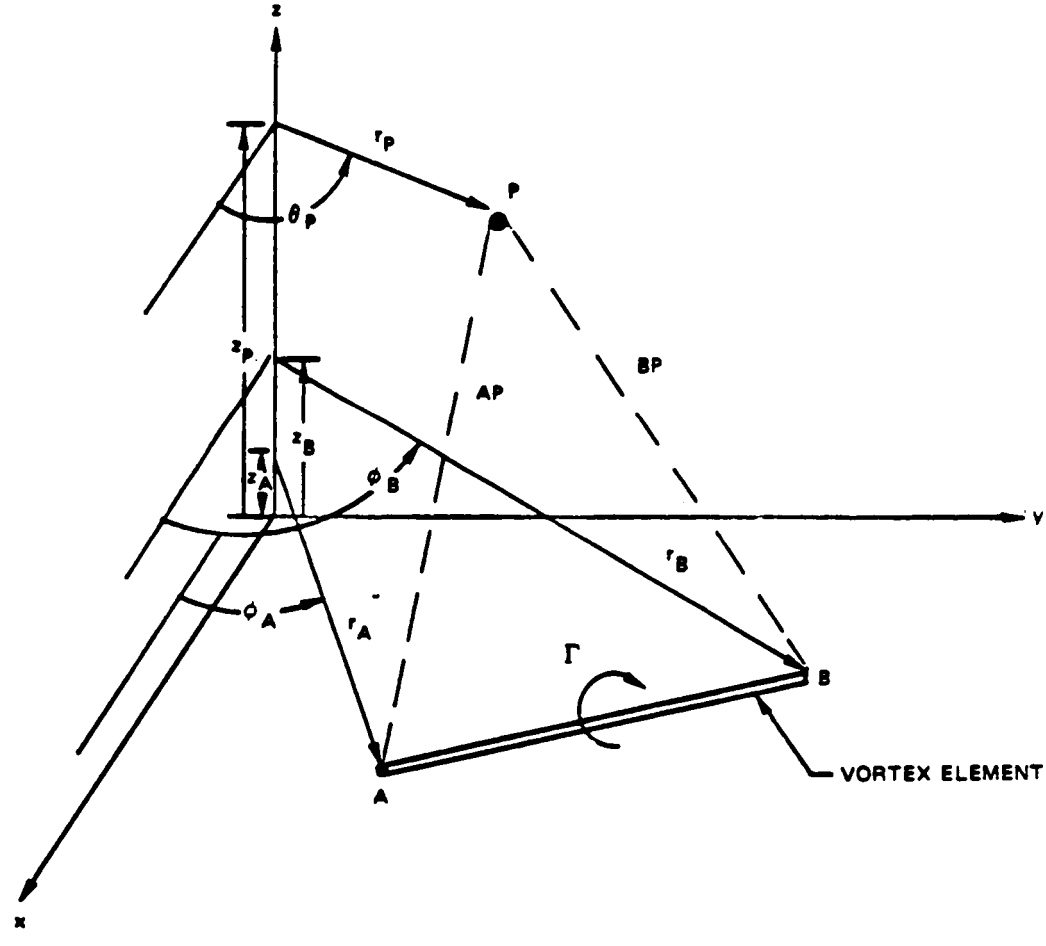

Figure 86. Field Point and Vortex Segment in Cartesian and Cylindrical Coordinate Space

★U.S. GOVERNMENT PRINTING OFFICE: 1989 -627-064/ 86010

NASA
National Aeronautics and Space Administration

Report Documentation Page

1. Report No.	2. Government Accession No.	3. Recipient's Catalog No.
NASA CR-4199		

4. Title and Subtitle

An Analysis for High Speed Propeller-Nacelle Aerodynamic Performance Prediction

Volume I—Theory and Application

5. Report Date

November 1988

6. Performing Organization Code

7. Author(s)

T. Alan Egolf, Olof L. Anderson, David E. Edwards, and Anton J. Landgrebe

8. Performing Organization Report No.

None (E-4382)

10. Work Unit No.

535-03-01

9. Performing Organization Name and Address

United Technologies Research Center
Silver Lane
East Hartford, Connecticut 06108

11. Contract or Grant No.

NAS3-20961, NAS3-22142, and NAS3-22257

13. Type of Report and Period Covered

Contractor Report
Final

12. Sponsoring Agency Name and Address

National Aeronautics and Space Administration
Lewis Research Center
Cleveland, Ohio 44135-3191

14. Sponsoring Agency Code

15. Supplementary Notes

Project Managers, Lawrence J. Bober and Christopher E. Hughes, Propulsion Systems Division, NASA Lewis Research Center.

16. Abstract

A computer program, the Propeller Nacelle Aerodynamic Performance Prediction Analysis (PANPER), was developed for the prediction and analysis of the performance and airflow of propeller-nacelle configurations operating over a forward speed range inclusive of high speed flight typical of recent propfan designs. A propeller lifting line, wake program was combined with a compressible, viscous center body interaction program, originally developed for diffusers, to compute the propeller-nacelle flow field, blade loading distribution, propeller performance, and the nacelle forebody pressure and viscous drag distributions. The computer analysis is applicable to single and coaxial counter-rotating propellers. The blade geometries can include spanwise variations in sweep, droop, taper, thickness, and airfoil section type. In the coaxial mode of operation the analysis can treat both equal and unequal blade number and rotational speeds on the propeller disks. The nacelle portion of the analysis can treat both free air and tunnel wall configurations including wall bleed. The analysis was applied to many different sets of flight conditions using selected aerodynamic modeling options. The influence of different propeller-nacelle-tunnel wall configurations was studied. Comparisions with available test data for both single and coaxial propeller configurations are presented along with a discussion of the results.

17. Key Words (Suggested by Author(s))	18. Distribution Statement
High speed propeller performance Propfan performance Computer code	Unclassified—Unlimited Subject Category 02

19. Security Classif. (of this report)	20. Security Classif. (of this page)	21. No of pages	22. Price*
Unclassified	Unclassified	272	A12

NASA FORM 1626 OCT 86

*For sale by the National Technical Information Service, Springfield, Virginia 22161